Experimental and Numerical Investigation of Adhesively Bonded Composite Patch Repair of an Inclined Center Cracked Aluminium Panel under Static and Fatigue Load

R. Srilakshmi

A Dissertation Submitted to

Indian Institute of Technology Hyderabad

In Partial Fulfilment of the Requirements for

The Doctor of Philosophy

भारतीय प्रौद्योगिकी संस्थान हैदराबाद

Indian Institute of Technology Hyderabad

Department of Mechanical and Aerospace Engineering

September 2014

Declaration

I declare that this written submission represents my ideas in my own words, and where others' ideas or words have been included, I have adequately cited and referenced the original sources. I also declare that I have adhered to all principles of academic honesty and integrity and have not misrepresented or fabricated or falsified any idea/data/fact/source in my submission. I understand that any violation of the above will be a cause for disciplinary action by the Institute and can also evoke penal action from the sources that have thus not been properly cited, or from whom proper permission has not been taken when needed.
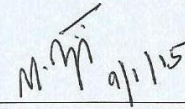
_____
(Signature)
R. Srilakshmi
ME10P001

Approval Sheet

This thesis entitled "**Experimental and Numerical Investigation of Adhesively Bonded Composite Patch Repair of an Inclined Center Cracked Aluminium Panel under Static and Fatigue Load**" by R. Srilakshmi is approved for the degree of Doctor of Philosophy from IIT Hyderabad.
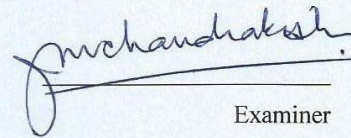
Adviser

Dr. M. Ramji,

Associate Professor

Department of Mechanical and Aerospace Engineering,

IITH

Examiner

Dr. J. M. Chandra Kishen,

Professor

Dept. of Civil Engineering,

Indian Institute of Science, Bangalore.

Acknowledgements

Dedications

To my Mother *&* my Professor

Abstract

Composite patch repair is gaining importance in extending the fatigue life of an aging aircraft. An aircraft, during its service life, it is subjected to severe structural and aerodynamic loads which results from repeated landings and take off, fatigue, ground handling, bird strikes and environmental degradation such as stress corrosion. However due to limited budgets and escalated procurement costs in replacing the aircraft, aircrafts service life need to be extended beyond their design life. Hence, a reinforcement or repair of damaged aircraft is essential to improve its service life. Among various available repair techniques bonded composite repair is mostly preferred. There is lot of research carried out in the safety and life prediction of composite patch repair applied on straight center cracked panels under in plane tensile load. In field, always cracks that appear on structures are of mixed mode and therefore, it is necessary to study the behavior of composite patch repair applied to inclined center cracked panels under in plane tensile static and fatigue loads.

In the present work, a three dimensional finite element analysis (FEA) is carried out to study and compare the performance of single and double sided patch bonded over an cracked aluminum panel (2014-T6) having an inclined crack at 45˚. Carbon fiber reinforced polymer (CFRP) is the patch material chosen as part of this work. From FEA based study, it has been found that in case of single sided repair the stress intensity factor (SIF) at the unpatched surface tends to be higher than that of the unrepaired panel SIF. This is due to additional bending load arising due to shift in neutral axis after repair. Further, there are different parameters such as patch lay-up, patch thickness and patch shape and dimensions which affect the performance of the repaired panel. Out of them, patch shape plays a major role on SIF reduction. A detailed finite element based study has been carried out to arrive at the effective patch shape. Later, a genetic algorithm (GA) based optimization technique is employed in conjunction with FEA to arrive at an optimum patch dimensions resulting in higher reduction in SIF near the crack-tip. Further, to predict the whole field strain over the patch surface and also the shear strain distribution over the thickness of adhesive layer, an experimental investigation has been carried out using digital image correlation (DIC) technique. Lastly, three dimensional fatigue analysis using FEA has been conducted to study the crack growth in repaired and unrepaired panel. DIC is also effectively used to monitor the crack growth during the fatigue loading. The obtained experimental results have been compared with FEA estimates for their accuracy and they are in good coherence. It is found that the static strength and fatigue life of double sided repaired

panel is higher than single sided repaired one. The utility of DIC as an accurate experimental technique for whole field strain prediction in repair applications is shown and turned out to be accurate when compared with FEA prediction thereby recommended for repair studies.

Table of Contents

5. Fatigue Crack Growth Estimation of Cracked and Repaired Panel : FEA and Experiment

6. Conclusions and Recommendations for Future work

Appendix

List of Figures

xiv

List of Tables

Nomenclature

β	Crack inclination angle
K_{I}	Mode I SIF
K_{II}	Mode II SIF
K_{III}	Mode II SIF
$2a$	Crack length in mm
R	Reduction parameter
V_{i}	Relative displacement along y- direction
V_{ii}	Relative displacement along x-direction
V_{iii}	Relative displacement along z-direction
E	Young's modulus
E_{xx}	Modulus in x direction
E_{yy}	Modulus in y direction
E_{zz}	Modulus in z direction
G_{xy}	In plane shear modulus
G_{xz}	Out of plane shear modulus
G_{yz}	Out of plane shear modulus
υ	Poisson's ratio
υ_{xy}	In plane Poisson's ratio
υ_{xz}	Out of plane Poisson's ratio
υ_{yz}	Out of plane Poisson's ratio
C, m	Fatigue material constants
G_{Ic}	Critical interface fracture toughness in mode I
G_{IIc}	Critical interface fracture toughness in mode II
ΔK_{c}	critical value of SIF range
da	crack growth increment
da/dN	Crack growth rate
ΔK_{th}	Threshold SIF value
R	Load Ratio
$\delta_{\max}$	Maximum displacement in mm

P_{max} Maximum Load

F_{xi} Reaction force at crack tip node i along x-direction

F_{yi} Reaction force at crack tip node i along y-direction

F_{zi} Reaction force at crack tip node i along z-direction

u_j, v_j, w_j Displacements at node j along x, y *and* z direction respectively

u_m, v_m, w_m Displacements at node m along x, y and z direction respectively

t_a Adhesive thickness

E_a Young's modulus of adhesive

k_I Stiffness of the adhesive

$k_I{}'$ Stiffness after degradation

μ Shear modulus

G_{ERR} Energy release rate

θ Crack propagation angle

G_{eq} Equivalent energy release rate

K_{eq} Equivalent SIF

ΔK_{eq} Range in equivalent SIF $= (K_{\text{eq}})_{\text{max}} - (K_{\text{eq}})_{\text{min}}$

$u(x,y)$ In-plane displacement fields along x direction

$v(x,y)$ In-plane displacement fields along y direction

ΔK_{eq} Range in equivalent SIF $= (K_{\text{eq}})_{\text{max}} - (K_{\text{eq}})_{\text{min}}$

Abbreviations

SIF   Stress intensity factor

CFRP Carbon fiber reinforced polymer

FCG   Fatigue crack growth

APDL Ansys parametric design language

2D   Two dimensional

3D   Three dimensional

FEA   Finite element analysis

GA   Genetic algorithm

SCF   Stress concentration factor

VCCT Virtual crack closure technique

CZM   Cohesive zone modeling

Chapter 1

Introduction and literature review

1.1 Introduction to repair technology

During the service life of an aircraft, it is subjected to severe structural and aerodynamic loads which results from repeated landings and take off, fatigue, ground handling, bird strikes and environmental degradation such as stress corrosion. These loads cause the damage in the aircraft structure. Figure 1.1 shows the presence of cracks in an aircraft structure due to fatigue load [1, 2]. The Aloha Airlines flight 243 had a major accident due to fatigue in aid with stress corrosion resulting in partial rip of fuselage during flight. Figure 1.1 (b) shows the crack development in south west jet leading to a five-foot hole which got ripped off during midflight in the year 2011.
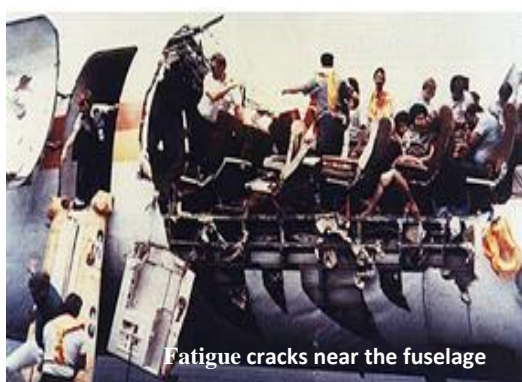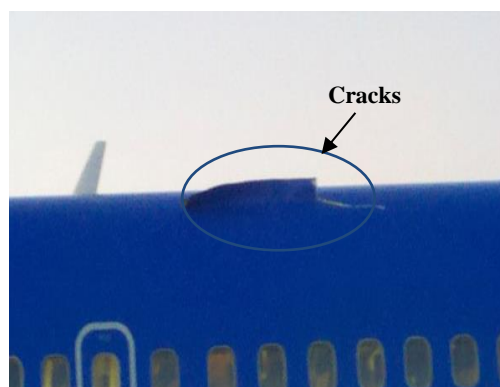
(a)   (b)

Figure 1.1: Fatigue failure in aircraft structure [1, 2] (a) Aloha airlines 243 (b) South west Jet

With age, these cracks are bound to occur under the service conditions. Therefore, repair or restoration of damaged structural parts is a must. The aging aircraft problems can be addressed as: 1) replacement of entire aircraft, 2) replacement of part and 3) part repair. Firstly, aircraft replacement is not a suitable option because of the high cost factor involved. Generally, the approximate cost of common modern day military and commercial aircraft can vary from $18 million to $1 billion. Due to limited budgets and the demand for industry to make a profit creates a need to continue using the current aircraft for a longer time frame

[3]. Part replacement can produce many problems for older aircraft, such as the KC-135 and B-52, parts can be very difficult to obtain because they may not be in production anymore. Parts may have to be specially manufactured, leading to longer waiting periods and high costs. Also, replacing an entire aircraft part takes very long time in training and mission sortie rates, especially in the case of fleet-wide problems. Therefore, part repair is the easiest and cheapest way to address the problem. Hence, repair or reinforcement of damaged aircraft structural component is essential to improve its service life, as opposed to replacing the entire part or airframe. Also it is economically viable and less time consuming.

1.1.1 Bonded repair vs mechanical fasteners

Repair of aircraft involves two options firstly, bolted or riveted mechanically fastened repair and secondly, adhesively bonded repair with either metal or composite patches. Most structural repair manual (SRM) approach recommends use of bolted or riveted metal plates, generally of a similar alloy to the parent material with one gauge thicker. Bolted repairs are easy to fabricate with less installation time. The utmost advantage of this repair technology is that it can be successively disassembled at any time based on the necessity. However, there is lot of disadvantages in bolted repair as compared to adhesively bonded repairs. Baker et.al [3] have carried out experimental fatigue investigation on cracked panel with bolted repairs and boron/epoxy composite doubler under fatigue loading (see Fig. 1.2). They revealed that the fatigue life improvement in adhesively bonded repair is twice that of the bolted repair one.

(a)   (b)
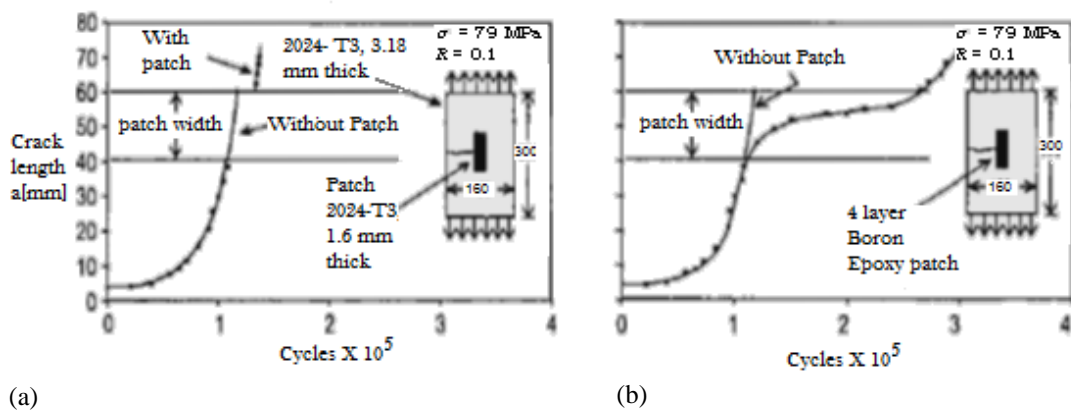
Figure 1.2: Fatigue life assessment of the aluminium panel taken from Ref. [3] (a) bolted repair (b) composite patch repair

However, bolted or riveted repair methodology involves the drilling of holes in the structure which reduces the load carrying capability of these structural members. The main disadvantages of mechanical fastened repairs are: drilling of holes near the damage area

results in high stress concentration at fastener holes, poses difficulty in detecting cracks under the patch as well as corrosion of panel beneath the patch. Adhesively bonded composite repair involves bonding of composite or metal patch over the damage area. These adhesively bonded composite patch repairs have many advantages over mechanically fastened repairs like no new stress concentration produced by new fastener holes, high stiffness-to-weight and strength-to-weight ratios of the patch, patches are readily formed into complex shapes, permitting the repair of irregular components, high fatigue and corrosion resistance of the composite patch and potential time savings in installation. Therefore, adhesively bonded repair technology began to emerge as a viable alternative to mechanically fastened repairs. The two main types of materials used for reinforcements are metals and composites. In order to fulfill the objective of a bonded repair such as restoration of the damaged structure back to its original strength, the most obvious choice of repair material chosen is same as that of the parent structure already made from. Some of the advantages of metallic patches are long shelf life and high coefficient of thermal expansion. A metallic patch repair is able to withstand multi-axial loads and possibly high levels of through-thickness stresses. On the other hand, many repairs are required on structure where the loads causing cracking are in one direction and hence the use of unidirectional composites can produce a much more efficient repair. Nevertheless, metallic patch repair requires careful surface treatment as they are susceptible to corrosion and fatigue. Finally, metals give themselves best to relatively flat repair locations due to the difficulty in accurately forming a metallic sheet to a curved profile. This is one of the distinct strength of composites where the desired shape can be easily formed during the repair by curing depending on the panel geometry.

Repair of aircraft aluminium structures using composite patch has been initiated by Baker et al. [3] in the early 1970s mainly in order to enhance fatigue life of cracked components. Figure 1.3 shows the application of composite patch repair in the lower wing skin of F-111 aircraft and near the fuselage of commercial aircraft such as Boeing 787 [5, 6].

(a)

Application of adhesively bonded patch repair over the fuselage
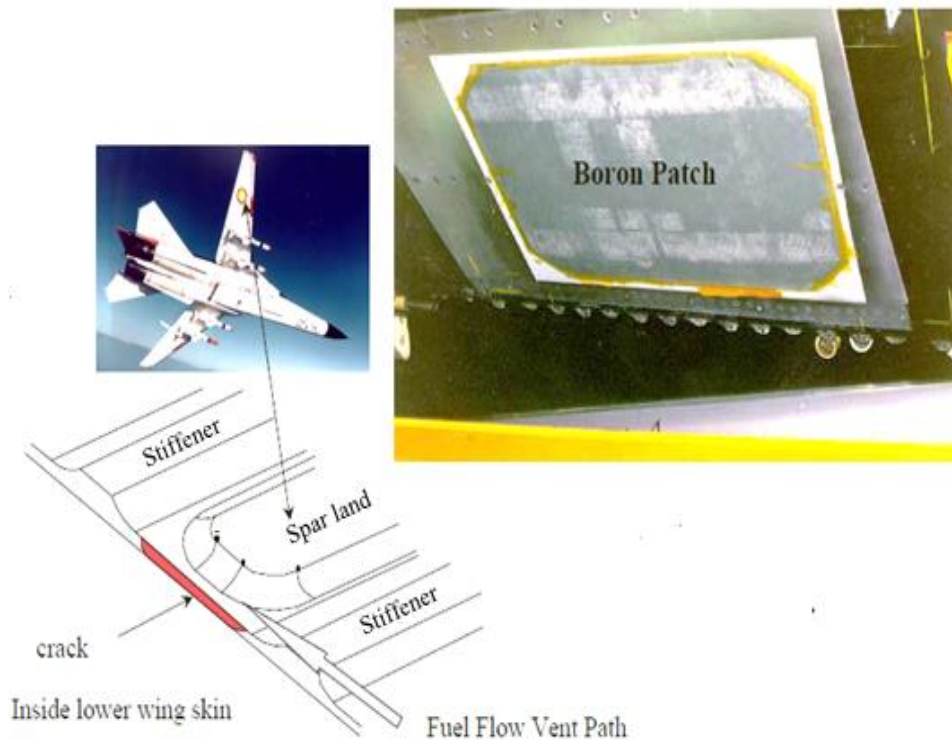
(b)

Figure 1.3: Bonded patch repair applied at the lower wing skin and fuselage taken from Ref. [5, 6] (a) F-111 aircraft wings (b) Boeing 787 aircraft fuselage

These repairs can be possibly achieved by using bonded patches made of unidirectional composite over the cracked area. The bonded repair reduces stresses in the cracked region and prevents the crack from opening and therefore from growing. From geometrical consideration, bonded repairs fall into two main categories: double sided (symmetric) and single sided (asymmetric). Figure 1.4 shows the schematic representation of single and double sided patch repair configuration. In most of the practical cases, both sides of the cracked panels are not available to perform a symmetrical repair. Therefore, single sided repair is often adopted such as in case of aircraft wings [4].
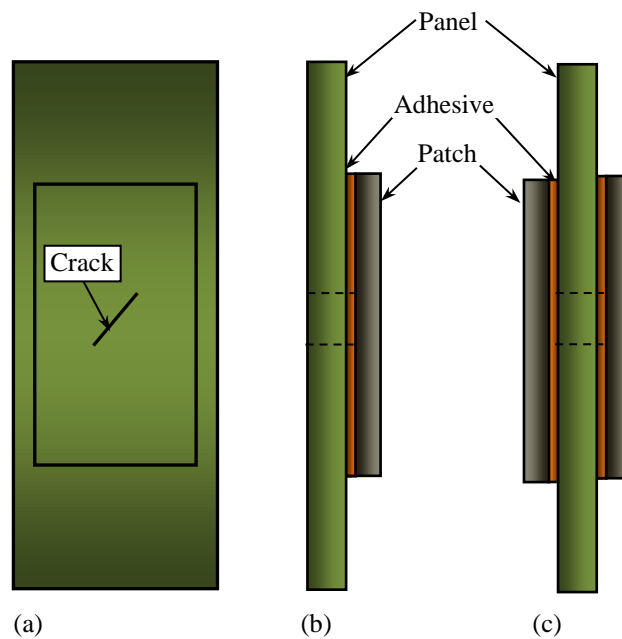
Figure 1.4: Schematic of adhesively bonded composite patched panel
(a) front view of the panel (b) side view of single sided patched panel
(c) side view of double sided patched panel

However, from technological aspects composite repair is categorized as active and passive repair. Over the last two decades, the performance of the repaired structure is analyzed by employing passive patch work methodology. In recent years, attention has been paid by the researchers to explore active patch repair by incorporating smart materials [7]. In active patch repair, the smart patches made of piezoelectric actuators are used which can enable the active restoration of strength and stiffness of repaired structure by introducing a local moment / force in opposite sense thereby reducing the stress intensity factor (SIF) [8]. This technique is still employed at lab scale and more work needs to be done in that direction for making it to the certification stage.

5

1.1.2 Elements of fracture mechanics

Understanding the failures of the structures and components subjected to different types of loading is very important for design engineers. It is well known fact that the presence of the flaws such as crack, sharp notches etc. in these engineering structures and components reduces their strength considerably and is mainly responsible for initiation of cracks, further leading to complete fracture under service load. The presence of the crack results in the redistribution of stresses and strains around the crack-tip. Knowledge of the stress field around the tip of such cracks is of big importance for the economic design of the structural component and the estimation of the structure's residual strength. Stress field in any linear elastic cracked body is given by Eq. 1.1:

$$\sigma_{ij} = \frac{K}{\sqrt{2\pi r}} f_{ij}(\theta) \qquad (1.1)$$

where, σ_{ij} is stress tensor, r and θ are defined in Fig.1.5 (a) and K is stress intensity factor (SIF). From the above Eq. 1.1, it is observed that the stress near the tip is proportional to $1/\sqrt{r}$. As r approaches zero the stress becomes infinity, thus the stress near the tip varies with $\sqrt{r}$ singularity for elastic case. For example, when the cracked panel is subjected to a uniform remote tensile stress, the portion of that region near the crack tip, where the stress field σ_{yy} approaches a constant value σ_{∞}, is called singularity dominated zone and is shown in Fig. 1.5 (b). To characterize the amplitude of the stress values near the crack tip SIF is introduced [9]. SIF depends on the far field stress (σ), flaw size (a), component geometry and the mode of loading.

(a)   (b)
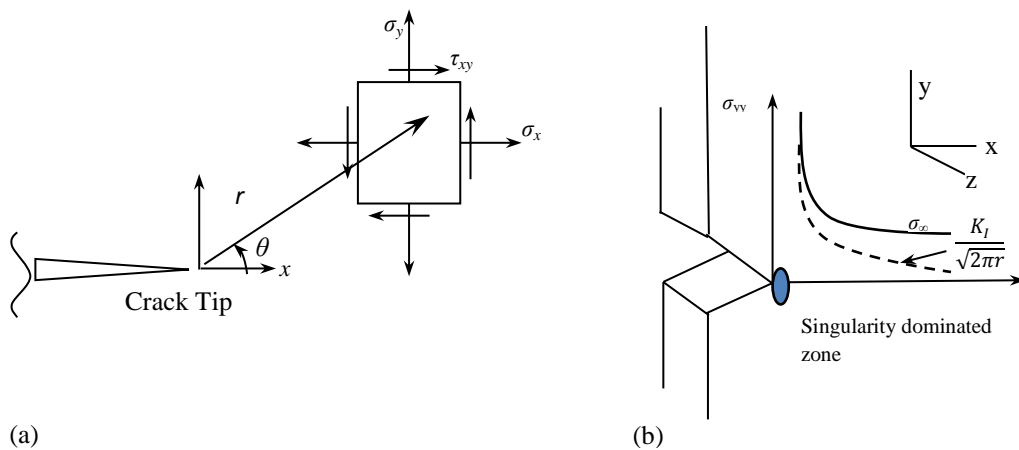
Figure 1.5: Stress state near the tip (a) coordinate system with respect to crack tip (b) stress normal to the crack plane in mode I problem [9]

There are three different modes of loading that can be applied to cracked body. Firstly, Mode I also called as opening mode where the principal load is applied normal to the crack plane, and it tends to open the crack face. The crack tip displacement is normal to the loading direction. Mode II corresponds to in plane shear loading and they tend to slide one crack face with respect to the other. In sliding mode crack tip displacement is parallel to loading direction. Lastly, Mode III refers to out of plane shear also known as tearing mode. In mode III loading, the crack plane displacement is out of plane and crack front displacement is normal to loading. Figure 1.6 illustrates the three modes of fracture. In practical applications cracks that appear are of mixed mode nature predominantly.

(a)   (b)   (c)
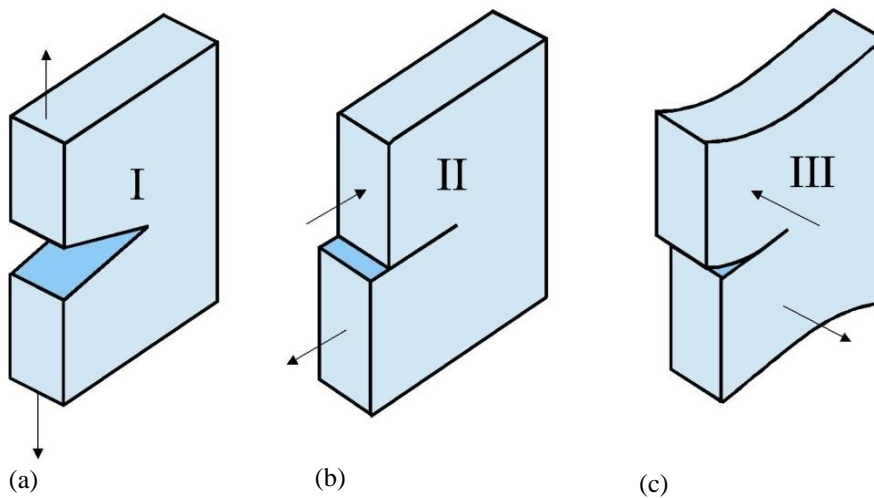
Figure 1.6: Schematic of different modes of cracks (a) opening mode (Mode I) (b) sliding mode (Mode II) (c) tearing mode (Mode III) [9]

An inclined crack in a component can be modelled as a superposition of the three modes, where the effect of each mode can be analysed separately under linear elastic fracture mechanics (LEFM) frame work. All three SIF's need to be estimated individually and can be evaluated analytically, numerically and experimentally [9-15]. Most of the analytical solutions are based on highly idealized models of the component geometry and give the basic relations between the parameters affecting the fracture. Analytical closed-form solutions are available for various simple configurations [11]. However, analytical techniques are rigorous and mostly applicable for simple geometries. For complex configurations, SIF need to be extracted by numerical analysis. Off late, finite element method (FEM) has gained lot of popularity in area of the computational fracture mechanics and it has become a separate domain by itself. A variety of methods are used to compute the SIF based on results obtained from FEA [12-15]. They are virtual crack closure technique,

7

J-integral approach and displacement extrapolation technique. In the virtual crack closure method (VCCT) the crack is physically extended, or closed, during the finite element analyses. The method is based on the assumption that the energy E is released when the crack is extended by Δa from a to $a+ \Delta a$ is identical to the energy required to close the crack. In this method the energy release rate is calculated from the global forces on a structural level are multiplied with global deformations [13]. From the energy release rate the SIF's are estimated using VCCT [13] and it can only be applied for linear elastic fracture mechanics problem.

In the *J*-integral approach, SIF is estimated by computing the *J*- integral value locally at the crack front and the displacements ahead of the crack tip. It is a straight forward approach since the path independent contour integral can be obtained directly by using the finite element technique. In recent scenario, the *J*-integral approach gradually became an attractive alternative to *G* or *K* in studying elastic-plastic fracture problems [12, 14].

In the displacement extrapolation approach, SIFs are estimated from the relative displacement of the pair of nodes on either side of the crack face in local modes I, II and III orientations. From these relative displacements, crack tip displacement is extrapolated, and subsequently the SIFs are assessed. This approach can be applied for linear elastic fracture mechanics problems [15].

1.1.3 Composite materials: an overview

A composite material consists of two or more constituents that are combined at a macroscopic level which are not soluble in each other. One constituent material is called the reinforcing phase and the other one in which it is embedded is called the matrix. The reinforcing phase or discontinuous phase material is in the form of fibers, particles, or flakes. The matrix phase materials are generally continuous such as epoxy, polyester etc. Examples of composite systems contain concrete reinforced with steel and epoxy reinforced with carbon fibers. In the highly competitive airline industry, one is looking for way to lower the overall mass of the aircraft with high stiffness and strength resulting in lower operating cost. This is possibly achieved by using composite materials [16]. Composites offer several other advantages over conventional materials. They include improved strength, stiffness, low density, fatigue and impact resistance, thermal conductivity, corrosion resistance, etc. have rapidly increased its application in various engineering fields like aerospace, automobile and marine. Especially in aircraft structure lot of composite applications has come into the fore. Even if the composite material costs may be higher, the reduction in the number of parts in an assembly and the savings in fuel costs make them

more profitable. Composites are used extensively in both military and commercial aircrafts. Figure 1.7 (a) shows the application of composite material as speed brake in the military aircraft such as Vought A-7 [16]. Usage of this speed brake in military aircraft reduces its weight by one third of its weight compared to metallic alloy. Figure 1.7 (b) shows the usage of composite material in various parts of Boeing F-18. Reducing 0.453 kg of mass in a commercial aircraft can save up to 1360 liters of fuel consumption per year and fuel expenses are nearly 25% of the total operating costs of a commercial airline [16].

(a)   (b)
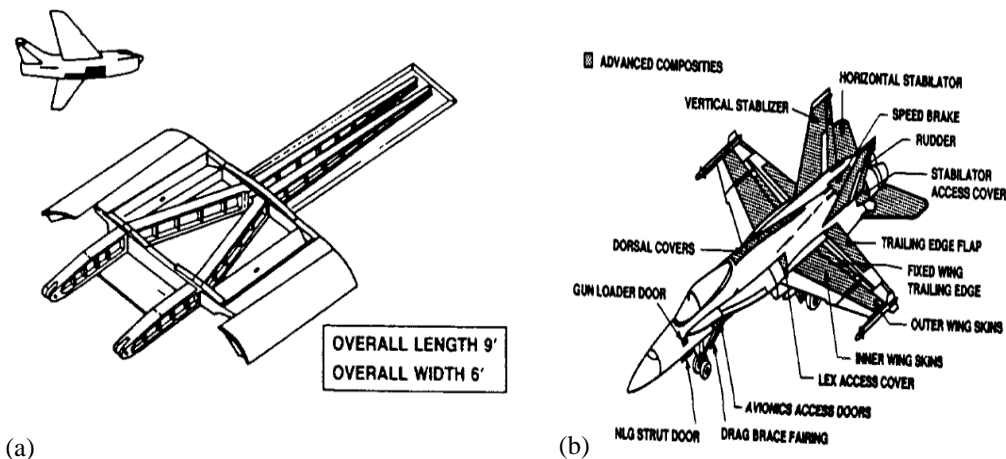
Figure 1.7: Application of composite materials in aircraft components (a) speed brake of military aircraft (b) usage of composite materials in different parts of Boeing aircraft [16]

In real life applications, any mechanical components are subjected to the several harsh static and fluctuating loads. There is a chance of failure of these structural components made of lightweight Aluminium alloys. As these structures are subjected to damage during its service life, for enhancing its structural integrity adhesively bonded patch repair work is preferred. Mostly carbon fiber reinforced polymers (CFRP) are used as the patch material [17].

1.1.4   Design considerations in adhesively bonded patch repair

The ultimate aim of a repair is to restore the panel to its original state capable of bearing its intended design load. Repaired panels should not only meet previous static strength requirements, but also fatigue strength recommendations. Hence, the repair must be adequately carried out without any further degradation of the parent structure. The repair methodology should be able to arrest or substantially retard future crack growth, while still maintaining required design strength. In adhesively bonded patch repair, there are many parameters which influence its performance. They are broadly classified as patch and adhesive parameters. In bonded repair, the applied load is transferred to the patch through

the adhesive. Adhesive layer is the weakest link therefore choice of adhesive material and it's thickness is very important. It is found that good adhesive bonds can be formed only in a small range of thickness (typically 0.1 mm–0.25 mm) [3]. As the thickness of adhesive is more it tends to act as porous and weak where as thin adhesive bonds are too stiff and brittle, thus, thickness of adhesive layer is also an important issue while designing an efficient repair. From literature it is found that thin adhesive layer perform better than the thicker one.

The other important factor of the repair design process is selection of adhesive material. Two adhesive types that are commonly used for bonded repairs are the epoxies and modified acrylics. Epoxies are normally available in both paste and film form. Film adhesives have the resin and curing agents are pre-mixed and then coated onto a thin carrier cloth or scrim made in the form of a thin film. The film adhesives are easier to apply and easy to achieve uniform thickness bond thickness. The main drawback of film adhesive is increased cost and the resin starts curing as soon as the hardener is mixed and therefore film adhesives must be refrigerated to provide a reasonable shelf life. Paste adhesives come in one or two-part mixture and are prepared (mixed) and spread manually using a spatula or applicator gun with nozzle. Two-part paste adhesives, which use chemical curing agents rather than heat as catalysts, reduce the need for refrigerated storage of the adhesives [3]. Therefore, two part epoxy based adhesives AV138/HV998 and Araldite 2011 are used in this study. These adhesives are generally classified as brittle, intermediate and ductile in nature. AV138/HV998 adhesive material is of brittle by nature whereas Araldite 2011 which is of intermediate in nature (brittle and ductile). Depending upon the combination of parent panel and patch material one can choose the kind of adhesive. Typically, failure of the adhesive layer happens in the form of peel and cleavage failures. These failures can be avoided by providing patch tapering at the overlap ends, or increasing overlap length as suggested by Baker et al. [3].

Surface preparation is also one of the important factors which influence the durability of the repair. The strength of the adhesive bond is the most critical aspect of the bonded repair technology. Durability of the repair and patched component is largely determined on the pre-treatment (surface preparation) of the metal surface. Primary considerations of these pre-treatments are simplicity and safety. There are different surface preparation process are mentioned based on the panel material [18]. The different surface preparation process that are preferred for the aluminium alloy panel are FPL etching (Sulfo-Chrom etch), Phosphoric acid anodize (PAA), P2 etch (Sulfo- Ferric etch) and Chromic acid anodize (CAA) method [18].

Selection of the patch material is also one of the important parameter which affects the performance of repair. To improve the static strength as well as fatigue strength of the repair, patch material chosen for repair should have static strength greater than or equal to the parent material. There are different types of composite materials such as boron/epoxy, graphite epoxy, glass epoxy and carbon epoxy are used as patch materials by various researchers [3, 14]. The boron/epoxy composite patch material have been widely used by the Australian for repair of military aircraft due to its high strength and high stiffness composite and also it allows the use of thinner repairs. Because of less availability and high cost of Boron/ epoxy composite system Carbon/epoxy is used as the patch material in this study. CFRP is an extremely strong and light which contains Carbon fiber in an epoxy matrix. CFRP has been widely used in various applications especially in aerospace, marine, automotive and sports industries. Because of their low density, high tensile strength and rigidity, excellent resistance to impact and corrosion, easy formability lead to wider applicability of CFRP in repair applications as a patch material.

1.1.5 Experimental techniques for strain measurements

Traditionally, researchers have used reflection polariscope [19] and strain gauges [20], for strain measurements in repair study. Reflection photoelasticity involves bonding of a reflective coating layer on to the specimen. It is not a straight forward process and one has to be adept in bonding the coating layer on to the specimen. In case of strain gauges measurement is highly localized and one cannot get the whole field strain distribution. Of late, digital image correlation (DIC) is used in the field of experimental mechanics due to its accuracy and relatively simple optics capable of whole field estimation of displacement and strain. The DIC refers to the class of non-interferometric, non-contact optical methods of experimental stress analysis that acquire images of an object, store these images in digital form and perform image analysis to extract full-field shape and deformation measurement [21-23]. It directly provides information about the displacements and strains by comparing the digital images of the specimen surface in the un-deformed (or reference) and deformed states respectively. In principle, DIC is based on pattern matching and numerical computing [22]. In DIC, one of the most commonly used approaches employs random patterns and compares sub-regions (subsets) from 'un-deformed' and 'deformed' images to obtain a full-field sensor-plane measurements [21]. The basic principle of DIC is the matching of the small subsets between the digitized images of the specimen surface recorded in un-deformed (reference) and deformed state as schematically illustrated in Fig. 1.8. The matching process is performed to locate the corresponding position of each reference subset within each

deformed image. In order to evaluate the degree of similarity between the subsets from reference image and the deformed image, a zero-normalized cross-correlation (C) coefficient is used which is defined in Eq. 1.2:

$$C(u,v) = \frac{\sum\limits_{i=1}^{m}\sum\limits_{j=1}^{m}\left[f(x_i,y_j)-\overline{f}\right]\left[g(x'_i,y'_j)-\overline{g}\right]}{\sqrt{\sum\limits_{i=1}^{m}\sum\limits_{j=1}^{m}\left[f(x_i,y_j)-\overline{f}\right]^2}\sqrt{\sum\limits_{i=1}^{m}\sum\limits_{j=1}^{m}\left[g(x'_i,y'_j)-\overline{g}\right]^2}}$$
(1.2)

where,

$\overline{f}$ = mean intensity value of reference subset

$\overline{g}$ = mean intensity value of deformed subset

$$x' = x + u_0 + \frac{\partial u}{\partial x}dx + \frac{\partial u}{\partial y}dy$$

$$y' = y + v_0 + \frac{\partial v}{\partial x}dx + \frac{\partial v}{\partial y}dy$$

where, $f(x, y)$ and $g(x', y')$ represent the gray levels of reference and deformed images, respectively; and (x, y) and (x', y') are the co-ordinates of a point in the subset before and after deformation respectively. Once the maximum value of this correlation coefficient is detected, the position of the deformed subset is determined. Then, in-plane displacement vector at any point can be calculated using the difference in the positions of the reference subset center and the deformed subset center [21].
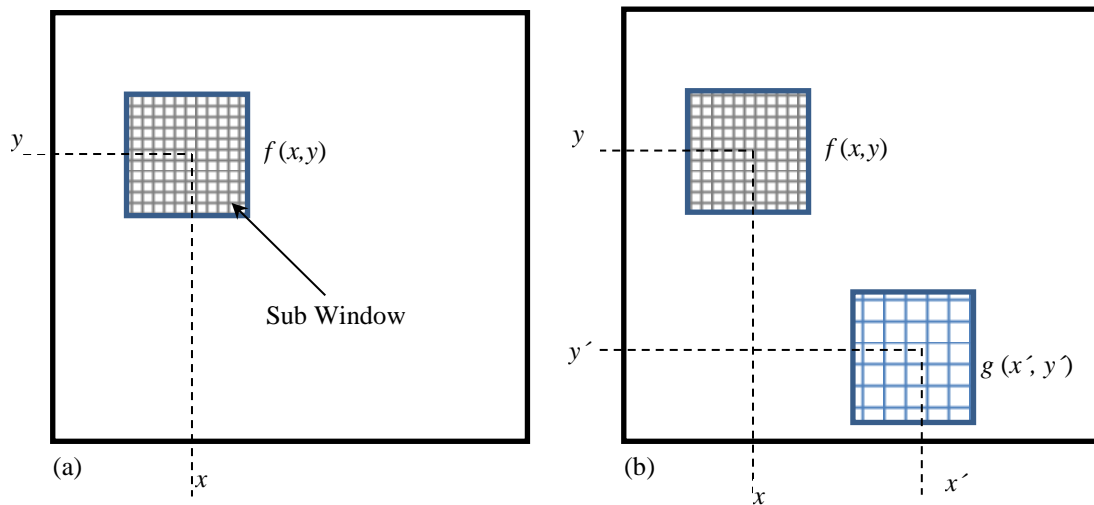
Figure 1.8: Schematic of subset matching in DIC technique (a) un-deformed state (b) deformed state

In many fields, experimental estimation of material properties and prediction of whole field strain distributions is more important and desirable. But, less work has been focused on the reliable estimation of strain fields from the displacement field given by DIC [21]. Probably, this can be attributed to the fact that the displacement gradients or strains can be directly calculated using the Newton-Raphson method. Typically, the relationship between the strain and displacement can be described as a numerical differentiation process. The numerical differentiation process is considered as an unstable and risky, because it can amplify the noise contained in the computed displacement. Therefore, the resultant strains are unreliable if they are calculated by directly differentiating the estimated noisy displacements [21]. There are different algorithms which are developed for smoothing the displacement field followed by a numerical differentiation of the smoothed data to get the in-plane strain components [24-26]. More recently, Pan et al. [27] used the point wise local least-squares fitting technique for strain estimation. They proposed that this technique is a simpler and most effective one for the calculation of strains for the points located at the image boundary, hole, cracks and the other discontinuity areas.

There are two configurations being used in DIC, namely 2D and 3D setup and its schematic is shown in Fig. 1.9. In 2D DIC [23], the plane surface of the specimen is observed by a single camera and is preferred for measurement of in-plane displacements (see Fig. 1.9 (a)). Investigators have extended DIC concepts to stereovision systems. A typical stereovision system employs two or more cameras to record digital images of a common object region from two or more viewpoints. In 3D DIC, the surface of the specimen is observed by two cameras as shown in Fig. 1.9 (b). It involves detailed calibration procedure to get distance in terms of camera coordinate system. Once the cameras are calibrated, the sensor plane locations in the two views for the same object point can be used to determine an accurate estimate for the three-dimensional position of the common object location. After the calibration, the image acquisition process is synchronized so that both the camera acquires images simultaneously after triggering. In case of 3D DIC, one can get out of plane displacement in addition to in plane displacement and strain. The method has seen remarkable growth in recent years, with applications in various fields. The 3D-DIC system is theoretically capable of extracting accurate, in-plane surface deformations, even when the object is undergoing large, three-dimensional rigid body rotation and translation.
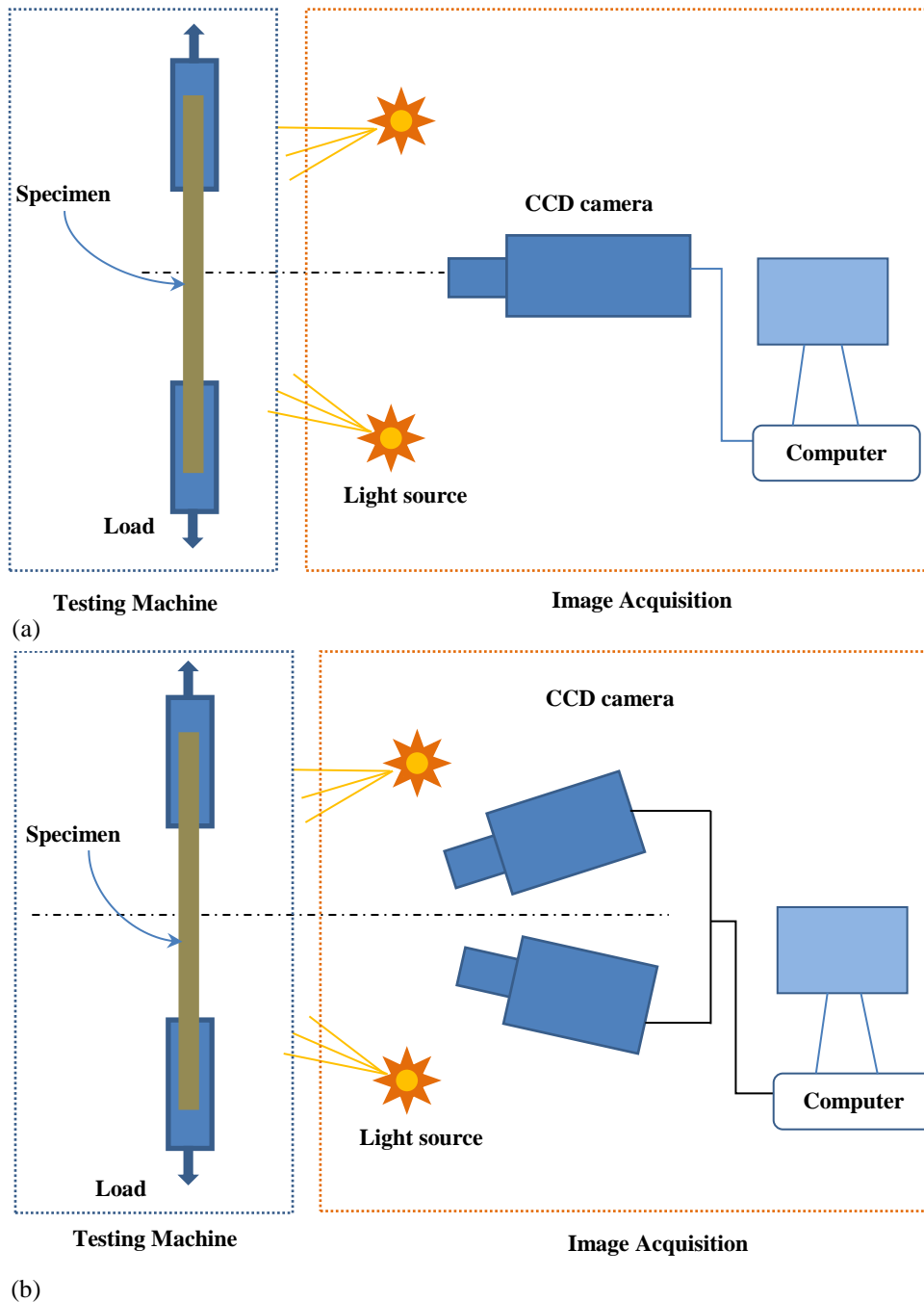
Figure 1.9: Schematic of data acquisition system (a) 2D DIC set up (b) 3D DIC setup

The method of DIC has many advantages over other optical methods. Firstly, any class of material could be studied and the specimen surface preparation is simpler. Secondly, optics involved is quite simpler. Thirdly, the displacement information is retrieved by direct comparison of the speckle patterns before and after deformation, therefore no fringe analysis and phase-unwrapping is needed in this method. Fourthly, there is no fringe density

limitation in DIC, so the measurement range is much larger than other techniques. Additionally, it is truly a non-contact by nature and provides full field data.

Nevertheless, DIC still suffers some disadvantages. It requires specimen with random speckle pattern and needs optical access to the specimen. It is sensitive to light fluctuations and rigid body motion. It requires moderately large amount of computation time and poses difficulty of correlation at the edge. It does not provide full-field strain resolution better than 0.1%. The DIC technique provides displacement resolution of sub-pixel accuracy typically $1/50^{th}$ of a pixel and the maximum strain accuracy is of the order of 0.02 %. The least strain that can be measured using DIC is 50 micro strain [28].

1.1.6 Introduction to fatigue loading and crack growth study

Generally, aircraft structures are subjected to fluctuating loads during their service life. These fluctuating loads are generally of two types, firstly, constant amplitude cyclic load and secondly, variable amplitude load. Mostly from academic stand point constant amplitude cycle is studied in case of fatigue crack growth study. Figure 1.10 shows the constant amplitude cyclic loading having maximum stress σ_{max} and minimum stress σ_{min} with the stress range $\Delta\sigma$ given by:

$$\Delta\sigma = \sigma_{max} - \sigma_{min} \tag{1.3}$$

It can be expressed in terms of SIF as $\Delta K = K_{max} - K_{min}$ which is a driving parameter for determining crack growth rate. Another important parameter is the stress ratio

$$R = \frac{\sigma_{min}}{\sigma_{max}} = \frac{K_{min}}{K_{max}} \tag{1.4}$$
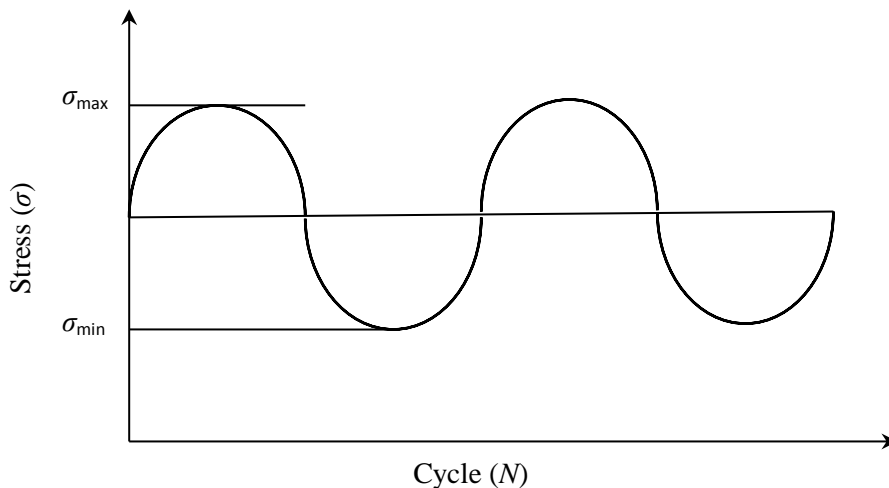
Figure 1.10: Constant amplitude cyclic loading

Generally, fatigue failure involves three main stages: crack initiation, stable crack propagation and final failure [29]. Initiation of crack generally occurs due to coalesce of the

micro voids or dislocations. This initiation of crack happens at high stress concentration regions such as notch, an inclusion or surface defects. The total failure life of a component is divided into initiation period and propagation period. The number of cycles required to initiate a crack and then make it grow to a detectable length is known as initiation life; on the other hand the number of cycles required to grow the smallest detectable crack to a critical size is known as propagation life. Stable crack propagation period is an important phase where principles of fracture mechanics are applied. This prediction of critical crack size is the ultimate goal for the prevention of catastrophic failure of cracked or damaged components. By selection of appropriate repair technique, one could increase the propagation life by retarding the crack growth in repaired structure. The driving force for fatigue crack growth (FCG) is influenced by ΔK which characterizes the inherent stress riser near the crack tip and can be used to predict the crack growth. Generally, ΔK and crack growth data are represented on a log – log plot of crack growth rate (da/dN) versus ΔK as shown in Fig. 1.11 taken from Ref. [9]. Typically, the log – log relationship between ΔK and da/dN characterizes three stages of crack growth. Firstly, region I is the near-threshold region in which very slow crack growth occurs and where no growth occurs below a threshold value of ΔK ($da/dN \sim 10^{-9}$ m/cycle), denoted as ΔK_{th}. Region II is the linear, steady-state region of the crack growth curve. Lastly, Region III corresponds to rapid and unstable crack growth as final fracture is approached when ΔK equals critical SIF (ΔK_c), the fatigue fracture toughness of the material. The linear region of log – log data is described by Pari's equation (crack growth law) as given in Eq.1.5:

$$\frac{da}{dN} = C \Delta K^m \tag{1.5}$$

where C and m are empirical constants defining the linear portion of the curve through the slope and y intercept [30]. The application of Paris law, describing stage II of the crack progression, is sufficient for most aerospace material applications due to the fact one is mostly interested in predicting growth of existing cracks during reasonably stable growth periods.
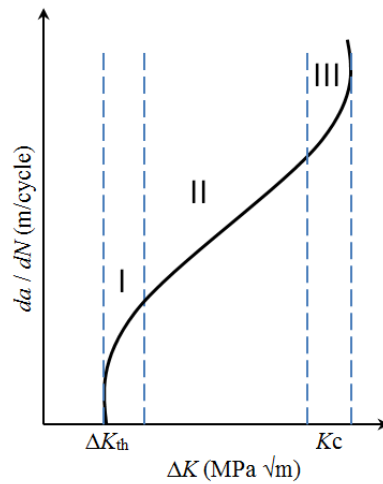
Figure 1.11: Schematic of crack growth rate vs number of cycles (Sigmoidal curve) [9]

From the fracture mechanics point of view mixed mode loading is the combination of two or more types of loading. The mixed-mode cracked panel with static and fatigue loads behaviour is different as compared to mode I situation. In practical cases, mostly mixed mode cracks develop and therefore study about them is of practical importance.

1.2 Motivation

Based on the introduction, fracture analysis of repaired aluminium panels using adhesively bonded composite patches are mainly focused on the safety evaluation and life prediction under mode-I loading. However, in practical applications, aircraft structures are subjected to various kinds of loading resulting in development of cracks of mixed mode nature in it. Study of bonded repair applied to mixed mode loading is quite complex and is of practical relevance. Further, study of the behavior of such repaired panel having an inclined crack under both static and fatigue load is fundamental. A detailed study about the mechanics of single and double sided CFRP patch repaired panel under tensile load need to be carried out. There are various patch and adhesive parameters which influence the performance of the repaired panel and it needs to be carefully studied for arriving at optimum parameters towards maximum performance. Experimental stress/strain analysis of the patch repaired panel under tensile or fatigue loading needs to be carried out to predict its actual behavior. Finally, the fracture process in the repaired panel needs to be captured from the design perspective.

1.3 Literature review

There has been extensive research has been carried out on repair of aircraft structures. The following sub sections describe the summary of literature review pertaining to engineering and design issues involved in the adhesively bonded repair of cracked metallic panels.

1.3.1 Mechanics based study of composite patch repair

In practical applications, single sided and double sided patch repair are applied based on requirement and space availability. Single sided repair is mostly preferred for repair of aircraft wings. Whereas applying patches to both sides of a plate containing a crack reduces the SIF at the crack tip greater than that of a patch on one side of the panel [3, 4]. A single-sided repair causes a shift in the neutral axis of the patch and panel system away from the center of the panel. As a result, a significant bending field is induced in addition to in-plane tensile load, which increases the SIF at the crack tip beyond the value compared to an equivalent two-sided patch repaired panel. This bending stress reduces the repair efficiency and hence fatigue life of the repaired panel gets lower. Jones [31] developed theoretical and design aspects for predicting the loss in efficiency due to single sided repair. They have proposed that usage of unbalanced lay-up configuration reduces the SIF in the single sided repaired panel. Wang et al. [32] investigated the variation in SIF for a single sided repaired panel and double sided patch repaired panel. They proposed that the variation in SIF is higher in single sided repair than the two sided patch repaired panel. They found that SIF does not increase indefinitely to the crack length, but instead approaches asymptotically a finite upper limit. They have also further derived an analytical expression to determine the upper bound of SIF, providing a conservative estimate suitable for design purposes and parametric studies. Later on, considerable studies have been performed in composite patch repair areas by various experimental and numerical methods.

Over the last two decades, an enormous development has taken place in the field of FEA and in particular its application of composite repair [31 -70]. The determination of SIF at the crack tip is one of the means for analyzing the performance of the bonded patch repaired panel. Naboulsi and Mall [33] established the three-layer technique using FEA. They have introduced this technique using Mindlin plate elements to model the cracked aluminum plate, adhesive and composite patch. Their study investigated the effects of geometric nonlinearity on the damage tolerance of the cracked plate by computing the SIF and fatigue crack growth rate in the cracked panel. Umamaheswar and Ripudiman Singh [34] performed FEA of single sided patch repairs applied to thin aluminium plate having straight center crack. They reported that single sided patch repairs lead to large rotations involving non-

linear analysis. They also showed the SIF variation across the thickness of the panel assuming straight crack fronts. Further they discussed the effect of adhesive and patch thickness on the repair configuration.

Chukwujekwu Okafor et al. [35] conducted both experimental and FEA for analyzing the stress distribution of cracked plates repaired by octagonal patches. They found that the zone of maximum stress shifted from the crack front (for a cracked specimen) to the edge of patch (for the patched specimen) due to high peel stress development at the patch overlay edge. The peel stresses in bonded joints normally peak at the overlap edge, which in turn can cause failure of the adhesive layer there by reducing the performance of the repair. To reduce the severity of peel stresses occurring at the overlapped ends, Duong [36] suggested usage of tapered composite laminate. Tsamasphyros et al. [37] has conducted numerical and analytical study of composite patch repair of a straight cracked panel. In their investigation they have performed analytical study on Rose's equation. They have found that the results obtained by both FEA and analytical methods are in good agreement with double sided repair and is not same in case of single sided repair due to existence of additional bending stresses. Sabelkin et al. [38] have been performed experimental and numerical analysis to characterize strain distribution, out-of plane displacement, curing temperature and fatigue crack growth rate of thin aluminium panel repaired by the single sided bonded patch. All the above research is pertaining to the mode I cracked panels and none addresses the repair of mixed mode cracked panels. Bachir Bouiadjra et al. [39] has conducted FEA to estimate SIF in single and double sided repairs in mode I and mixed mode edge cracked panels. They have shown that the adhesive and patch properties have a significant and beneficial effect on the symmetrical patch. All these previous works does not thoroughly investigate the effect of additional bending stresses that developed in single sided patch repair.

1.3.2 Optimization study of patch repair

There are many patch parameters like patch thickness, patch lay-up, patch shape and adhesive parameters which influence the performance of the repair. Mahadesh Kumar and Hakeem [40] conducted the numerical analysis for optimum patch shape in case of symmetric repair of center cracked panel. They have studied the effect of different patch shapes of circular, elliptical and rectangular and have estimated SIF reduction. They proposed that skewed shape patch is the most optimum shape patch for double-sided repair of center cracked panels. A skewed patch resembles a dickey bow shape of the dimension perpendicular to the crack less than the dimension parallel to the crack. They have found

that the skewed shape reinforces more of the high stress area and less of the low stress area resulting in a lower SIF [40].

But their work dealt with only mode I crack problem. Albedah et al. [41] have conducted FEA to estimate SIF for single and double sided repairs having a circular patch shape. They have compared the mass gain for both the cases. Recently, Rachid et al. [42] have found that the *H* shape patch performs better than the rectangular patch. They also concluded that the *H* shape patch with arrow heads improves the performance of the bonded repair. But they considered only mode I crack for their analysis. Bouiadjra et al. [43] have carried out the FEA to compare the repair performance of patches with rectangular and trapezoidal shapes applied to mode I problem. They concluded that the trapezoidal patch shape works far better than the rectangular patches up to certain crack length. Ouinas et al. [44-46] have carried out 2D FEA to analyze the mechanical and geometrical properties of patch on SIF reduction. They have considered octagonal and semi-circular patch in their study. They found that the patch geometry and adhesive properties influences the SIF reduction in the repair of mode I cracked panel. Mathias et al. [47] have conducted genetic algorithm (GA) based optimization analysis for getting optimum ply orientations and patch shape in case of repair of aluminium plate having a center hole. They have used (CFRP) as patch material. Brighenti et al. [48] have employed GA based optimal search processes for finding the optimum patch shape applied to the straight center cracked panel. They have found that skewed patch performs best for such panel. All the research is on the estimation of optimum patch shape preferred to mode I cracked panels.

Composite patch stacking sequences, or patch lay-up orientations is another important parameter which offers significant improvements in fatigue life. In the mode I condition the patch with lay-up configuration of [90°] to the crack performs well and that achieves greatest reduction in SIF [49, 50]. Previous research studies proposed that combination of [90°], [45°] and [0°] acts as an optimal lay-up configuration for mixed mode cracked panel [50].

Adhesive is the weakest link which fails first under applied loads. Adhesive thickness and adhesive properties play a role in the repair design. Ait Yala and Megueni [51] have adopted experimental design method to investigate the effect of patch thickness and adhesive properties in order to achieve an optimization of the repair configuration.

Another design factor is the optimum patch dimensions such as patch length, width and thickness. Patch width depends on the crack length and a patch length chosen should depend on the shear stress of the adhesive and thickness of the panel to be repaired [4]. Patch thickness depends on the stiffness ratio [4]. There is very limited research study exists on

the estimation of optimum patch dimensions applied to an inclined center cracked panels involving GA optimization technique.

1.3.3   Fatigue crack growth study

Tay et al. [52] have carried out the experimental investigation of an aluminum panel with a cracked bolt hole repaired with the Boron FRP patch. They showed that the patched specimens with the press fitting plugs survived longer than the notched specimens with a very little crack growth. Schubbe and Mall [53] have conducted the experimental analysis on the FCG behavior of both thick and thin aluminum panels repaired with a single-sided patch. They have done a parametric study varying the stiffness ratio as well as patch length and found that the fatigue life of the repaired thick panel is not influenced by the patch length. They have also observed that the increase in the stiffness ratio of patch to panel improved the fatigue life of repaired panels. Denny and Mall [54] have further studied the FCG response of the aluminum panels repaired with the adhesively bonded Boron FRP patch. They have found that the partially debonded patch repairs failed in lesser numbers of cycles as compared to a completely bonded patch repaired panel. They also proposed that the size and location of disbonds affect the fatigue life. Dae-Cheol and Jung-Ju [55] have carried out both numerical and experimental studies on the fatigue crack growth (FCG) behavior of the thick cracked panel repaired with a single-sided composite FRP patch. They have studied panels with either skewed or uniform crack front for the fatigue life estimation involving FEA. They found that, in the single-sided repairs, skewed crack front modeling predicted the fatigue life more accurately as compared with the experiments. Saberlink et al. [56] have investigated the FCG behavior of stiffened and unstiffened cracked panels repaired by a composite patch. They have also studied the effect of residual stresses developed during patch bondings and suggested a method to estimate the effective curing temperature. In their study, effectiveness of the patch repair is expressed in terms of SIF and fatigue life.

Woo-Yong Lee and Jung-Ju Lee [57] performed the experimental and numerical studies on the FCG behavior of the aluminum plate with a straight crack repaired with single-sided composite patch. They observed that the single-sided repair is effective for the thin plates as compared to thicker ones. Tsai and Shen [58] performed both the experimental and numerical analysis of thick aluminum panels repaired using the single-sided Boron FRP patch and investigated the fatigue crack propagation characteristics. Hosseini-Toudeshky et al. [59-60] have carried out experimental and numerical analysis of single-side repaired aluminum panels under mode-I condition. They have carried out both uniform crack growth

(UCG) and non-uniform crack growth (NUCG) analysis by modeling straight crack front and curved crack front through the thickness (see Fig. 1.12). They found that the fatigue lives obtained with NUCG analysis are close to those obtained from experimental results [59-60].
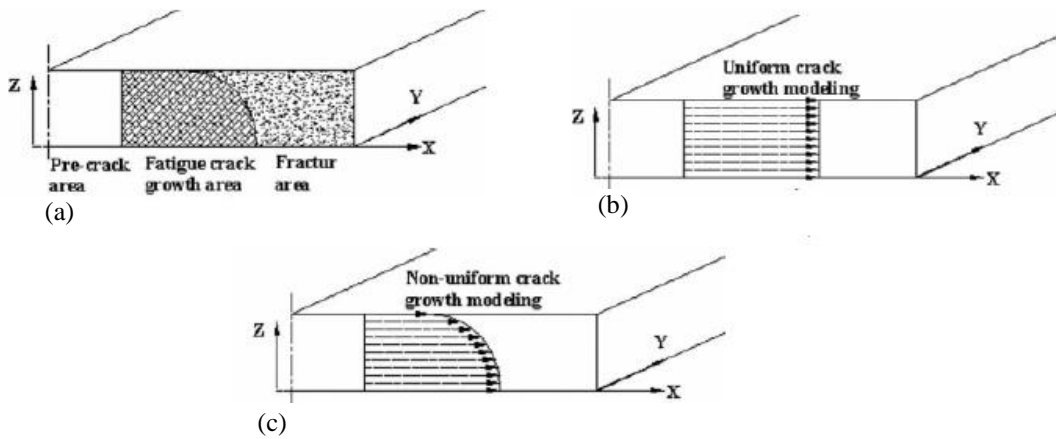
**Figure 1.12: Crack front shape in single sided patch repair and its propagation
(a) real fracture surface (b) crack front at UCG (c) crack front at NUCG [60]**

The previous literature review deals with the life prediction of repaired components having mode-I fracture behavior. In many engineering structures, cracked components are subjected to mixed mode loading conditions and not much understanding is available in literature on its behavior. Ayatollahi and Hashemi [61, 62] have done FEA to investigate the effect of composite patching on the SIF reduction for an inclined center crack panel under different mixed loading case. Chung and Young [63] performed the FCG tests for the single sided composite patch repaired thick plates having an edge crack with different inclination angle of the crack. They have studied the fatigue crack growth rate and crack propagation direction in the patch repaired panels having a single-sided patch. Their experiments showed that the crack grows through the panel thickness non-uniformly. Hosseini-Toudeshky et al. [64-67] have carried out the FCG tests for the single-sided repaired thick and thin panels containing an inclined center crack with different patch lay-up configurations. They observed that the crack growth is non-uniform through the thickness, similar to the findings of Chung and Young [63]. They also found that the patch lay-up influences the fatigue life of the panel.

They have extended their research study on debonding behavior of patch using FEA. Recently, Hosseini-Toudeshky et al. [68] have carried out FE based progressive damage analyses of the adhesive layer under quasi static and cyclic loading. They have implemented the progressive failure analysis at the interface using the cohesive zone concept. They considered the modeling of the adhesive layer with the cohesive zone elements. In their investigation they had studied the impact of the patch width, thickness and the adhesive thickness on the progressive damage in the adhesive interface. They found that the damage to the adhesive layer in a single-sided repaired panel having mode I crack is minimal with the lesser patch and adhesive thickness. Similarly, the damage is also lesser with the increased shear strength of the adhesive and the patch width.

1.3.4 Estimation of whole field strain distribution in repaired panel using digital image correlation

There is innumerable analysis study exists on the full field estimation of shear and peel strain distribution within the bonded joints of composite panels [17, 69]. Very few literatures available on strain analysis of bonded joints between aluminium panels and composite patch. Moutrille et al. [70] have performed experimental procedure to assess the shear stress distribution in an adhesively bonded joint between composite and aluminium using 2D-DIC. They found that through- thickness shear strain distribution is more uniform away from the free edge. But these studies don't involve the effect of the notch in the panel. Whole field experimental strain analysis would give us an overall insight into the mechanics of bonded patch repair models. Vanlanduita et al. [71] have monitored the crack propagation during cyclic fatigue tests using digital image correlation (DIC). Further, from the sub-sampling principles of DIC they slowed down the high frequency dynamics. And they also estimated the SIF at the crack tip by identifying the crack front position using displacement contours.

1.4 Scope and Objectives

Based on the literature review one could observe that the mechanical behavior of composite patch repair applied over straight center cracked and edge cracked panel pertaining to mode I loading has been well established. But very few work exist corresponding to mixed mode panels and their repair. Also, no full field experimental stress/ strain analysis of repaired panel exist. It is very important to predict its behavior under actual loading. Also, fatigue crack growth study of a repaired panel having an inclined crack is very limited and any fundamental contribution towards their behavior would be of great interest to the repair

community. Based on the short comings in the literature and necessity, the following objectives of the thesis are described below as salient points:

- To investigate the influence of important and relevant parameters in design of both single-sided and double sided CFRP patch for a thin inclined center cracked aluminium panel (Al 2014-T6) under uni- axial tensile load.

- To determine the optimized patch shape for the given panel using mechanics based approach. Further, the optimized patch parameters such as its length, width and thickness are arrived at using FEA in conjunction with genetic algorithm.

- To predict the whole field strain around the crack tip and over the patch surface on the repaired panel using DIC technique. Also to investigate the final fracture mechanism of the repaired panel containing both single and double sided adhesively bonded patch.

- To estimate the adhesive peel and shear strain through the thickness of the adhesive layer using DIC technique. Since they are the weakest link, it is of fundamental interest to understand their behavior under actual loading.

- To investigate the fatigue crack growth behavior of both unrepaired and repaired panel using FEA and experiment.

The steps involved in the research work are clearly explained with the schematic diagram shown in Fig. 1.13.
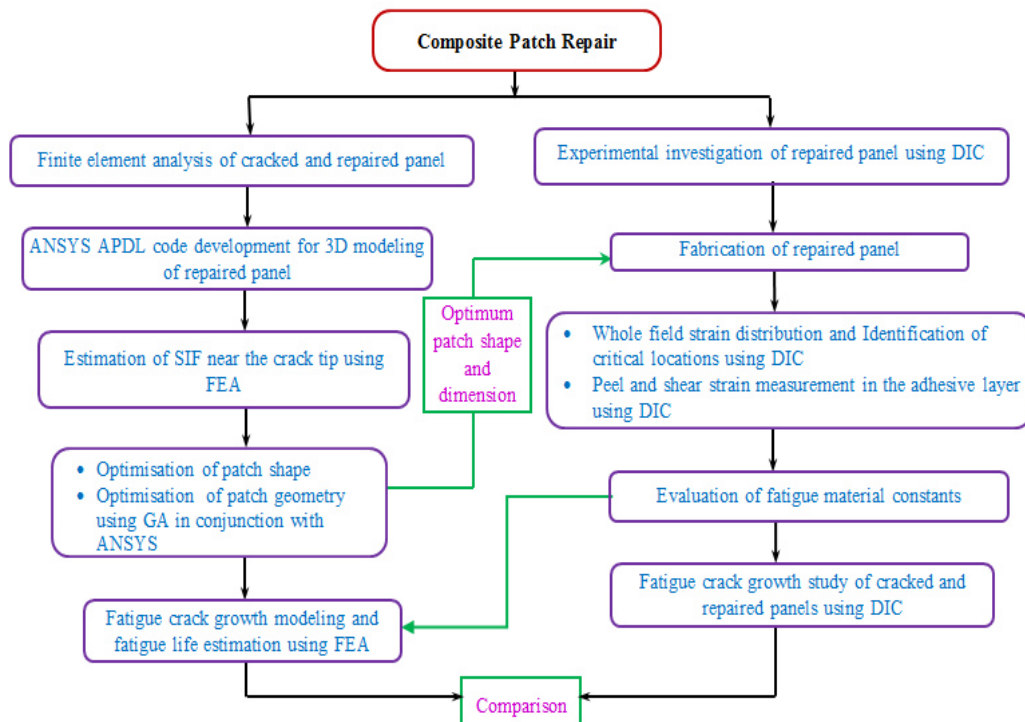
Figure 1.13: Work carried out as part of thesis work

24

1.5 Thesis Layout

Chapter 1 explains briefly about elements of fracture mechanics, composite materials and its application in repair technology, failure mechanism in repaired panels under tensile loading followed by full field strain analysis of the repaired panel under actual loading. Finally, behaviour of repaired panel under fatigue loading is described. Further, a brief introduction of DIC technique employed in the present work is briefly described. A brief literature review on the above mentioned areas is carried out to find the short comings related to repair study. Motivation, scope and objectives including layout for the work carried out is included at the end.

The Chapter 2 describes study of the mechanical behaviors of both single and double sided patch repair applied on an inclined center cracked aluminium panel (Al 2024 – T3) using FEA. Estimation of the SIF's using J-integral approach is presented. A comparative study on the performance of single and double sided repair on an inclined cracked panel is presented in detail. The behaviour of single sided repair configuration is quite different from the double sided repair. In single sided repair there exist an out of plane bending leading to higher SIF at the unpatched surface. This peculiar behavior of single sided repair is explained in Chapter 2. The focus of this study is to learn how these repair methodologies perform and how they improve the load carrying capacity of the cracked panel. For single sided patch repair configuration, in order to reduce SIF at the unpatched surface and to improve it's fatigue life, some recommendations are given at the end.

The Chapter 3 describes the finite element analysis of double sided repaired panel with different patch geometries. From this FEA based comparative study the optimum patch shape is identified for an inclined center cracked panel. Later, the optimization of patch dimensions using GA based as well as mechanics based approach is presented at the end. Importance of tapering of overlap patch edge is also explained for alleviating peel and shear stress levels in the adhesive layer in a repaired panel.

In Chapter 4, initially material characterization of Al 2014-T6 alloy is carried out involving DIC. Further, the whole field strain analysis of cracked and patch repaired aluminium panel using DIC is presented. Both shear and peel strain distribution in the adhesive layer is also captured using DIC setup with magnified optics. Finally, both FEA and experimental results are compared qualitatively.

The Chapter 5 deals with the behaviour of repaired panel under fatigue loading. Three dimensional modeling of FCG behavior in both unrepaired and repaired panel is carried out using FEA. Debonding behavior of patch is captured using cohesive zone modeling. Experimental estimation of fatigue life of unrepaired and repaired model is carried out and they are compared with the FEA prediction. The crack growth is monitored using the DIC technique coupled with image processing algorithm.

The conclusions and recommendations for future work are given in Chapter 6.

Chapter 2

Design and Performance Study of Repaired and Unrepaired Panel Using FEA

2.1 Introduction

One of the important facets of adhesively bonded repair technology is the stress analysis of the entire system which include stress in the panel / adhesive layer / patch and estimation of fracture parameters. The nature of the stress state near the crack tip, and also that of individual constituents patch, adhesive and panel can be critical. Much effort has been invested in understanding the mechanics of bonded repairs involving FEA [31-45]. Design of an appropriate patch for a given cracked panel needs inputs from the mechanics study. Over the last two decades an enormous development has taken place in FEA particularly its application to composite patch repair. However, the choice of a modelling technique for an adhesively bonded patch repair is not obvious because of the geometry and the resulting state of stress. Baker et al. [3] carried out two dimensional FE analyses which did not include out-of-plane deformations caused by the bonded patch. Their study is limited to the thin skin cases where restricted bending occurs. To maintain low-cost and simplicity in the models, yet still provides reasonable predictions for design of bonded patches, most of the previous methods involve simplified two-dimensional approaches. Sun et al. [72] have developed a two-dimensional FE model using Mindlin plate elements for both patch and the panel. The Mindlin plate is modeled as layer element and adhesive is modeled as a spring element as shown in Fig. 2.1(a). The shear spring elements are connected to each of the Mindlin plate layers through displacement constraint equations which satisfied the Mindlin plate assumptions. They have used crack closure method to estimate the SIF. Alternatively, Naboulsi and Mall [73] have modeled the adhesive layer as an elastic continuum medium. This technique uses two-dimensional FEA consisting of the cracked plate, adhesive and composite patch modeled as the three Mindlin plate layers as shown in Fig. 2.1(b). The

motivation behind this model is to capture three dimensional behaviours and further performance of the adhesive layer. They have also accurately estimated the SIF near the crack tip [37]. Off-late, repaired panel is completely modeled as a three dimensional solid element (as shown in Fig. 2.1(c)) for accurately predicting the SIF at the crack tip. In this case, panel/adhesive and patch/adhesive interface nodes are connected by using simple contact algorithm or by incorporating displacement constraint equations [14, 64].
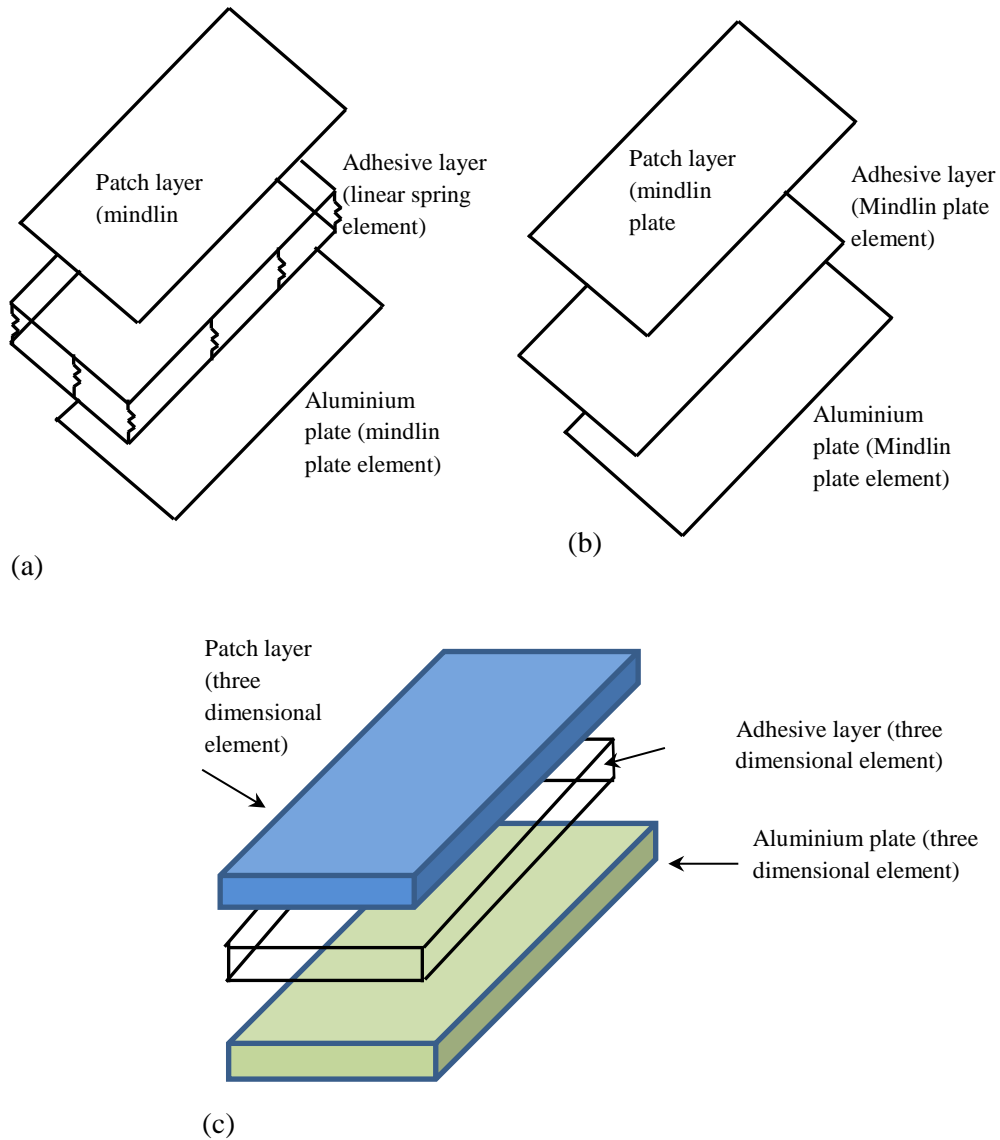
Figure 2.1: Different modeling techniques adopted for Adhesive modeling (a) Effective spring model (b) Three layer technique model (c) Adhesive is modeled as three dimensional solid element

There are different parameters involved in the repair domain and they are adhesive thickness, patch parameters such as patch stacking sequence, patch shape, patch material,

patch thickness, patch length and width etc. Better understanding of the impact of these parameters will improve the efficiency of the repair [4, 49, 50]. In this chapter, out of those parameters, paramount importance is given to the patch stacking sequence, patch thickness and adhesive thickness. While designing repair, it is necessary to match the repair stiffness as close as possible to the original structure in order to regain its residual strength. Increasing the patch thickness improves the stiffness of the panel and further it improves the load sharing capacity. In contrast to the patch thickness, adhesive thickness inversely affects the stress in the panel [35].

In the present chapter, an elaborate study on the mechanics of patch repaired panel involving three dimensional FEA has been carried out to investigate the effects of composite reinforcement on the fracture parameters of an aluminium panel having an inclined crack. Comparison of the performance of both single and double sided repair will be carried out. Further in this chapter, a mechanics based design approach using FEA is presented through a parametric study which involves analyzing the influence of different parameters like patch stacking sequence, patch thickness, and adhesive thickness on SIF value at the crack tip. This parametric study would help us in improving the repair performance. In the last part of this chapter, the effect of tapered patch on peel stress variation is explained, which further improves the integrity of the patch under increased loading.

2.2 Geometry and material properties

The panel is made of aluminium alloy 2024 -T3 plate with a thickness of 3.175 mm and its dimensions are shown in Fig 2.2. It contains an inclined center crack '$2a$' of length 10 mm. The crack is inclined at an angle of $\beta = 45º$ with the horizontal as shown in Fig. 2.2. The plate is subjected to a uni-axial load of 15 kN. The patch is of composite laminate in which each layer thickness is taken as 0.375 mm. The dimension of the composite patch is considered as 25 x 25 x 1.5 mm^3. In the present chapter, Boron/Epoxy composite patch is used. It is bonded un-symmetrically and symmetrically using FM -73 film adhesive material. The general material properties of aluminium panel, composite patch and adhesive are given in Table 2.1 which is taken from Ref. [14]. The specimen dimensions follow the ASTM E-647 standard [30].
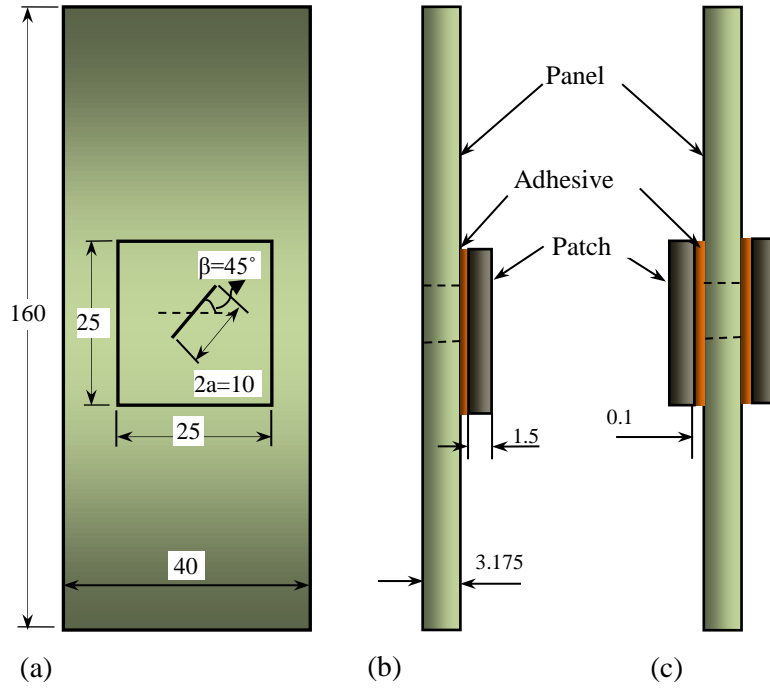
Figure 2.2: Geometry of the repair model considered (a) front view (b) side view of single sided patch (c) side view of double sided patched model (All dimensions are in mm)

Table 2.1: Material properties of Al 2024 –T3 panel, adhesive and Boron/ Epoxy patch

Material	E_x (GPa)	E_y, E_z (GPa)	v_{xy}, v_{xz}	v_{yz}	G_{xy}, G_{xz} (GPa)	G_{yz} (GPa)
Aluminium	71.02	-	0.3	-	-	-
Adhesive	1.83	-	0.33	-	-	-
Boron/Epoxy	208.1	25.44	0.1677	0.035	7.24	4.94

2.3 SIF evaluation using *J* –integral approach

There are several traditional methods available for calculating the fracture parameters (K_I and K_{II}) numerically [12,14]. In the present work, SIF's have been computed using *J*-integral approach. The value of *J*-integral is equal to the energy release rate (*G*) in linear elastic fracture mechanics (LEFM) frame work. After the initial formulation of the *J*-integral method by Rice [74], Shih et al. [75] modified the initial contour integral to an area integral in two dimensions and a volume integral in the three dimensional case. Recent developments and a wide range of applicability in FEM codes make the estimation of SIF using domain integral or *J*-integral method, the most preferred. The *J*-integral definition considers a balance of mechanical energy for a translation in front of the crack along the *x*-

axis is as shown in Fig. 2. 3. The path independent contour integral is defined as mentioned in Eq. 2.1 [9, 12]:

$$J = \oint_c \left(W n_1 - \sigma_{ij} n_j \frac{\partial u_i}{\partial x} \right) ds \tag{2.1}$$

where, W is strain energy density; σ_{ij} are stress components; u_i are the displacements corresponding to local i-axis; s is the arc length of the contour; n_j is the jth component of the unit vector outward normal to the contour C, which is any path of vanishing radius surrounding the crack tip.
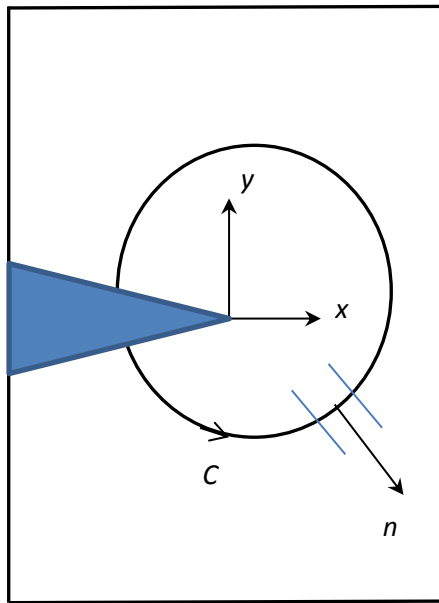
Figure 2.3: Schematic representation of contour integral [9]

In this analysis, it is assumed that the crack-front remains perpendicular to the panel's surface lying on a plane and therefore mode III SIF is neglected. The J-integral value is obtained from ANSYS directly by the domain integral method [76]. Using the assumption of LEFM, K_I and K_{II} are related to the J-integral as given below:

$$J = {K_I}^2 \big/ E' + {K_{II}}^2 \big/ E' \tag{2.2}$$

where, E' is modulus of elasticity, $E' = E$ for plane stress conditions and $E' = E / (1 - v^2)$ for plane strain conditions, v is poisson's ratio. In order to determine K_I and K_{II}, the ratio of K_I over K_{II} is obtained from the ratio of the normal distance to the horizontal distance of two closest nodes to the crack-tips which they have been coincided before loading as shown in Fig. 2.4 [14]. The ratio of K_I over K_{II} is estimated from the below Eq. 2.3:

$$\frac{K_I}{K_{II}} = \frac{\Delta u_y}{\Delta u_x} \tag{2.3}$$

where Δu_x is the horizontal distance of the two closest nodes and Δu_y is the normal distance of two closest nodes (see Fig. 2.4).

(a)

(b)
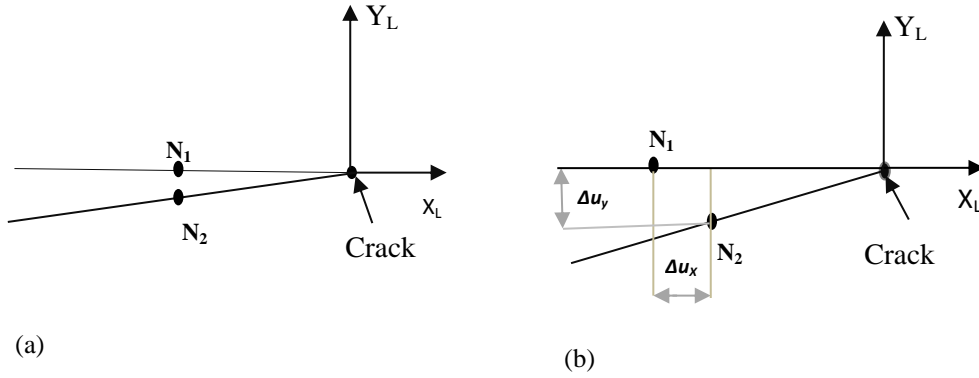
Figure 2.4: Estimation of K_I/K_{II} ratio (a) two coincident nodes near the crack tip before loading (b)two nearest nodes near the crack tip after loading [14]

2.4 Finite element modeling

2.4.1 Modeling of cracked panel

FEM is the most effective tool for computing SIF in 3D fracture models. Modeling and analysis is done using ANSYS 12.1 which is a commercially available FEA package. Numerical computation of SIF's with conventional elements near the crack tip is carried out by several researchers [17, 77]. Investigations on the accuracy of computation of SIF's using quarter point elements around the crack yielded a reasonably accurate result but, later on it is proved that very fine mesh size around the crack tip gives $1/\sqrt{r}$ singularity precisely [78]. Nakmura and Parks [78] have modeled crack tip, like a circular disk with super fine meshing around the crack tip in order to capture very high stress gradient. Same procedure is adopted in this work. Initially individual areas are created around the crack tip and meshed with plane element having eight nodes. Here, the radial extent of the outer most nodes is 0.8766t and the crack tip element size is 0.0005 t (where t is the thickness of panel). The crack tip mesh has a total of 7128 elements (36 circumferential, 33 radial; 6 elements through the thickness around the crack tip region (see Fig. 2.5(c)). Outside the disk, a structured area mesh has been done in the panel as per the dimensions (see Fig. 2.5(a)). Later, all the areas are extruded in thickness direction to generate volume. Finally, all the generated volumes are meshed with 20-noded solid-186 element through sweep mode as shown in Fig. 2.5 (b). A tensile load of 15 kN is being applied as a pressure load on the top

surface of the panel and the bottom face is arrested. The *J*-integral values for the unrepaired panel are directly obtained from the ANSYS using domain integral approach. From the *J*-integral values K_I and K_{II} are estimated as mentioned in previous section.

20 noded hexahedral element

(b)

15 noded triangular element near the crack tip

(c)

(a)
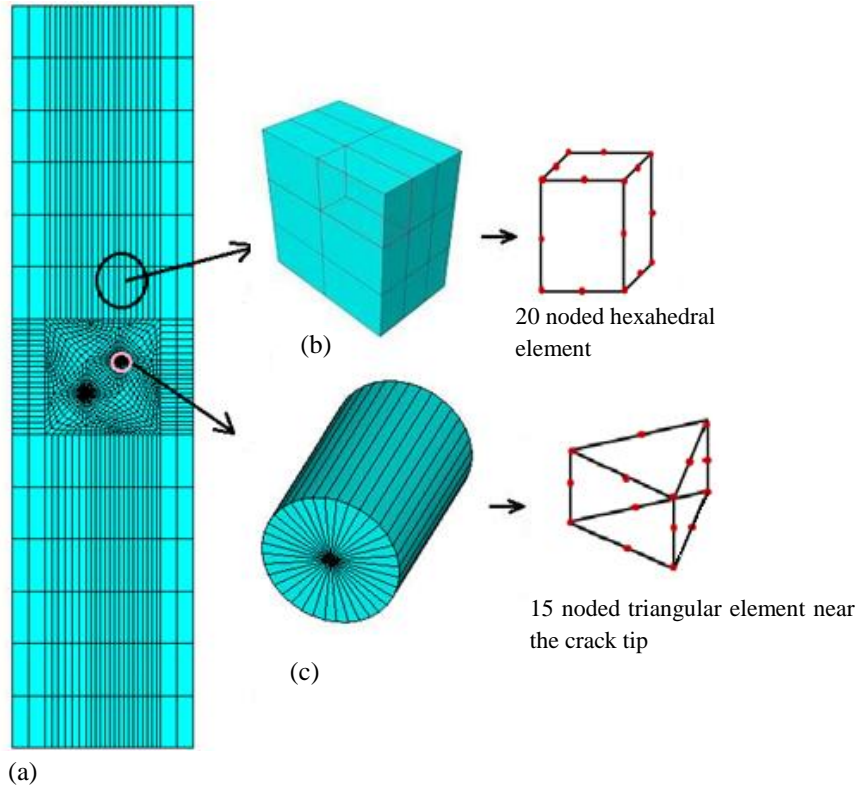
Figure 2.5: Finite element mesh of cracked panel (a) entire panel (b) element outside the crack tip mesh (c) around the crack tip

2.4.2 Mesh convergence study

A convergence study is performed on the cracked plate, to quantify the number of elements surrounding the crack tip and to get a converged value. The *J*-Integral value is evaluated; and its variation with respect to the number of radial elements surrounding the crack tip is plotted as depicted in Fig. 2.6 (a). Even though, a steady value of *J*- value is being attained at 25 elements, the model with 33 elements was chosen for further study. Similarly, convergence study is performed with increasing the number of elements along circumferentially around the crack tip and the convergence plot is shown in Fig. 2.6(b). From the Fig. 2.6(b) it is observed that there is not much effect in the *J*- value with increasing the number of elements around crack tip circumferentially. On overall comparison the mesh around the crack tip is modeled with 33 elements radially and 36 elements circumferentially for further study.
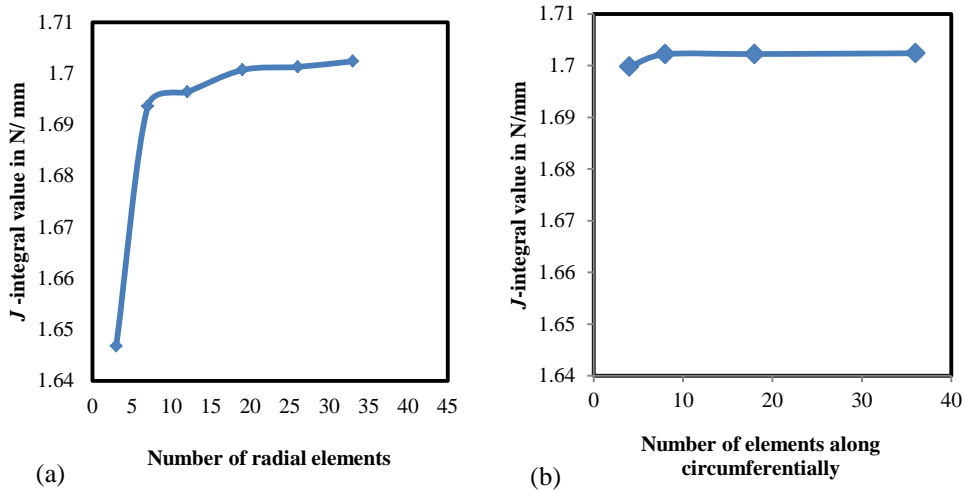
Figure 2.6: Convergence study (a) radial elements (b) circumferential elements

2.4.3 Comparison of analytical and numerical SIF of the cracked panel

Figure 2.7 show the SIF distribution through the thickness of the panel having inclined center crack at $45^{°}$. In this subsection, both analytical SIF and numerical values (from FEA) are being compared. The expression for estimating analytical SIF for the mode I and mode II are given in the Appendix A.1 which is taken from Ref. [11]. In case of numerical SIF distribution, one can see that there is a reduction of K_I at edges and it peaks at the center of the panel while K_{II} is higher at the edges and it reduces at the center of the panel. This variation at the free edge is because of the corner singularity effect [9]. The order of corner singularity is different from the crack tip singularity.

(a)   (b)
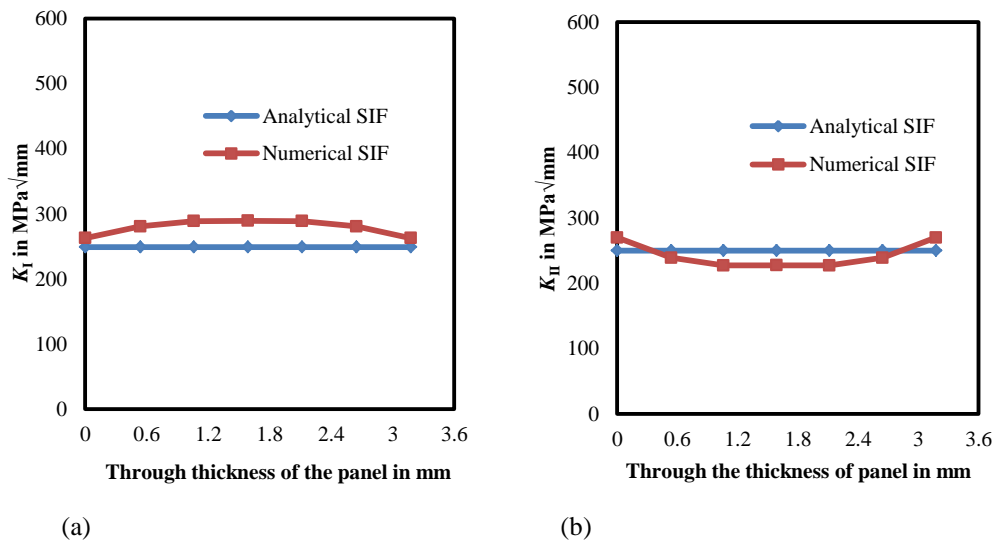
Figure 2.7: Comparison of numerical SIF variation through the thickness with the analytical
2.4 SIF value (a)K_I(b)K_{II}

34

As mentioned in the introduction of this chapter the patch and adhesive are modeled with three dimensional solid elements. The pattern of area meshing of patch/adhesive and adhesive/panel interface is generated similar, so that it can be easily coupled with respect to each other at the interface. In the thickness direction, the panel is meshed with six elements, adhesive with one element and patch with four elements. As the patch is made of composite laminate having different lay-up orientation, the layer angles are defined by assigning the element coordinate system to the patch elements [79]. Each layer is assigned one element in thickness direction. It is assumed that patch is perfectly bonded to panel by the adhesive. Appropriately the nodes are coupled at the respective interfaces to reflect the perfectly bonded behavior. During coupling, all the three degrees of freedom are constrained at the interface. Another method of gluing the interface areas is using the multi- point constraint algorithm (MPC). The advantage of MPC algorithm is that the patch and adhesive need not have similar mesh pattern as that of the panel therefore providing a greater flexibility. More detail about the MPC is mentioned in chapter 3. The total number of elements in single sided and double sided repair configurations is 43536 and 57480 respectively. Figures 2.8(a) and 2.8(b) show the finite element model of single sided repaired panel in exploded view and assembled view. Similar boundary conditions mentioned in the previous subsection: 2.4.1 is applied to the repaired panel. Later, SIFs is estimated using the same approach as discussed in the previous section 2.3.

(a) (b)
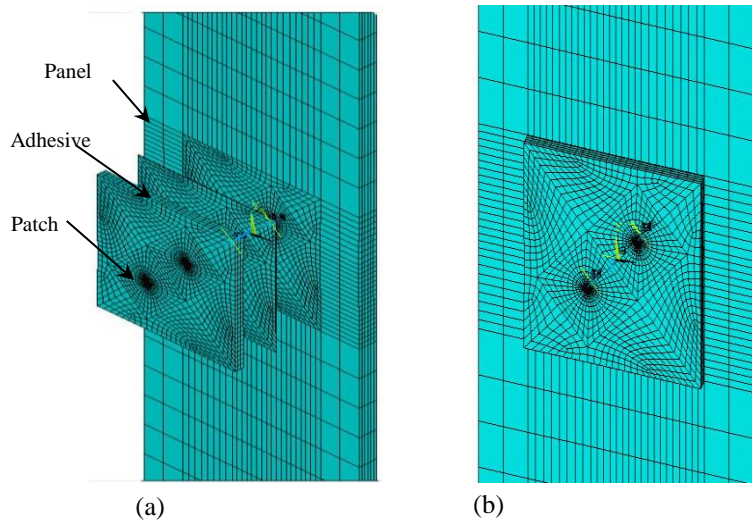
Figure 2.8: Finite element model of single sided repaired panel (a) exploded view (b) assembled view

2.4.5 Variation of SIF in unrepaired and repaired panel

35

SIF variation through the thickness of single sided and double sided patched panel being compared to un-repaired panel is shown in Fig. 2.9. In double sided repair and unrepaired panels, the K_I values are lower and K_{II} values are higher at the edges when compared to the center of the panel (see Fig. 2.9 (a) and 2.9 (b)). As a crack intersecting a free surface in a 3D model, the order of singularity weakens and it is different from the crack tip singularity [9]. Figure 2.9 shows that there is a reduction in K_I and K_{II} about 78% in case of double sided patch repair and the variation is symmetric through the thickness of the panel. In case of single sided repair at the unpatched surface there is a reduction of K_{II} about 8% as compared to un-repaired panel (see Fig. 2.9(b)). But the value of K_I obtained for a single sided repaired panel at the unpatched surface is higher than the un-repaired panel and double sided patched panel (see Fig. 2.9(a)). This is due to existence of additional bending stresses which in turn causes higher K_I at the unpatched surface and a similar trend has been observed in Ref. [67]. Therefore, design consideration for single and double sided patch repair has to be different and must be addressed individually as their fundamental behaviors are completely different. Also because of higher SIF at unpatched surface the static strength of the panel gets reduced. Therefore in this work, effect of patch thickness is studied, to reduce K_I at unpatched surface so that the static strength and fatigue life can be improved.
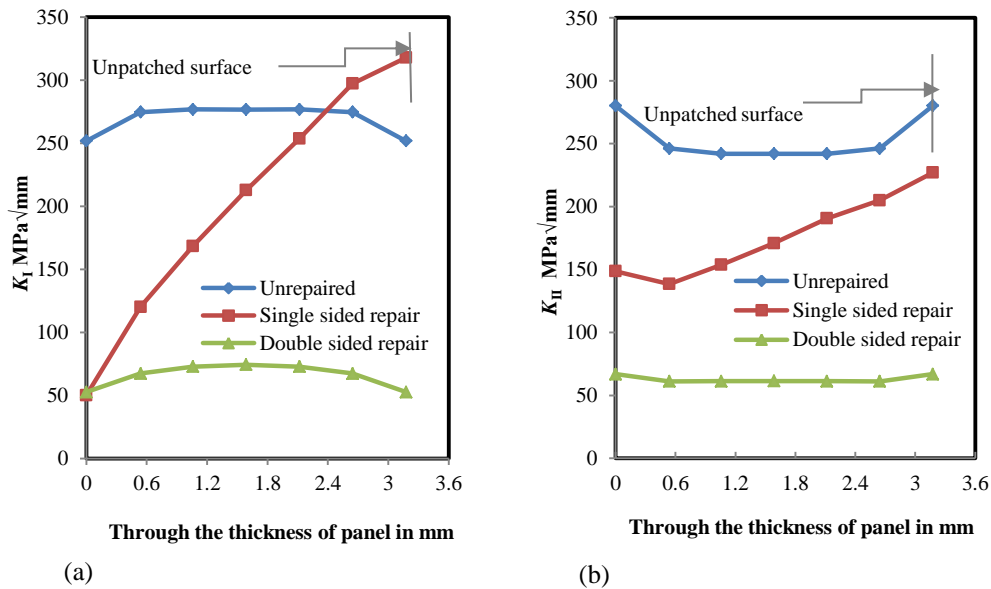
Figure 2.9: Comparison of SIF variation through the thickness of the unrepaired and repaired panel (a) K_I (b) K_{II}

2.4.6 Variation of normal stress in unrepaired and on repaired panel

Figure 2.10 shows the variation of normal stress through the thickness of the panel. The variation of normal stress (σ_y) through the thickness of the panel is linearly increasing in case of single side repaired model and is constant in case of unrepaired and double side repaired model (see Fig. 2.10). This linear variation of (σ_y) in turn causes SIF to vary linearly across the thickness in case of single sided repair. On the other hand, in case of double sided repair SIF reduction is very prominent and the composite patch works very effectively. But there are few issues in case of single sided repair mainly higher SIF (K_I) value at the unpatched surface because of its linearly increase in bending stress across the thickness. The SIF at the unpatched surface is reduced by increasing patch thickness and usage of unbalanced laminate which is described in the subsequent subsections.
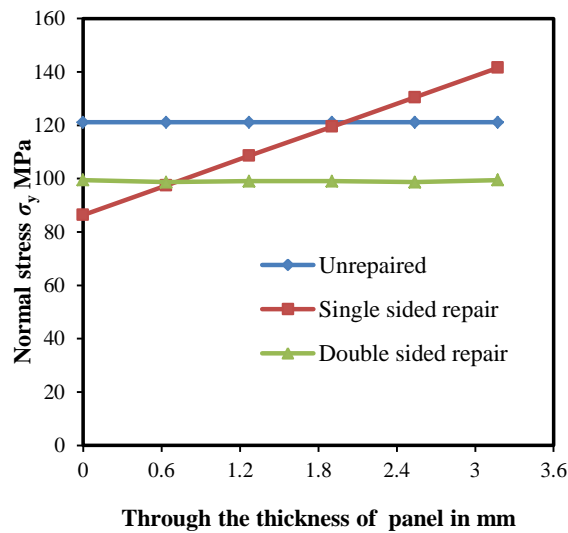
Figure 2.10: Comparison of normal stress through the thickness of the unrepaired and repaired panel

2.4.7 Effect of patch lay-up configuration on repaired panel

Figure 2.11 shows the variation of SIF through the thickness of the panel repaired with a single sided and double sided patch having different lay-up orientations such as $[-45]_4$, $[0]_4$, $[-45]_2/[45]_2$, $[0]_2/[90]_2$. In case of single sided repair it is clear that K_I is lower and K_{II} is maximum for the patch lay-up configuration of $[-45]_4$ and $[-45]_2 / [45]_2$ as shown in the Fig. 2.11 (a) and 2.11 (b). From the Fig. 2.11(a) it is found that there is a reduction of K_I at the unpatched surface about 4% with the patch lay-up configuration of $[0]_2/ [90]_2$ as compared to the balanced patch lay-up configuration of $[0]_4$. The unbalanced laminate exhibits the counter bending effect against the bending stresses that present at the unpatched surfaces.

In case of double sided patch repair the variation of the SIF value is symmetric for all patch configurations and is minimum for the patch lay-up configuration of $[0]_4$ (see Fig. 2.11 (c),

2.11 (d)). The patch lay-up configuration of $[0]_4$ is considered for the preceding sections, since it gives lower SIF at the crack tip as compared to other configurations.
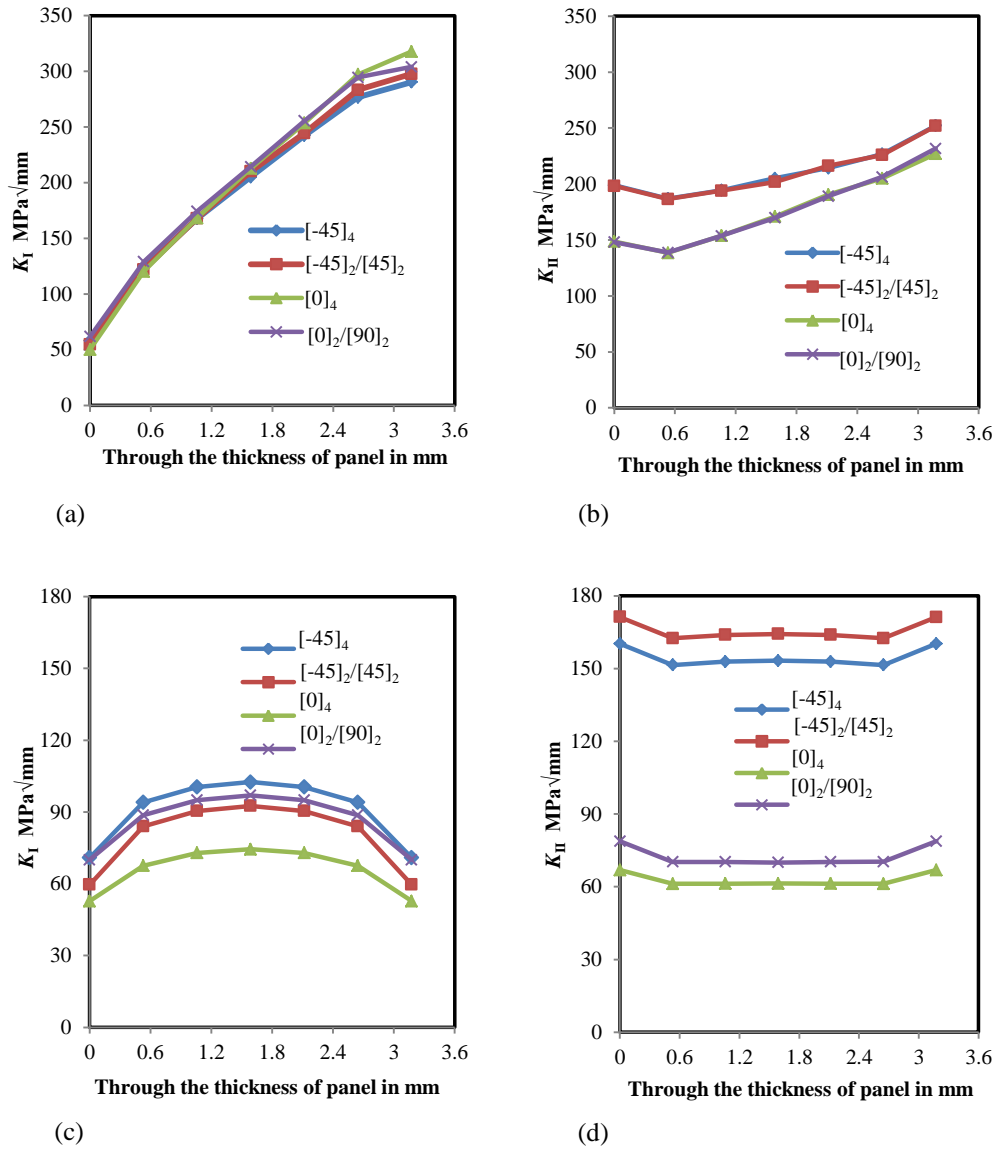
Figure 2.11: Variation of SIF across the thickness of the repaired panel having patch with different ply orientation (a), (b) single sided repair (c), (d) double sided repair

2.4.8   Effect of patch thickness on repaired panel

In this section effect of patch thickness on SIF reduction is studied. The patch is having different number of lay and each layer is of thickness 0.375 mm. Also the layer orientation is $[0]_4$, so that they are aligned parallel to the loading direction there by maximizing load carrying capacity. The SIF (both K_I and K_{II}) variation through the thickness of the panel for a single sided and double sided repaired model with varying number of layers is shown in Fig. 2.12. From Fig. 2.12(a) it is evident that as the patch thickness increases K_I value at the

unrepaired side decreases. It is the also same with K_{II} but not much variation is seen (see Fig. 2.12 (b)). This reduction in SIF value is because of additional reinforcement over the crack zone (i.e, more load transfer through the patch) with an increased number of layers in the patch. Also, greater reduction of K_I about 21% has been observed in the eight lay configuration as compared to other two configurations. Still, K_I at the unpatched surface is slightly more than the unrepaired value and also the order of the patch thickness is comparable to panel thickness in the case of eight layers. Hence increasing layer thickness seems to be a possible solution for the reduction of SIF at unrepaired surface in case of single sided repair. In double sided repair increasing patch layers doesn't show much effect in SIF reduction in both K_I and K_{II} is shown in Fig. 2.12(c) and (d).
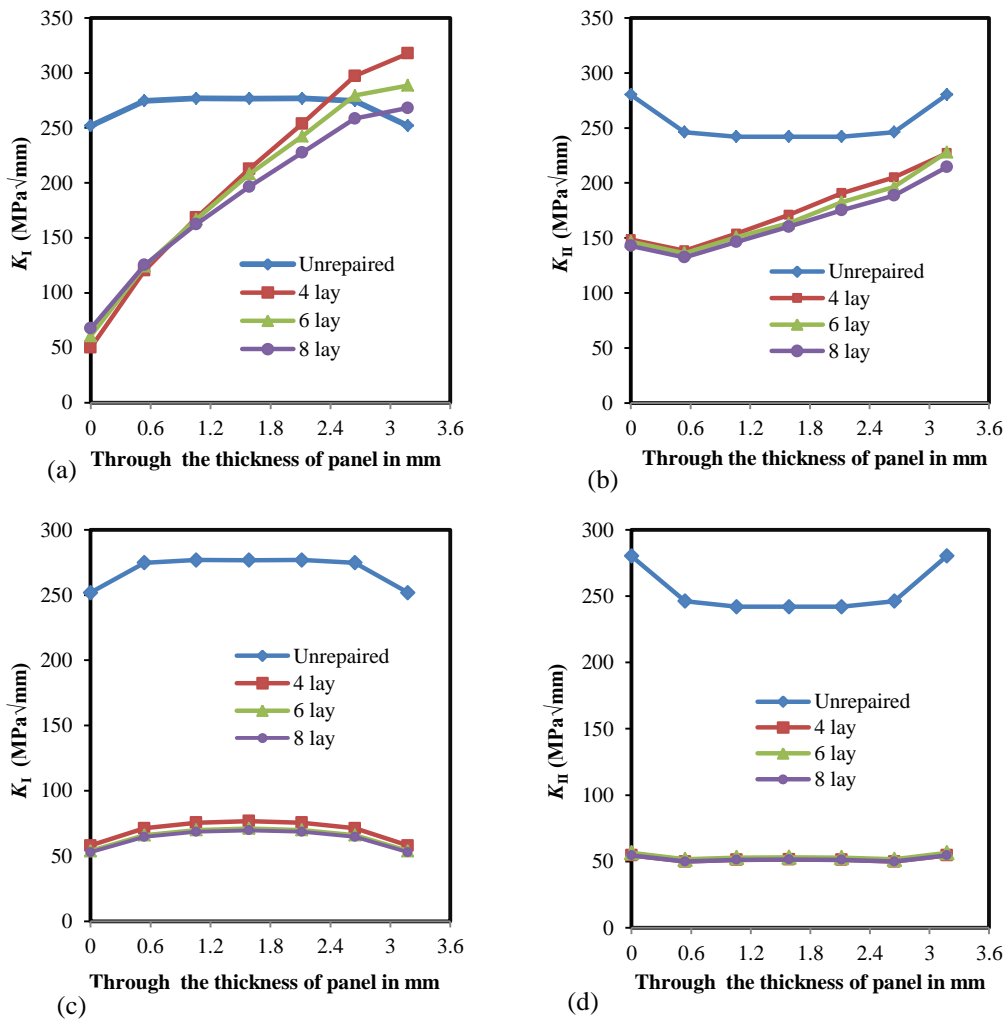
Figure 2.12: Variation of SIF through the thickness of the panel with increasing patch thickness (a), (b) Single sided repair and (c),(d)Double sided repair

2.4.9 Effect of adhesive thickness on repaired panel

In this section effect of adhesive thickness on SIF reduction is presented. Figure 2.13 shows the SIF (both K_I and K_{II}) variation through the thickness of the panel for a single sided and double sided repaired panel with increasing thickness of the adhesive. From Fig. 2.13(a) it is evident that as the adhesive thickness increases K_I value at the unrepaired side of single sided repaired panel increases. It is the also same with K_{II} but not much variation is seen (see Fig. 2.13(b)). Higher the adhesive thickness strengthens adhesion but it weakens the load transfer towards the patch thereby decreasing the beneficial effect of the patch resulting in increase in SIF. From the Fig. 2.13(c) and 2.13(d) it is observed that there is increase in SIF (both K_I and K_{II}) in case of double sided repaired panel with increase in adhesive thickness. Increasing adhesive thickness leads to porous and weakening the interface.

(a)

(b)

(c)

(d)
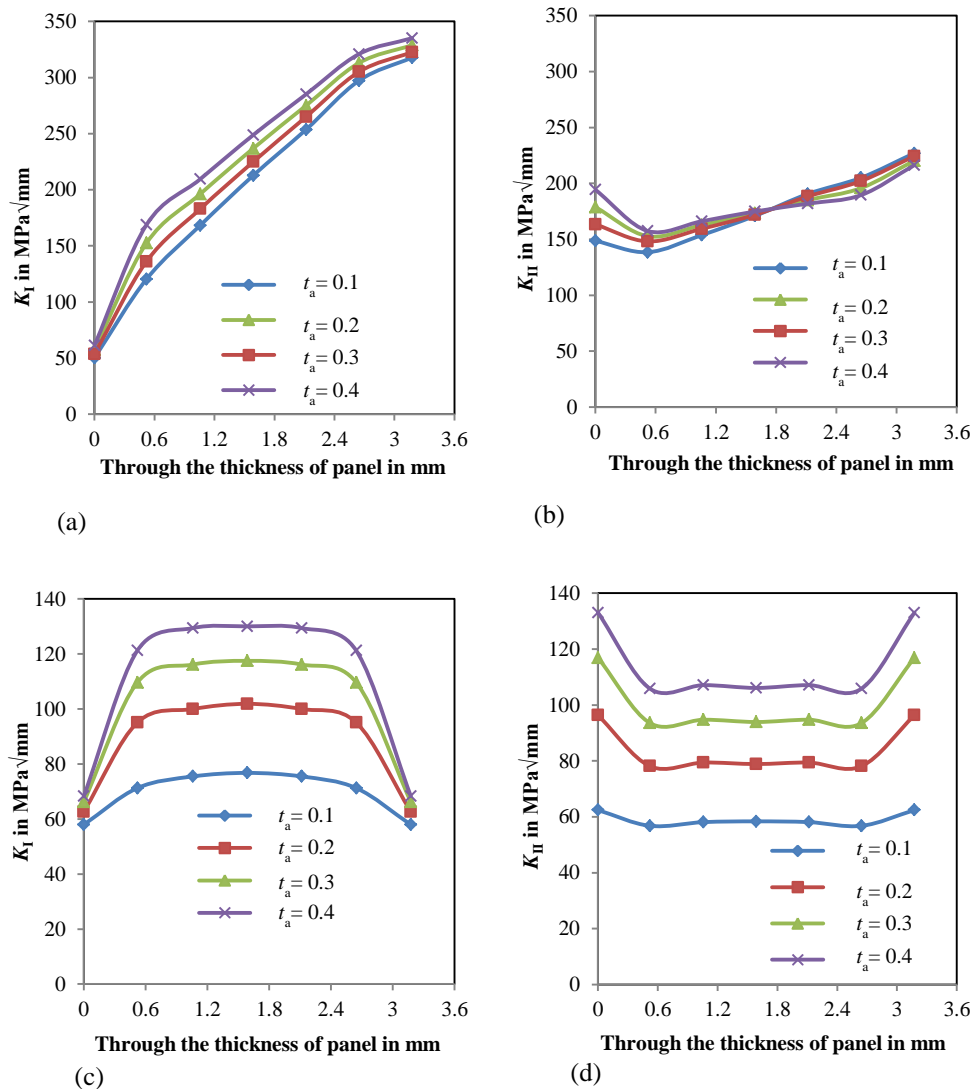
Figure 2.13: Variation of SIF through the thickness of the panel with increasing adhesive thickness (t_a) (a), (b) single sided repair and (c), (d) double sided repair

Hence from the above analysis it can be observed that the adhesive thickness of 0.1 - 0.2 mm gives lower SIF in both single and double sided repaired panels. Hence the same adhesive thickness is used for the subsequent sections.

2.5 Effect of tapered patch on peel stress distribution

In case of single sided patch repair, application of the remote stress will cause secondary bending, and hence a more severe adhesive shear and peel stresses will be developed at the extremities of the load transfer regions. Patch deboning occur due to development of high peel stress (σ_z) at the overlap end. To minimize these peel stresses a tapering (1:20) is provided along the patch edge. Figure 2.14 shows the variation of peel stress along the panel length from the overlap end. Schematic representation of location of the peel stress distribution in the bonded repair is shown in Fig. 2.14 inset. It can be observed that the tapering at the overlap end reduces peel stress by 46% compared to straight edge patch.
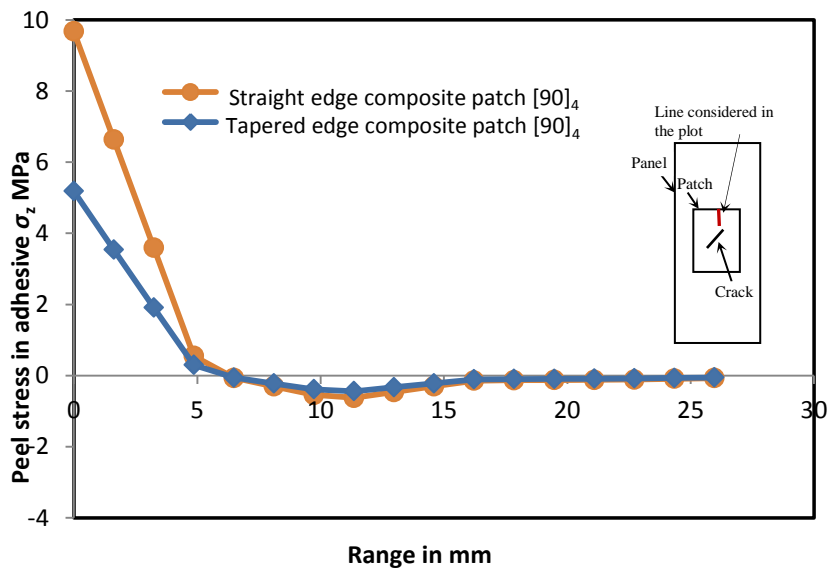
Figure 2.14: Variation of peel stress along the panel length in the single sided repair

2.6 Closure

A three dimensional FEA is carried out to compare the performance of single and double sided patch repaired configurations. It is found that the behavior of single sided repair is completely different from the double sided repair. In case of double sided repair there is a drastic reduction in SIF of about 78% as compared to the unrepaired panel SIF and variation is symmetric through the thickness of the panel. On the contrary in case of single sided

repair K_I at the unpatched surface exceeds the value that of unrepaired panel due to additional bending arising due to eccentric loading. Therefore, variation of both K_I and K_{II} is not symmetrical through the thickness of the panel. At the patched surface of single sided repair, it is found that there is a reduction of K_I about 78% and K_{II} about 40% as compared to unrepaired SIF value. Whereas at the unpatched surface, it is found that K_I exceeds by 26% and K_{II} reduces by 8% as compared to unrepaired SIF value. In case of single sided repair to alleviate SIF especially K_I at unpatched surface, a study is carried out by either increasing patch thickness or usage of unbalanced laminated. As the patch thickness increases, the stiffness of the patch increases aiding in more load transfer and hence both K_I and K_{II} values gets lowered especially K_I at the unpatched surface. There is a reduction of 4% in K_I value at the unpatched side in case of patch having $[0]_2/[90]_2$ layup as compared to the balanced lay-up configuration. In the case of repaired panel, presence of patch shifts the maximum stress from the crack tip to the overlap patch edge and there is every chance that it will fail from that location. Therefore, tapering is recommended at the patch edges with a ratio of 1:20 towards reducing the peel stress. It showed a reduction of 46% with the tapered edge as compared to the straight edge patch for the same layup configuration. Severity of these peel and shear stress also depends on the patch shape and patch geometry. In order to enhance the repair performance and to reduce the stress level near the crack tip and at the patch overlap edge, a detailed study is carried out to arrive at optimal patch geometry for the repair of an inclined center crack panel in the succeeding chapter.

Chapter 3

Optimum Design of Patch Geometry and Dimension

3.1 Introduction

Integrity enhancement of cracked aircraft structures through composite repair is attracting considerable engineering attention in recent years. The purpose of the patch in bonded repair is to bypass the load away from the cracked zone, thereby reducing the stresses surrounding the crack tip. Generally, in an externally bonded patch repair, the SIF at the crack tip is the most dominant parameter which governs the failure. Another parameter that influences the repair efficiency is the skin stress concentration factor (SCF) which arises at the patch overlap edge. This high stress concentration on the overlap edge is because of high peel and shear stresses that develop due to abrupt jump in geometry. This hampers the high efficiency of externally bonded patch repairs. Therefore, both SIF and skin SCF needs to be considered for repair performance. To improve the repair efficiency, an optimum design of the patch needs to be arrived at which would result in maximum reduction of peel stresses, SIF and skin stress concentration factor. Very limited research study exists on the optimization of patch shape and patch dimensions applied to mode I cracked panel [40, 45 and 46]. However, no work exist on the influence of patch shape and geometry on repair performance for the mixed mode case.

In the present chapter, firstly the influence of different patch shapes like circle, rectangle, square, ellipse, and octagon on repair efficiency is carefully studied. Later, comparison of the performance of bonded repair with different patch shapes is carried out based on SIF reduction at the crack tip. For comparative study, only double sided patch repaired panel configuration is considered. Also no tapering is given at the overlap edge of the patch. The best performing patch shape is then identified and further the dimensional optimization of the selected patch geometry towards higher performance is determined using genetic algorithm based approach coupled with FEA. Multi objective optimization is performed for

arriving at optimal patch dimensions such as patch length, width and thickness. Further, the SIF variation (all three modes) through the thickness of the repaired panel is also obtained for the same optimal patch configuration using virtual crack closure technique (VCCT).

3.2 Material properties

Same specimen configurations are used which is shown in Fig. 2.2. In the present chapter instead of 2024- T3 Al alloy, 2014- T6 Al alloy has been used. Further, epoxy based AV138 / HV998 adhesive material is used instead of FM 73. Also, Carbon epoxy is used as patch material instead of boron/epoxy material due to its rare availability and high cost. The effectiveness of the patch depends on the stiffness ratio which is nothing but the ratio of patch stiffness to the panel stiffness ($E_p t_p / E_s t_s$). Normally the recommended stiffness ratio ranges from 1 to 1.6 as mentioned in Ref. [35]. In this study the stiffness ratio is around 1 and it would definitely reinforce the panel at the defect area helping in more load transfer happening across the defect thereby reducing SIF at the crack tip.

Table 3.1 Material properties of Al 2014-T6 panel, adhesive and CFRP patch

Material	E_x (GPa)	E_y, E_z (GPa)	v_{xy}, v_{xz}	v_{yz}	G_{xy}, G_{xz} (GPa)	G_{yz} (GPa)
Aluminium	73.1	-	0.33	-	-	-
Adhesive [80]	4.57	-	0.48	-	-	-
CFRP [40]	135	9	0.3	0.02	5	8

3.3 Finite element modeling of double sided patched panel with different patch shapes

The modeling process starts with assigning of the input parameters such as crack inclination angle, dimensions of panel, patch and adhesive parameters. These parameters are read in APDL (ANSYS Parametric Design Language). The program models the crack tip mesh as a circular disk with 36 circumferential elements and 33 radial elements, similar to the procedure described in the previous chapter. Later, the macro models 3D panel, patch and adhesive as per the dimensions. Finally, the macro develops the double sided repaired panel and performs analysis for evaluating *J*-integral value and SIF's.

In this analysis, different patch shapes like circular, rectangular, square, elliptical, and octagonal patches are modeled and analyzed upfront. The next subsection explains the modeling procedure of different patch shapes.
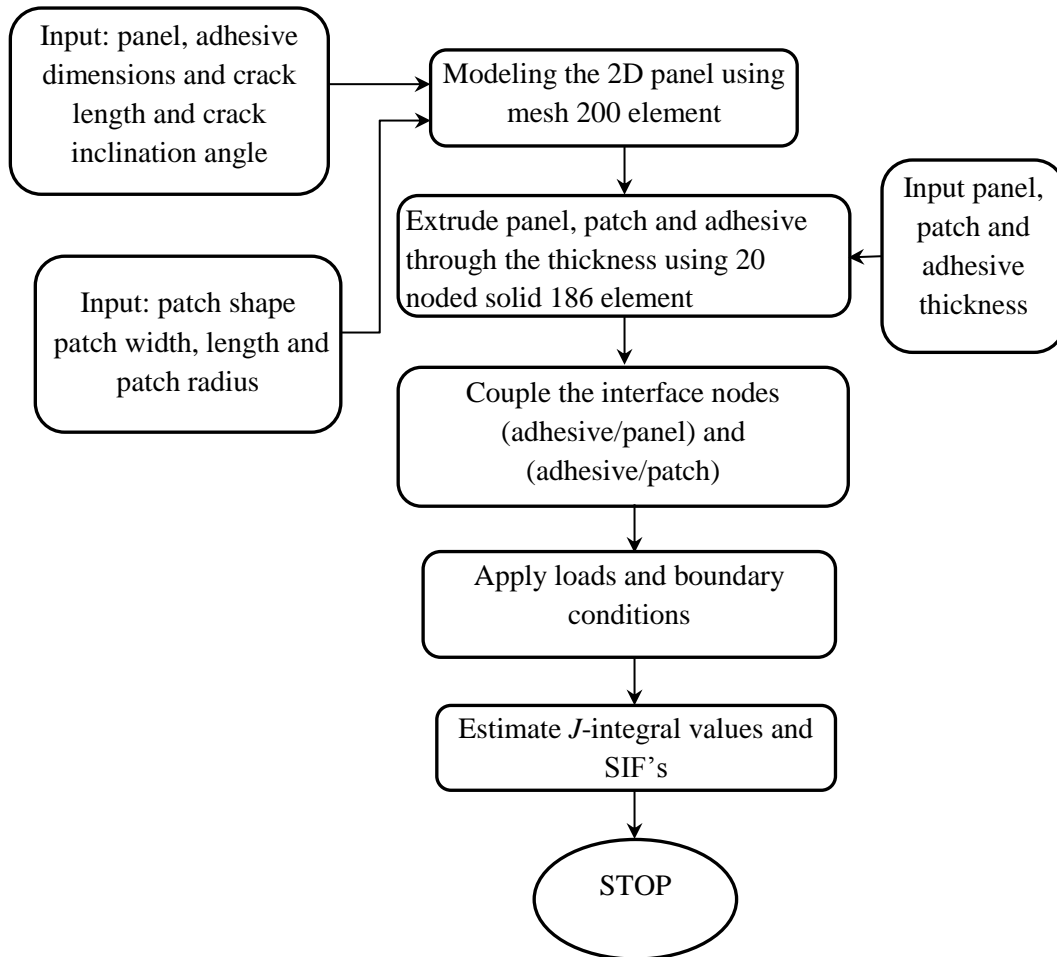
Figure 3.1: Flow chart describing the APDL macro for FE modeling of different patches shapes

3.3.1 Circular patch modeling

In this study circular patches of four different radii is considered and they are 12.5, 14, 15 and 16 (in mm) corresponding to an area of 490, 616, 706 and 804 (in mm^2) respectively. Firstly, around the crack tip a circular mesh pattern is created. Encompassing the circular pattern another circular area is created, so that it encloses the circular patch area sufficiently. Finally, each area is meshed individually as shown in Fig. 3.2.
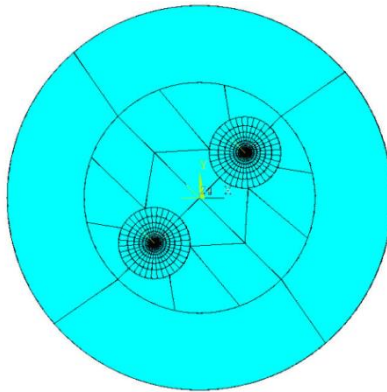
Figure 3.2: Circular patch shape modeling

3.3.2 Rectangular patch modeling

Two possible models are studied in case of rectangular patches. Firstly maintaining a constant width (B) of 25 mm and varying patch length (H). They are varied as 26, 28, 30 and 32 (all are in mm) leading to four different cases (see Fig. 3.3(a)). Similarly an opposite scenario is also studied by maintaining constant patch length (H) as 25 mm and varying its width (B) as 26, 28, 30 and 32 mm (see Fig. 3.3(b)). The corresponding areas are 650, 700, 750 and 800 (in mm^2). Similar to circular patch model around the crack tip a circular mesh pattern is created and then encompassed with in another circular area. Finally, a rectangular area is built around it as shown in Fig. 3.3(a) and 3.3(b). Finally, each area is meshed individually.

(a)

(b)
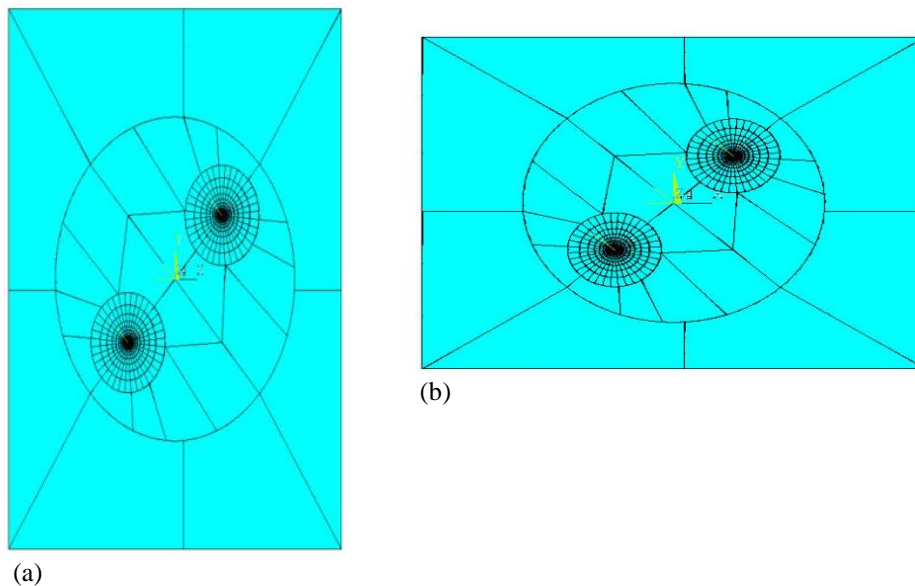
Figure 3.3: Rectangular patch shape modeling (a) H>B (b) B>H

3.3.3 Square patch shape modeling

Square patch is also modeled same as rectangular patch with side length varying as 22, 24, 26, 28 (all are in mm) having areas 484, 576, 676 and 784 (in mm^2) respectively. The meshing procedure is similar to that of rectangular patch model (see Fig. 3.3).

3.3.4 Elliptical patch modeling

Elliptical patch area is generated by appropriately scaling the circular area. In this work two cases are considered: firstly horizontal ellipse, having the major axis along *x*-axis and secondly rotated ellipse where major axis is along *y*-axis. In this work the minor axis of the ellipse is taken as 25 mm and four different major axis lengths of 26, 28, 30 and 32 (all are in mm) are considered. The corresponding areas are 510, 550, 589 and 629 (in mm^2). The meshing is done similar to that of circular patched panels (see Fig. 3.4(a) and 3.4(b)).

(a)

(b)
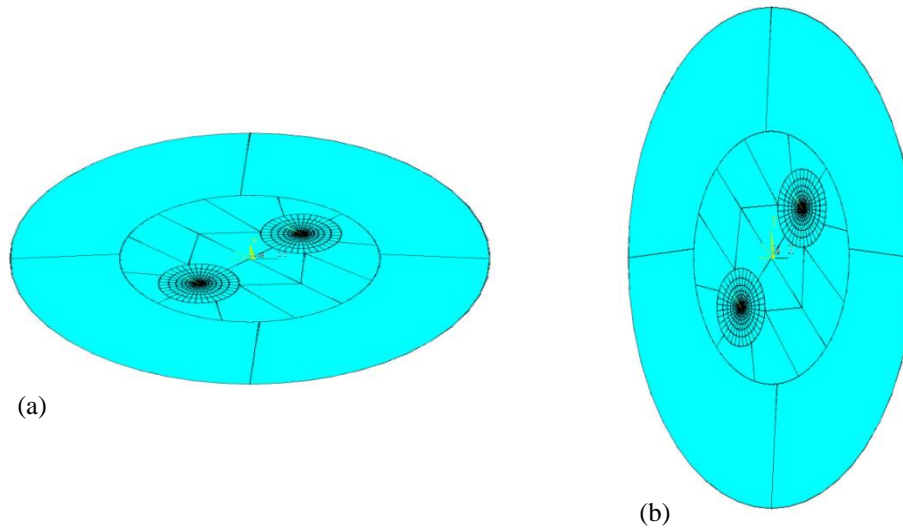
Figure 3.4: Elliptical patch shape modeling (a) horizontal ellipse (b) rotated ellipse

3.3.5 Octagonal patch shape modeling

The octagon is created by circumscribing the circle with radius '*R*' which is shown in Fig. 3.5 (a). For the first case a regular octagon is considered having sides of length 10.3, 11.5, 12.4, 13.25 mm circumscribed within the circle radii of 12.5, 14, 15 and 16 mm respectively. The corresponding areas are 517, 648, 744 and 848 (in mm^2). For the second case, extended octagon is created by increasing two parallel side's length in such a way that the area of extended and regular octagon is kept same is shown in Fig. 3.5(b). But the corners are chamfered at 45˚ (see Fig. 3.5(b)). For these models meshing procedure is adopted similar to the rectangular patch model (see Fig. 3.5(a) and 3.5(b)).

(a)   (b)
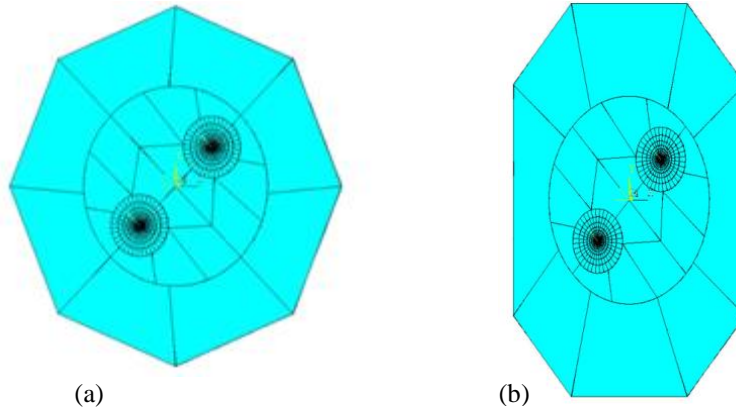
Figure 3.5: Octagonal patch shape modeling (a) regular octagon (b) extended octagon

Once the panel, patch and adhesive are modeled the interface nodes of adhesive/panel and adhesive/patch are coupled at the respective interfaces to reflect the perfectly bonded behavior. During coupling, all the three degrees of freedom are coupled at each node. Similar boundary condition and loads are applied as mentioned in the previous chapter. Then J-integral values are extracted from the ANSYS software using domain integral approach [76]. From the J-integral values K_I and K_II are estimated. Figure 3.6 shows the FE model of the repaired panel with different patch shapes.

3.4 SIF and reduction parameter (R) variation in double sided repair

For a quantitative estimation of effective patch shape for the mixed mode cracked panel a parameter R is introduced which is defined in Eq. (3.1) as:

$$R = \sqrt{\left[\left(\frac{K_I{}^U - K_I{}^R}{K_I{}^U}\right)^2 + \left(\frac{K_{II}{}^U - K_{II}{}^R}{K_{II}{}^U}\right)^2\right]} \tag{3.1}$$

where $K_\mathrm{I}{}^\mathrm{U}$ and $K_\mathrm{II}{}^\mathrm{U}$ represents unrepaired mode I and mode II SIF value, $K_\mathrm{I}{}^\mathrm{R}$ and $K_\mathrm{II}{}^\mathrm{R}$ represents mode I and mode II SIF value for the repaired model. This parameter combines both K_I and K_II reduction into one value so that comparison becomes easier and straight forward. Higher the R value, better the patch performance with respect to SIF reduction. For comparison purpose SIF and R value at the mid-plane location is considered.
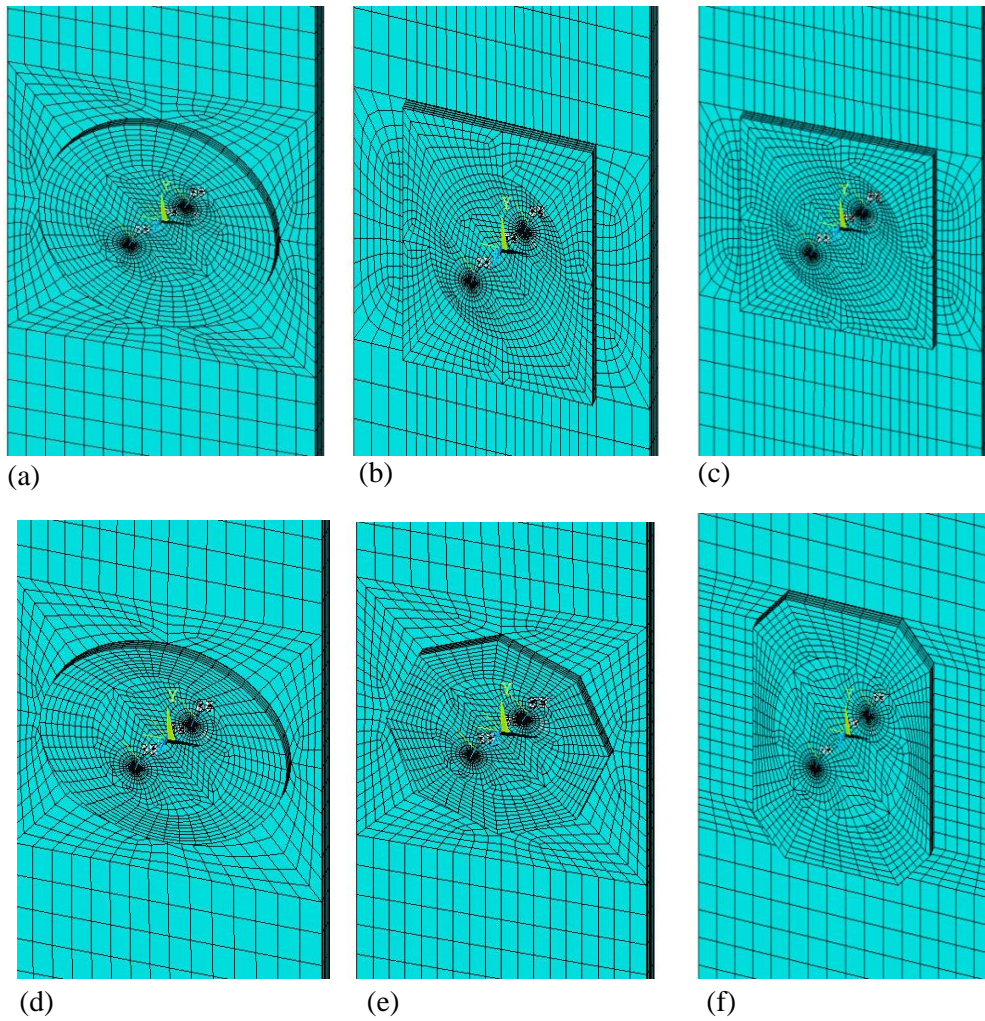
Figure 3.6: Finite element model of composite repaired panel having patches of different shapes (a) circular, (b) rectangular, (c) square (d) elliptical (e) regular octagon and (f) extended octagon

3.4.1   Variation of SIF and reduction parameter in circular patch

Figure 3.7 shows the variation of K_I, K_{II} and R with respect to the diameter D of circular patch. From Fig. 3.7(a) and (b) it can be observed that as the diameter of patch increases, overlapping area increases hence SIF decreases. Same trend is also seen in Fig. 3.7(c), where R value increases with patch diameter as more load transfer by patch happens with increased area. Hence, patch having maximum permissible area is preferred in the case of circular shape.
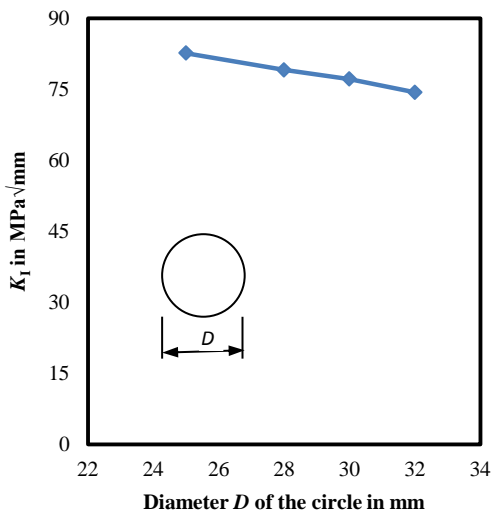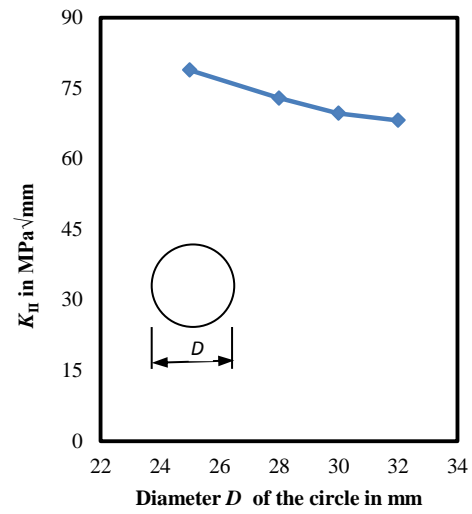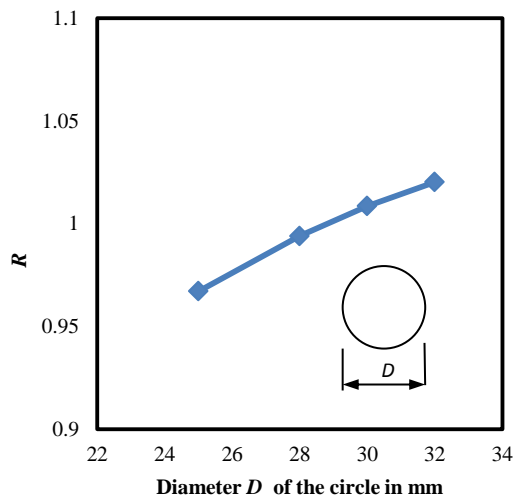
Figure 3.7: Variation of SIF and factor R with the diameter D of circular patch (a) K_I (b) K_{II} (c) R, inclined crack having crack length 2a =10 mm

3.4.2 Variation of SIF and reduction parameter in rectangular patch

Figure 3.8 shows the variation of K_I, K_{II} and R with respect to size of the rectangular patch. From Fig. 3.8(a) it can be observed that for fixed length and increasing width of rectangle K_I gets lowered and K_{II} becomes greater. For the other case, fixed width and increasing length of rectangle K_{II} gets lowered and K_I becomes greater (see Fig. 3.8(b)). Looking at Fig. 3.8(c) it can be found that R is higher for the rectangular patch with fixed width and increasing length. Hence it can be concluded that rectangular patches with larger length performs better

as compared to the one with larger width. Because stiffness offered by a lengthier patch along loading direction is greater, as compared to the one in the width direction.

(a)

(b)

(c)
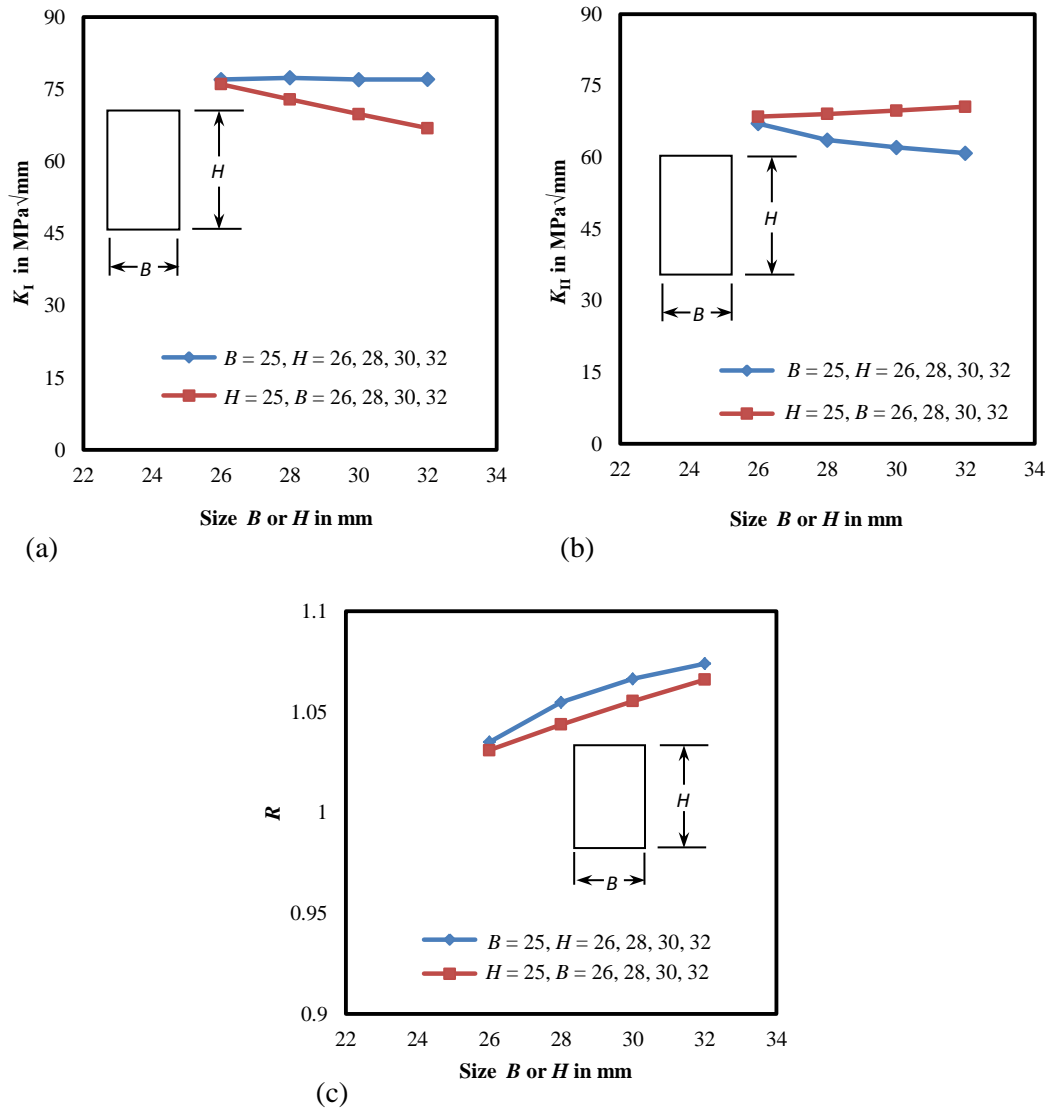
Figure 3.8: Variation of SIF and factor R against size B or H of rectangular patched panel having a crack length $2a = 10$ mm (a) K_I (b) K_{II} (c) R

3.4.3 Variation of SIF and reduction parameter in square patch

Figure 3.9 shows the variation of K_I, K_{II} and R with the size of square patch. From Fig. 3.9(a) and 3.9(b) it is evident that as the size of patch increases, overlapping area increases hence SIF decreases similar to that of circular patch. Also the R value increases with increasing patch areas as shown in Fig. 3.9(c) similar to that of circular patch model behavior.

(a)

(b)

(c)
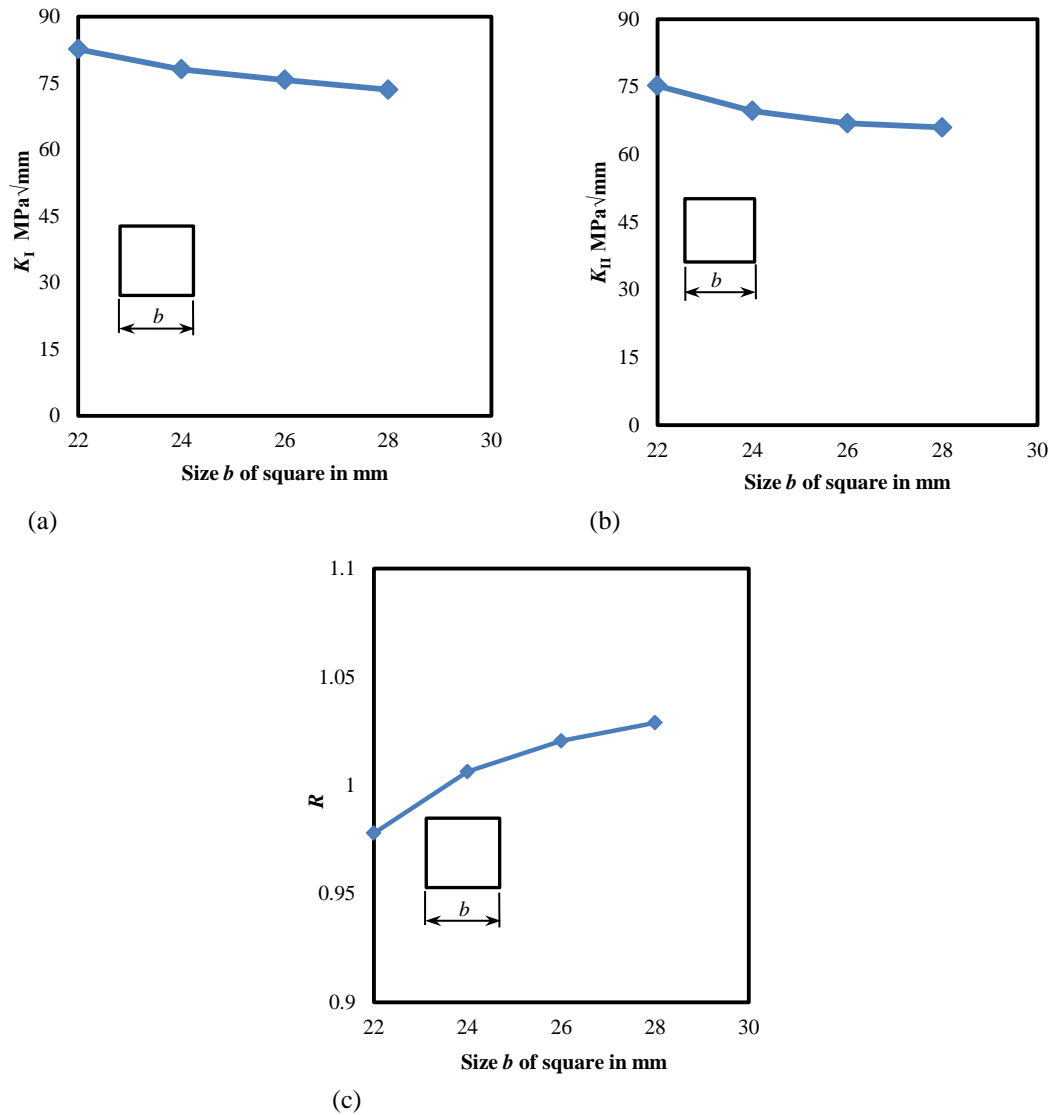
Figure 3.9: Variation of SIF and factor R with the size b of square patched panel having crack length 2a=10 mm (a) K_I (b) K_{II} (c) R

3.4.4 Variation of SIF and reduction parameter in elliptical patch

Two forms of elliptical patch shapes are considered. One with the major axis along x-axis (horizontal ellipse) and other with the major axis along y-axis (rotated ellipse). Figure 3.10 shows the variation of K_I, K_{II} and R with respect to increasing major axis length while maintaining a fixed minor axis length. Looking at Fig. 3.10(a) and 3.10(b), it can be found that for rotated ellipse K_I is higher and K_{II} gets reduced with increasing major axis length. The behavior of elliptical patches is similar to that of rectangular patches. From Fig. 3.10(c) it can be observed that R is higher for the rotated elliptical patch. The stiffness offered by rotated elliptical patches along loading direction is more as compared to the horizontal one.
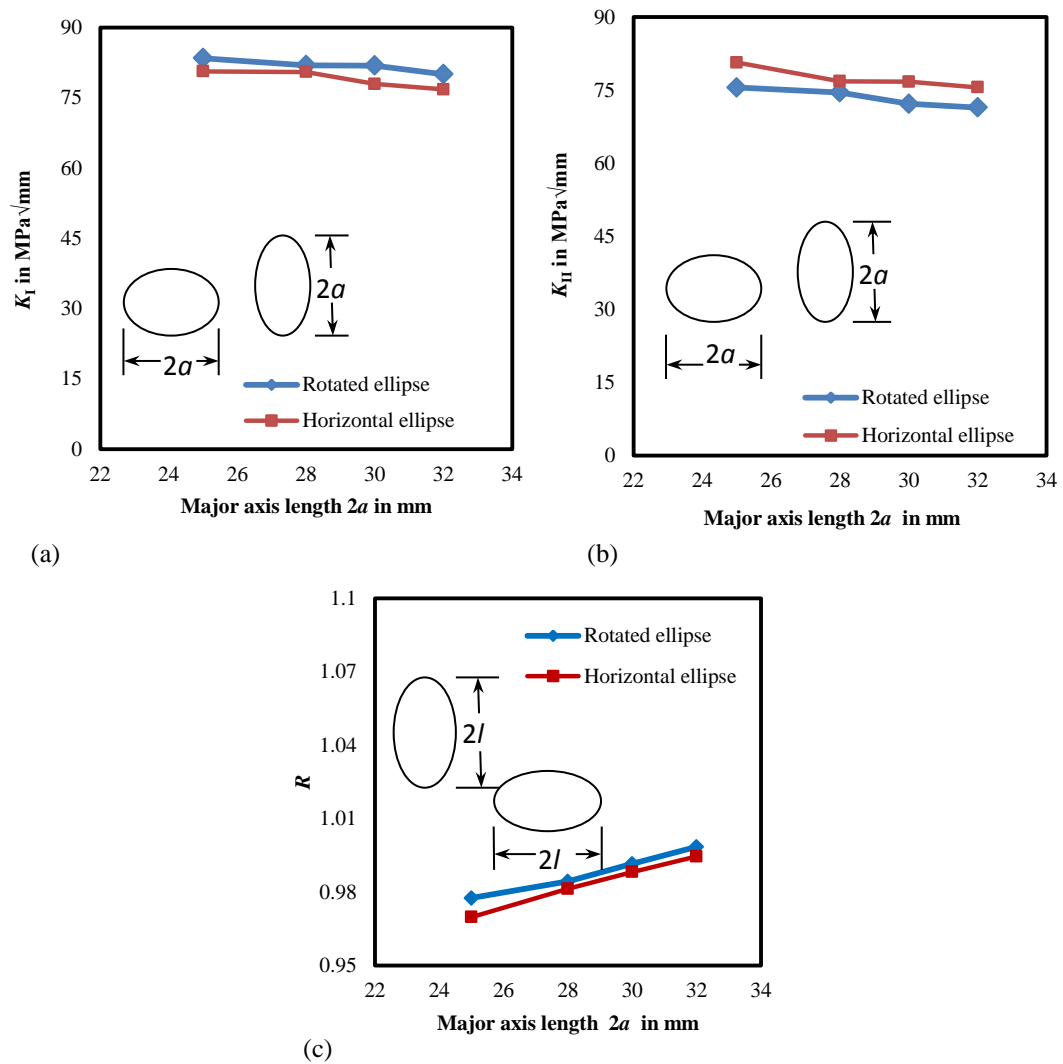
Figure 3.10: Variation of SIF and factor R with major axis length $2l$ for elliptical patched panel having a crack length $2a = 10$ mm (a) K_I (b) K_{II} (c) R

3.4.5 Variation of SIF and reduction parameter in octagonal patch

Figure 3.11 shows the variation of K_I, K_{II} and R values with respect to distance between two parallel sides (d). Looking at Figure 3.11(a) and 3.11(b) it can be seen that K_I is higher whereas K_{II} is lower in case of extended octagon as the distance d of octagon increases and vice versa in case of regular octagon. From Fig. 3.11(c) it can be observed that R is higher for the extended octagonal patch shape compared to regular octagonal patch shape. Hence extended octagonal shape is preferred.
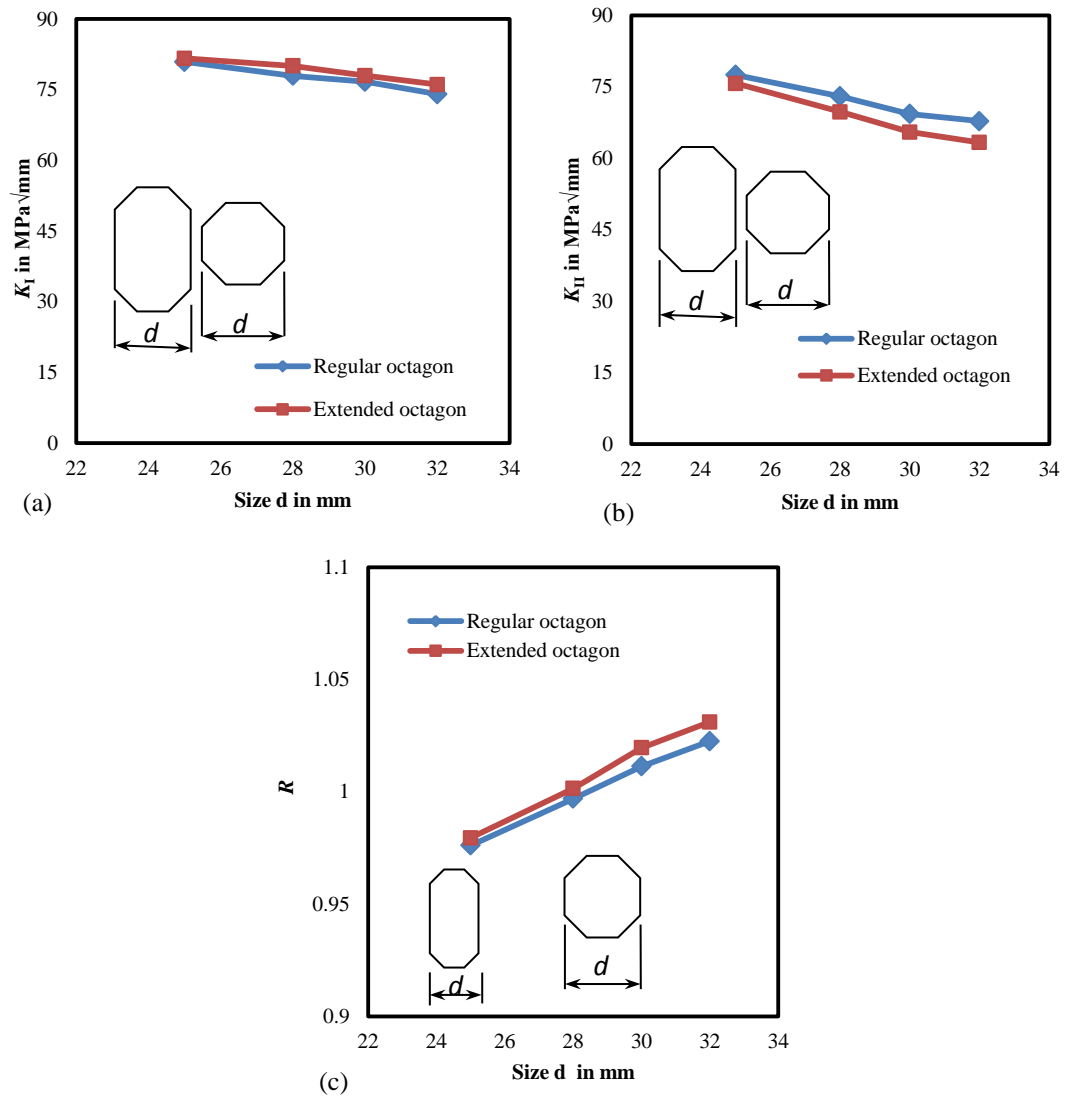
Figure 3.11: Variation of SIF and factor R with the distance d for regular and extended octagonal patches (a) K_I (b) K_{II} (c) R

3.5 Performance of different patch shapes on panel having different crack inclination angles in double sided repair

In the present section the influence of patch shapes on SIF reduction for different inclined cracks is analyzed for a fixed patch area of 804 mm², corresponding to the circle of radius 16 mm. Figure 3.12 shows the variation of SIF (K_I and K_{II}) and R at the mid plane location for different crack inclination angles. By closely observing Fig. 3.12(a) one can see that K_I is maximum at $\beta = 0°$ and is minimum at $\beta = 90°$. The reason for this is that at $\beta = 0°$ there is a maximum crack opening displacement whereas at $\beta = 90°$ it is nil. It is also observed that for a double sided patch there is a significant reduction of K_I for the square, rectangular and

octagonal patch shapes. From Fig. 3.12(b) it can be seen that K_{II} is maximum at 45° and zero at crack angles $\beta = 0°$ and 90°. On overall observation there is greater reduction in SIF with the rectangular and extended octagonal patches. Figure 3.12(c) shows the variation of R with different crack inclination angles. At $\beta = 90°$ the SIF is nil hence R is not considered for this case. It is found that R is maximum at all the inclination angles in case of extended octagon and rectangular patch shape. On careful observation of Fig. 3.12, it is clear that patch shape influences SIF and its impact is different for different crack inclinations. Therefore one needs to do a trade-off for arriving at an optimum patch shape.

(a)

(b)

(c)
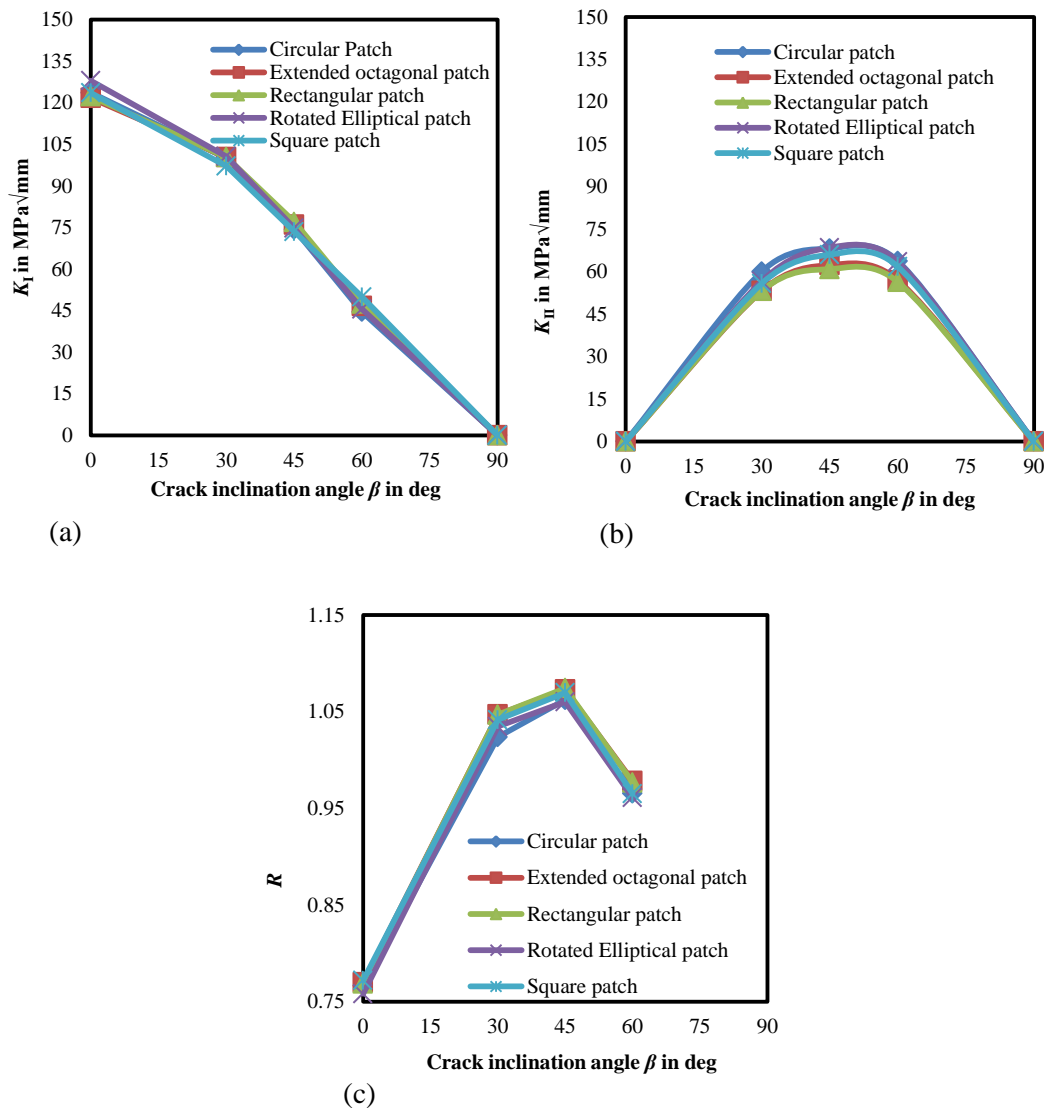
Figure 3.12: Comparison of SIF variation for different patch shapes with respect to the crack inclination angle β (a) K_I (b) K_{II} (c) R

3.6 Comparative study of different patch shapes on SIF reduction

In the previous section 3.4, the effect of SIF reduction for various possibilities within a given patch shape is been studied. Based on that study certain patch shapes are chosen. In the present section a comparative study is done among those chosen patch shapes to identify the best performing shape for the mixed mode cracked panel with crack inclination angle of 45˚. In this section authors have carried out a detailed study on the influence of patch shape on SIF reduction maintaining same volume. Three different patch areas are considered: 804, 706 and 616 (in mm^2) and they correspond to the circle of radius 16, 15 and 14 (in mm) respectively. The patch thickness is kept same and all the patch shapes are arrived at by fixing only one dimension such as length/major axis length same as that of circle diameter. From the previous section it is shown that rectangular patch with greater length performs better than the one with greater width. Hence the rectangular patch with greater length than width is considered here. Square patch is also considered having similar areas with an exception that length is not same as that of circle diameter. Similarly rotated ellipse and extended octagon are chosen as they perform better compared to their counter parts.

Figure 3.13 shows the variation of SIF at mid plane location with respect to area for all the patch shape considered. Looking at Fig. 3.13(a) and 3.13 (b) it can be observed that the SIF is decreasing with increasing patch area because load transfer by patch increases with increasing patch area. In Fig. 3.13(c), *R* value is compared against the patch area for different patch shapes. It is found that extended octagonal patch is more efficient in terms of SIF reduction followed closely by rectangular patch. Compared to rectangular patch extended octagonal patch performs better because it's width is more for a given area compared to the rectangular patch and load transfer is kept away from the crack tip. Also, in most of the repair work researchers [3, 4 and 35] have preferred extended octagonal patch shape in their study which further strengthens our prediction. Furthermore the sharp corners are avoided in the extended octagonal patch making it more resistant against debonding as compared to the rectangular patch.
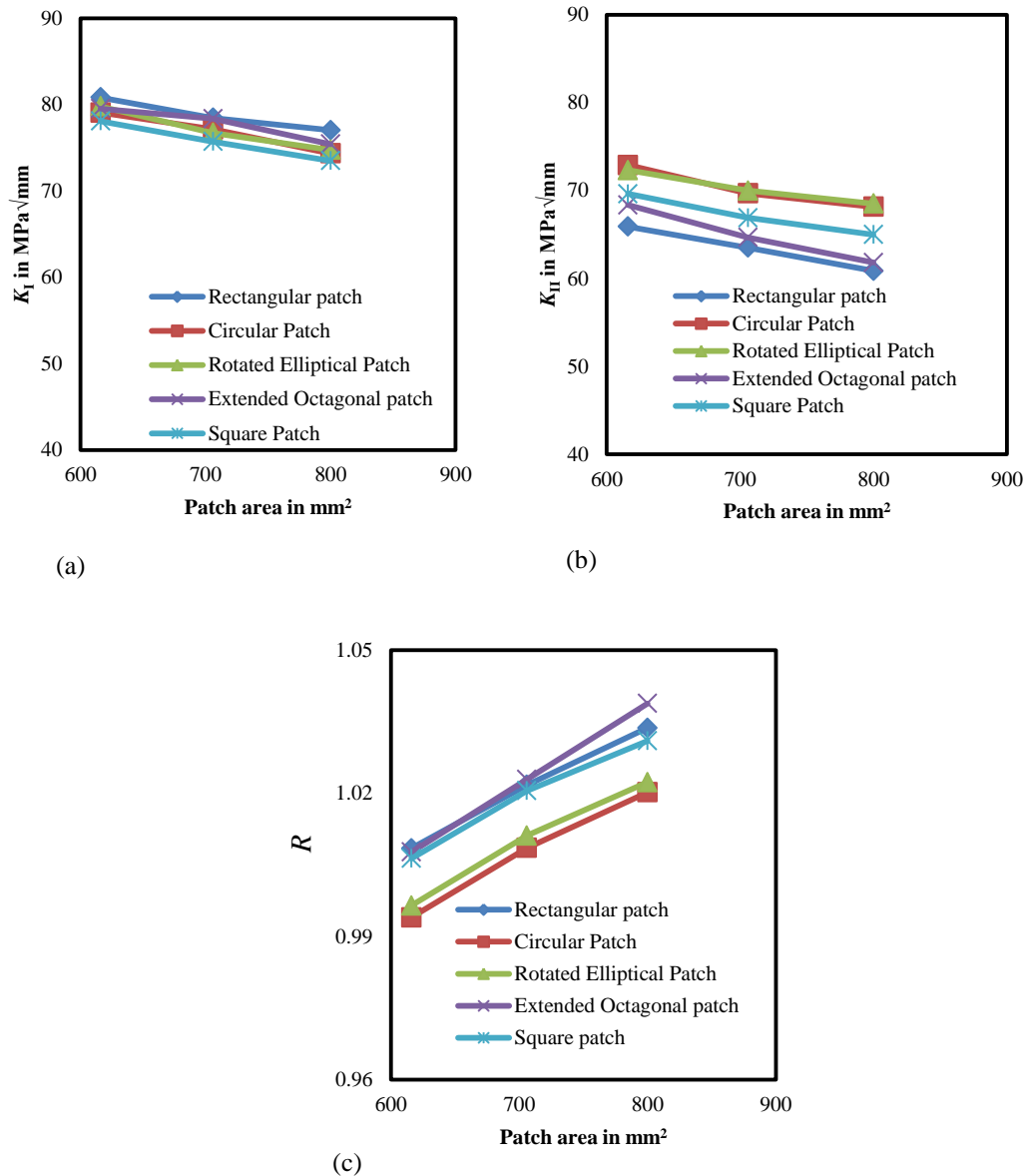
Figure 3.13: Variation of SIF and factor *R* with the patch area for double sided patch with different patch shapes (a) K_I (b) K_{II} (c) *R*

Table 3.2 shows the comparison of *R* value obtained for different patch shapes. From the Table 3.2 it is clearly evident that on overall comparison extended octagonal patch has the highest *R* value and therefore it is preferred for mixed-mode cracked panel. The performance of rectangular patch (having greater length) is also comparable to extended octagonal patch but from debonding perspective octagon is preferred. The limitation of this approach is applicable only to fixed panel size and one cannot generalize it for other panel dimensions. The optimization of patch dimensions such as width, length and thickness for an extended octagon patch shape is carried out in the coming sections.

Table 3.2: Comparison of _R_ value with different patch shapes for different patch areas

Patch area in mm²	Rectangular	Square	Circular	Rotated Elliptical	Extended Octagon
616	1.0084	1.0063	0.9940	0.9964	1.0077
706	1.0217	1.0205	1.0085	1.0111	1.0229
804	1.0337	1.0310	1.0202	1.0205	1.0388

3.7 Comparative study of patch shape on SIF reduction in single sided repair

In the present section, the influence of patch shape on SIF reduction in single sided repair is carried out. Figure 3.14 shows the variation of SIF through the thickness of the panel for different patch shapes and is being compared with the unrepaired SIF. Here, the patch volume is maintained constant. From the Fig. 3.14 it is observed that there is a very slight reduction in K_I and K_{II} with the octagonal and rectangular patch shapes. But the reduction is very small. Hence it is found that in case of single sided repaired panel, there is no effect patch shapes on SIF reduction. Hence the extended octagonal patch shape is used for the single sided patch repaired configuration. The next section describes the optimization of patch dimensions such as patch length, width and thickness from mechanics based and GA based optimization approach.

(a)

(b)
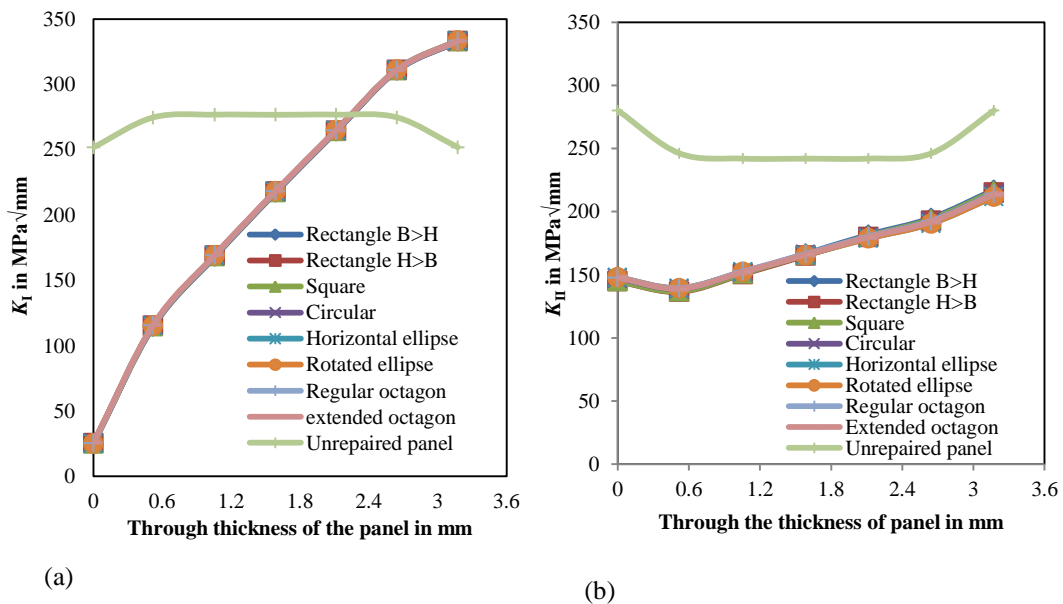
Figure 3.14: Variation of SIF through the thickness of the panel in single sided patch repair with different patch shapes (a) K_I (b) K_{II}

3.8 Dimensional optimization of octagonal patch

From the previous section 3.6 the best performing patch shape is identified as extended octagonal patch shape. In this section, the dimensional optimization of extended octagonal patch is carried out using multi objective genetic algorithm optimization technique. The optimization process is performed by developing an interface between GA and FEA for gaining higher reduction in SIF at the crack tip and SCF at the overlap edge. In this study, unidirectional CFRP laminate with 0° lay-up angle is considered. The material properties of CFRP laminate are given in Table 3.3. The material properties are determined experimentally from base line tests as explained in detail in Appendix C.2. Araldite-2011 adhesive is used for bonding the patch over the cracked panel. The general material properties of aluminium panel, composite patch and adhesive are given in Table 3.3.

Table 3.3: Material properties of Al 2014-T6 panel, Araldite 2011 adhesive and CFRP patch

Material	$E_x{}^a$ (GPa)	E_y, E_z (GPa)	$v_{xy}{}^b, v_{xz}$	v_{yz}	$G_{xy}{}^c$, G_{xz} (GPa)	G_{yz} (GPa)
Aluminium	73.1	-	0.33	-	-	-
Adhesive [81]	1.148	-	0.4	-	-	-
Carbon/Epoxy [17]	81.9	6.15	0.34	0.49	2.77	2.05
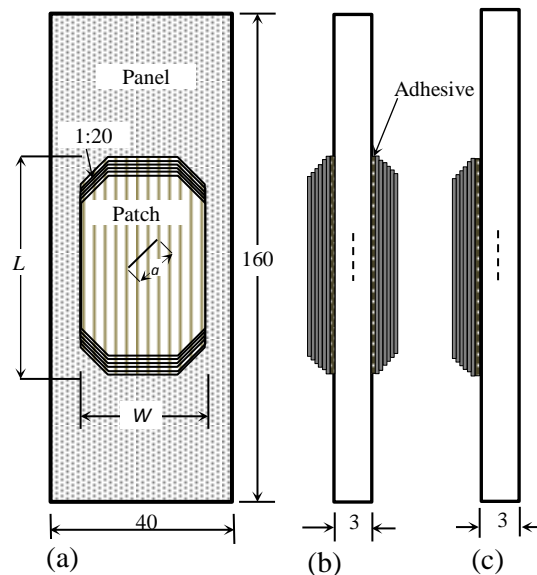
Figure 3.15: Geometry of the repair model with extended octagonal patch (a) front view (b) side view of symmetrical patch (c) side view of asymmetrical patch (All dimensions are in mm)

In the present optimization study, to reduce the computation time the crack tip mesh has been modified. Here, the crack tip mesh has a total of 3456 elements with 16 radial, 36 circumferential and 6 elements through the thickness. The panel, patch and adhesive are modeled with the same 20 noded solid 186 element as per the dimensions. In the thickness direction, the panel is meshed with six elements, adhesive with one element and patch with six elements. Here, multipoint constraint contact (MPC) technique is employed to simulate the perfect bonding between adhesive/panel and adhesive/patch interface. MPC algorithm involves contact and target surfaces which are coming into contact with one another. MPC internally adds constraint equations to "tie" the dof's of the corresponding nodes between contacting surfaces such that no relative displacement exists between nodes / surfaces. It is a direct, efficient way of bonding surfaces at interface [76]. This contact algorithm does not require similar mesh patterns at the interface such as adhesive/panel and adhesive/patch. Figure 3.16(a) show the finite element model of the inclined center cracked panel. The zoomed portion of mesh surrounding the crack tip is shown in Fig. 3.16(b). Figure 3.16(c) shows the front view of double sided repaired panel with extended octagonal patch with tapered edges.
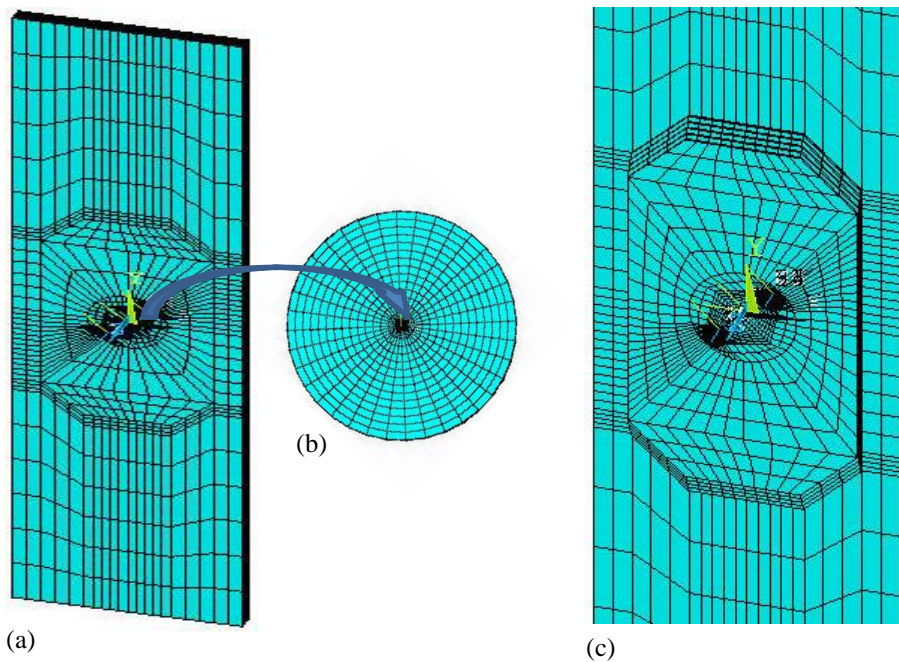
Figure 3.16: Finite Element Modeling of (a) cracked panel (b) zoomed portion of crack tip (c) zoomed portion of repaired panel

3.9   Estimation of optimal patch dimensions from mechanics based approach

3.9.1   Influence of patch thickness

In the present section, the effect of patch thickness on repaired panel is studied. Patch thickness is one of the governing parameters which have a direct influence on the repair efficiency since the stiffness of the repaired panel depends on the patch thickness. The selection of patch thickness mainly depends on the thickness of the parent structure. Thus, to estimate the optimal patch thickness a series of analyses have been performed by varying the composite patch thickness and the resultant change in *J* integral and SCF (stress concentration factor) is illustrated in Fig. 3.17. From the Fig. 3.17 it is clear that increase in patch thickness leads to reduction in *J*-integral value. This reduction in *J*-integral value is because of additional reinforcement over the crack zone (i.e., more load transfer through the patch) with an increased number of layers in the patch. There is an inverse relationship exists between SCF and *J*-integral value. From Fig. 3.17 it is evident that as the patch thickness increases, SCF on the panel skin (at the overlap edge) increases. Looking at the Fig. 3.17 one can conclude that where both SCF and *J*-integral value intersect, that point shows the optimum patch thickness. Here, from the figure the optimal patch thcikness is of 2.2 mm corresponding to six layers.
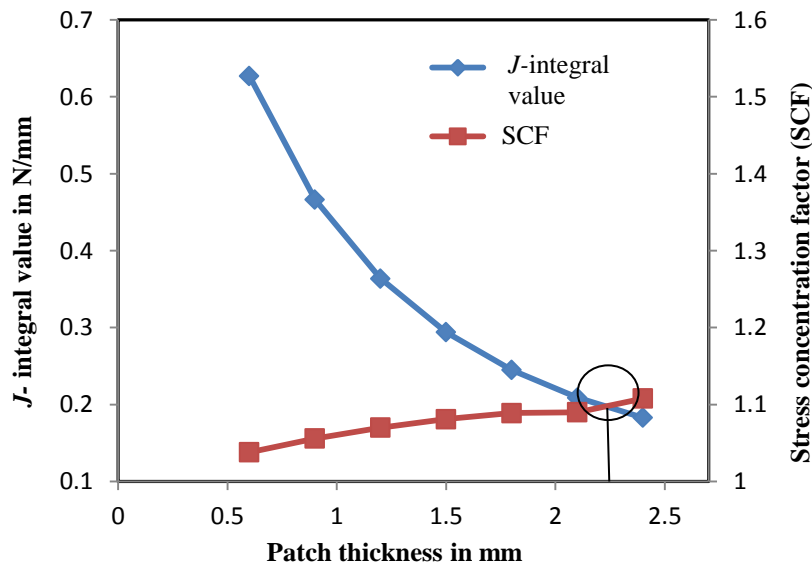
Figure 3.17: Variation of *J* integral value and SCF with increasing patch thickness

3.9.2   Influence of patch length on *J*-integral value, peel and shear stresses

In this section the patch length is varied for fixed patch width of 25, 30, 35 and 38 mm respectively. The thickness of CFRP patch is taken as 2.2 mm. Figure 3.18(a) shows the

variation of *J*-integral value with patch length. From Fig. 3.18 (a) it is clear that as patch length increases, the *J*-integral value decreases up to certain length and further it increases with increasing patch length. Also it can be observed that the *J*-integral value is minimum for patch length 70 mm and width 38 mm as shown in Fig. 3.18(a). Generally, as the patch overlap or bond length is too short, the most of the adhesive layer is under high shear stress [35]. As the overlap length increases, stress level is minimum at the center of the panel except at overlap ends. Since there is abrupt change in cross section that leads to high shear stresses at the overlap edge. Further to see the influence of patch length on shear and peel stresses, the adhesive shear stress and peel stress distribution is plotted with respect to overlap length (see Fig. 3.18(b) and 3.18(c)) for a patch width of 38 mm. From the Fig. 3.18(b) it can be identified that as patch length increases from 35 mm to 70 mm, there is a gradual reduction in peel stress at the overlap edge and there is not much reduction is seen with further increasing in patch length. Figure 3.18(c) shows the variation of shear stress distribution with half the patch length. From the Fig. 3.18(c) it is evident that shear stress τ_{yz} is minimum at the center of the panel and maximum at the overlap edge. On overall comparison, patch length of 70 mm is chosen considering minimal *J*-integral value, shear and peel stress. The estimated patch length obtained from mechanics based approach is compared against the CRMS guidelines as mentioned in Appendix B.1.
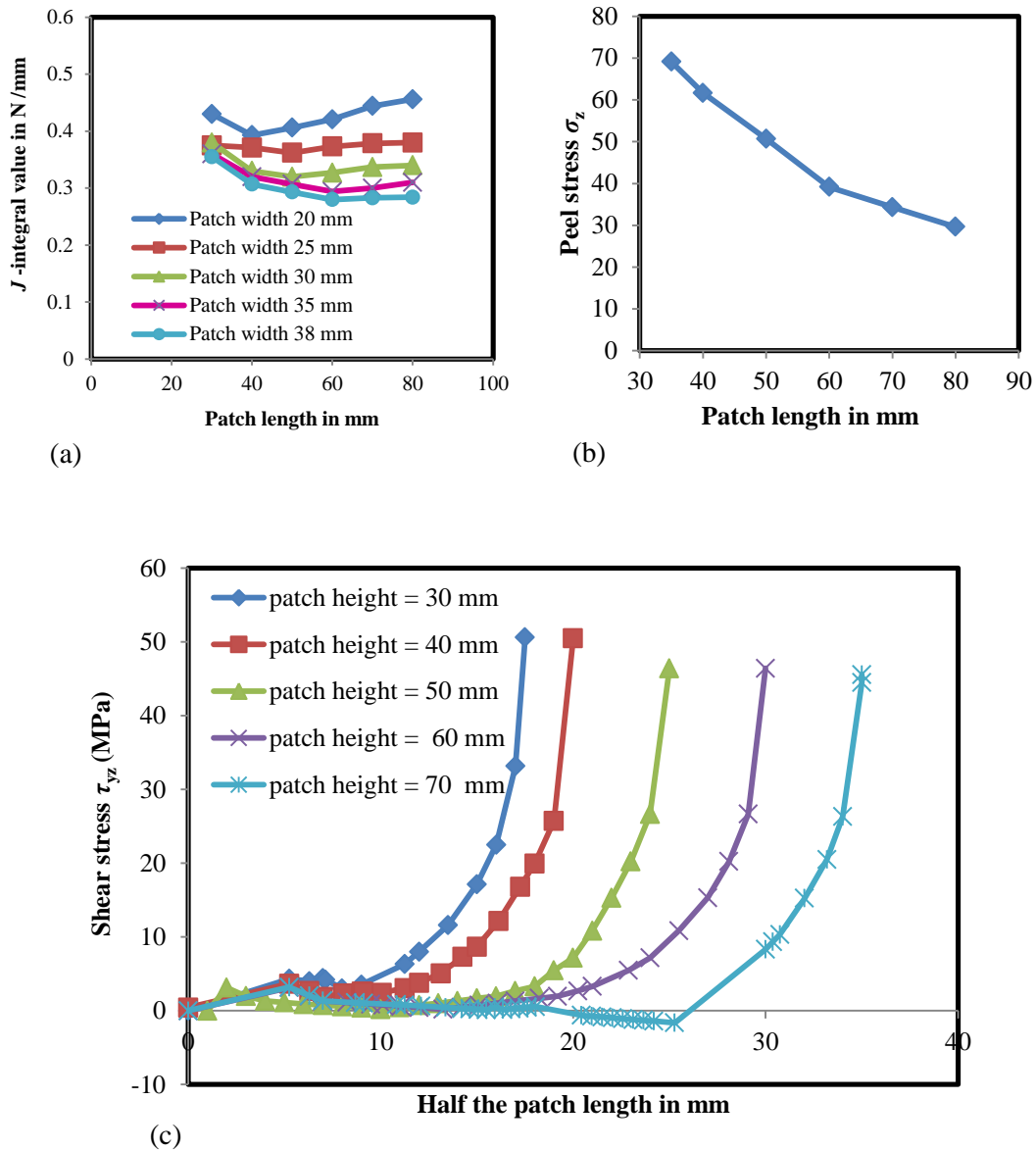
Figure 3.18: Effect of patch overlaps length (a) on J integral value (b) peel stress (c) shear stress τ_{yz} in adhesive layer

3.10 Optimization of patch dimensions using Genetic algorithm based approach

Genetic algorithm is an efficient global search optimization method which operates on a population of potential solutions rather than from one single solution [82]. It works on principle of natural selection and genetics. In recent years increasing number of GA's applications to single-objective optimization have been observed in the field of reliability and maintainability analysis. In single objective optimization the solution is only a single point but in multi objective optimization the solution is the family of points known as Pareto-optimal set. In case of a single objective the comparison is trivial since a vector

solution *X* is better than *Y* if the corresponding objective function (fitness) value *f(X)* is greater than *f(Y)*. If there is an *N* objective functions, two solutions *X* and *Y* must be related in terms of dominance of one solution over the other with respect to all *N* objectives. As a result of the multi-objective search process, convergence is achieved on a Pareto-optimal region of non-dominated solutions which can be subjectively managed by the decider to identify the preferred solution [82]. The application of GA and other rank based algorithms to multi-objective optimization is of great attention in mechanics area. Mostly numerical technique such as FEA is preferred for generating the initial population for GA based optimization study.

The optimization problem can be stated as

Minimize $f_i(x)$, where $i = 1, 2, ..N$

Subjected to $x_j^L \leq x_j \leq x_j^U$ where $j = 1,2,3,…,N$

$$(3.2)$$

where $f_1(x), f_2(x),… f_N(x)$ are the objective functions, x_i and x_j are the design variables and x_j^L and x_j^U are lower and upper bound of the design variables. In this work patch dimension influences both *J*-integral value at the crack tip and stress concentration factor (SCF) (which is the ratio of nominal stress on the panel at the overlap edge to the applied stress) at the overlap edge. In multi objective optimization process, *J*-integral value is considered as first optimization parameter and stress concentration factor (SCF) is considered as the second optimized parameter. Hence, these two parameters should be minimized. The patch dimensions such as length, width and thickness are considered as the design variables. The optimization scheme implemented in the present study is represented by a flowchart as given in Fig. 3.19. The optimization is performed by developing an interface between optimization tool box in MATLAB [82] and FEA software ANSYS. The optimization process starts with assigning an initial value of the parameters. These parameters are read in to APDL (ANSYS Parametric Design Language) code and then stress analysis is carried out to evaluate SCF and *J*-integral value. The estimated SCF and *J*-integral value is later read into optimization algorithm and it is then checked for solution optimality and convergence criteria. If the solution is optimal and convergence is achieved program terminated with optimal design variables. If not the search continues till the optimal design variables are arrived.
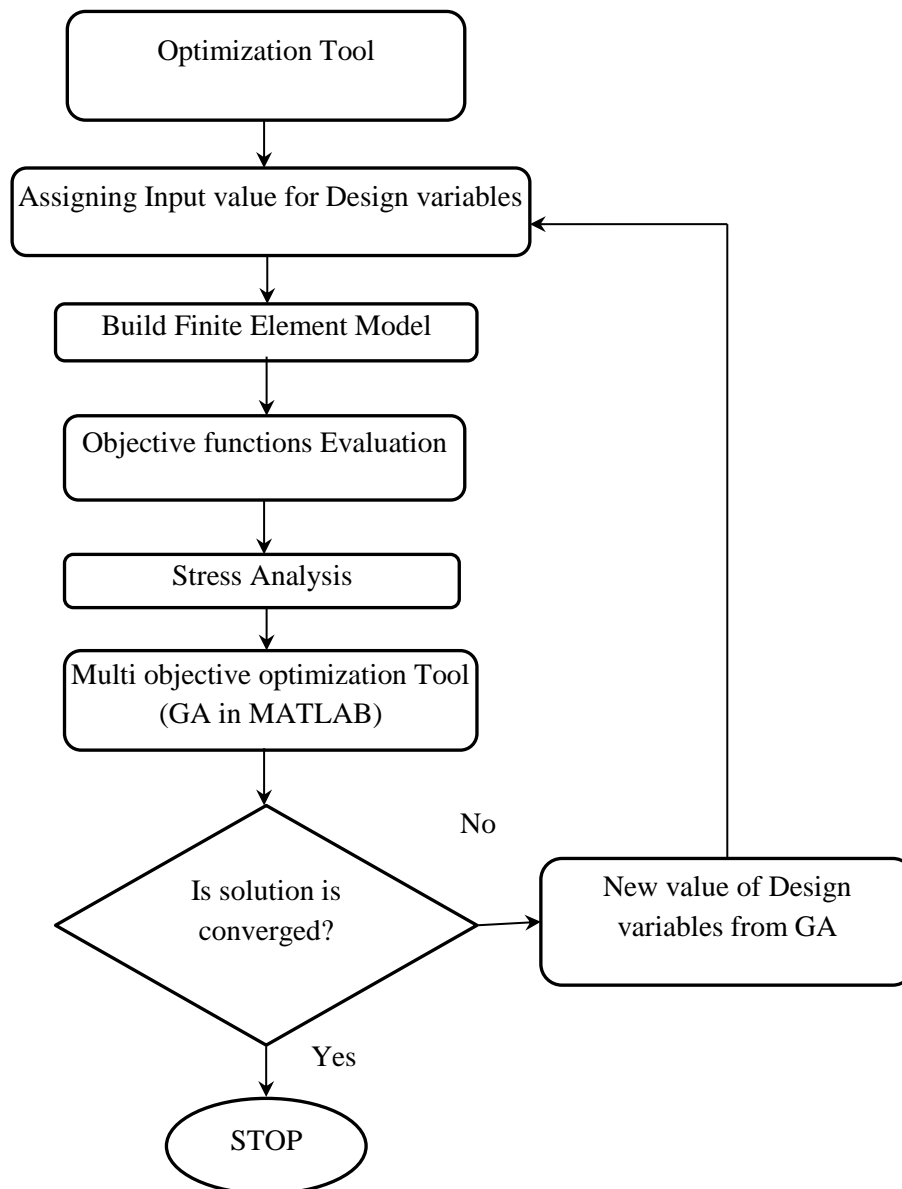
Figure 3.19: Flow chart describing the optimization procedure using genetic algorithm in conjunction with finite element analysis

3.11 Optimal solution from GA based approach

The GA technique is applied to determine the optimal patch dimensions of a patch for repair of an inclined center cracked panel under mixed mode loading. Here, the optimization is carried out for double sided repair panel. The lower bound and upper bounds of design variables and the GA parameters used in optimization algorithm are summarized in Table. 3.4. The upper and lower bounds are governed by the panel geometry. The multi-objective GA solver in MATLAB is used to solve multi-objective optimization problems and the

optimal solution is arrived from the Pareto front as shown in Figure 3.20(a). Pareto plot shows the trade- off between two objective functions SCF and *J*-integral value. It is also defined as the set of non-inferior solutions. A non-inferior solution is the one in which an improvement in one objective requires a degradation of another. For example, in the Fig. 3.20(a) *A* and *B* are clearly non-inferior solution points because an improvement in one objective leads to degradation in the other objective, i.e., at point *A, J*-integral value is higher whereas at point *B,* SCF is higher. Therefore selection of non-inferior solution point would be at point *C* leading to lower *J-* value and SCF. In this study convergence is assumed to be reached when the function tolerance limit of 1e-3 is reached. Figure 3.20(b) shows the average spread with the number of generations. In this procedure each generation is assumed as 90 iterations. From the Fig. 3.20 (b) one can see that the convergence is achieved after 30 generations and is the same afterwards until it gets terminated. This algorithm has terminated with minimum SCF value of 1.04 and *J-* value of 0.19 for patch geometry of 38.2 x 78.3 x 2.1 mm^3. These optimum dimensions are compared against the composite repair manual system (CRMS) guidelines as mentioned in Appendix B.1.

Table 3.4: Optimization Parameters

Genetic algorithm options	Value	
Population size	90	
Number of generations	72	
Tolerance limit	1e-3	
Design variables	Lower bound (mm)	Upper bound (mm)
Patch width	20	39
Patch length	30	80
Patch thickness	0.6	2.4
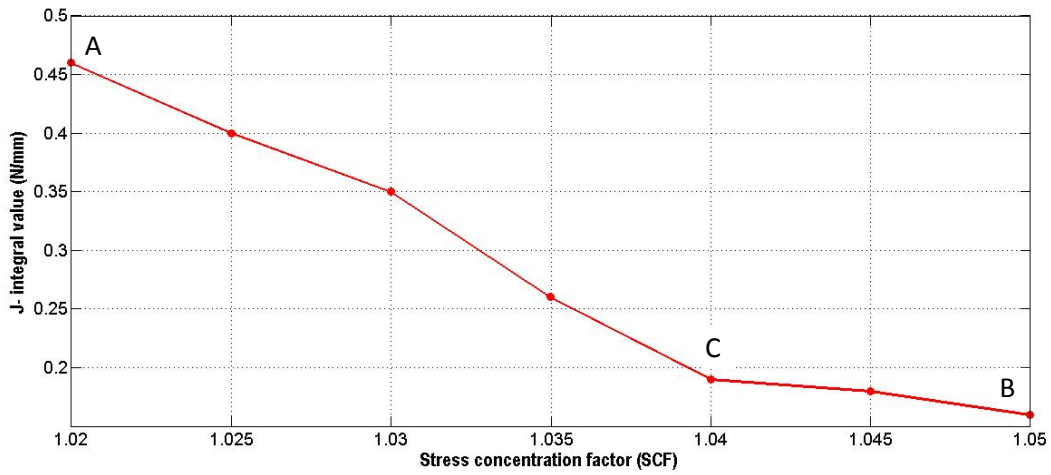
(a)
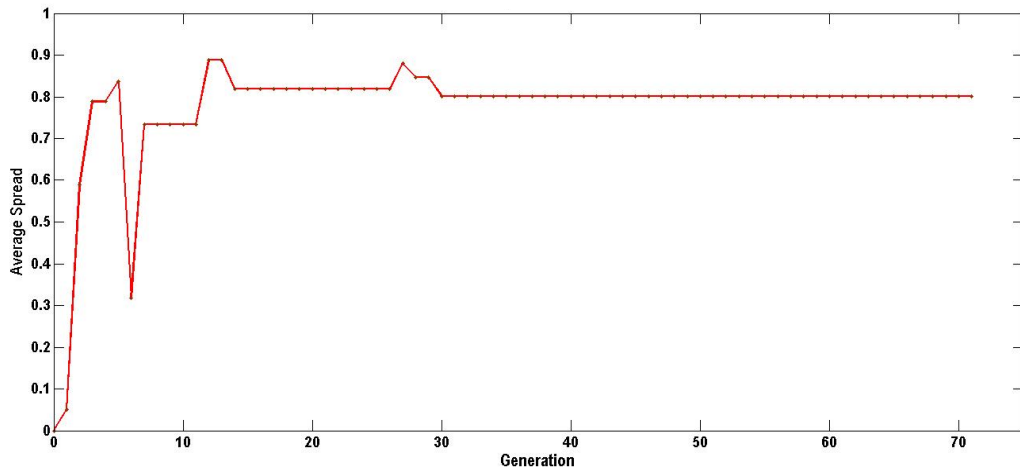
(b)

Figure 3.20: Parametric optimization plots (a) average spread (b) pareto plot

The patch dimensions obtained from both the mechanics based and GA based approach are in good agreement with the CRMS guidelines as shown in Table 3.5. The optimum patch dimensions arrived from GA based approach are presented in terms of panel width (see Fig. 3.21). The optimum patch dimensions obtained from GA based approach are considered for further analysis: patch width is 38 mm, patch length is 78 mm and patch thickness is 2.1 mm. To avoid the severity of these peel stresses occurring at the overlapped ends, tapering is provided at the edges with a tapered ratio of 1:20 according to standards as mentioned in Ref. [4]. The same patch dimension is also kept for the single sided repair configuration.

Table 3.5: Comparison of Optimized patch dimensions arrived from different approaches

	Patch width	Patch length	Patch thickness
CRMS guidelines	$\geq 1.2\,a$	**1.875 W**	$> t_s / 2$
Mechanics based approach	**7 a**	**1.75 W**	**0.74 t_s**
GA approach	**7.6 a**	**1.95 W**	**0.7 t_s**

a: Half the crack length , *W* :Width of panel and t_s : Thickness of the panel in mm
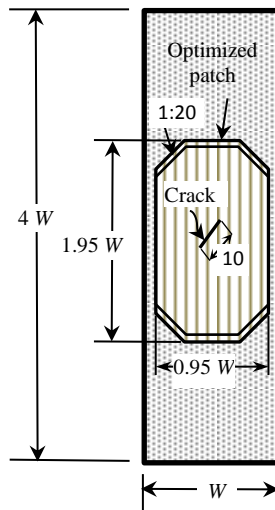
Figure 3.21: Optimal patch dimensions using genetic algorithm

3.12 SIF estimation using VCCT technique in optimal repaired configuration

The single sided and double sided repaired panel is modeled with the arrived optimal patch dimensions and also the edge of patch is tapered with a tapering ratio of 1:20 as shown in Fig. 3.16. In the previous chapters, the crack front is assumed to be normal to the panel surface but in real situation as the crack front grows it need not be perpendicular to the panel's surface resulting in mode III SIF. Hence, in this study all the three modes is considered and respective SIF's are estimated from energy release rate (*G*) using virtual crack closure technique (VCCT). The analysis is carried out in the linear elastic fracture mechanics (LEFM) frame work. SIF is estimated from ERR [13]. The energy release rate

for all the modes can be estimated using the procedure as mentioned in appendix B.2. From three G-values, SIF's are estimated using the following equations:

$$K_I = \sqrt{E'G_I} \tag{3.2}$$

$$K_{II} = \sqrt{E'G_{II}} \tag{3.3}$$

$$K_{III} = \sqrt{2\mu G_{III}} \tag{3.4}$$

where E' is modulus of elasticity, $E' = E$ for plane stress conditions and $E' = E / (1-v^2)$ for plane strain condition.

3.12.1 SIF variation through the thickness of panel using VCCT technique

Figure 3.22 shows the SIF variation through the panel thickness for single and double sided patch model is compared with the un-repaired panel. From Fig. 3.22 it is clear that reduction of K_I, K_{II} and K_{III} values of about 78% in case of double sided repair and the variation is symmetric through the thickness of the panel. In case of single sided patch repaired panel, due to presence of additional bending stresses in addition to in-plane tensile stresses, both K_I and K_{III} values are higher at unpatched surface as compared to the patched surface. This trend has been observed because of load eccentricity in the single sided repaired configuration which results in additional bending stresses. From Fig. 3.22, it is observed that SIF reduction is highest in case of double sided repair and it works very effectively. Further, it is found that the effect of K_{III} is very small as compared to K_I and K_{II} in case of cracked panel with 45˚ inclination angle.

Table 3.6 shows the SIF reduction without and with optimal patch configuration. From the Table 3.6, it is observed that optimized repair configuration improves the repair efficiency in terms of SIF reduction by 33% in case of double sided repair and by 8% in case of single sided repair.

Table 3.6 Comparison of SIF with and without optimal patch configuration

	Double sided repair		Single sided repair	
	K_I (MPa√mm)	K_{II} (MPa√mm)	K_I (MPa√mm)	K_{II} (MPa√mm)
Without Optimized patch	78.8	73.7	342.6	242.32
With Optimized patch	51.2	50.2	299.7	247.8
%difference	35	31	13.3	2
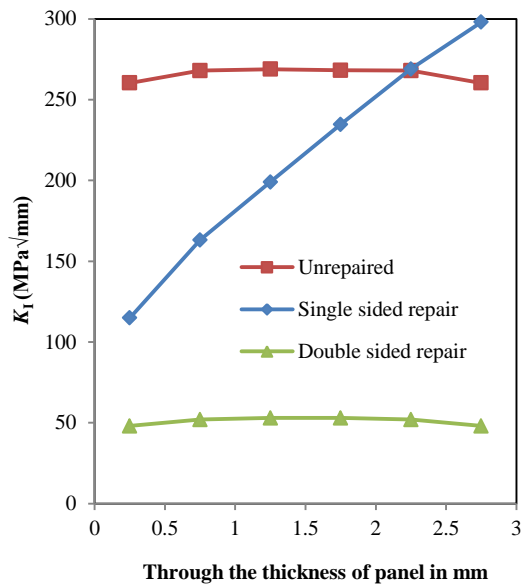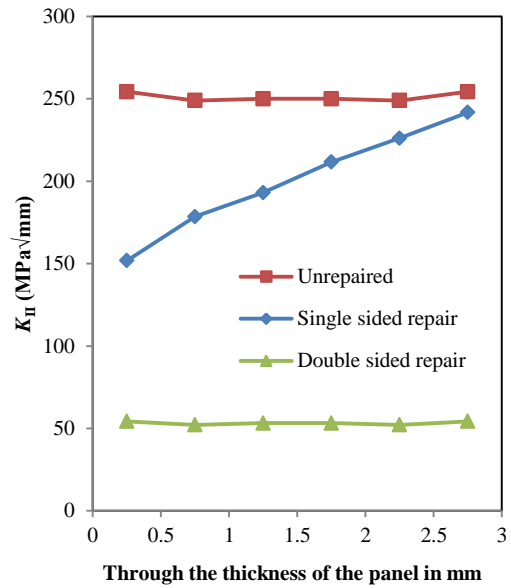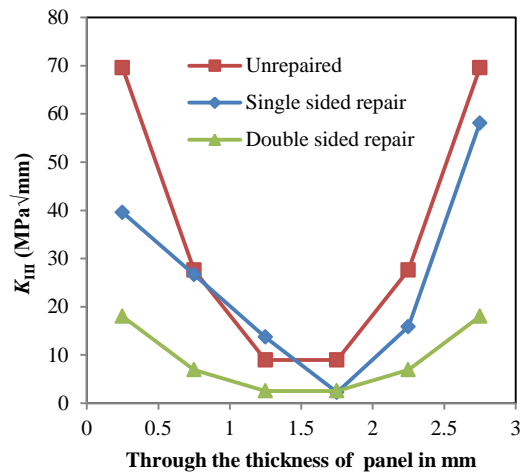
Figure 3.22: SIF variation through the thickness of the panel using VCCT technique (a) K_I (b) K_{II} (c) K_{III}

3.13 Closure

Finite element analysis based study has been carried out to understand the influence of patch shapes on inclined center crack panel. Five different patch shapes such as circular, rectangle, square, elliptical and octagonal has been considered. Rectangular patch shape having greater length has performed better compared to the one with greater width. On the other hand rotated elliptical patch has performed better than the horizontal one. Finally in case of octagonal patch, one with the extended side length has performed well. Also greater the

patch area, higher the SIF reduction because of increased load transfer by the patch. Including the circular and square patch on overall comparison, extended octagon has performed better showing highest R value. It is closely followed by the rectangular patch shape. Therefore, extended octagonal patch shape made of CFRP with maximum permissible area is recommended in case of repair of inclined cracked panel. Further, FEA based study is carried out to evaluate the optimum patch dimensions using mechanics based approach and GA based optimization technique. From the mechanics based study it is found that increasing patch thickness reduces the SIF at the crack tip but leads to high stress concentration at the overlap edge. Further, it is observed that increasing overlap length leads to reduction in J- integral value at the crack tip, shear and peel stresses in the adhesive. From the multi objective GA based optimization study, it is found that the width of the patch is of 7.6 times of crack length and 0.9 times width of panel; patch length is twice the width of the patch. These optimal patch dimensions are compared against both CRMS guidelines and mechanics based recommendations and it satisfies them. Moreover, it is observed that optimal repaired configuration reduces the SIF by 35% in double sided patch repaired model and by 10% in case of single sided patch repaired model, as compared to the original configuration. In the next chapter repair specimen is fabricated with the arrived optimal patch dimensions. Later, experimental strain analysis of the repaired panel under tensile load is carried out using DIC technique for both qualitative and quantitative comparison.

Chapter 4

Experimental Investigation of Bonded Patch Repaired Panel using DIC

4.1 Introduction

In the previous chapters, entire stress analysis is carried out using FEA and no experimental validation exists. Therefore, a need arises to carry out the experimental strain analysis for both the repair configurations for understanding their behavior under actual tensile loading. The investigation of three-dimensional nature of the strain field in the adhesively bonded repaired panels necessitates an experimental method that provides full-field strain measurement with sufficient sensitivity. As explained earlier in the introduction chapter, strain gauges capture strain at a single point and it is very tedious to get the whole field distribution. There are many non-contact techniques based on both interferometric and non-interferometric principles which could provide either displacement or strain field over the specimen surface under loading. In case of interferometry techniques, electronic speckle pattern interferometry (ESPI), Moiré interferometry and reflection photoelasticity are commonly employed [83-85]. All these interferometric methods require a coherent light source, and the measurements are normally conducted in a vibration-isolated platform in the laboratory except reflection photoelasticity. Interferometric techniques measure the deformation by recording the phase difference of the scattered light wave from the test object surface before and after deformation. The measurement results are often presented in the form of fringe patterns; thus, further the fringe processing and phase analysis techniques are required. In case of non-interferometric technique, grid method and digital image correlation (DIC) [21] are being used. DIC is a non-interferometric whole field optical technique that has been widely accepted and commonly used as a powerful and flexible tool for the surface deformation measurement in the field of experimental solid mechanics. This comprehensive coverage enables complete characterization of regions with high strain gradients. Also, identification of these high strain gradient regions could help in predicting

the damage initiation sites. In composite repair, strength of adhesive joint plays an important role in structural integrity as they are weakest link. An extensive amount of analytical, numerical and experimental research has been carried out to understand the behavior of adhesively bonded joints [69, 70]. Only their work related to adhesive lap joint interface study between metal and composites. Experimentally, study related to prediction of the adhesive shear and peel strain in patch repaired panel under tensile loading is of primary importance. Also one could capture the behaviour of adhesive layer under actual loading condition where one could zero in on the high strain locations in adhesive layer.

In the present chapter, an experimental study is presented to analyze the behavior of adhesively bonded patch repair of inclined center cracked aluminium panel under tensile loading. The panel is made of Al 2014-T6 and initially material property estimation of the panel is carried out. Later, an elaborate study involving DIC is carried out to get the whole field surface strain distribution over the repaired panel. To simulate the behavior of repaired panel, an extended octagonal patch shape with tapered edges is chosen. The study is conducted with optimized patch dimensions obtained from GA based optimization technique as mentioned in the previous chapter. The performance and behaviour of both single and double sided CFRP patch repaired panel are analyzed. The strain distribution over the patch and region closer to the overlap edge area are also carefully analyzed for understanding how the load transfer over the cracked region is happening through the patch. The strain measurement over the unrepaired and repaired panel is carried out using 3D DIC. Also, a 3D linear finite element based numerical study is then carried out for the same model to obtain the whole field strain distributions over cracked and repaired panels. The results from FEA are compared against the experimental prediction. In the last part of this chapter, estimation of peel and shear strain distribution in the thin adhesive layer is obtained using magnified optics coupled with 2D DIC setup. This study would give an insight into complex and localized strain distribution occurring over the thin adhesive layer especially at overlap edges leading to damage initiation. Finally, the results obtained from FEA and DIC are qualitatively compared.

4.2 Digital image correlation : an overview

DIC is an innovative full field non-contact optical technique used for measuring strain and displacement in components over a wide range of length scales. It is a versatile technique that is now being used extensively in experimental mechanics in a diverse range of applications like high temperature strain mapping, crack tip and crack propagation studies, material characterization and deformation of large structures. This technique is well suited

for the characterization of material properties both in the elastic and plastic ranges. DIC enables non-contact surface strain measurement of the entire specimen during the test. DIC works on a comparison between two images of the specimen coated by a random speckle pattern in the undeformed and deformed state [21]. Image of the object's surface one before and another after deformation is recorded, digitized and stored in the computer in digital form. These images are then compared to detect displacement by invoking a pattern matching principle. Since it is impossible to find matched points using single pixel, areas (called as subsets) containing multiple pixels are used for the analysis [21, 22]. The subset size varies with respect to the problem. The basic principle of 2D DIC is the tracking (or matching) of the same points (or pixels) between the two images recorded before and after deformation as schematically illustrated in Fig. 4.1. In order to compute the displacement of point P, a square reference subset of $(2M+1) \times (2M+1)$ pixels centered at point P (x_0, y_0) from the reference image is chosen and used to track its corresponding location in the deformed image (See Fig. 4.1). The reason why a square subset, rather than an individual pixel, is selected for matching is that the subset comprising a wider variation in gray levels will distinguish itself from other subsets, and can therefore be more uniquely identified in the deformed image [27].
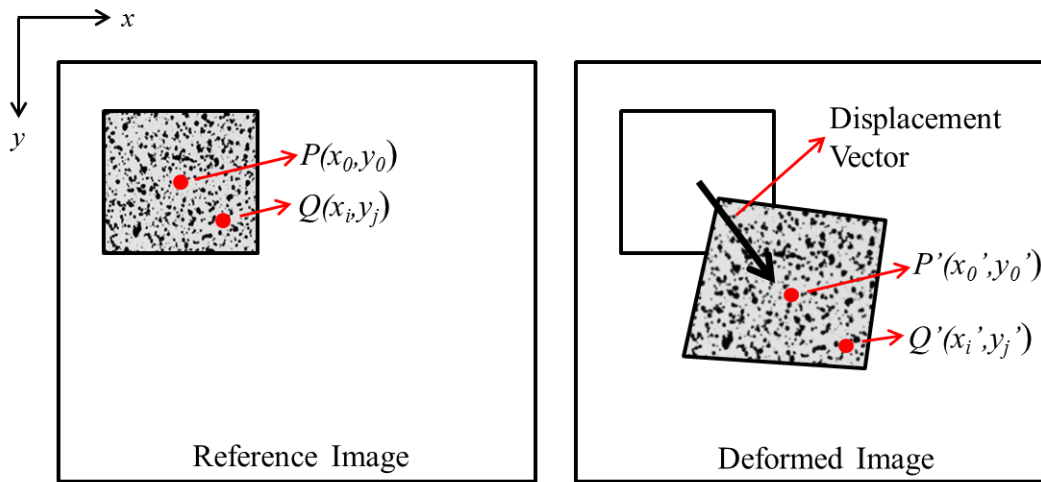
Figure 4.1: Schematic illustration of a reference square subset before deformation and a deformed subset after deformation.

In order to evaluate the degree of similarity between the subsets from reference image and the deformed image, cross-correlation criteria (CC) is used and is given below:

Cross-correlation (CC)

$$C_{CC} = \sum_{i=-M}^{M} \sum_{j=-M}^{M} \left[f(x_i, y_j) g(x'_i, y'_j) \right] \tag{4.1}$$

Normalized cross-correlation (NCC)

$$C_{NCC} = \sum_{i=-M}^{M} \sum_{j=-M}^{M} \left[\frac{f(x_i, y_j) g(x'_i, y'_j)}{\bar{f}\,\bar{g}} \right] \tag{4.2}$$

Zero-normalized cross-correlation (ZNCC)

$$C_{ZNCC} = \sum_{i=-M}^{M} \sum_{j=-M}^{M} \left[\frac{\left[f(x_i, y_j) - f_m \right] \times \left[g(x'_i, y'_j) - g_m \right]}{\Delta f\,\Delta g} \right] \tag{4.3}$$

where,

$$f_m = \frac{1}{(2M+1)^2} \sum_{i=-M}^{M} \sum_{j=-M}^{M} f(x_i, y_j) \tag{4.4}$$

$$g_m = \frac{1}{(2M+1)^2} \sum_{i=-M}^{M} \sum_{j=-M}^{M} g(x'_i, y'_j) \tag{4.5}$$

$$\bar{f} = \sqrt{\sum_{i=-M}^{M} \sum_{j=-M}^{M} \left[f(x_i, y_j) \right]^2} \tag{4.6}$$

$$\bar{g} = \sqrt{\sum_{i=-M}^{M} \sum_{j=-M}^{M} \left[g(x'_i, y'_j) \right]^2} \tag{4.7}$$

$$\Delta f = \sqrt{\sum_{i=-M}^{M} \sum_{j=-M}^{M} \left[f(x_i, y_j) - f_m \right]^2} \tag{4.8}$$

$$\Delta g = \sqrt{\sum_{i=-M}^{M} \sum_{j=-M}^{M} \left[g(x'_i, y'_j) - g_m \right]^2} \tag{4.9}$$

$$x' = x + u_0 + \frac{\partial u}{\partial x} dx + \frac{\partial u}{\partial y} dy \tag{4.10}$$

$$y' = y + v_0 + \frac{\partial v}{\partial x} dx + \frac{\partial v}{\partial y} dy \tag{4.11}$$

f(x, y) and *g(x′, y′)* represent the gray levels of reference and deformed images, respectively; and (*x, y*) and (*x′, y′*) are the co-ordinates of a point in the subset before and after deformation respectively and *M* is the number of points from the center of the subset to the edge of subset. The matching procedure is completed through searching the peak position of the distribution of correlation coefficient. Once the correlation coefficient extreme is detected, the position of the deformed subset is determined. The differences in the positions of the reference subset center and the deformed subset center yield the in-plane displacement vector at point *P*, as illustrated in Fig. 4.1. The strain is estimated by smoothing the calculated displacement fields first and then differentiating them. Based on these considerations, several researchers proposed different smoothing algorithms for accurate estimation of strain [21-26]. The more practical and recent technique for strain estimation being used in DIC measurement is the point wise local least-squares fitting technique developed by Pan et al. [27]. In case of 2D DIC setup only one camera is used for the measurement of in-plane surface displacement and strain components. From 3D DIC measurement, both in plane and out of plane displacements one obtained apart from in-plane strains.

4.3 Material characterization of Al 2014-T6 alloy

4.3.1 Specimen Geometry

Figure 4.2 shows the tensile specimen dimensions. Three specimens are prepared from a 3 mm Al 2014-T6 alloy sheet according to ASTM E8 standard. Specimens are fabricated using electronica wire cut electro discharge machine (EDM). The surface of the specimen is cleaned using isopropanol in order to obtain a dust and oil free surface for making speckle pattern.
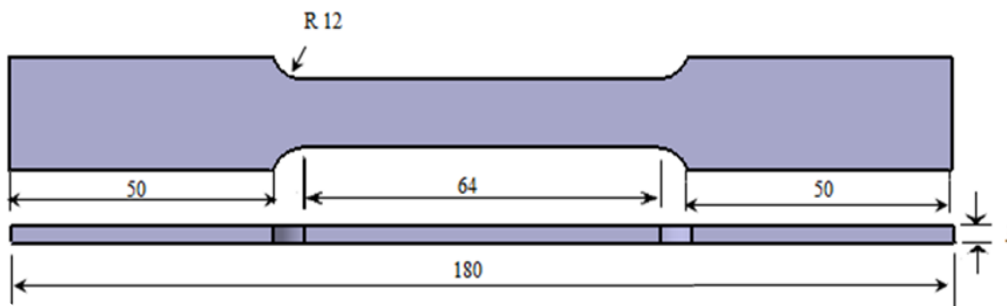
Figure 4.2: Tensile specimen drawing (All dimensions are in mm)

4.3.2 Preparation of speckle pattern

To perform the DIC experiment, random speckle patterns are created over the specimen surface by spraying acrylic paints of black and white color (from Golden Artist Colors Inc.).

Figure 4.3 shows the speckle pattern applied over the specimen. The specimen surface is first cleaned using isopropyl alcohol. Golden® acrylic paint of titanium white color (8380-Series NA) is then applied over the specimen surface using an air brush (from Iwata-Medea, Inc.) as shown in Fig. 4.4. Only one layer of white paint is applied to avoid changing the shape of the surface due to the higher thickness of paint coating. Once the specimen is dried, acrylic paint of carbon black color (8040-Series NA) is applied over the specimen surface (white color painted) in a random fashion using an air brush to get a random speckle pattern as shown in Fig. 4.4(a). The air brush used is having a nozzle of diameter 0.5 mm. Always generation of speckle pattern is by trial and error method depending on the specimen size, geometry and region of interest. An example of typical random speckle pattern obtained using this procedure is shown in the Fig. 4.3.

(a)

(b)

Figure 4.3: Speckle pattern (a) specimen (b) enlarged view of speckle pattern applied with air brush

(a)

(b)

Figure 4.4: Accessories used for generating Speckle pattern (a) Compressor with air brush (b) Titanium white & carbon black paints

4.3.3 Experimental setup

Figure 4.5 shows the DIC setup along with the loading equipment used in the present study. The DIC setup is from correlated solutions Inc, US. The 3D DIC system comprises of a pair of two Grasshopper® CCD Camera (POINT-GREY-GRAS-50S5M-C and frame rate of 15 fps) having a spatial resolution of 2448×2048 pixel^2, coupled with Schneider Xenoplan lenses of 35 mm focal length and a white LED light source of 30 watts to ensure adequate image contrast. Cameras are connected to image grabbing portable workstation laptop fitted with a data acquisition card (DAC). DAC supplied by National Instruments, it is used to provide an interface between MTS controller and image grabbing system for storing the load and displacement data for every image being grabbed during the test. The specimens are loaded using a computer-controlled MTS Landmark® servo-hydraulic cyclic testing machine of 100 kN capacity. Self-adjusting hydraulic test fixtures are used to grip the specimens. Uniaxial tensile load is applied along the longitudinal direction of the test specimens using displacement control mode with a crosshead speed of 1 mm / min. Initially, after adjusting the focus and aperture of CCD cameras, they are calibrated for each specimens individually using standard grid pattern. The images are grabbed at predefined rate of three images per second after calibration.

1.CCD cameras 2.LED light source 3.Specimen
4.Tripod stand 5.Loading fixture
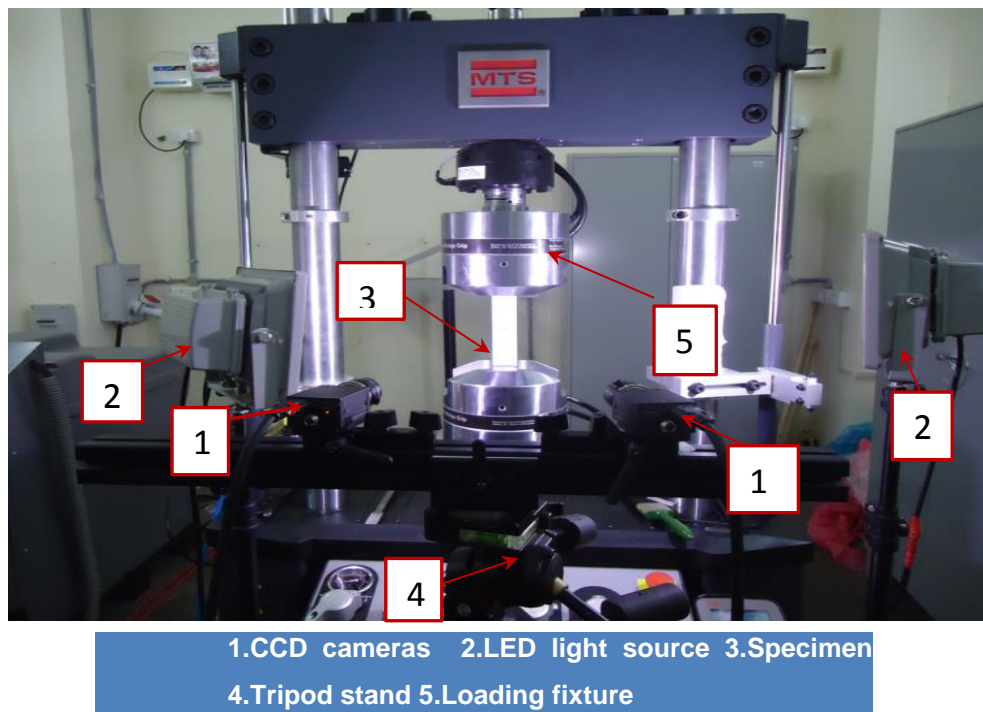
Figure 4.5: Experimental setup involving 3D DIC setup

4.3.4 Tensile properties of Al 2014-T6 alloy

The tensile properties of the aluminium panel are estimated using 2D DIC. In 2D DIC, same experimental setup as shown in Fig. 4.5 is used but only one camera is placed perpendicular to the specimen surface. The experimental procedure starts with the specimen fixing into hydraulic wedge grips and specimen straightness is ensured using a try square. Extensometer is connected at the center of the specimen. Both cameras are mounted on a tripod. Horizontal level of the cameras is checked using spirit level and adjusted accordingly. Heights of the camera are adjusted in the tripod to ensure full view of the specimen. The camera is aligned with respect to the specimen and positioned. The distance between the camera and the specimen is adjusted depending on the specimen area to be captured. The surface of interest is focused by adjusting both lenses to get a sharper speckle pattern. The aperture of the lenses is adjusted to get sufficient intensity and also to avoid saturation of the pixels over the field of view. Finally images are grabbed at a rate of two images per second while the uniaxial tensile load is applied along longitudinal direction of the test specimens using displacement control mode with a crosshead speed of 0.5 mm / min. While grabbing the images the output from the load cell is synchronized with the image for obtaining the load value using data acquisition system.

Posts processing of the acquired images are done using VIC-2D 2010 software [86] acquired from Correlated Systems. The region of interest (ROI) is selected and the subset sizes are chosen as 25 x25. Seed point is chosen by the user from where the software starts the correlation. Here it is selected at the top of ROI as shown in the Fig. 4.6 (a). An example of the strain field obtained is shown in Fig. 4.6(b) and 4.6(c).

Stress-strain curves are generated using the DIC strain data as well using the strain obtained from MTS. MTS measure the strain through the extensometer upto the 0.7% of strain and the remaining part is measured using platen movement. Modulus of elasticity is calculated from the initial slope of the stress- strain curve and yield strength values are then estimated. Figure 4.7 shows the stress strain curves obtained from MTS and DIC [87]. From three tests, it is observed that the average value of Young's modulus of the Al 2014-T6 alloy is 73.1GPa and yield stress 430MPa and poisons ratio 0.33. It is found that there is a good coherence exists between MTS and DIC values. These material properties are used in the estimation of whole field strain distribution of cracked and repaired panel involving FEA.
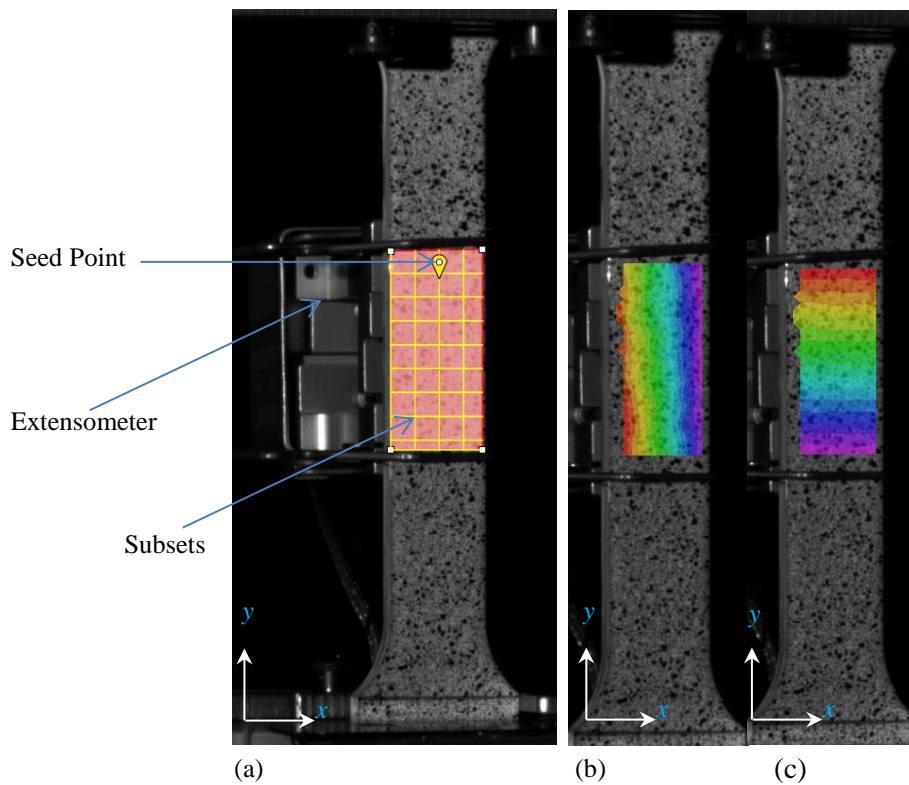
Figure 4.6: Post processing on acquired image (a) extensometer, ROI (b) strain (ε_{xx}) plots in ROI (c) strain (ε_{yy}) plots in ROI [87]
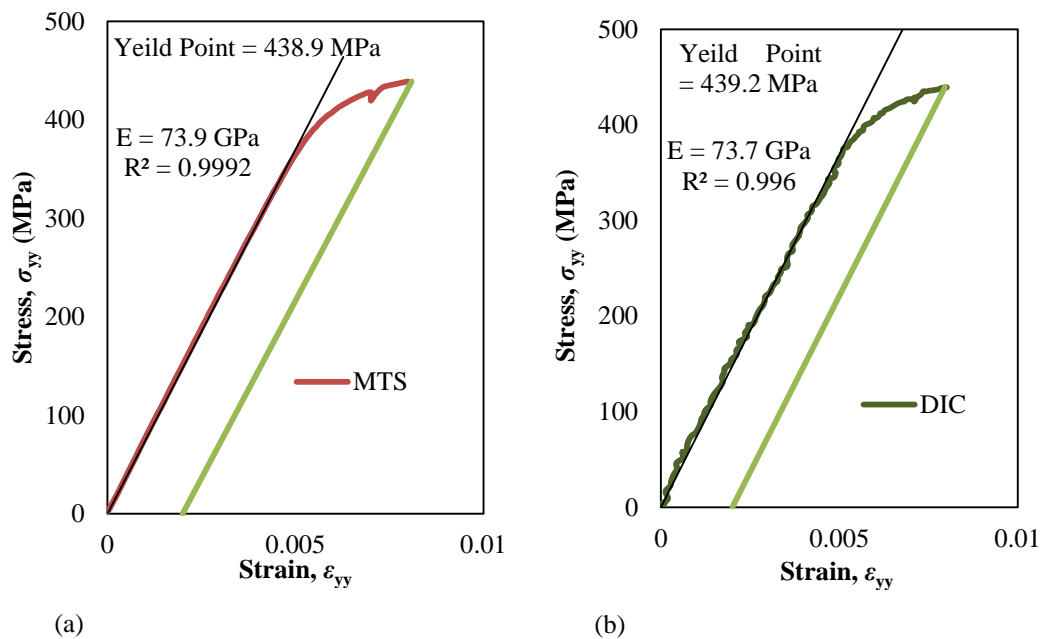
Figure 4.7: Stress-Strain Curves of tensile specimen (a) MTS Stress-Strain curve

(b) DIC Stress-Strain Curve

4.4 Specimen Fabrication

4.4.1 Fabrication of cracked panel

The panel is made of 2014-T6 aluminium alloy having a thickness of 3 mm. The dog bone specimen is made from 3 mm 2014-T6 aluminium alloy sheet as per the dimensions shown in Fig. 4.8(a). Then, inclined center crack of 10 mm is introduced using a wire EDM involving 0.15 mm brass wire. The crack is introduced by drilling 2 mm hole at the center followed by notch of 4 mm on both sides at 45° angle is made using wire cut EDM is shown in Fig. 4.8(b). The pre-crack is generated at a fatigue load cycle of 5000, frequency of 5 Hz, target load of 3.85 kN and amplitude of 3.15 kN (see Fig 4.8(c)). Figure 4.8(d) shows the cracked panel with center inclined notch.

(a)

(b)

(c)

(d)
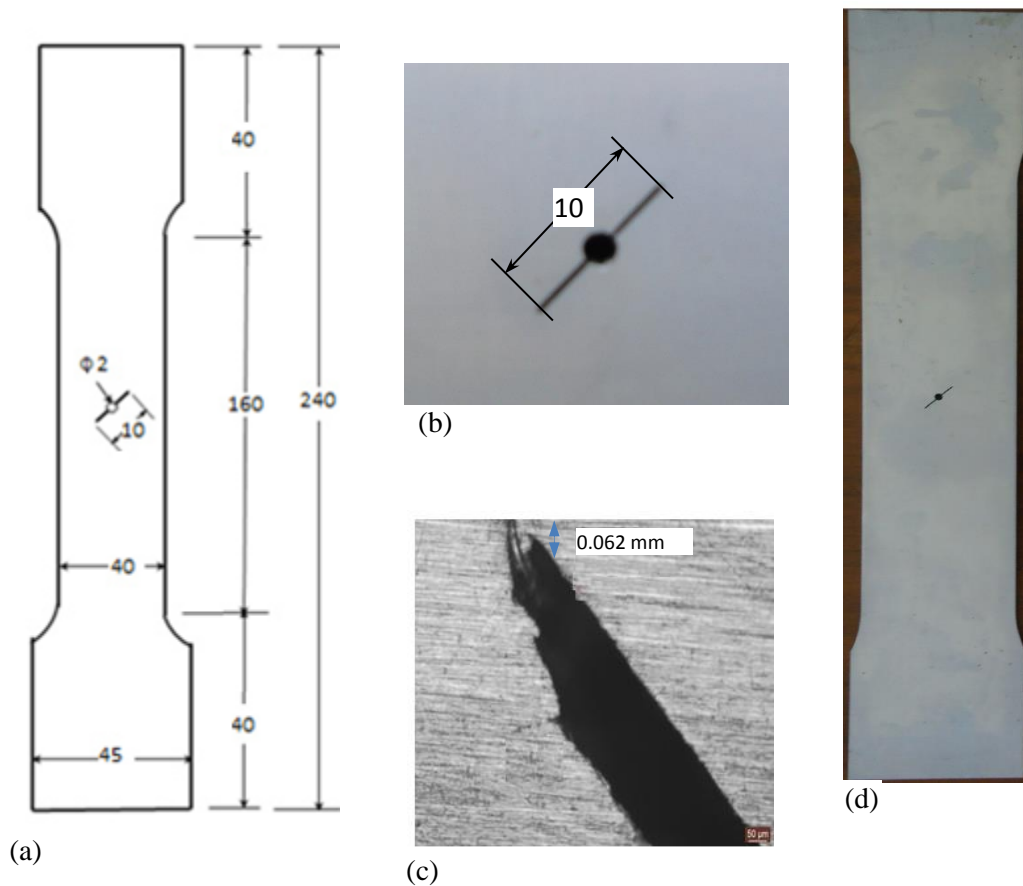
Figure 4.8: Fabrication of cracked panel (a) specimen drawing (b) zoomed view of crack tip (c) zoomed view of crack tip after pre-cracking (d) entire panel

4.4.2 Fabrication of repaired panel

The specimen surface is prepared with *forest products laboratory* (FPL) etching process [18]. In this method the surface of the panel is degreased with methyl ethane ketone and abraded with emery cloth, and then alkaline cleaning is done. The panel is soaked for 2

hours at room temperature in FPL etch mixture containing 6.4% potassium dichromate, 23.4 % H_2SO_4 and 63.2 % water. Later, it is washed with clean cold running water, and dried in a hot air oven. The panel is repaired by bonding an extended octagonal CFRP patch over the notched region using Araldite 2011 adhesive supplied by Huntsman's group. The Araldite 2011 is an intermediate strength adhesive having higher toughness and is generally used for repair applications [81]. It is a two part adhesive system and is applied over the specimen using an applicator gun to ensure thorough mixing and uniform layer thickness as shown in Fig. 4.9(a). It is cured at room temperature for 24 hours. CFRP laminate is made with the hand lay-up process and the steps involved in fabrication of CFRP laminate is explained in Appendix C.1. From the prepared composite sheet the rectangular patch is fabricated as per the dimensions using abrasive cut-off wheel mounted on hand-held saw. Rectangular CFRP specimens are then accurately machined to the necessary dimension by a milling machine with carbide coated end mills. From the rectangular patch the extended octagonal patch is arrived by filling the chamfered edges using metal templates and filing tools as shown in Fig. 4.9(b) and 4.9(c). Since the number of layers is only six and to avoid the delamination while making stepped patches, tapering is provided on the straight edged octagonal patches using a smooth filing operation. This is more like a first cut approximations for making the tapered patch. Care is taken while bonding the patch on to the cracked panel such that the fibers in the patch are kept parallel to the loading direction. Both single and double sided repair behavior is studied. The fabricated specimen (repaired panel) is shown in Fig.4.9 (d).

(a)

(b)

(c)

(d)
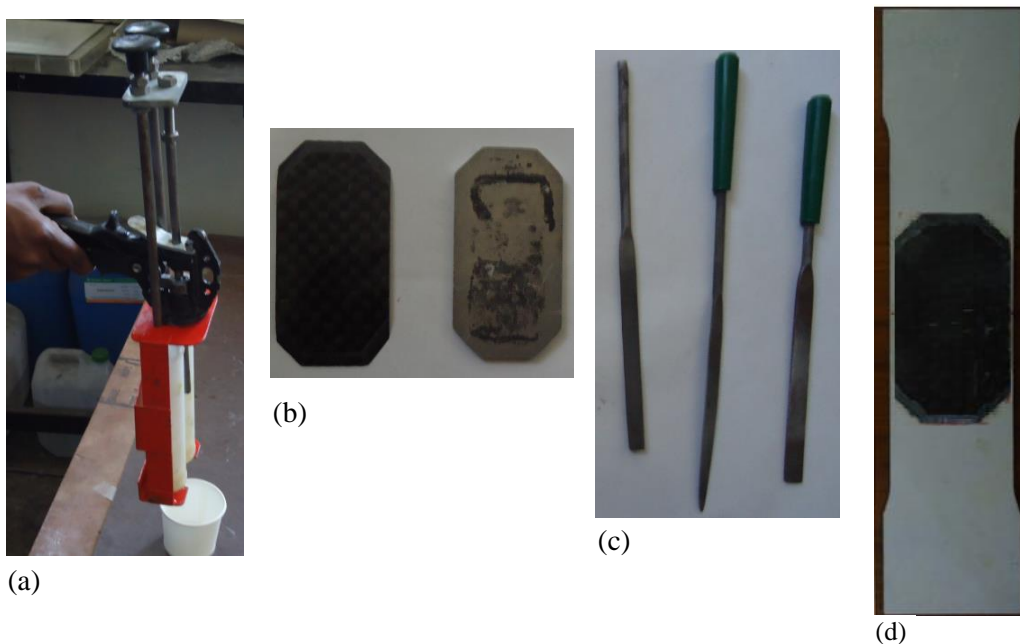
Figure 4.9: Fabricated repaired specimen (a) adhesive applicator gun (b) CFRP patch and octagonal patch template (c) tools used for making patch (d) single sided repaired panel

The surface of the specimens is then coated with a thin layer of white acrylic paint and over-sprayed with carbon black paint using an airbrush to obtain a random black-and-white speckle pattern. The specimen containing the speckle pattern is shown in Fig. 4.10(a). Here the air brush nozzle diameter of 0.24 mm. For the whole field strain analysis of cracked and repaired panel the speckle size of approximately140 dots are applied over $1mm^2$ of area (see Fig. 4.10(a) and Fig. 4.10(b)). It results in an average speckle size of 94 μm. But in case of adhesive shear strain measurements authors have taken a magnified image with higher spatial resolution (see Fig. 4.10(c)) and approximately 3-6 speckle dots are present along the adhesive thickness. As the adhesive thickness is 134 μm, the average speckle size turns out to be in the range 20–60μm.

(a)   (b)   (c)
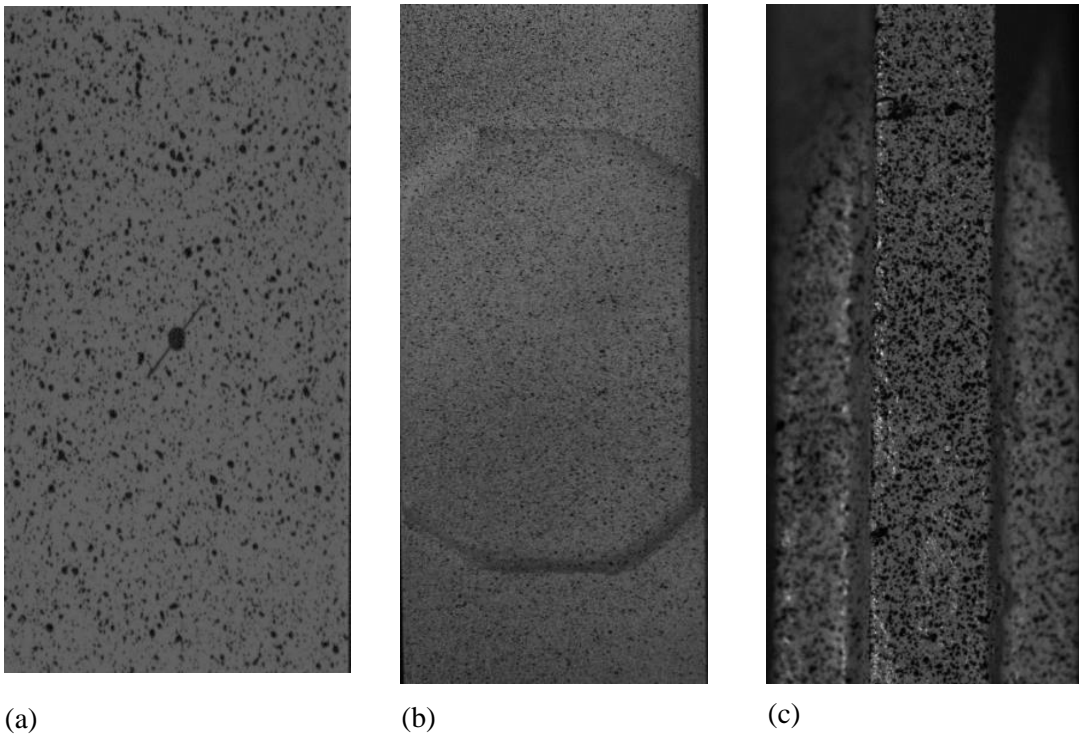
Figure 4.10: Speckle pattern (a) cracked panel (b) panel repaired with extended octagonal patch (c) Double sided repair along the thickness

4.5 Whole Field Strain Prediction

4.5.1 Strain prediction in cracked panel

The behavior of cracked panels subjected to tensile load is studied using 3D-DIC technique. The same experimental setup which is shown in Fig. 4.5 is used for the estimation of whole field strain distribution over the cracked panel. Once the cameras are set, calibration need to be done. Several calibration plates are supplied with the system; the calibration plate with

the overall size closest to the specimen size is used. The calibration plate is located at approximately at 10 mm distances from the specimen during testing. The images are captured with different positions and rotations of calibration plates. Once the calibration is done the cameras position should not be changed. During testing ten images are grabbed per second. The images acquired by the camera system are post-processed using the available Correlated Solutions Vic-3D software [86] to obtain the whole field displacement and strain field in the vicinity of the crack tip in case of unrepaired specimen. The region of interest (ROI) for the correlation is chosen as 334 x 870 pixels. A subset size of 29 x 29 pixels is selected with a step size of 7 pixels for DIC calculations. Figure 4.11(a) shows the contour plot of ε_{yy} for cracked panel obtained from DIC at a load of 15 kN. It is evident that the crack propagates along a plane perpendicular to the loading direction as the load increases being a mixed mode one. Overall, authors have used the same scale for plotting the strain contour obtained from both DIC and FEA for qualitative comparison. Always the FEA contour scale is adjusted with the DIC scale for all comparative plots. Figure 4.11(b) shows the whole field strain surrounding the crack tip obtained from FEA. In DIC measurement, the algorithm avoids the data very close to a crack tip as it contains the boundary and precisely one does not get the crack tip strain field. Therefore, Vic-3D software leaves out few pixels close to the boundary and exactly it doesn't estimate the strain on those pixels. Due to this one cannot get sharp contours near the crack tip from DIC as compared to FEA plot. On overall bases, the feature of the fringe pattern surrounding the crack tip looks similar for both DIC and FEA strain contour plots under same scale.
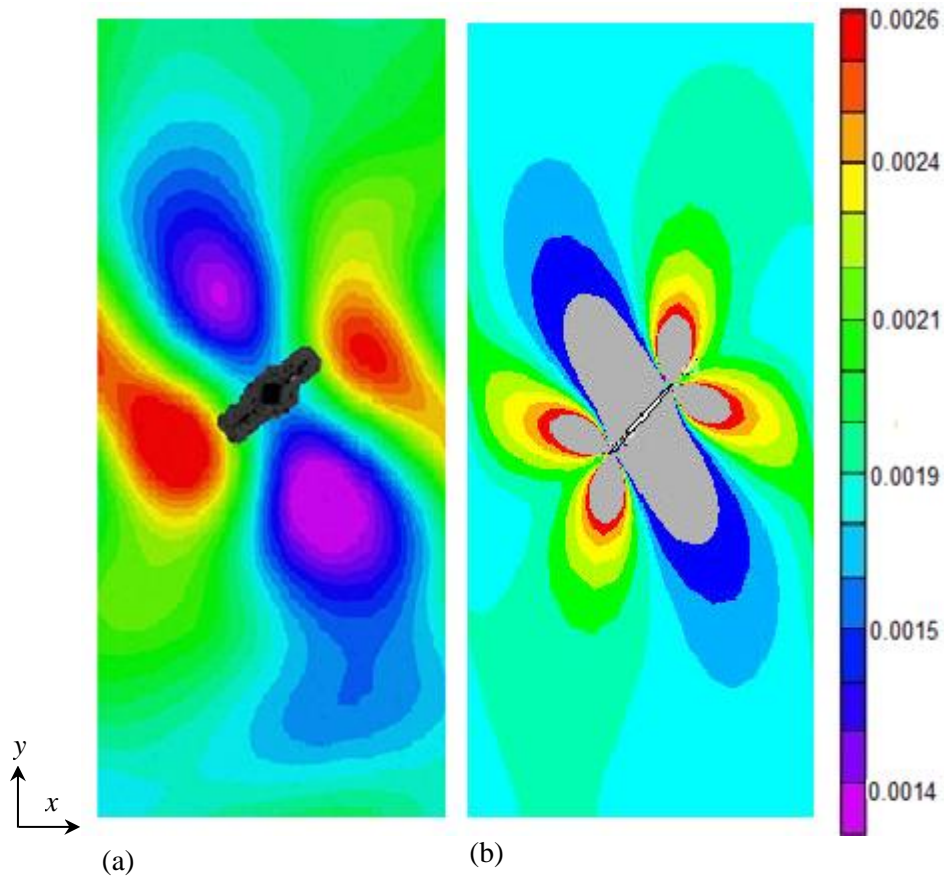
Figure 4.11: Contour plot of longitudinal strain (ε_{yy}) over the crack area at a load of 15 kN for unrepaired panel (a) DIC (b) FEA

4.5.2 Whole field strain prediction in single sided repaired panel

Further, whole field strain analysis over the patched area of single sided repair is studied. The ROI for the correlation is chosen as 39 x 109 mm which corresponds to 466 x1740 pixels. Figure 4.12 shows the comparison of whole field strain contours obtained from DIC with the FEA result at a load of 15 kN. The maximum value of ε_{yy} is observed at upper and lower edge of the patch along y-direction (loading direction) and is lower at patch center (see Fig. 4.12(a)). This is because one cannot measure the strain at the crack tip since it is covered by the patch. In repaired panels, the overlap edge bears the maximum strain due to high stress concentration, leading to patch debonding from the panel as the load increases. Figure 4.12(b) shows that the whole field ε_{yy} strain contour obtained from FEA. Here too, the strain values are higher at overlap edges other than the crack tip location. In the contour plots, the patch shape of the specimen and FE model look slightly different because in case of FE model the tapering is provided by modeling stepped patches whereas in experiment the patch edge is tapered with smooth filing operation as mentioned in previous section 4.4.

From this study, it is found that the failure initiates with partial patch debonding at overlap edge followed by the fracture of the panel with increasing load. On an overall basis the longitudinal strain (ε_{yy}) contour obtained from DIC and FEA agree well.
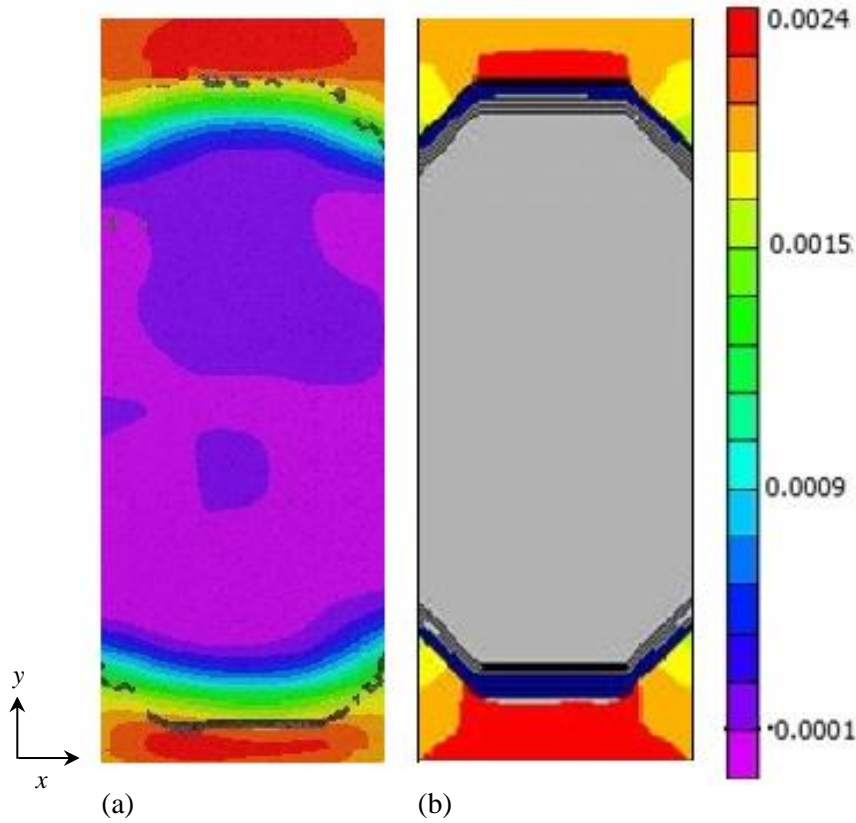
Figure 4.12: Comparison of whole field strain contour (ε_{yy}) over the patch area for the single sided patch repaired panel at a load of 15 kN (a) DIC (b) FEA

4.5.3 Whole field strain prediction in double sided repaired panel

The whole field strain distribution over the patched area of double sided repair is estimated by taking ROI as 39 mm x 104 mm which corresponds to 448 x 1670 pixels. Contour plots of ε_{yy} for double sided repaired panels obtained from DIC and FEA are shown in Fig. 4.13 corresponding to 15 kN load. The contour plot of ε_{yy} (see Fig. 4.13(a)) is similar to that of single sided repaired panels. In DIC plot highly strain zone appears at the patch edge. The strain field predicted from FEA and DIC agree broadly at contour level. In this case too, the failure initiates with partial patch debonding at the overlap edge followed by complete fracture of the panel which is very similar to the single sided patch behavior.
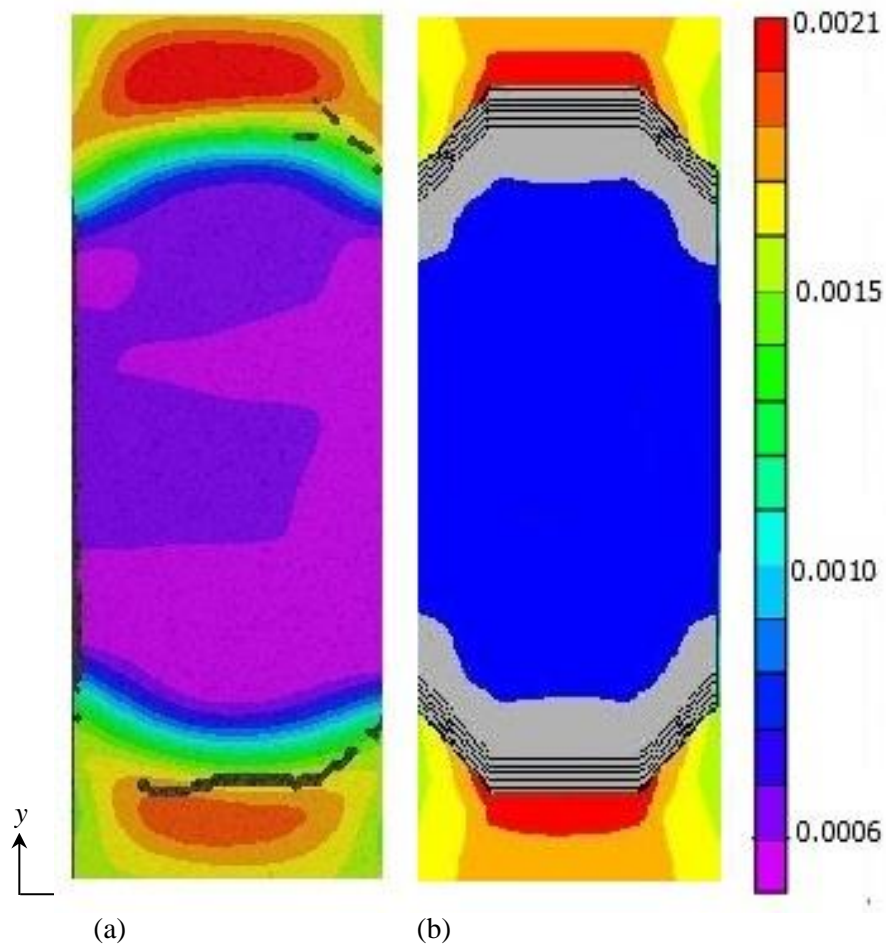
Figure 4.13: Comparison of whole field strain contour (ε_{yy}) over the patch area obtained from DIC and FEA for the double sided patch repaired panel at a load of 15 kN (a) DIC (b) FEA

4.6 Strain Field in the Adhesive Layer

The average thickness of the adhesive layer is 0.134 mm and is measured using an optical microscope (see Appendix C.3). In the repair panel, the shear and peel stresses are higher at the edge of the adhesive especially at the interface between adhesive / patch and adhesive / panel [88]. Also, the load is transferred by the adhesive layer to the patch over the crack zone by shearing phenomena. To perform the strain measurement in the adhesive layer using 2D DIC setup, CCD camera is focused on the thickness side of the specimen and it is fitted with a Tamron zoom lens of focal length 180 mm as shown in Fig. 4.14.

1.CCD cameras 2.LED light source 3.Side view of Specimen 4.Tripod stand 5.Loading fixture 6. Tamron lens
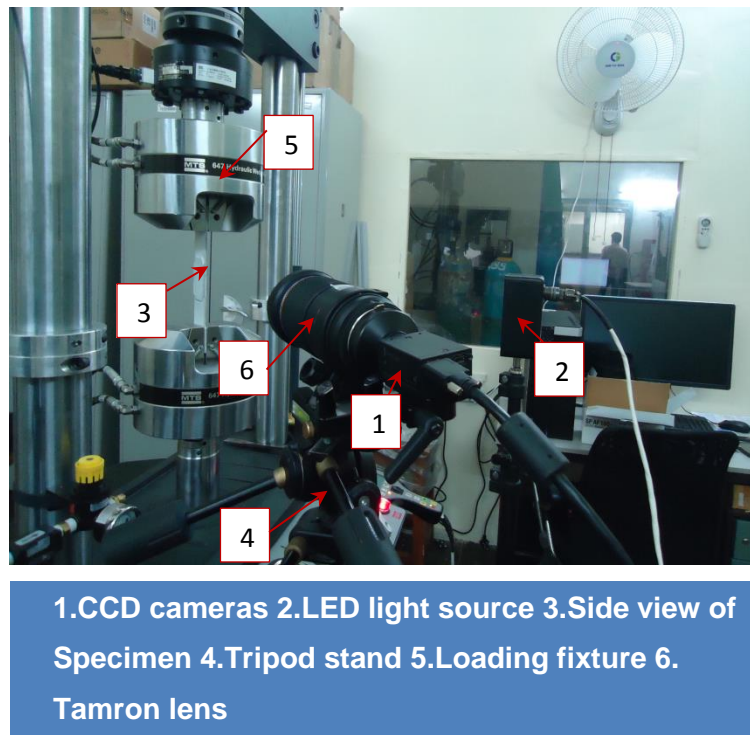
Figure 4.14: Experimental setup involving 2D DIC

4.6.1 Peel and shear strain prediction in adhesive layer of single sided repair

Figure 4.15(a) show the side view of the single sided repaired panel along with the region of interest whereas Fig. 4.15(b) shows adhesive layer with speckle pattern and a very fine speckle patterns has been applied for strain measurement in the adhesive layer. Here too, 10 images are grabbed per second. Later, Correlation solutions Vic 2D software is used to get the adhesive shear and peel strain distribution through the thickness. The observed area is about 6 mm x 14 mm, ROI is 41 x 41 pixels, and the sub step size is 7 pixels. Figures 4.15(c) & 4.15(d) show the peel strain contour (ε_{zz}) at 34% and 60% of failure load. It can be observed that the peel strain is maximum at the patch overlap edge. This high stresses concentration near the patch overlap edge leads to patch debonding as the load increases (see Fig. 4.15(d)). Figure 4.15 (e) & 4.15(f) shows the peel and shear strain (ε_{zz} and ε_{yz}) distribution in the adhesive layer of a single sided repair specimen at a load of 15 kN. From Figure 4.15(e) it can be observed that the peel strain is maximum at the overlap edge. This high stress concentration near the free edge, leads to patch debonding as the load increases. Figure 4.15(f) shows the shear strain variation and it is evident that the maximum strain is located at the patch overlap edge between adhesive/patch interface. This shear strain concentration is due to abrupt change in geometry at the patch end. For qualitative comparison purposes, the peel and shear strain field in the adhesive layer obtained from

FEA is also shown there. The shear strain concentration also happens at the interface between the adhesive / patch there by confirming DIC prediction. It can also be observed that shear strain is maximum at the overlap edge and gradually reduce as the distance from the overlap edge increases. One can conclude that the shear and peel strain concentrate near the overlap edge of the adhesive resulting in patch debonding.
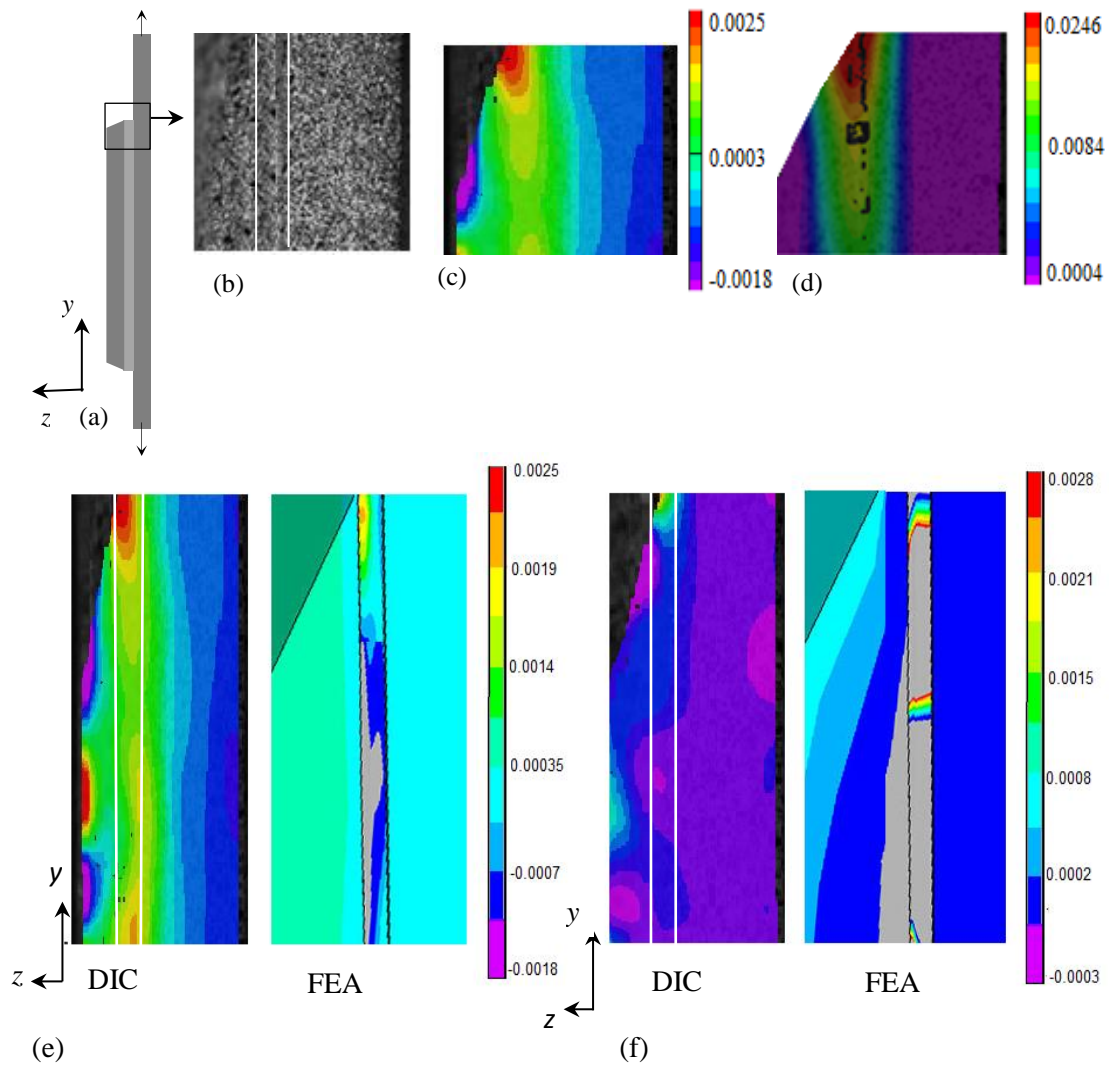
Figure 4.15: Surface speckle pattern and peel strain distribution in single sided patch repair (a) line diagram of setup (b) speckle pattern along with marked adhesive layer (c) peel strain (ε_{zz}) field at 35% of failure load and (d) peel strain (ε_{zz}) field at 60% of failure load and comparison of strain contour obtained from DIC and FEA at a load of 15 kN (a) ε_{zz} (b) ε_{yz}

4.6.2 Peel and shear strain prediction in double sided repair

Generally, in case of adhesively bonded patch repair, the damage initiates from the adhesive / panel interface due to adhesive layer failure. The strain field of ε_{zz} and ε_{yz} obtained in case

of double sided repair at 15 kN load is shown in Fig. 4.15. It could be observed that a high peel strain occurs in the adhesive layer closer to inner sides of adhesive/panel interfaces and subsequently patch peels from the panel as the load level increases. Shear strain distribution in the adhesive layer is shown in Fig. 4.16(b). Looking at the DIC plot, one can see that a maximum value occurs at the right side overlap edge. This shows that patch debonds from the upper edge of the right side patch and at bottom edge in the left side patch. Due to development of high shear strain, adhesive layer fails in with increasing load. This lead to patch debonding and then load is directly taken by the cracked panel leading to complete panel fracture under higher loads. From Fig. 4.16 it is understood that strain contour plots (ε_{zz} and ε_{yz}) obtained from FEA are matches with DIC contour on overall bases.

The damage progression in the double sided repaired panel at a load of 38.1 kN is shown in the Fig. 4.17. It is observed that peel strain is maximum at the overlap edge and leads to adhesive failure which is shown in Fig. 4.17(a) and 4.17(b).
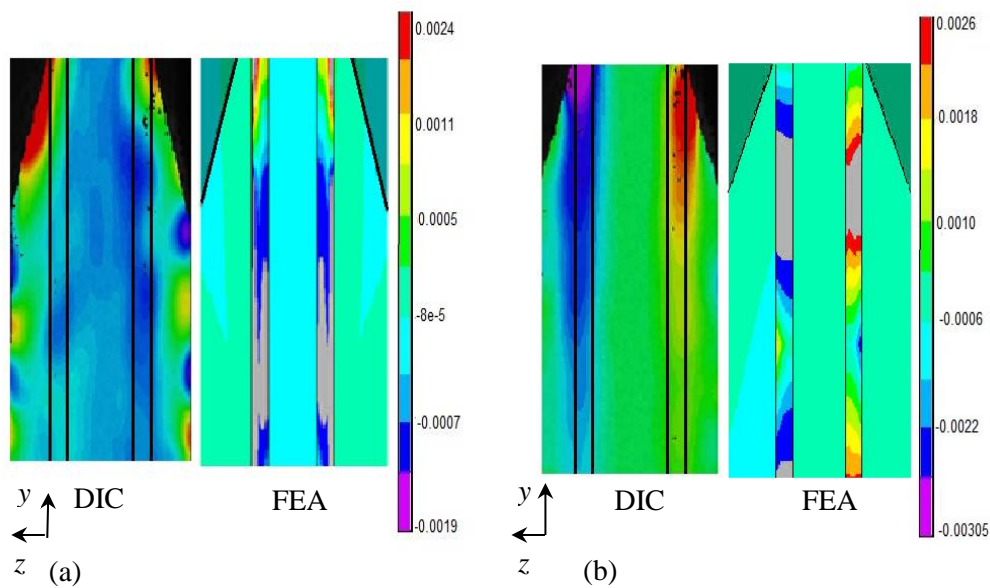
Figure 4.16: Comparative plot of strain along adhesive/ patch interface involving both DIC and FEA at a load of 15 kN for double sided patch repaired panel (a) ε_{zz} (b) ε_{yz}

.
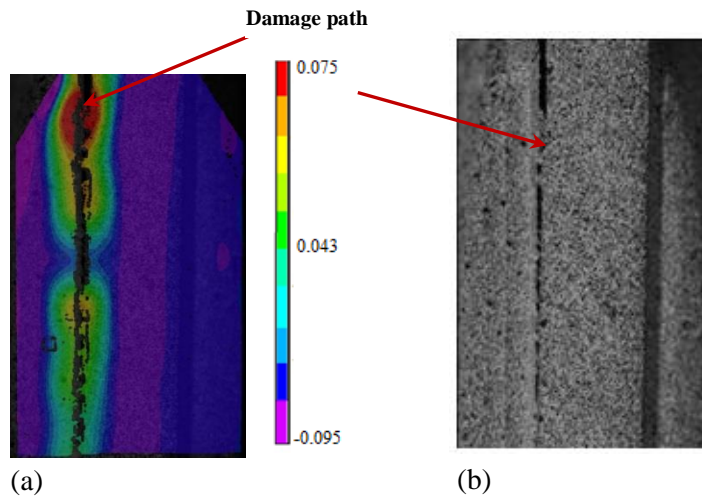
Figure 4.17: Damage path in adhesive layer of double sided repair at a load of 38.1 kN (a) peel strain (b) damage path

4.6.3 Shear strain variation along the interface in double sided repair

Figure 4.18 shows line plot of the shear strain variation along the adhesive / patch interface edge. The shear strain decreases as one moves away from the overlap edge and a reasonable correlation exists between DIC and FEA prediction.
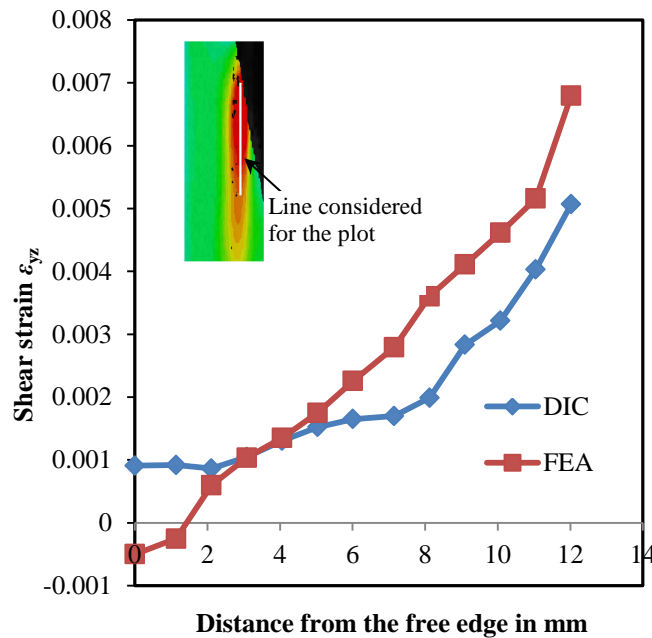
Figure 4.18: Variation of shear strain along adhesive/ patch interface involving both DIC and FEA at a load of 15 kN for double sided repair

4.7 Failure mechanism

The failure mechanism observed in cracked as well as single and double sided patch repaired panel is shown in Fig. 4.19. It can be observed from figure that crack propagates along a plane perpendicular to the loading direction as the load increases (see Fig. 4.19(a)). In case of repaired panels due to shear and peel strain concentration in adhesive layer near the patch overlap edge results in partial patch debonding followed by the fracture of the panel similar to the cracked panel (see Fig. 4.19 (b) and 4.19 (c)). The partial debonding happens due to adhesive layer failure.

(a)   (b)   (c)
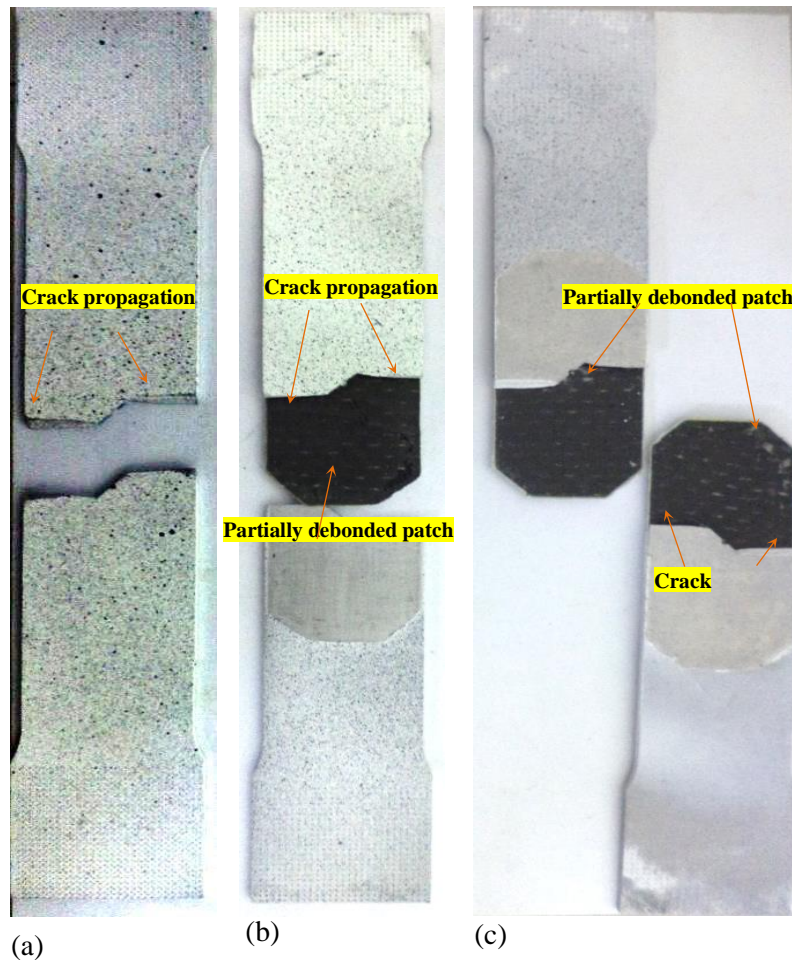
Figure 4.19: Fracture mechanism (a) cracked panel (b) single sided repaired panel (c) double sided repaired panel

4.8 Experimental performance of repaired and unrepaired panel

The key interest in the composite repair system is the stress transfer from crack fronts to the patch overlap edge. The variation of longitudinal strain ε_{yy} for cracked and repaired specimens is plotted with respect to the applied stress in Fig.4.20. From the Fig.4.20 it can

be observed that the reduction in strain due to repair is relatively small at the initial load and reduction is high at higher loads. It is observed that the strain in the double sided repair is lower that the single sided repair. It can be confirmed that the stiffness of double sided repaired panels is highest.
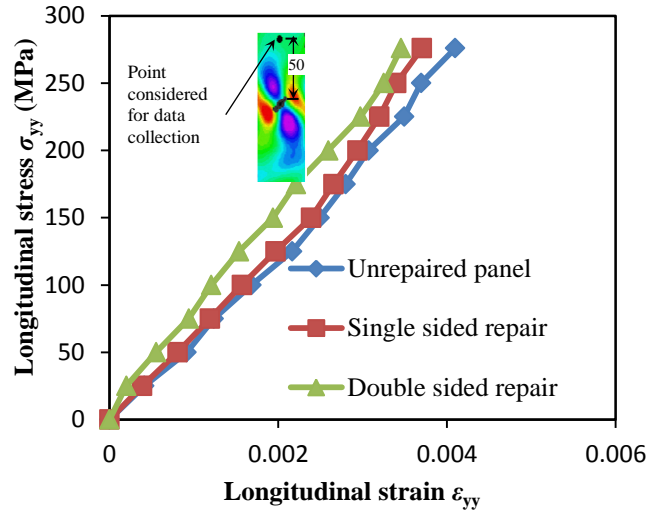
Figure 4.20: Longitudinal Stress (σ_{yy}) Vs. longitudinal Strain (ε_{yy}) obtained from DIC at a location far away from the crack zone

4.9 Comparison of strength of repaired and unrepaired panel using MTS

To compare the strength of the unrepaired and repaired structure load versus displacement curve for all the three cases is plotted in Fig. 4.21 and they are obtained from experiment. From the Fig.4.21, it is clear that the load carrying capacity of double sided repair is higher than the other two configurations. The failure strength is estimated as failure load upon gross cross-sectional area of the specimens. On that basis for the unrepaired panel the failure strength is 316.66 MPa whereas for single and double sided repaired panel it is 341.6 MPa and 383.34 MPa respectively. Table.4.1 shows the standard deviation of three successive tests carried out for all the configurations. From the Table 4.1 it is clear that ultimate load carrying capacity and the strength of the double sided repaired panel is higher than both single and unrepaired panel and therefore it is generally preferred for repair applications.

Table 4.1: Load Vs displacement obtained from MTS test machine

	Ultimate tensile load (kN)			Average Value	Standard deviation	Restoration of strength
	Test 1	Test 2	Test 3			
Unrepaired panel	39.03	42	41.14	40.7	1.42	
Single sided repaired panel	41.40	44.77	44	43.12	2.04	75%
Double sided repaired panel	43.9	44.1	46.2	45.06	2.14	82%
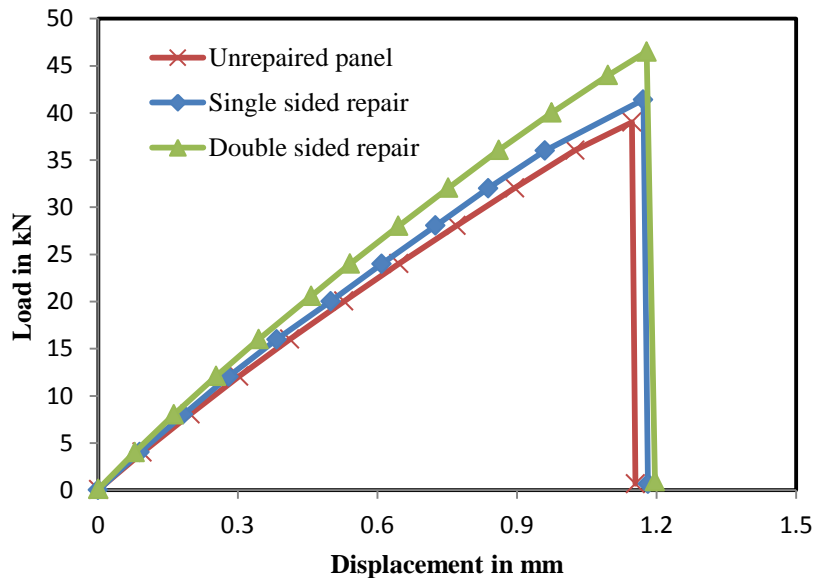
Figure 4.21: Load Vs displacement obtained from MTS test machine

4.10   Closure

In the present study, experimental investigation involving DIC technique is carried out to evaluate the performance of bonded patch repair of an inclined center cracked aluminium panel. Whole field surface strain variation over the panel as well as the patch is predicted. It is found that highly localized strains always develop around the patch overlap edge and the crack propagation in the panel is always normal to the loading direction. The peel and shear strains are found to be maximum near the corner or root of adhesive joint at the patch overlap edge in both single and double sided patch configuration. This concentration in the adhesive layer at the patch overlap edge result in adhesive layer failure leading to partial patch debonding at the overlap edge. The partial debonding reduces the load transfer

capability of the patch leading to complete fracture of the panel at higher loads. For both single and double sided repaired panels, partial debonding of the patch followed by complete failure of the panel is observed. Full field strain variations obtained from the experiment are compared with finite element results and they appear to be in good coherence. The failure strength of double sided patch repaired panel is found to be 5 % more than that of single sided patch repaired configuration. The utility of DIC as an accurate experimental technique for whole field strain prediction in repair application is established. Also along with magnified optics DIC is able to predict shear and peel strain field over the thin adhesive layer. It has been experimentally confirmed that shear and peel strain are maximum at the patch overlap edge in the adhesive layer where the patch debonding takes place with increased loading. Next chapter describes the behavior of bonded patch repaired panels under fatigue loading.

Chapter 5

Fatigue crack growth study of CFRP patch repaired Al 2014-T6 panel having an inclined center crack using FEA and DIC

5.1 Introduction

For the damage tolerance design of aircraft structures, fatigue tests are required at all structural levels to support and validate the crack growth life predictions. Crack initiation, its propagation and ultimate fatigue strength prediction of aircraft structure are of paramount importance for developing reliable and a safer design for utilizing them as primary load bearing one. There are several aspects in both the practical fatigue testing and the development of predictive models. In developing highly durable structural element, testing the fatigue strength is very crucial. Fatigue life prediction of cracked panel repaired by composite patch seems to be complicated due to possible failure modes, such as adhesive layer failure, patch debonding and growth of existing crack in the aluminum panel [89]. Denny and Mall [8] have studied the fatigue crack growth response of aluminum panels repaired with adhesively bonded composite patch with pre-existing debond and without debond in the bond line of the repair. They revealed that fatigue life of the bonded composite repair depends on the location and size of the disbonds and also concluded that the partially bonded repairs are damage tolerant. They also found that the presence of debonding increases the SIF considerably. Therefore, from the above works it is found that the presence of debonding significantly affects the effectiveness of the repairs. Typically there are two types of criteria's used for predicting the debonding behaviour of the adhesive layer involving FEA. Firstly, study of debonding behaviour by degrading the material properties of adhesive. Papanikos et al. [90, 91] performed the progressive failure analysis of double sided patch repaired aluminium panel having a straight center crack using FEA. They concluded that geometry of the model such as patch thickness, adhesive thickness, patch width, patch length and tapered length impacts the initiation of debonding of patch from the panel. All the above mentioned work is related to the debonding behavior under static load. Maligno et al. [92] have carried out both experimental and numerical fatigue analysis of

edge cracked panel bonded with the CFRP composite patch. They have studied the FCG analysis using Zencrack software. In their study, they considered the debonding behavior by degrading critical adhesive layer element property to predict the fatigue life with increased precision. A second damage criterion is based on the modeling the panel /patch interface using cohesive zone concept [68]. Hosseini-Toudeshky et al. [68] have carried out FE based failure analyses of the adhesive layer under static and cyclic fatigue loading. They have implemented the failure analysis at the interface using the cohesive zone modeling. In their examination they had studied the impact of the patch width, thickness and the adhesive thickness on the progressive damage in the adhesive interface.

Most of the existing work in the area of composite repair involves FEA based study and limited studies exist on the experimental fatigue analysis applied to repaired panels having inclined crack. Fatigue tests usually require large testing times. This testing time further increases drastically when one periodically has to interrupt the fatigue test to manually measure the crack length. Existing techniques such as ultrasonic [93], vibration based methods [94], strip gauges, crack mouth opening displacements (CMOD) gauge [95] and DCPD [96] all have restrictions that make them unsuitable for fatigue testing's applied to inclined crack. Vanlanduita et al. [71] have monitored the crack propagation during cyclic fatigue test using DIC technique. They used sub-sampling principle in DIC to slow down the high frequency dynamics of the test specimen. Further, they also estimated SIF at the crack tip along with the crack front location using displacement contours. They were able to predict crack growth verses number of cycles accurately.

In the present chapter, initially, Paris law constants are determined through standard fatigue crack growth test as per the ASTM E647 standards for Al 2014-T6 panel. Subsequently, a constant amplitude fatigue loading is applied on both unrepaired and repaired panel to predict their fatigue life and respective crack growth behaviour experimentally. In order to monitor the crack propagation during cyclic fatigue test, displacement field surrounding the crack tip obtained from DIC technique is utilized along with image processing algorithm to get the crack tip location. Later on, a three-dimensional finite element based FCG study of an inclined center cracked aluminum panel repaired by CFRP patch is carried out. Both single and double sided repaired configurations are considered. The crack growth rate is determined using Paris law and the crack growth direction by maximum energy release rate criterion [97]. Furthermore, a cohesive damage model for adhesive is introduced in order to simulate the effect of abrupt loss of adhesive failure between the CFRP patch and the Al2014-T6 panel. Finally, the results obtained from experiment are compared against the

FEA prediction. The failure mechanism and fracture profile of unrepaired, single sided and double sided repaired panels are captured individually.

5.2 Determination of Paris law constants by base line tests

The ASTM standard E-647 outlines two types of fatigue tests, firstly K- decreasing test or load-reduction test (LR test) and secondly, constant load test or K- increasing test [30]. In the early 1970s, the load-reduction test method was developed by Paris to generate data at low values of SIF ranges and approaching threshold conditions. A LR test normally starts at an initial ΔK_i level, and the maximum and minimum loads are reduced as the crack grows too slowly and at the same time ΔK reduces, and maintains constant R. After the threshold is reached, an increasing load test is generally conducted to obtain the upper region of the fatigue crack growth curve. This is named as a load reduction and load-increasing (LRI) test. The LR test method may produce data, which exhibits fanning (larger spread in fatigue crack growth data) in the threshold regime. This tendency at threshold region is due to plasticity and higher closure levels.

Fatigue crack growth rate tests following the ASTM standard [30] are performed on middle tension specimens. Three specimens are tested for getting average C and m values. During test crack length is measured periodically by measuring compliance. In order to measure compliance during cyclic loading, COD gauge of gauge length 12 mm is used. To estimate the compliance, knife edged grooves are attached to the specimen at a distance of 6 mm from the crack center. All the experimental tests were performed at room temperature with a constant stress ratio R = 0.05 and a frequency of 10Hz. The specimens are loaded using a computer-controlled MTS Landmark® servo-hydraulic cyclic testing machine of 100 kN capacity with a computer data acquisition system. Initially, the specimen is pre-cracked at the load ratio of 0.05 and initial ΔK value of 8MPa√m. The FCG tests were subsequently carried out as per the aforementioned two tests. In the present study, for load shedding test, the initial driving force ΔK is applied as 8 MPa √m and the normalized dK/da gradient value is of -0.08/mm. If a lower ΔK value is used, such as ΔK, a lower threshold may be generated. After the K-decreasing test K-increasing test is carried out with the same load where the last test is stopped. The test data presented in both tests is collected and plotted as sigmoidal curve which is shown in Fig 5.1(a). Here, the crack growth rate da/dN is plotted against stress intensity factors range (ΔK). From the Fig. 5.1(a) it is observed that crack grows very slowly at $da/dN = 10^{-9}$ that defines the threshold region. The average value of threshold SIF for the Al 2014-T6 material is 4.84MPa√m (see the Table 5.1). It is observed from the Fig. 5.1(a) that there exists a stochastic nature, in the crack growth data that has

been elaborated by means of a best-fit method. The most suitable methods for data analysis are suggested by ASTM Standard [30], are the secant method and the incremental polynomial method. In this work, the material constants *C* and *m* are determined by quadratic polynomial fitting of the log-log data of *da/dN* Vs ΔK is shown in Fig. 5.1(b). Table 5.1 shows the arrived material constants and average values from three tests for the *R* = 0.05. The average values of material constants are given as input for determining the fatigue crack growth rate and fatigue life of repaired panel using FEA.

Table 5.1: Fatigue material constants of Al 2014-T6

Property	Specimen 1	Specimen 2	Specimen 3	Average
C (m/cycle)	5.5e-11	5.67e-011	4.46e-11	5.21e-11
M	3.34	3.22	3.3	3.28
ΔK_{th} (MPa√m)	4.78	4.9	4.84	4.8
ΔK_c (MPa√m)	22.9	24.7	23.9	23.8

(a)   (b)
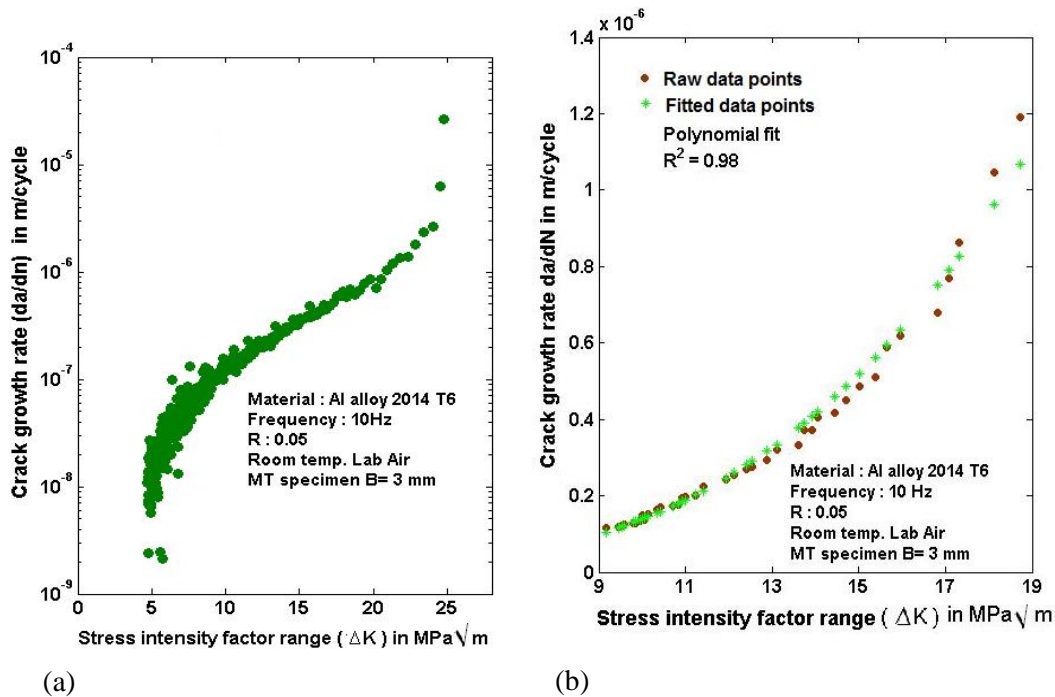
Figure 5.1: FCGR versus the stress intensity factor (SIF) range for the 2014 -T6 (a) sigmoidal curve (b) polynomial curve fit for linear zone

5.3   Introduction to Zencrack

Zencrack is a state-of-the-art software tool for FEA based software being used for fatigue crack growth 3D models simulation [97]. Figure 5.2 illustrates the detailed flow chart of the FEA based fatigue crack growth analysis using Zencrack and ANSYS. Zencrack takes an

un-cracked 3D mesh supplied by the user and inserts one or more crack blocks into the regular mesh according to user requirement. The cracked mesh is then solved with the specified loads. Results of the FEA are extracted and processed automatically to calculate fracture mechanics parameters. Both crack growth direction and crack increment length is calculated using the post processing of first step results. The above procedure is repeated for the next new crack tip coordinates. This analysis gets stopped as a reaches to critical crack length or SIF reaches to K_{IC}.
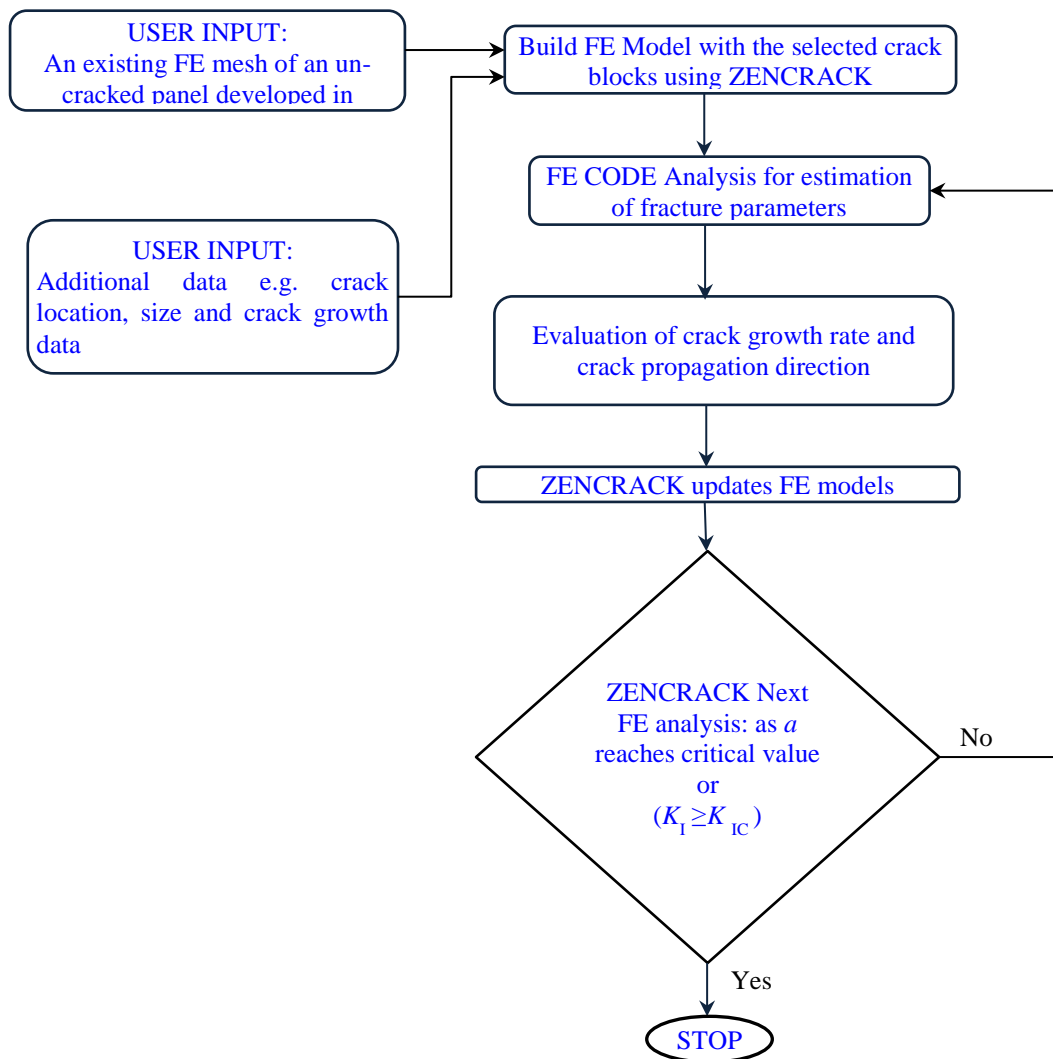
Figure 5.2: Flowchart of overall methodology of three-dimensional fatigue analysis [97]

5.3.1 Finite element modeling of three-dimensional cracked panel

Finite element method is the most effective tool for computing fatigue life in 3D fracture models. Modeling and analysis of the inclined center cracked Al 2014-T6 is done using Zencrack 7.6 interfaced with ANSYS 12.1 commercial FEA package. Initially the panel is

modeled without crack tip elements as per the dimensions in ANSYS (se Fig 5.3(a)). Then automatic generation of 3D crack elements for crack propagation analysis has been implemented by writing a macro in Zencrack which has a direct interface with ANSYS. In this analysis the standard type of crack block s02t19x1 is used (see Appendix D.1). They have 8 circumferential elements with quarter point nodes around the crack tip as shown in Fig. 5.3 (b). Six crack blocks are used along thickness for each of the crack front, there by twelve crack blocks in total for each of the crack front. The panel is meshed with three elements along the thickness direction using an eight- noded solid 185 element. Meshed model of the entire panel geometry including the crack tip blocks is shown in Fig. 5.3 (c). Similarly, patch is meshed with six elements along the thickness direction using a eight noded solid 185 element.
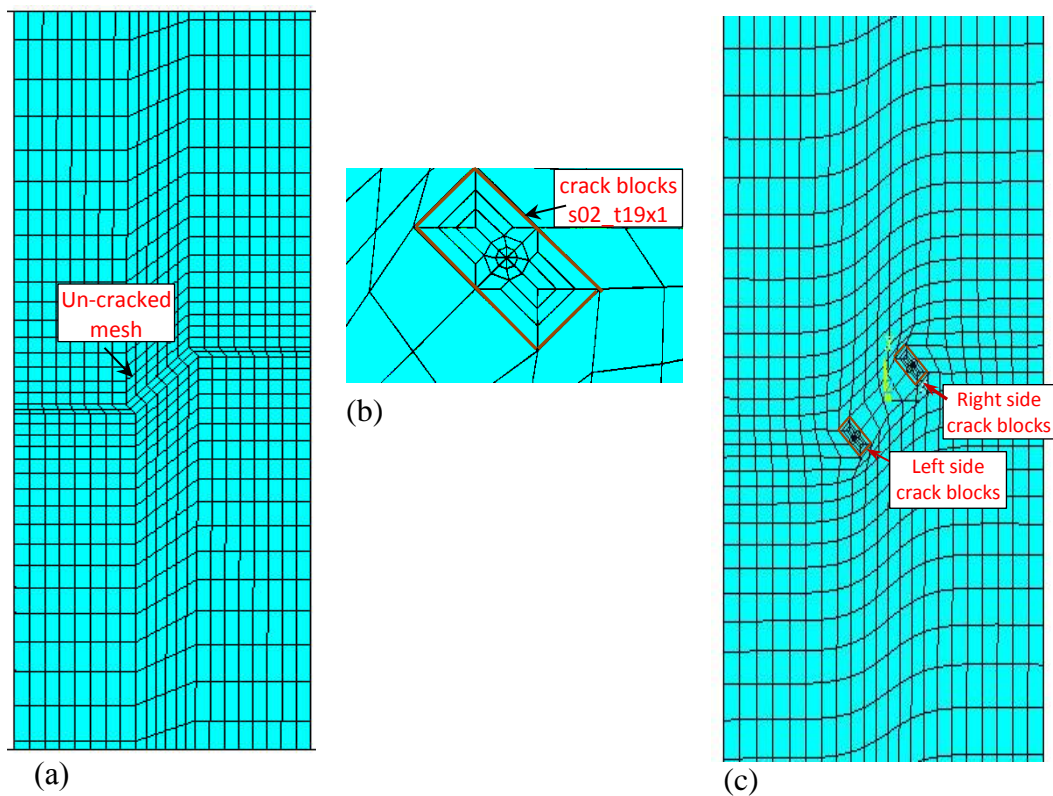
Figure 5.3: Finite element model (a) un-cracked mesh (b) zoomed portion of crack tip (c) cracked panel

5.3.2   Finite element modeling of repaired panel using Zencrack

The patch is modeled with the eight-noded solid 185 elements as per the dimensions similar to that of the panel. In this analysis the composite patch with fibers oriented parallel to the loading direction is considered. The extended octagonal patch shape is chosen for understanding the fatigue behavior of repaired panel. Figure 5.4 (a) illustrates the meshed

model of the repaired panel with the tapered extended octagonal patch. However, the interface between the panel and the patch is modelled as contact pair using cohesive zone modeling (see section 5.3.3 for detailed information). During fatigue analysis a constant amplitude cyclic load of 14.16 kN is applied with a stress ratio (R) of 0.05 on the panel and fatigue crack growth behavior is predicted. To simulate the crack growth, Zencrack does the adaptive re-meshing at every incremental advance and estimates the fracture parameters as well as the crack front growth which is described in the flowchart (see Fig. 5.2).

5.3.3   Interface Modeling : cohesive elements

In case of adhesively bonded joints, the adhesive interface is the weakest link which fails first under the applied cyclic load. Hence, it is important to include the adhesive layer failure for accurate estimation of fatigue life of the repaired panels. Typically, there are two types of criteria's used in the literature for predicting the debonding behavior of the adhesive layer [68, 90]. Papanikos et al. [90] used the maximum shear stress criteria to model damage of the adhesive. According to this damage theory, the property of adhesive is degraded when the shear stress in the adhesive layer reaches the specified maximum value in the adhesive layer element [90]. In the second approach, a damage criterion of the adhesive layer is obtained based on the cohesive zone modeling involving interface elements [68]. Here, the contact pair based cohesive modelling is adopted to simulate the damage of the adhesive interface layer.

The concept of cohesive failure is illustrated by assuming that a cohesive zone is present at the interface. With the increasing load, the cohesive zone surface which is intact initially is separated to a distance due to the influence of high stress state at the interface. The cohesive zone surface resists a distribution of tractions T which are function of the displacement across the surface δ. The relationship between the traction T and separation δ is defined as a constitutive law for the cohesive zone surface. Ban et al. [98], categorized the several cohesive laws into the different groups. In the present analysis, the bi-linear cohesive zone law is used and is shown in Fig. 5.4(b) [68]. To capture interface debonding, the contact elements are modelled as the cohesive zone elements with bilinear material behavior characterized by maximum traction and critical energy release rate as shown in Fig. 5.4(b). The critical fracture energies required for the cohesive modelling of the adhesive interface are obtained by us through series of novel experiments in combination with finite element analysis as explained in the Appendix D.3- Appendix D.5. Hence, to implement the debonding behavior, the interface fracture toughness (G_{Ic} and G_{IIc}) of adhesive layer is defined. Here, both mode I and mode II interface fracture toughness are considered and their

values are listed in Table 5.2. These material properties are obtained from the base line standard tests illustrated in Appendix D.3 and Appendix D.4 respectively. Further, the adhesive stiffness is determined as $k_I = E_a/t_a$ where, E_a is the Young's modulus of the adhesive material and t_a is the adhesive thickness, $k_I^{'}$ is stiffness after degradation which is considered as $1/100^{th}$ of k_I [90].
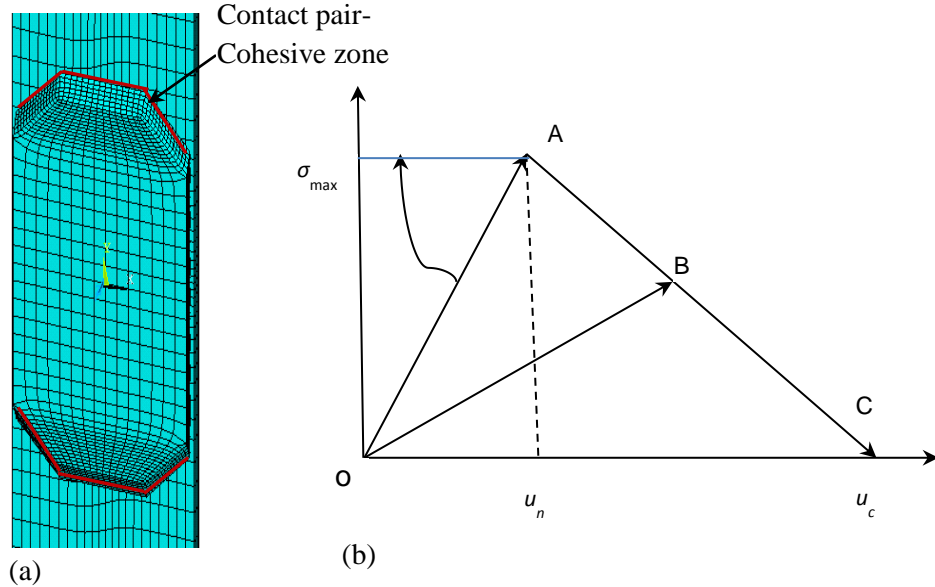
Figure 5.4: (a) FE mesh of repaired panel (b) Bilinear cohesive zone material modeling

Table 5.2: Adhesive material properties for FEA modeling

Property	Araldite 2011
Stiffness (k_I)	11400 N/ mm
Fracture toughness in mode I (G_{IC})	2.1 N/ mm
Fracture toughness in mode II (G_{IIC})	0.65 N/ mm
Stiffness after degradation ($k_I^{'}$)	114 N/ mm

5.3.4   Crack growth criterion

In order to predict the crack growth based on linear elastic fracture mechanics (LEFM) frame work, the basic parameters such as SIF, crack propagation direction and crack-growth need to be determined. The methodology to determine SIF and the crack propagation direction is discussed below.

5.3.4.1 Estimation of SIF from displacements

In this analysis the SIF's in all three modes are evaluated from the relative displacement of the pairs of nodes on either side of the crack face in local mode I, II and III orientations.

From these relative displacements, crack tip displacement is extrapolated, and subsequently the SIF's (K_I, K_{II}, K_{III}) are estimated using the following equations [97]:

$$K_I = \frac{E'V_i}{4}\sqrt{\frac{2\pi}{r}} \tag{5.1}$$

$$K_{II} = \frac{E'V_{ii}}{4}\sqrt{\frac{2\pi}{r}} \tag{5.2}$$

$$K_{III} = \mu V_{iii}\sqrt{\frac{\pi}{2r}} \tag{5.3}$$

where E and μ are the Young's and shear modulus of the panel material, $E'=E$ for plane stress condition and $E'= E /(1-v^2)$ for plane strain, V_i, V_{ii} and V_{iii} are the relative displacements along y, x and z directions respectively with respect to the crack tip coordinate system and r is the distance from the crack front. The crack growth process involves evaluation of the magnitude and direction of the energy release rate. The energy release rate along 3-D crack front is calculated using stress intensity factors (K_I, K_{II}, K_{III}) as described by the following equation [97]:

$$G_{eqiv} = \frac{B}{E}(K_I^2 + K_{II}^2) + \frac{1}{2G}K_{III}^2 \tag{5.4}$$

On simplification of Eq. 5.4 in terms of K_{eq} can be expressed as:

$$K_{eqiv} = \sqrt{K_I^2 + K_{II}^2 + (1+\vartheta)K_{III}^2} \tag{5.5}$$

By considering the difference of Eq. 5.5 at maximum and minimum loading, ΔK_{eq} is written as:

$$\Delta K_{eq} = (K_{eq})_{max} - (K_{eq})_{min} \tag{5.6}$$

The Paris law is used to calculate the number of cycles. On substitution of Eq.5.6 in fatigue crack grow law Eq. 1.2, the crack increment size da for a given number of fatigue load cycles dN as shown in Eq. 5.7:

$$\Delta a \approx C(\Delta K_{eq})^m \Delta N \tag{5.7}$$

The material constants for crack growth estimations in the above equation are taken from Table 5.1. The crack growth process involves the estimation of crack growth magnitude and direction of each node on the crack front. This allows the crack to be advanced through the model. The crack growth is generally a two-pass process to ensure that all nodes grow by the same number of cycles from one step to the next. In general the da will vary from node to node along the crack front [97]. During the update of the crack front to a new position, the mid-side nodes are positioned in such a way as to try to obtain a smooth crack front.

5.3.4.2. Estimation of crack propagation direction

In order to determine new crack-front positions, the crack propagation direction must be computed. Several crack growth criteria used for mixed mode problem are the minimum strain density criterion, the maximum tangential stress criterion and the maximum energy release criterion [100]. In here, the maximum energy release rate criterion is adopted for estimating crack growth direction. It states that a crack will grow in the direction of maximum energy release rate. The crack propagation direction is then determined by using the criteria mentioned in Eq. 5.8:

$$\left(\frac{dG_{ERR}}{d\theta}\right)_{\theta=\theta_0} = 0, \quad \left(\frac{dG_{ERR}}{d\theta}\right)^2_{\theta=\theta_0} \leq 0 \tag{5.8}$$

ERR is numerically computed through *J*-integral [76] using the virtual crack extension (VCE) method [97]. The VCE method has been explained in detail in Appendix E.2. And, the new crack front coordinates are estimated at every crack increment da. This procedure is repeated until a desired crack length (*a*) or number of fatigue cycles (*N*) is reached.

5.3.5   Fatigue life prediction

Figure 5.5 shows the variation of fatigue life with the crack length for the unrepaired and repaired panels. Blue curve represents the unrepaired panel, red and green represents the single- and double-sided patch repaired configuration respectively. It is observed that the fatigue life of both single and double-sided patch repaired panels is higher than the unrepaired panel. The additional reinforcement over the crack faces improved the fatigue life considerably. It is also evident that at the initial cycles the crack growth is very slow and once the ΔK reaches the critical value it grows faster within a few cycles. And it is observed that the fatigue life of the double-sided configuration is twice that of the single-sided repair configuration. Hence the double-sided repair configuration is recommended for the adhesive patch bonded repair application.
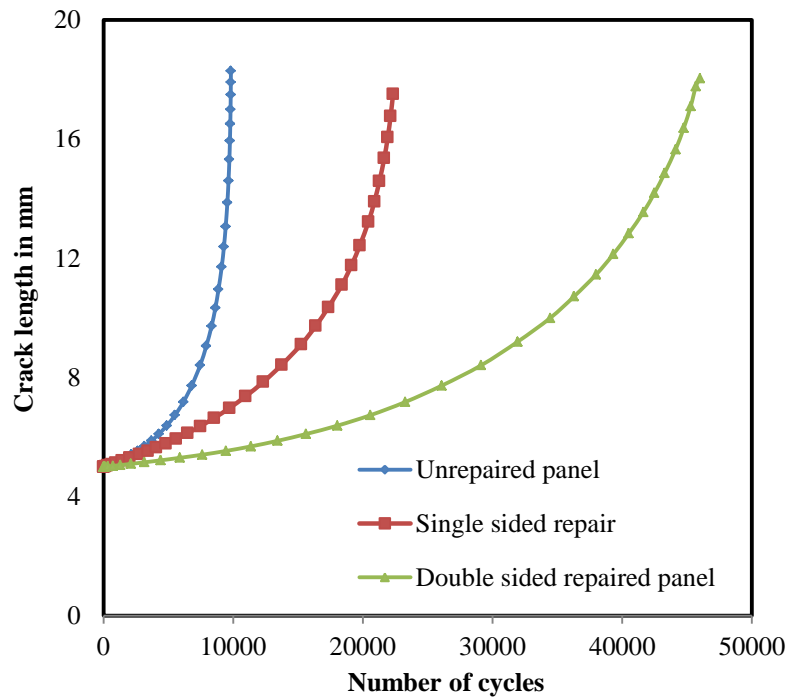
Figure 5.5: Comparative plot of crack growth verses number of cycles between unrepaired and repaired configurations.

5.3.6   SIF variation with crack growth

Figure 5.6 shows the variation of SIF's (K_{I} , K_{II} and K_{III}) with the crack length for the unrepaired and repaired panels obtained from FEA simulations as mentioned in Sec. 5.3.4.1. In case of single sided repair, SIF from the unpatched surface is considered for plotting. Figure 5.6(a) shows the variation of K_{I} vs crack length. In here, blue color curve represents the variation of SIF for unrepaired panel whereas a red and green curve represents the single and double sided patch repair's SIF variation respectively. Similarly, K_{II} and K_{III} variation vs crack length is too plotted in Figs. 5.6(b) and 5.6(c) respectively. It can be observed from the Fig. 5.6(a) that K_{I} increases with the increasing crack length as expected. Further, it is observed that there is slight to significant reduction of SIF for the single and double sided repaired panels respectively as compared to that of the unrepaired panel. From this analysis it is also observed that K_{I} at the unpatched surface of the single sided repair is higher than the cracked panel surface at initial crack length. This tendency is observed due to a slight shift in the plate neutral axis and which induces bending stresses in addition to the in-plane tensile loading which is clearly explained in chapter 2. The K_{II} and K_{III} value decreases with the increasing crack length, as shown in the Fig. 5.6(b) and 5.6(c) respectively. It is because with the increasing crack growth, crack tends to propagate perpendicular direction to the loading axis. Hence, relaxing the K_{II} and K_{III} but maximizing the K_{I} value. However, in case

of single sided repair K_{II} initially shows a declining trend, but with further increase in crack length it gradually shows a slight increment. This increment in SIF is attributed to the increase in mode mixity due to the additional bending stress induced because of the shift in neutral axis due to unsymmetrical patch geometry. Finally, it is found that with increasing cycles (i.e. higher the crack length), K_I is predominantly more when compared to other modes.

(a)

(b)

(c)
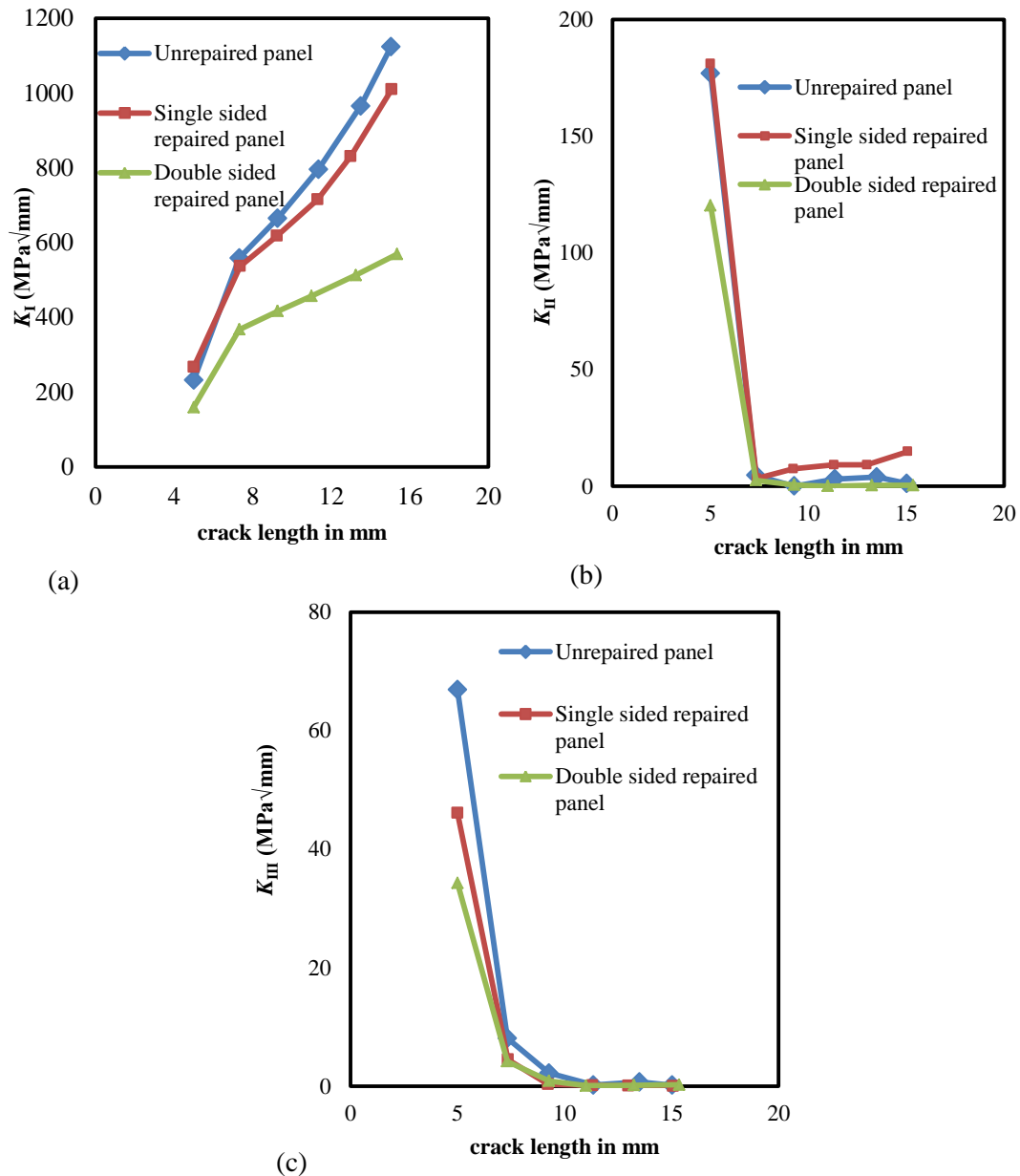
Figure 5.6: SIF variation with increasing crack length (a) K_I (b) K_{II} (c) K_{III}

5.3.7   Crack front shapes

In this subsection the crack front shape through the thickness of the panel is presented, which is obtained using the analysis as explained in Sec. 5.3.4.1. Figures 5.7(a)-(c) represent the fatigue crack front shape through the thickness of unrepaired as well as single and double sided patch repaired panel respectively. A uniform and symmetrical crack front is observed in the unrepaired and the double-sided repaired panels, as shown in Figs. 5.7(a) and (c). On contrary, a non-uniform crack front that is curved in profile is observed in the single sided repair, as shown in the Fig. 5.7(b). Further, in the single sided repaired panels, it is observed that crack grows at a faster rate at the unpatched surface as compared to the patched surface. This non-uniform crack growth is mainly due to additional bending phenomenon arising due to the shift in the neutral axis of the single-sided repaired panel (see Sec. 5.3.6). This resulted in linear variation of SIF through the thickness of panel for a given crack length as discussed in the second chapter.
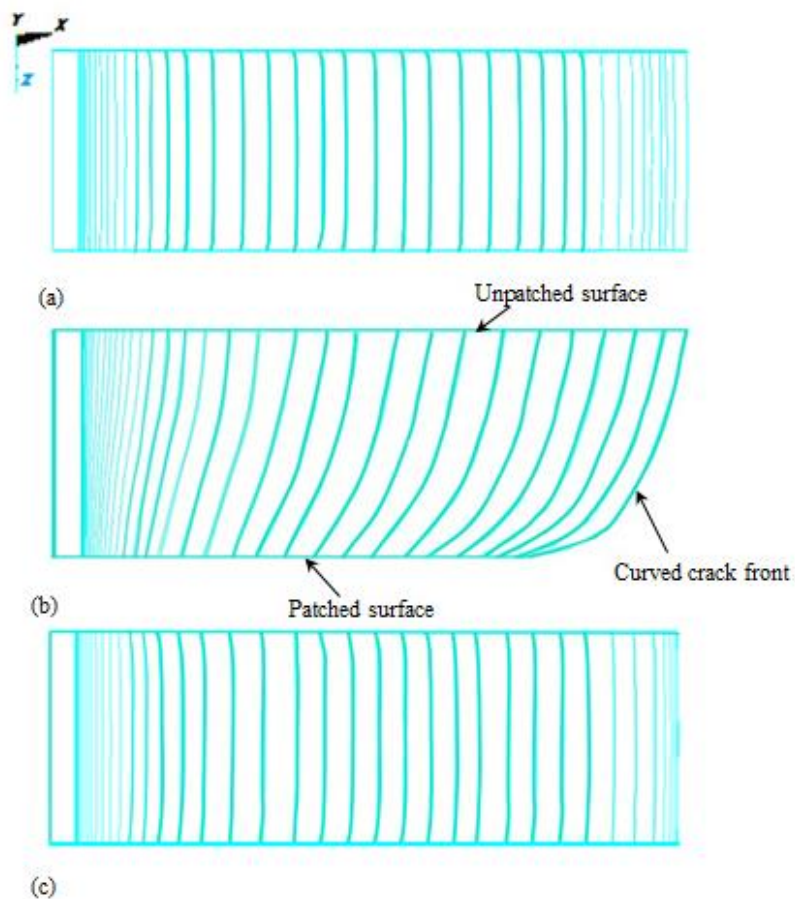
**Figure 5.7: Crack front profiles using FEA (a) unrepaired panel (b)
single sided repaired panel (c) double sided repaired panel**

5.4   Test Procedure using DIC

5.4.1   Experimental Setup

The cracked panel and repaired panel are fabricated as per the procedure mentioned in the previous chapter in section 4.3. In this analysis, to monitor the crack growth during fatigue loading 2D DIC setup is used along with magnified lenses. Figure 5.8 shows the 2D DIC setup along with the servo hydraulic loading equipment. A constant amplitude tension-tension load (0.7 -14.16 kN) is applied along the longitudinal direction with a test frequency of 10 Hz. The experimental setup comprises of a CCD camera (POINTGREY-GRAS-50S5M-C) having a spatial resolution of 2048 x2448 pixels filled with a Tamron zoom lens of 180 mm focal length. The camera is connected to a laptop for image acquisition and specimens are illuminated using two LED light sources to ensure adequate image contrast. For obtaining precise correlation between the images and number of cycles, a controller is employed to trigger the camera at regular intervals of cycle at specified phase angles. In the present analysis the images are captured every hundredth cycle and at every 90° phase angle. Then the reference image is calibrated for the known length, to acquire physical coordinates of the pixels. Later, the displacement field surrounding the crack tip is intelligently used for obtaining the crack advancement length with the increasing number of cycles.
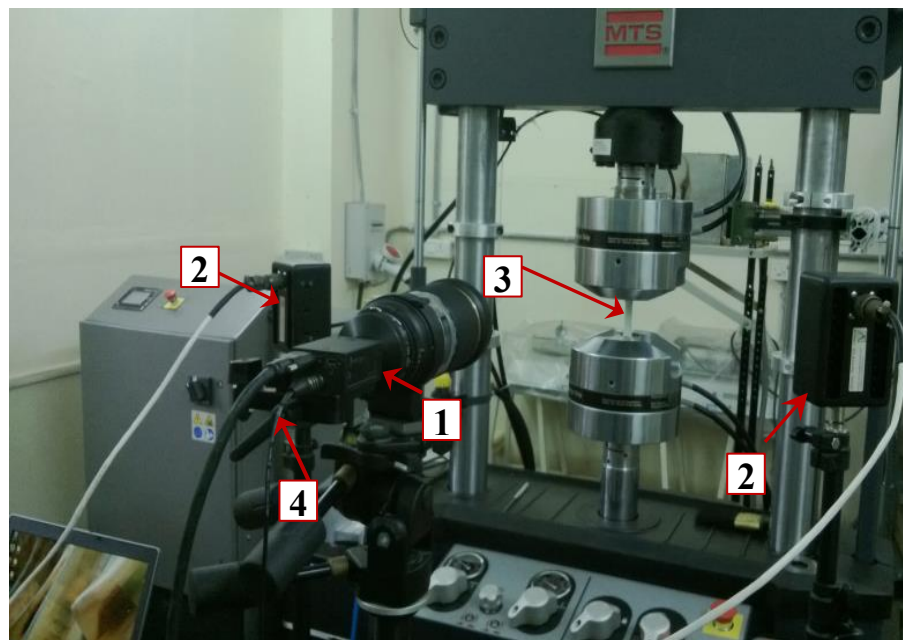
**1. CCD camera with Tamron lenses, 2. Light source,
3. Specimen 4. Triggering cable connected to camera**

Figure 5.8: Experimental setup involving 2D DIC

5.4.2   Crack length determination using DIC

In order to validate the numerical results, fatigue tests are performed under load control mode with a maximum load of 14.16 kN at a sinusoidal loading of 10 Hz frequency. Five images are recorded at every 100th cycle. The images acquired by the image acquisition system are analyzed using the commercially available Correlated Solutions, Vic-2D post processing software [86]. The region of interest (ROI) for correlation is chosen as 2266 x 909 pixels. A subset size of 19 x 19 pixels is chosen along with a step size of 5 pixels for performing the DIC estimation. The displacement fields along *y* direction are estimated from the recorded images at various cycles. The displacement field along *y* direction contains discontinuity in the zone where crack plane is present. In this study, the crack length is determined accurately using the image processing algorithm written in MATLAB. It is obtained by applying thresholding process in the *v*-displacement contours obtained over crack tip advancement [71]. Figure 5.9 shows the gray scale image of the *v*- displacement contours at different time instances. From the figure it is observed that there is a gradual increment in crack length with number of cycles. Here, the crack length is estimated by assuming that *y* position of the crack tip is constant and crack advancement length Δ*x* is measured using image processing tools by estimating the discontinuity length in the gray scale image at different time instances. The final crack length is estimated as mentioned in Eq. 5.9:

$$a = \sqrt{((x + \Delta x)^2 + (y^2))} \tag{5.9}$$

where *x*, *y* represents the initial crack tip position and Δ*x* represents the crack advancement length along *x* direction with respect to the number of cycles.

(a)   (b)   (c)

(d)   (e)   (f)
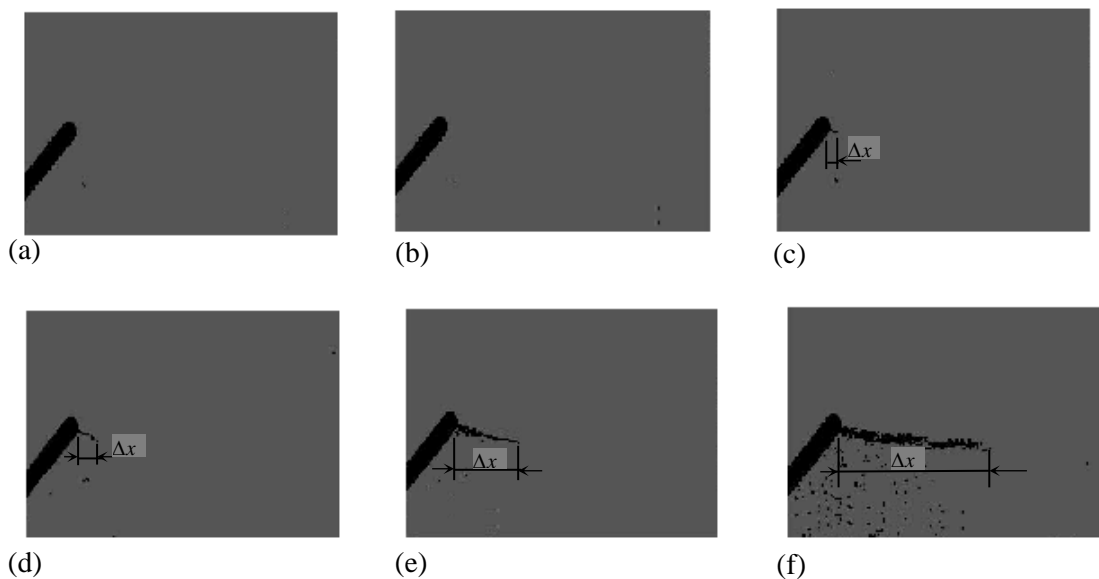
Figure 5.9: Estimated crack fronts in unrepaired panel after (a) 1002 (b) 3000 (c) 5000 (d) 6000 (e) 7500 and (d) 8500 fatigue cycles

To estimate the crack length in the case of single sided repaired panel the camera is focused on the unpatched surface. Figure 5.10 shows the gray scale image of the *v*- displacement contours at different time instances. In the Fig. 5.10; Δx represents, crack advancement length along *x* direction. Here, the crack advancement distance is measured from the right side crack tip using the procedure described earlier in the Sec. 5.4.2.

(a) (b) (c)

(d) (e) (f)
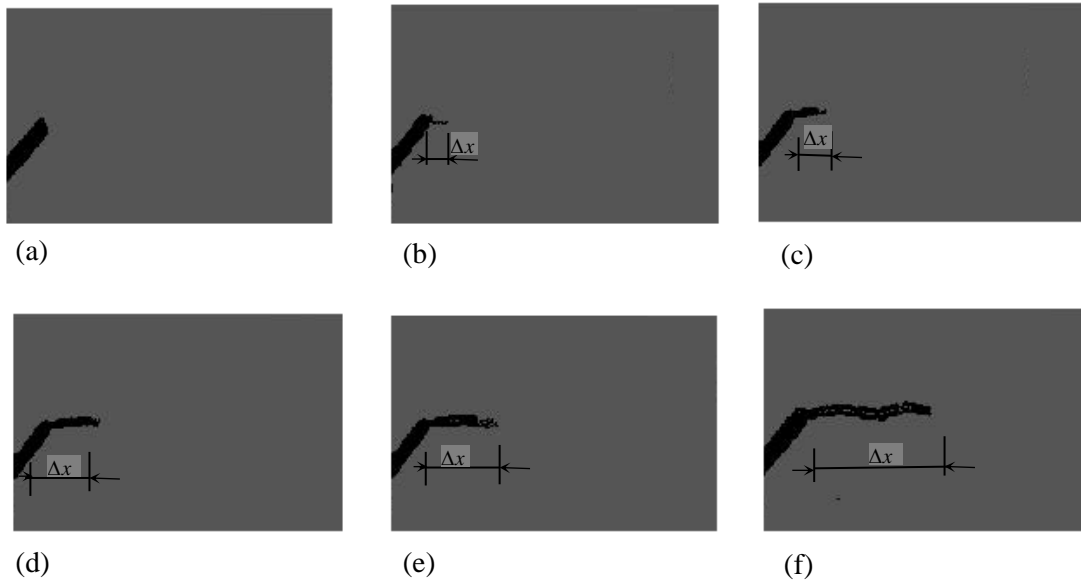
Figure 5.10: Estimated crack fronts at the unpatched surface of the single sided repaired panel after (a) 2300 (b)10102 (c)14502 (d)17500 (e) 19000 and (d) 21300 fatigue cycles

5.4.3 Comparison of *v*-displacement fatigue life of un repaired panel using FEA and Experiment

The *v*-displacement contours of unrepaired panel at different time instances corresponding to 6000, 7500 and 8500 fatigue cycles obtained from DIC and FEA are shown in Fig. 5.11(a), 5.11(b) and 5.11(c) respectively. The displacement contours from DIC and FEA qualitatively match to a reasonable extent but not quantitatively. The reason for such a mismatch arises due to several factors such as slight disorientation of initial crack plane, slight misalignment of test specimen with respect to loading and etc. It is observed from the Fig. 5.11 that there is a gradual increase in the crack length and it propagates downwards in the perpendicular direction to the applied load for the right side crack tip and vice versa for the left side crack tip.
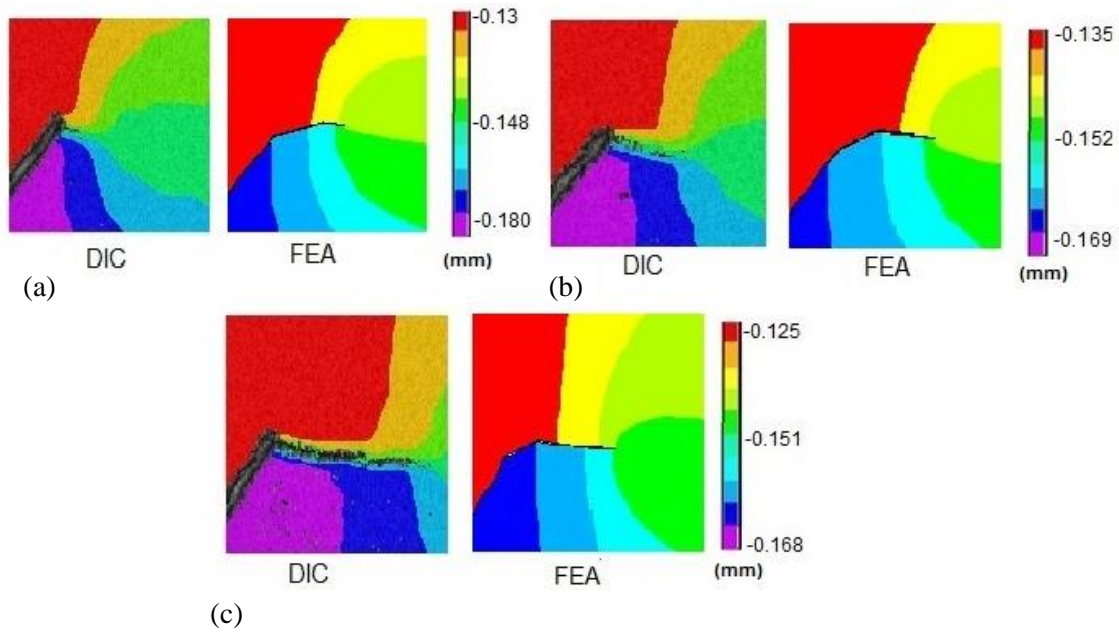
Figure 5.11: *v*-displacements contours obtained in unrepaired panel at different crack tip positions with respect to fatigue cycles (a) 6000, (b) 7500 and (c) 8500 : DIC and FEA

Figure 5.12 shows the experimental (green dashed line) and numerical variation (red solid line) of crack length versus number of cycles for an unrepaired panel. The region of interest for measuring the crack advancement distance is considered at the right side crack tip, as shown in Fig. 5.12 inset. Both the experimental and FEA exhibits similar crack growth behavior with number of cycles. There is a reasonable coherence that exists between the finite element and DIC results.
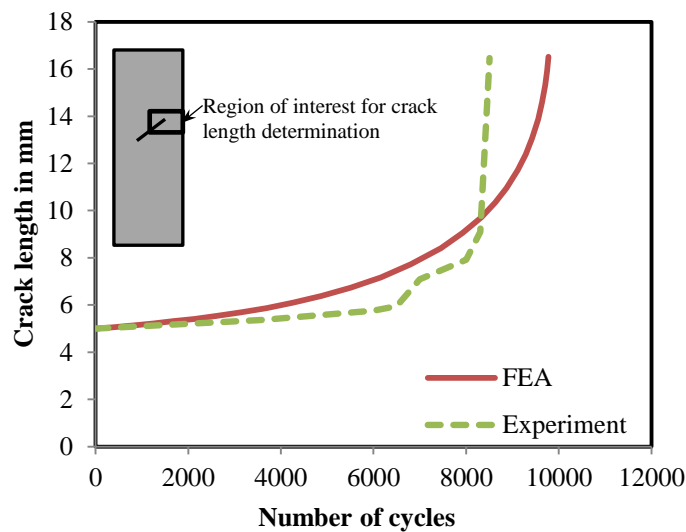
Figure 5.12: Crack length Vs Number of cycles: unrepaired panel

5.4.4 Comparison of *v*-displacement and fatigue life of single sided repaired panel using FEA and Experiment

The *v*-displacement contours of the single-sided repaired panel at different time instances corresponding to 17500, 19000 and 21300 fatigue cycles obtained from both DIC and FEA are shown in the Figs. 5.13(a), 5.13 (b) and 5.13 (c) respectively. The displacement contours from DIC and FEA qualitatively match to a reasonable extent but not quantitatively, due to reasons explained in the Sec. 5.4.3. There is a measured advancement in the crack length with the increasing number of cycles. It is also observed that crack is propagating in a perpendicular direction with respect to the applied load. The resulting crack growth advancement estimated from the displacement field clearly shows that the DIC method is a valuable technique to monitor the crack growth during the fatigue tests. Especially in case of inclined crack, the DIC technique is extremely handy to measure the crack growth where most of the conventional approaches cannot simply measure.
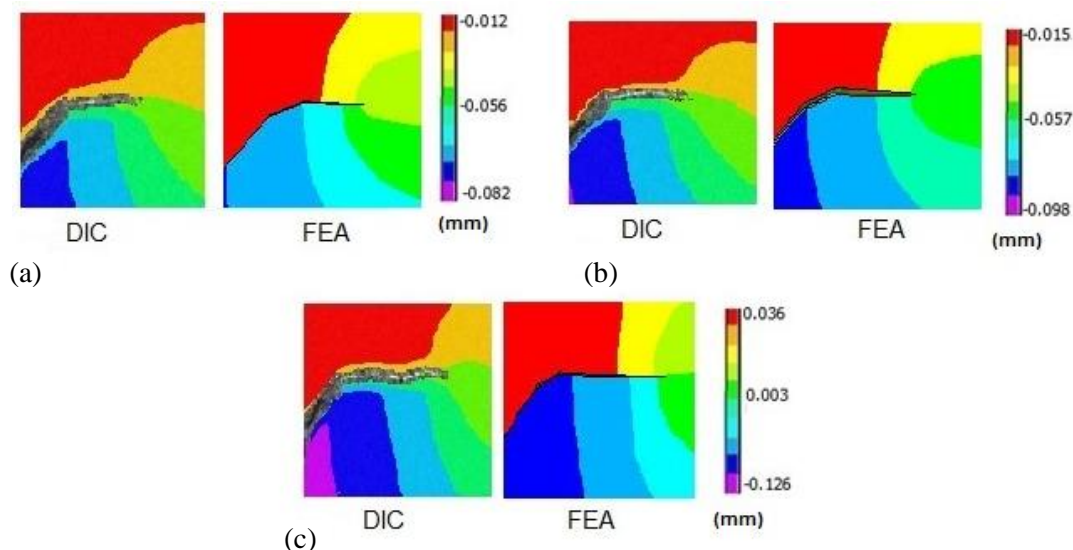
Figure 5.13: *v*-displacements contours obtained in single sided repaired panel at different crack tip positions with respect to fatigue cycles (a) 17500, (b) 19000 and (c) 21300: DIC and FEA

Figure 5.14 shows the experimental (green dashed line) and numerical variation (red solid line) of the crack length versus the number of load cycles for the single-sided repaired panel. The region of interest in measuring the crack advancement distance is considered at the right side crack tip, as shown in the Fig. 5.14 inset. Both the experimental and the FE exhibits similar crack growth behavior with the number of cycles thereby confirming the accuracy of the implemented cohesive models. The fatigue life of the repaired panel is more than the unrepaired panel, because of increase in the load transfer capability due to additional

reinforcement over the cracked region in the form of patch. Table 5.3 shows the comparison of fatigue life of the unrepaired and repaired panel obtained from FEA and experiment. It is observed that the fatigue life of the double-sided repair (FEA: 46440 cycles, Expt: 46379 cycles) is almost twice that of the single-sided repair (FEA: 22561 cycles, Expt: 21511 cycles) in both the FEA and the experimental predictions.

Table 5.3: Comparison of the crack growth life of the repaired and un-repaired panels

Configuration	Experiment: Fatigue life (cycles)				FEA (cycles)
	Specimen1	Specimen 2	Specimen 3	Average values	
Unrepaired panel	8503	7338	8102	7981	9824
Single-sided repaired panel	21511	20080	19980	20523	22561
Double-sided repaired panel	47305	46697	45135	46379	46440
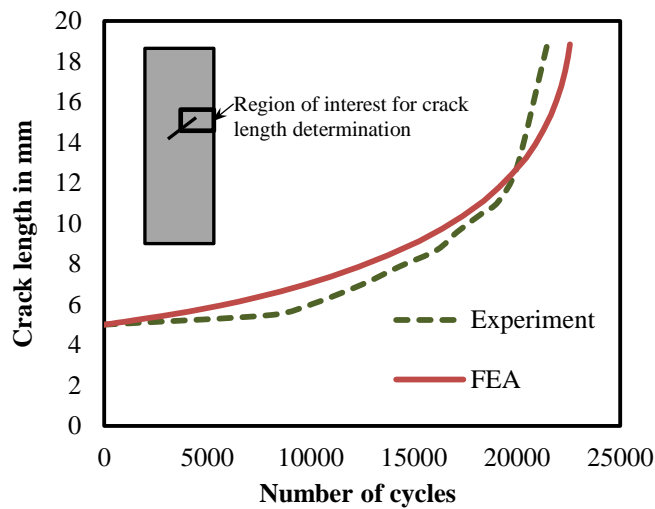
Figure 5.14: Crack length Vs number of cycles: single sided repaired panel

Figure 5.15 shows the crack tip trajectory of the unrepaired, single-sided and double-sided repaired panel obtained using FEA and DIC respectively. However, the experimental crack tip trajectory for the double-sided patch repair is not presented here as the crack is covered by the patches on both the sides of the panel and cannot be tracked using DIC. Both the

experimental and numerical results show that the major section of the crack growth is in the *x*-direction. The loading and the geometry of the crack produce equal normal and shear stresses for the initial crack length, as the crack inclination angle is of 45˚. But after a few steps of the crack propagation, the component of the K_I becomes dominant and the crack propagates in a perpendicular direction to the applied load. It is observed from the FEA and DIC results that the crack growth direction of the unrepaired and the double-sided repaired panel is almost similar but differs in case of the single-sided repair. This difference in the behavior of the single-sided repair panels could be attributed to higher SIF at the unpatched surface.
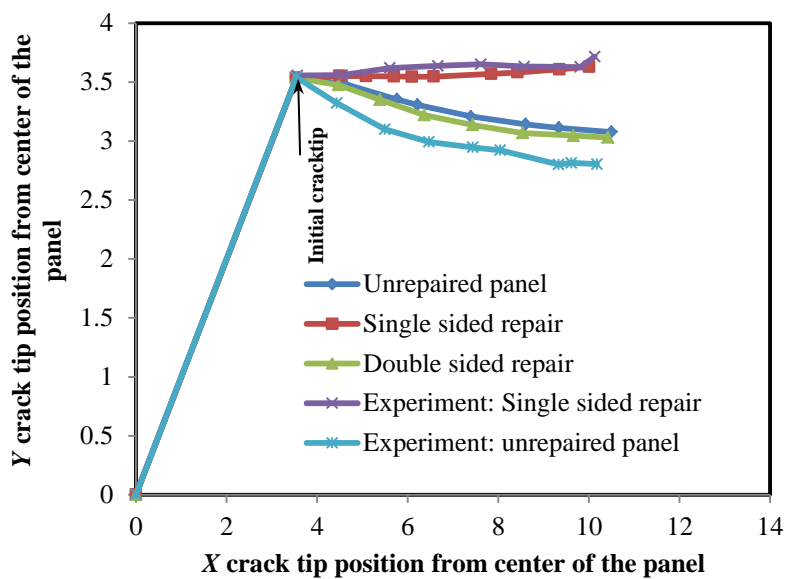
Figure 5.15: Crack Trajectory

5.4.5 Fracture mechanism and fracture surface

The failure mechanism observed in the unrepaired and the repaired panels are shown in the Figs. 5.16 (a), 5.16 (b) and 5.16 (c) respectively. It is observed from the figure that the crack propagates along a perpendicular plane to the loading direction as the number of cycles increases. Shear and peel strain concentration in the adhesive layers of the repaired panels near the patch overlap edge, results in the partial patch debonding followed by the fracture of the panel similar to that of the unrepaired panel (see Figure 5.16 (b) & 5.16 (c)). This partial patch debonding happens due to the adhesive layer failure.
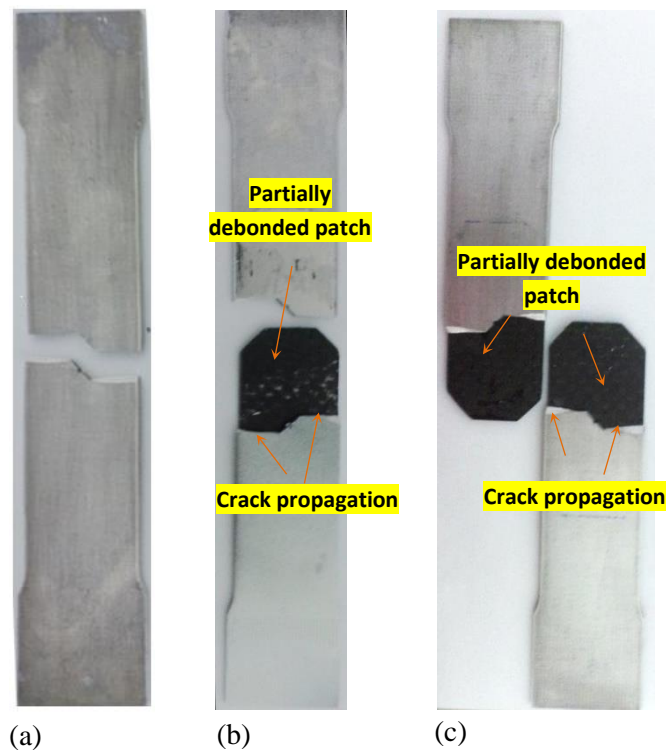
Figure 5.16: Failure mechanism in Al 2014-T6 center cracked panel with CFRP patch repair: (a) unrepaired panel (b) single sided repaired panel and (c) double sided repaired panel.

Figure 5.17 shows the fracture surfaces of the single sided repaired panel specimen obtained after experiment. The crack front shape of the single sided repaired panels is curved and non-uniform in nature due to the variation of SIF along the thickness (SIF minimum at the patched surface and maximum at unpatched surface). The crack front profile obtained from the FEA (see the Fig. 5.10(b)) is in agreement with the experimental profile, as shown in the Fig. 5.17.
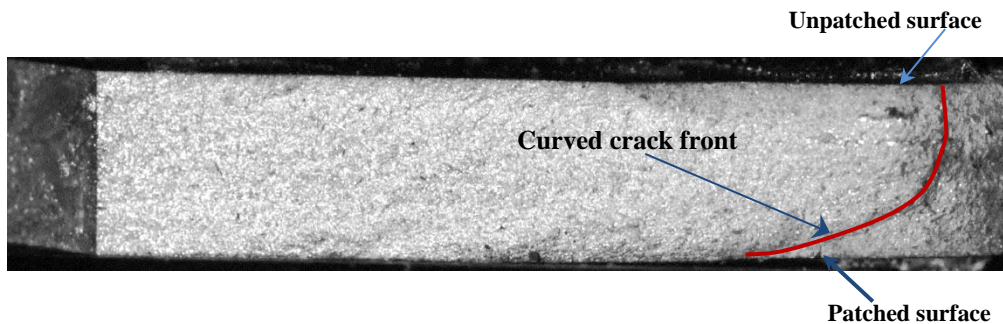
Figure 5.17: Non-uniform crack growth profile in single sided repaired panel

116

5.5   Closure

In this chapter, both DIC and FEA based study is carried out to evaluate the effect of single and double sided composite patch on an inclined center cracked Al 2014-T6 panel under fatigue loading. Paris material constants are estimated using FCG rate test for $R = 0.05$. The average values of the constants obtained from the test are $C = 5.21e^{-11}$ m/ (cycle x MPa$\sqrt{(m)}$), $m = 3.28$, $\Delta K_{th} = 4.84$ Mpa $\sqrt{m}$, and $\Delta K_c = 28.83$ MPa$\sqrt{m}$. These material constants are given as input for crack growth study involving FEA. It is found that fatigue life of both single and double sided patch repaired panels are generally higher than the unrepaired panels. Therefore additional reinforcement, in the form of patch, bonded over the crack zone improves the fatigue life in case of repaired panels as compared to unrepaired one. It is also observed that K_I increases with the increasing crack length, whereas K_{II} and K_{III} decreases. However, in the case of single sided repair configuration there is a marginal increase of K_{II} with increasing crack length. This increment is due to the mode mixity arising due to the bending phenomenon leading to additional shear stress development. Damage initiation and crack propagation in unrepaired and single sided repaired panel is successfully monitored based on the displacement data obtained using DIC coupled with image processing algorithm. It is observed that DIC is a suitable technique for measuring the crack growth rate under fatigue load. Using this technique the crack tip position is determined precisely. It is also witnessed that the crack growth profile of double sided and unrepaired panel is uniform and symmetric, whereas, in single sided repaired panel, non-uniform crack growth profile is observed due to the additional bending load arising due to eccentricity. This bending stress varies linearly through the panel thickness and it leads to non-uniform crack growth profile. Lastly, fatigue crack growth is simulated using FEA involving CZM approach at the adhesive interface layer. The CZM properties for CFRP/ Al 2014-T6/ Adhesive 2011 interface system are determined from experiment. In case of repaired panels, partial debonding of the patch is preceded before the complete failure of the panel is observed. In case of repaired panels, the cohesive zone modeling of adhesive layer predicted the debonding and the fatigue life more accurately. Generally, for a double sided repair configuration there is a drastic improvement in fatigue life as compared to the unrepaired and single sided repaired panels since SIF reduction is maximum comparatively. From our studies it is found that life of double side repaired panel is twice than that of single sided repaired panel. The fatigue life of unrepaired and repaired panel, obtained from finite element and experiments are found to be in reasonable agreement.

Chapter 6

Conclusions and Recommendations

6.1 Conclusions

Initial research on composite patch repair focused mainly on the study of mechanics of single and double sided patch repair applied towards the straight center cracked panel under tensile and fatigue loading. In field, the cracks that do occur in aircraft structures during its service life are of mixed mode nature and hence they need to be studied carefully. For life extension, these cracked structures are subjected to repair and one such common repair technique is adhesively bonded patch repair. In this thesis, a detailed numerical as well as experimental study is carried out to identify the effect of single and double sided patch repair on the panel having inclined center crack. Further, a thorough investigation is done to get the optimal patch shape, stacking sequence and dimensions preferred for repair of mixed mode panel. Moreover, a detailed study is also done on the experimental determination of strain field over the patched surface involving 3D DIC technique. Also, a complete study on the behavior of the adhesive layer interface in a repaired panel is carried out using 2D DIC coupled with magnified optics. Finally, an applied work is carried out to predict the behavior of repaired panel under constant amplitude fatigue loading using both FEA and experiment. The chapter wise summary of contributions made in this thesis is presented below.

In Chapter 2, a FEA based study is carried out to understand the behavior of single and double sided bonded patch repair of an inclined center cracked panel under tensile loading. From that study it is found that mechanics of single sided repair is very different from double sided repair. In the case of single sided repair both K_I and K_{II} vary linearly through the thickness of the panel. Further, it is found that K_I at the unpatched surface is higher than the K_I of unrepaired panel. This is due to the presence of additional bending behavior. To reduce the SIF at the unpatched surface a study is carried out with increasing patch thickness. It is found that higher the patch thickness greater the reduction in SIF especially K_I at the unpatched surface because repair stiffness mainly depends on patch thickness. On contrary, in case of double sided repair there is a reduction in both K_I and K_{II} of about 78% as compared to unrepaired panel thereby making it a preferred option for the repair

application. Patch lay-up configuration of 0˚ (i.e., fibers are aligned parallel to the loading direction) is recommended for the repaired panel under in-plane tensile load which results in lower SIF at the crack tip. Further from FEA based study, it is found that higher the adhesive thickness greater the SIF. Hence, it is recommended that adhesive thickness should be in the range of 0.1- 0.2 mm.

In Chapter 3, a detailed study is carried out on the optimization of patch geometry for obtaining lower SIF at the crack tip involving FEA. From the mechanics based optimization of patch shape using FEA, it is found that extended octagonal patch shape performs better in reducing SIF at the crack tip in a double sided repaired panel. Further, the optimal patch dimensions arrived from GA based approach are as follows: patch length is 1.95 *W*, patch width is 0.95 *W*, where *W* is the width of panel and a patch thickness of 0.7 times of panel thickness. It is recommended that a tapering ratio of 1:20 needs to be provided at the overlap edge so that the peel stresses reduces by 46% as compared to straight edge patch. This tapering ratio is taken from CRMS guidelines [4]. On an overall basis, in case of double sided repair, it is found that optimal patch geometry reduces the SIF by 35% as compared to patch geometry without optimization. The same extended octagonal patch shape is also applied for single sided repair configuration.

In Chapter 4, experimental strain analysis of the bonded patch repair panel is presented. DIC technique is employed for the strain analysis to get the whole field surface displacement and strain measurement over the unrepaired and repaired panel. From the whole field strain analysis of repaired panel, it is found that the longitudinal strain value is higher at the patch overlap edge due to abrupt jump in geometry. For the first time in literature, strain measurement in adhesive layer in a repaired panel has been carried out using 2D DIC in combination with magnified optics. Both shear and peel strain distribution in the adhesive layer are captured and based on the analysis one can conclude that the shear and peel strain concentrates at the patch overlap edge. It results in adhesive layer failure leading to partial patch debonding at overlap edge with increased loading. The final failure of repaired panel happens with partial debonding of the patch followed by complete failure of the cracked panel. Always the crack propagates in a direction perpendicular to the loading direction. The ultimate load carrying capacity of single sided repair is of 7% higher than the unrepaired panel, whereas double sided repair configuration has 12% higher than the unrepaired panel strength. Therefore, double sided patch configuration is always recommended for the repair application. Finally, full field strain variations obtained from

FEA are compared with the experimental results for both the configurations and they are found to be in good coherence.

In Chapter 5, behavior of bonded patch repaired panel under constant amplitude fatigue loading is studied. Initially, Paris constants for Al 2014-T6 alloy are estimated using standard fatigue crack growth test. Following the material property estimation, fatigue based study on both cracked and repaired panel is carried out experimentally. It is evident from the experimental results that in case of a double sided repair there is a drastic improvement in fatigue life as compared to single sided repaired panel. To monitor the crack front growth under fatigue loading, the displacement field information obtained at at different time instances obtained from DIC technique is utilized along with image processing algorithm. Further, a FEA based study is carried out phenomenologically to predict the fatigue life. Here, cohesive zone model is implemented to model the adhesive/panel as well as adhesive/patch interface. The cohesive zone properties are obtained from appropriate experiments. From the FEA based study it is found that the crack front profile of double sided and unrepaired panel is uniform and symmetric. On contrary, in single sided repair, non-uniform crack growth profile is observed due to the presence of additional bending behavior coupled with single sided patch effect.

Crack front position in single sided repaired and unrepaired panel obtained from the experiment are compared with FEA results and they are found to be in reasonable agreement. For both the repair configurations, partial debonding of the patch followed by complete failure of the panel is observed. The fatigue life of unrepaired and repaired panel, obtained from FE is compared with the experimental results and they appear to be in good coherence.

On an overall comparison, the double side repaired panel has got higher fatigue life since reduction in SIF is maximum as compared to both single sided patch repaired and unrepaired panel. From this study, based on the fatigue life it can be concluded that double sided patch repair performs better and it is recommended for repair applications.

6.2 Recommendations for future work

The result presented in Chapter 2 assumes linear elastic behavior of adhesive layer. Exact non-linear behavior of adhesive could be given as input and SIF can be deduced more precisely. In chapter 2, FEA has been used for SIF estimation but one could also explore DIC technique for SIF deduction involving displacement field surrounding the crack tip. Both unrepaired and single sided patch repaired panel could be studied.

The results presented in Chapter 3 describes the optimization of patch shape and patch dimensions for the given panel length and width and the procedure can be extended to any arbitrary panel width and length. An elaborate study needs to be done for arriving at the generic patch design approach.

The results presented in chapter 4, show that the longitudinal strain component obtained over the repaired panel from DIC matches closer to the FEA prediction. But there is a significant loss in displacement/strain data near the crack tip in case of unrepaired panel and also at the overlap edge in repaired panel. In DIC measurement, the algorithm avoids the data very close to a crack tip as it contains boundary and precisely one does not get the crack tip strain field. Due to this one cannot get sharp contours near the crack tip from DIC as compared to FEA. Therefore, it is suggested to develop an improved strain estimation algorithm that could carry out the correlation at the boundary for accurate displacement and strain measurement surrounding the crack tip. In the last section of Chapter 4, measurement of shear and peel strain in the adhesive layer is done locally involving DIC technique and the study can be further extended for shear and peel strain measurement in adhesive layer globally, to understand the complete behavior of adhesive layer.

The reliability of the repaired structure essentially depends on the skillfulness of the technician preparing the sample. Therefore, appropriate NDT method such as Infrared thermography can be explored to ensure proper adhesive bonding of the patch over the panel.

In chapter 5 experimental study of fatigue crack growth behavior in unrepaired and single sided repaired panel requires accurate measurement of crack tip location. Utilizing the displacement field data surrounding the crack tip from DIC technique, along with image processing technique, crack tip location is identified with number of cycles. Further, accuracy could be improved by using advanced image processing algorithm to precisely locate the crack tip there by removing any error associated with it.

Further, the behavior of the repaired panel under fatigue loading is of great importance for aircraft structural applications. In this work fatigue crack growth behavior of repaired panel under constant amplitude cyclic loading is only considered. However, in practical applications the loading on the aircraft structures is commonly a variable amplitude cyclic (spectrum) loading. Therefore, the current work could be extended for the study of behavior of patch repaired panel under variable amplitude cyclic loading.

Appendix

Appendix A

A.1 Analytical SIF expression for inclined center cracked specimen:

Figure A.1 represents the schematic of inclined center cracked panel. The analytical expression for SIF estimation of inclined cracked specimen is as given below [11]:

$$K_I = \sigma\sqrt{\pi a} \cdot F_I \tag{A.1}$$

$$K_{II} = \sigma\sqrt{\pi a} \cdot F_{II} \tag{A.2}$$

where, σ = far field applied stress

The values of F_I and F_{II} can be obtained from Fig. A. 2.
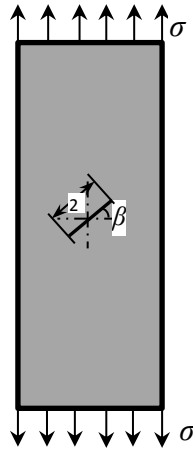
Figure A.1: Inclined center cracked panel
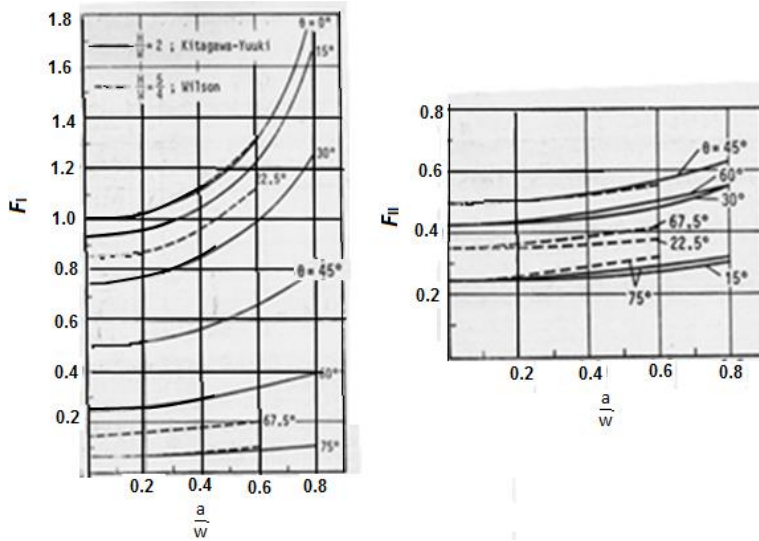
Figure A.2: F_I and F_{II} values for an inclined center cracked panel [11]

Appendix B

B.1 Composite repair manual system guidelines for effective patch length

The CRMS defines the following recommendations for finding the effective patch length and width based on the applied stress and stiffness of panel, patch and adhesive:

The total effective patch length is given as:

$$L_P = \frac{10}{\beta_a} + \frac{2\sigma_0 t_p}{\tau_y} + 2(n_{ply} - 1)dt_{ply} + L_D \tag{B.1}$$

where,

$$\beta_a = \left[\frac{\mu_a}{t_a}\left(\frac{1}{E_P' t_P} + \frac{1}{E_r' t_r}\right)\right]^{1/2} \tag{B.2}$$

$$\sigma_0 = \frac{\sigma_\infty}{(1+S)} \tag{B.3}$$

$$S = \frac{E_r' t_r}{E_p' t_p} \tag{B.4}$$

Approximately, $L_D = 0.79*a$

where n_{ply} is the number of layers, t_{ply} is the patch thickness; d is the drop off distance, σ_∞ is the applied remote stress, t_s is panel thickness, τ_{yz} is shear stress of adhesive and S is stiffness ratio, μ_a is the shear modulus of the adhesive, t_a is thickness of adhesive, E_p' and E_r' are the Young's modulus of panel and reinforcement and t_r is patch thickness. Patch width is also an important parameter which influences the SIF at the crack tip and its dimension depends on the crack length. Based on CRMS guidelines, patch width must be greater than $1.2a$, where a is half crack length. The recommended patch dimension for the given cracked panel is given in Table 3.5 along with the obtained optimum patch dimensions using GA. Looking at the Table 3.5, one can confirm that the arrived optimum patch dimensions satisfy the CRMS guidelines.

B.2 Estimation of energy release rate (ERR) using VCCT

Figure B.1 shows the reaction forces and displacements on twenty-noded solid element along the crack face (lower surface forces are omitted for clarity). The below equation gives the estimate of ERR for all three modes in an element along the crack front and the procedure is adopted from Ref. [13]:

$$G_I = \frac{1}{2\Delta A}[Fx_{Li}(v_{Ll} - v_{Ll^*}) + Fx_{Lj}(v_{Lm} - v_{Lm^*}) + Fx_{Mi}(v_{Ml} - v_{Ml^*}) + Fx_{Ni}(v_{Nl} -$$

$$v_{Nl^*}) + Fx_{Nj}(v_{Nm} - v_{Nm^*})] \tag{B.5}$$

$$G_{II} = \frac{1}{2\Delta A}[Fy_{Li}(u_{Ll} - u_{Ll^*}) + Fy_{Lj}(u_{Lm} - u_{Lm^*}) + Fy_{Mi}(u_{Ml} - u_{Ml^*}) + Fy_{Ni}(u_{Nl} -$$

$$u_{Nl^*}) + Fy_{Nj}(u_{Nm} - u_{Nm^*})] \tag{B.6}$$

$$G_{III} = \frac{1}{2\Delta A}[Fz_{Li}(w_{Ll} - w_{Ll^*}) + Fz_{Lj}(w_{Lm} - w_{Lm^*}) + Fz_{Mi}(w_{Ml} - w_{Ml^*}) +$$

$$Fz_{Ni}(w_{Nl} - w_{Nl^*}) + Fz_{Nj}(w_{Nm} - w_{Nm^*})] \tag{B.7}$$

where *Fx*, *Fy*, *Fz* represent the nodal forces along *x*, *y* and *z* axis respectively, *u*, *v* and *w* represents the displacements along *x*, *y* and *z* respectively and ΔA is the area of the element along thickness given as $\Delta A = b*\Delta a$ where *b* is the thickness of the element and Δa is the element length along crack face. Further, *L*, *M* and *N* represent the three planes passing along the nodes 1, 2 and 3 respectively of element *A* as shown in Fig. B.1.
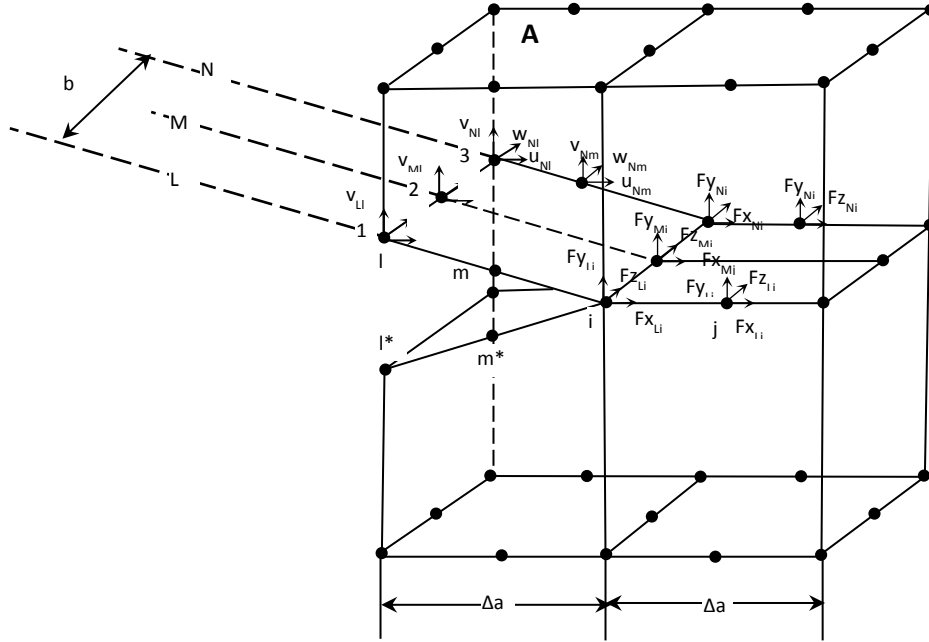
Figure B.1 Estimation of energy release rate for twenty noded brick element omitting forces along the bottom surface

Appendix C

C.1 Hand lay-up process

CFRP patch is made with the hand lay-up process. The fiber is of UD Carbon fiber mat having a weight of 230 g/m^2 (gsm) of Goldbond® make. The matrix is prepared from epoxy resin LY446 mixed with hardener HY941 (Huntsman grade). The resin and hardener are mixed carefully and gently to avoid bubble formation with a 10:1 ratio. Successive layer of Carbon fiber mat and resin mixture is poured and then rolled to squeeze out the excessive resin and make it free of air voids. The composite laminate is then allowed to cure at room temperature for twenty four hours. Figure C.1 shows the series of steps involved in making composite laminate by hand layup process [17].

1. Carbon fiber mat of 230 gsm, 2. Perspex sheet 3. Pouring resin

4. Distribution of resin over the surface 5. Squeezing out excess resin

6. Allowing to cure7. Fabricated laminated sheet 8. Machining

Figure C.1 Steps involved in fabricating composite patch [17]

C.2. Composite laminate characterization

CFRP composite laminates coupons are tested at room temperature under tensile and compressive load to determine the material properties and strength parameters in longitudinal and transverse direction. Also the shear constants are determined with ($\pm45^0$) sample. Tensile tests are performed as per ASTM standard D-3039 [101]. Unidirectional (0^0) specimens are tested to evaluate longitudinal properties. Ten images per second are grabbed at displacement control rate of 2 mm/min. Compression tests are performed as per ASTM standard D-3410[102]. Unidirectional (0^0 & 90^0) specimens are tested to evaluate strengths parameters under compressive load. Ten images per second are grabbed at displacement control rate of 1.124 mm/min. Shear tests are performed as per ASTM standard D-3418 [103]. The (45^0/-45^0) tensile specimens are tested which provides an indirect means to evaluate in-plane shear modulus and shear strengths parameters. Ten images per second are grabbed at displacement control rate of 1 mm/min.

Strain values for both tensile and shear tests are obtained from DIC. Young's moduli in longitudinal and transverse direction are calculated from initial slope of stress–strain curves. In-plane shear modulus is obtained from initial slope of shear stress–shear strain curve. Procedure followed for finding shear stress, shear strength and shear strain is as per ASTM D-3418 and is explained below. The in-plane shear strength for the ($\pm45^0$) laminate is calculated using equation C.1. For finding shear modulus, shear stress at each data point is calculated using equation C.2 and shear strain at each data point is calculated using equation C.3.

$$\tau_{12}{}^m = \left[\frac{P^m}{2A} \right] \tag{C.1}$$

$$\tau_{12i} = \left[\frac{P_i}{2A} \right] \tag{C.2}$$

$$\gamma_{12i} = \varepsilon_{xi} - \varepsilon_{yi} \tag{C.3}$$

where, P^m and $\tau_{12}{}^m$ are the maximum load and the maximum shear stress (shear strength) at or below 5% strain. P_i, τ_{12i} and γ_{12i} are the load, shear stress and shear strain at i^{th} data point. ε_{xi} and ε_{yi} are the longitudinal and lateral normal strains at i^{th} data point[17].

The orthotropic material is characterized by nine elastic constants namely E_{11}, E_{22}, E_{33}, G_{12}, G_{13}, G_{23}, v_{12}, v_{13} and v_{23}. The unidirectional fiber composite laminate is an orthotropic material in which fibers are in the 1–2 plane and the elastic properties are equal in 2–3 direction i.e., $E_{22} = E_{33}$, $G_{12} = G_{13}$, and $v_{12} = v_{13}$. However, the shear modulus G_{23} can be expressed in terms of E_{22} and v_{23} by Eq. C.4. Hence five independent elastic constants are needed to characterize the unidirectional fiber composites and can be considered as

transversely isotropic [16]. The Poisson's ratio v_{21} is expressed in terms of v_{12} by Eq. C.5. Christensen [104] has shown that v_{23} can be related to v_{12} and v_{21} by Eq. C.6 in case of unidirectional fiber reinforced composites. Thus, unidirectional fiber reinforced composites can be characterized by five independent elastic constants.

$$G_{23} = \frac{E_{22}}{2\left(1+v_{23}\right)} \tag{C.4}$$

$$v_{21} = v_{12}\left(\frac{E_{22}}{E_{11}}\right) \tag{C.5}$$

$$v_{23} = v_{12}\left(\frac{1-v_{21}}{1-v_{12}}\right) \tag{C.6}$$

Where E, G and v are the Young's modulus, shear modulus and Poisson's ratio respectively. The obtained material properties are shown in Table 4.3.

C.3 Adhesive thickness measurement

Figure C.2 shows the image taken from optical microscope to estimate the adhesive thickness in repaired panel. The optical microscope is Olympus STM 6 having a resolution of 1 μm. The sample is filed on one side such that it contains portion of patch, panel and adhesive. The sample is observed in the optical microscope at 5x magnification. The measurement is taken at three different locations across the adhesive cross-section. The average value of adhesive thickness obtained is 0.134 mm.
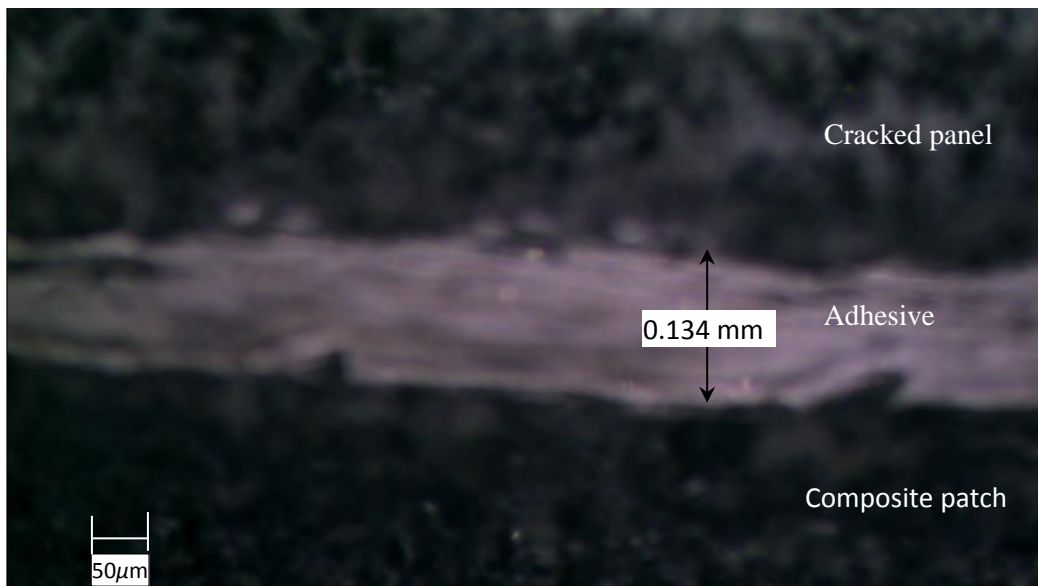
Figure C.2: Adhesive thickness measurement using optical microscope

Appendix D

D.1 History of Crack Blocks

A crack blocks are used to introduce one or more crack fronts into the un-cracked meshed model [97]. Figure D.1 shows the different types of crack blocks used for through thickness crack front modeling. The term crack-block refers to a collection of brick elements stored as a unit cube. These crack-blocks contain either a quarter circular or through crack front elements on one face as shown in Fig. D.1. Part of this face is allowed to open up under loading giving the opening crack face within the crack-block. The meshing procedure involves replacement of one or more 8 or 20 noded brick elements in a user supplied un-cracked mesh by crack-blocks. During the mapping process to introduce the crack-blocks the user can control the size and shape of the generated crack front section for each crack-block. Crack-blocks can be connected together to form distinct crack fronts of the required size in the cracked mesh.

(a)

(b)

(c)

(d)
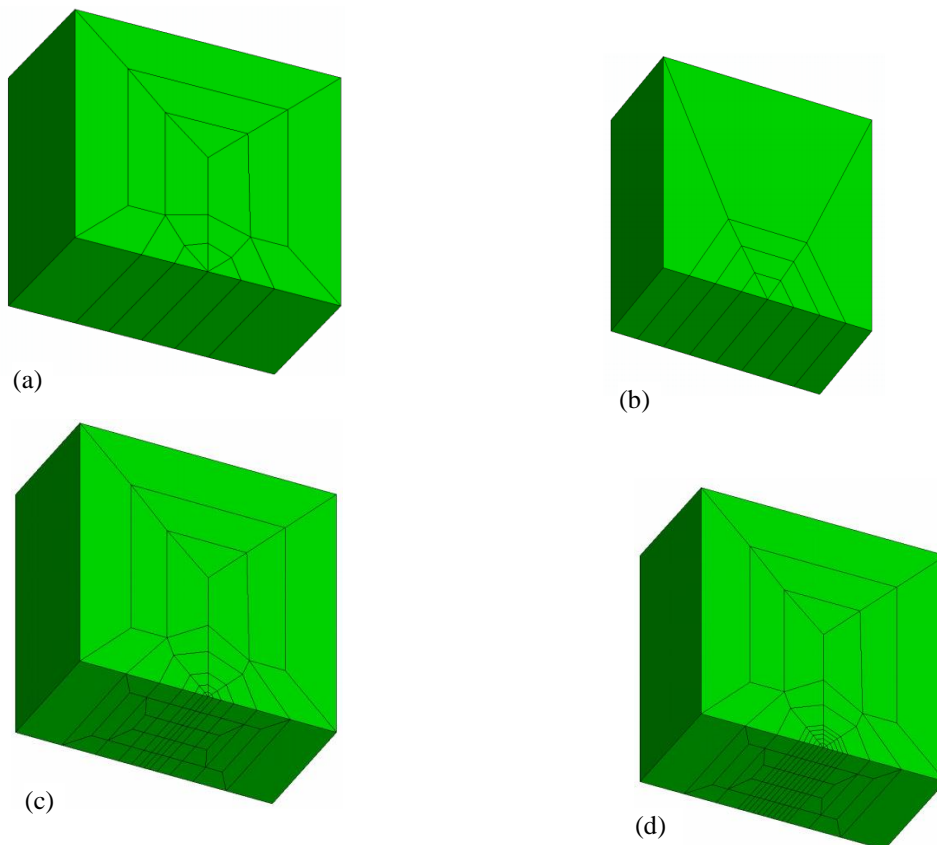
Figure D.1: Various types of crack-blocks (a) s02_t19x1 (b) s05_t12x1 (c) s_t111x5 and (d) s_t151x5 [97]

128

D.2   Estimation of fatigue crack growth direction using Virtual crack extension method

The calculation of energy release rate at a crack front via FEA analysis was first demonstrated by Helen [105]. In this method the change in energy is calculated for a virtual crack extension at the crack front. The accuracy of this method is known to depend upon the magnitude of the applied virtual crack extensions. VCE method estimates the maximum energy release rate at the crack front and its direction for every step increment in crack growth analysis. In this method to determine the direction of the crack growth at any node on a 3D crack front a normal plane is defined and this is a plane that is orthogonal to the crack front tangent at that node (see Fig. D.2). A series of virtual crack extensions in the normal plane will produce a distribution of energy release rates (G_1, G_2, etc.) as shown in Fig. D.2(a). At some angle (θ) to the local crack plane the energy release rate will be a maximum and is denoted as G_{max} (see Fig. D.2(b)). The corresponding angle θ made by G_{max} with the normal plane gives crack growth direction.

(a)   (b)
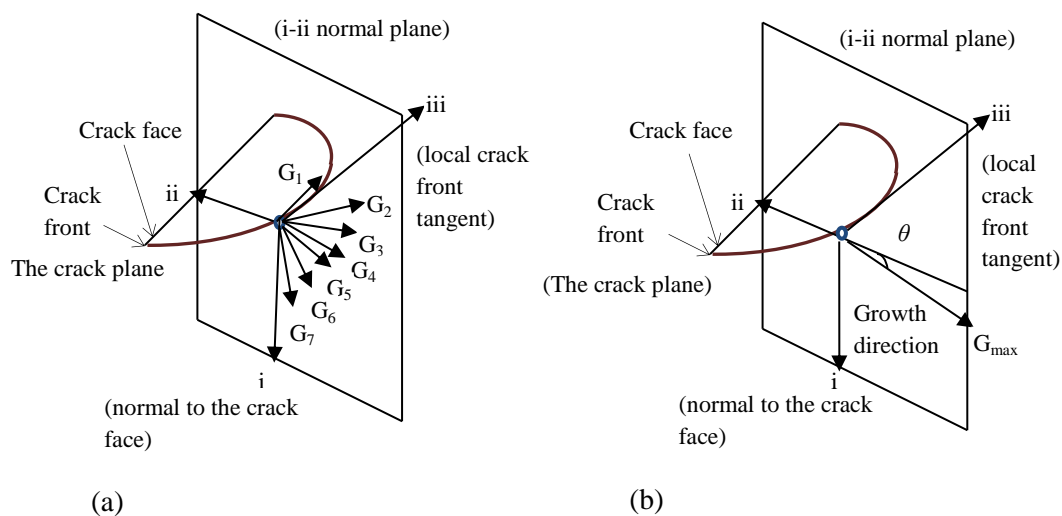
Figure D.2: Virtual crack extension method for identifying crack growth direction

D.3 Estimation of mode I interface fracture toughness

To estimate the mode I interface fracture toughness of the adhesive layer, the double cantilever beam (DCB) specimens are subjected to the pure mode I load. The DCB specimens are fabricated from the Al 2014-T6 plate and the CFRP laminate by bonding them using the Araldite 2011. The DCB specimen of length 125 mm is fabricated, as shown in the Fig. D.3(a). The bonded surfaces of the Al 2014-T6 panel and the CFRP laminate are abraded with the sandpaper (grit class 1200) and then chemically degreased using acetone.

A pair of aluminum piano-hinged loading blocks is then bonded with the DCB specimens. Pre-crack is of length 25 mm is made perpendicular to the loading axis during the specimen fabrication by inserting the 50 mm-long Teflon film of thickness 0.05 mm between the aluminum plate and the adhesive layer. Typical experimental setup for conducting the pure mode I test is shown in the Fig. D.3(b). The tests are performed in MTS landmark equipment under the displacement control mode at a constant rate 2.5 mm/min. The load versus the displacement recorded from the DCB specimen is shown in the Fig. D.4. The maximum displacement and force (1.014 mm and 60 N respectively) obtained from this experiment is taken as the input to the finite element model of the DCB specimen. The critical mode I ERR (G_{Ic}) is estimated using the virtual crack closing technique (VCCT) [106] from the FEA, as explained in the Appendix D.5.

(a)
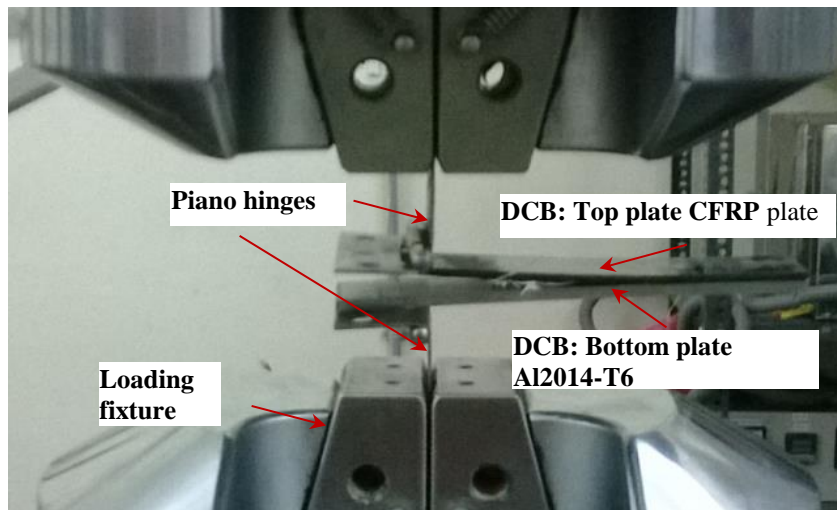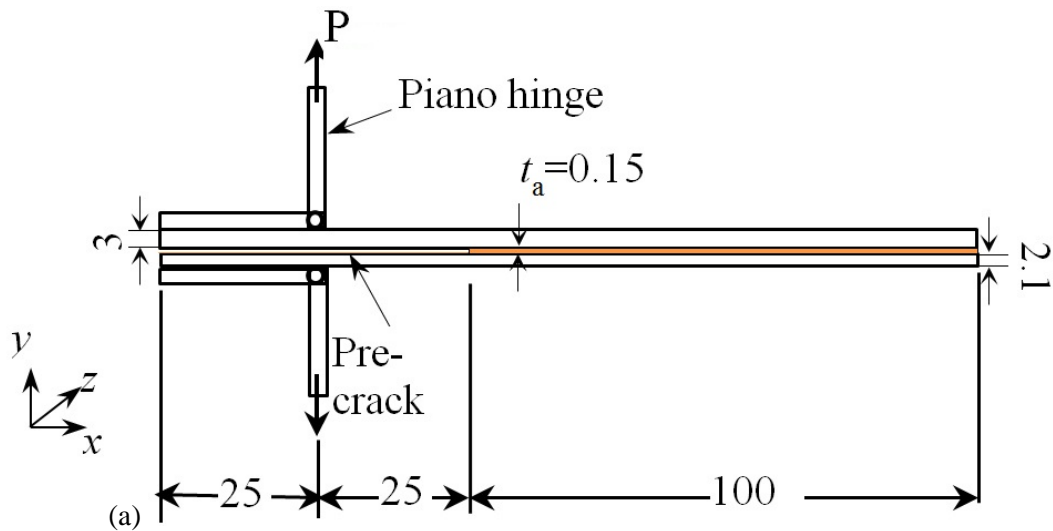
(b)

Figure D.3: DCB (a) Specimen dimensions (b) Test setup for pure mode I

(δ_{max}, P_{max}) : (1.104 mm, 60 N)
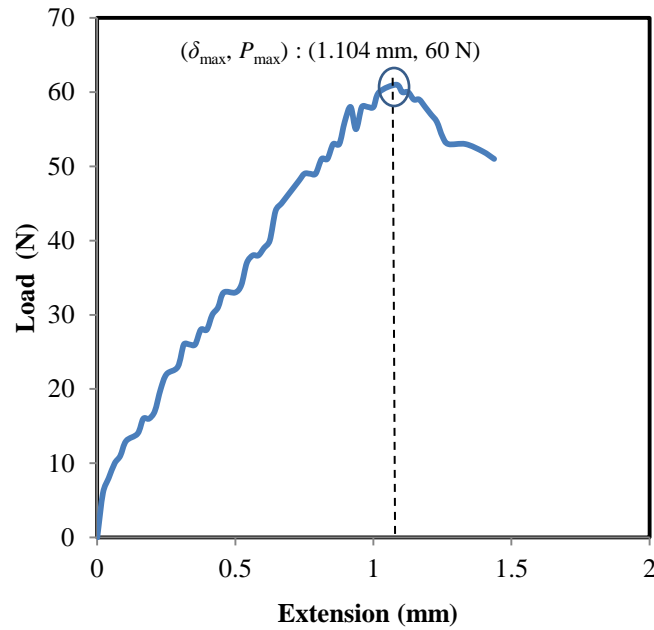
Figure D.4: Load vs extension curve for the DCB specimen

D.4 Estimation of mode II interface fracture toughness

The four point end notched flexure (ENF) specimens are fabricated using the same procedure mentioned in Appendix D.3. Figure D.5 shows the specimen dimensions of ENF specimen and 4 point bend test setup. The span of length 170 mm is considered [107]. Pre-crack of length 55 mm (shown in the Fig. D.5(a)) is made during specimen fabrication by inserting a 55 mm-long Teflon layer between the Al 2014-T6 plate and the CFRP laminate. The experiments are carried out under the displacement control mode at a loading rate 2 mm/min. The load versus the displacement recorded from the ENF specimen is shown in the Fig. D.6. The maximum displacement and force (8.5 mm and 674 N respectively) obtained from this experiment is taken as the input to the finite element model of the ENF specimen. The critical mode II ERR (G_{IIc}) is estimated using the virtual crack closing technique (VCCT) [106] from the FEA, as explained in the Appendix D.5.
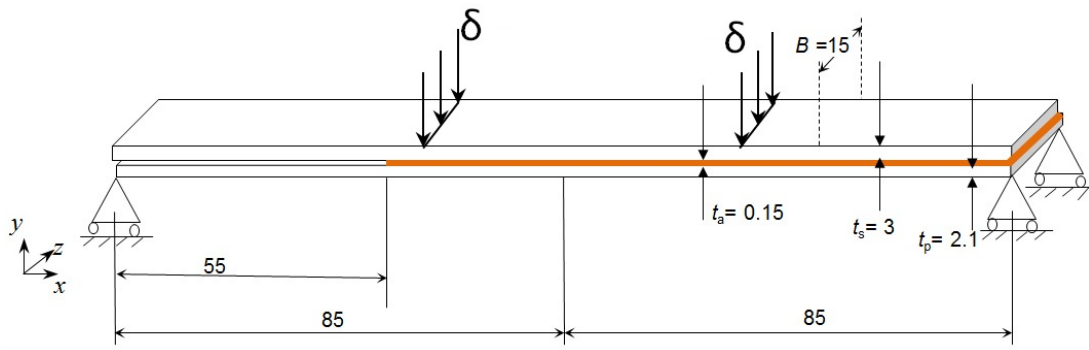
(a)
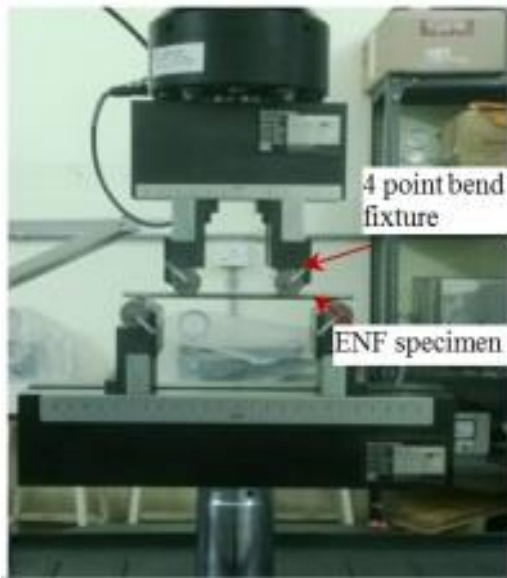
(b)

Figure D.5: ENF specimen under 4 point bend test (a) Specimen (All dimensions are in mm) (b) Test setup.
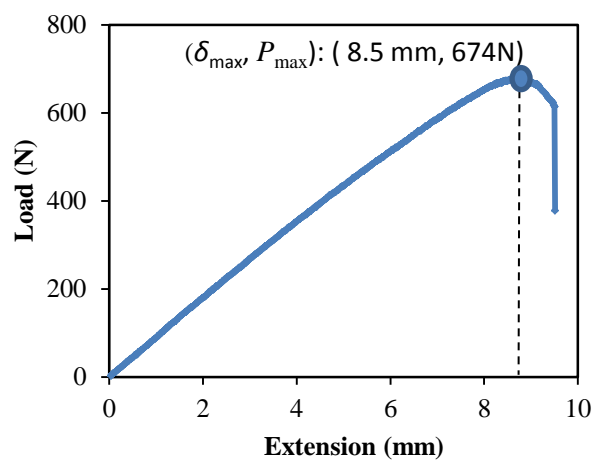
Figure D.6: Load vs deflection of ENF specimen under 4-Point bend test

D.5 Estimation of interfacial fracture toughness using VCCT technique

FEA has been carried out to estimate the interfacial fracture toughness using VCCT technique [106,107]. The DCB and ENF specimens are modeled in ANSYS as per the dimensions given in the Appendix D.3 and Appendix D.4 respectively. For 3D modeling, the 8 noded SOLID 185 element type is used. The DCB and ENF model comprised of 26000 and 36300 elements respectively. In the DCB specimen (mode I), all the nodes along the bottom left corner line are constrained for all the DOF. Similarly, the right corner nodes of the specimen are also constrained for all the DOF. The maximum displacement obtained from the DCB experiment (as shown in the Fig. D.4) is applied as point load at the top edge of the specimen along the Piano hinge (see the Fig. D.3 (a)). But in the ENF specimen (mode II), the displacement and load boundary conditions are applied, as shown in Fig. D.5 (a), that is, the left and the right corner nodes of the ENF specimen are constrained for v displacement. The maximum displacement obtained from the ENF experiment is then applied as point loads along AA´ and BB´ (see the Fig. D.3(a)). The lines AA´ and BB´ trisect the span of ENF specimen.

VCCT relies on the numerical calculation of the nodal forces at the crack tip (F_{xi} and F_{yi}) and the displacements of the adjacent nodes j and m for 3D model as shown in Figure D.7. G_I and G_{II} are then calculated as:

$$G_I = \frac{F_{Yi}\left(v_j - v_m\right)}{2\Delta a} \tag{D.1}$$

$$G_{II} = \frac{F_{xi}\left(u_j - u_m\right)}{2\Delta a} \tag{D.2}$$

The nodal displacement and forces of the initial crack length are obtained by solving the finite element models with above said boundary conditions. The ERR's G_{Ic} and G_{IIc} are estimated for the adhesive layer interface using VCCT from the nodal forces and displacements behind the crack tip, as shown in Eqs. D.1 and D.2 and the values estimated are tabulated in Table 5.2.
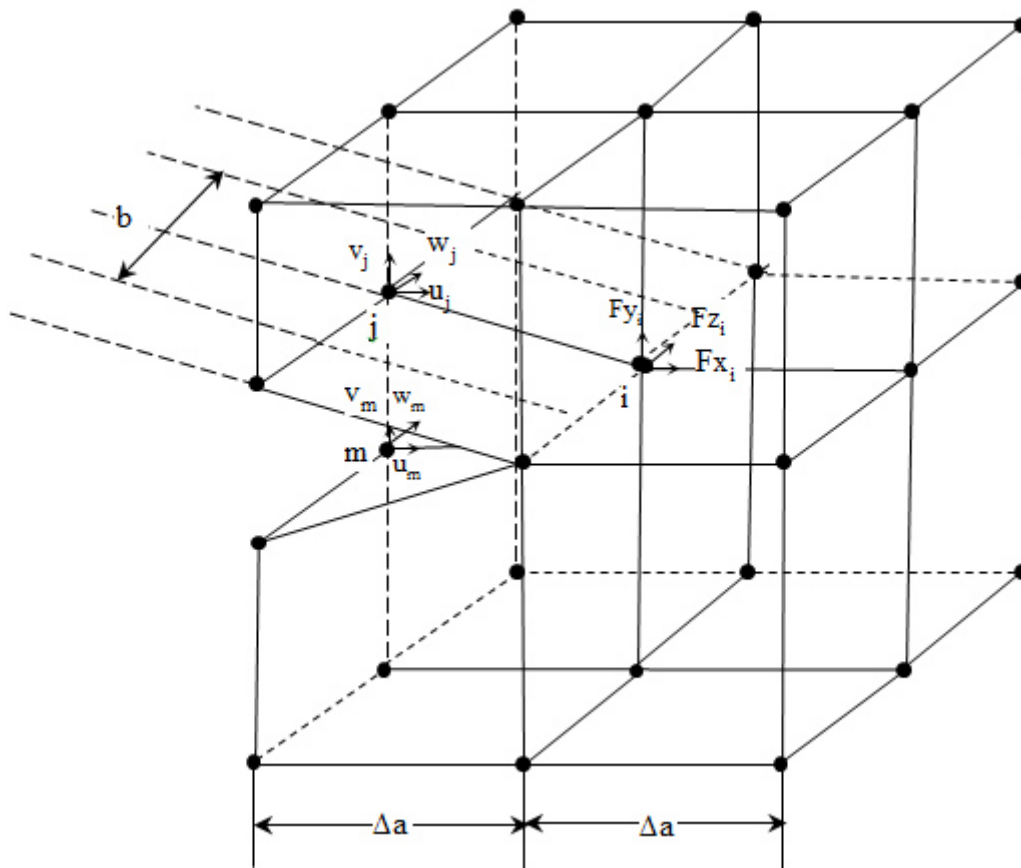
Figure D.7: 3D finite element model showing nodal forces and displacements at the crack tip for 8-noded solid element towards VCCT calculation.

Appendix E

Reviewer 1: Comments

1. P.30, Fig. 2.2, Is it a clear through-thickness crack?. As it is shown in the fig. it is a line crack lying in the middle plane of the panel!. Fig.2.2 (b),(c) need to be corrected.

   Yes, it is a through thickness crack. Fig.2.2 (b) and (c) are modified in the revised thesis.

2. P.37, last line, The unbalanced laminate exhibits the counter bending effect against the bending stresses that present at the unpatched surface. Explain.

   Unbalanced laminate is a fiber composite patch which when under tension exhibits the bending and shear coupling. This reduces the bending stresses that present at the unpatched surface of the single sided repaired panel.

3. P.41, Fig.2.14, The peel stress along the panel length from the overlap end increases linearly to a high value for some distance and then decreases to almost zero value as shown in Fig. 2.14. On the other hand, it is expected to have a high value at the overlap end and then decreases non-linearly inwards. Do you have a literature proof to substantiate your result.

   Yes, peel stresses are high at the overlap end and decreases non- linearly inwards. The same trend is observed in the FE analysis of bonded repair of SDS structure of aircraft which is taken from the Ref. [4]. Figure E.1 shows the variation of peel and shear stress with respect to the distance from the patch overlap end.
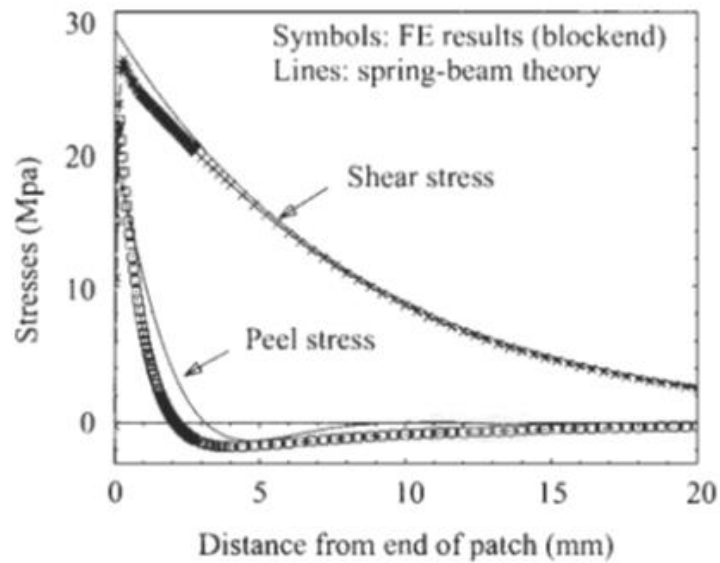
Figure E.1: Stress state in the repaired panel [4]

4. P.46, top line Rectangular patch modeling. It is appropriate to use 'length' instead of 'height' for symbol 'W'

   Authors thank reviewer for the suggestion. Suitably we have got modified "patch height" to "patch length" in the revised manuscript.

5. Fig.3.7, Fig 3.9, Fig.3.10, Fig.3.11: what are the lengths of crack?

   Here, we have carried out the FE analysis repaired panel with different patch shapes having the same crack length of $2a = 10$ mm.

6. P. 63, Fig. 3.18, C: Is it not better to change the text inside the fig. as 'patch length' instead of 'patch height'. Also give units for stresses.

   Authors thank reviewer for the suggestion. We have given units for stresses in the revised Fig. 3.18.

7. P.68, last line, The analysis is carried out in the linear elastic fracture mechanics frame work. Is the LEFM applicable to adhesive bonding layer and metallic panel?

   The cracked panel is of Al 2014 T6 which is of brittle nature. Hence, the plastic zone size will be small due to small scale yielding around the crack tip and one can use LEFM frame work for SIF estimation. Also analysis is not based on exact stress-strain behaviour of the panel and linear elastic model is assumed. In this work the modeling of adhesive layer is considered as an elastic material and not as

136

viscoelastic material which actually it is the case. The above said work can be a separate topic by its own and could be explored as a future work.

8. P.69, Fig. 3.21, This is a thin body subjected to in- plane loading and as such it does not satisfy the conditions of plane strain problem. Pl. refer to a standard book on mechanics.

In a thin plate containing through crack, a plane stress condition exists everywhere except in region near the crack front, where the state of stress is three dimensional (i.e, plane strain). This statement is applicable for plate thickness should be sufficiently small as compared to in plane dimensions of the plate. Nakmura and Park [77] have investigated exact stress field near the tip by determining the degree of plane strain $\sigma_{33}/\upsilon(\sigma_{11}+\sigma_{22})$. They found that the degree of plane strain is zero for plane stress case and it is 1 for plane strain case. This degree of plane strain is 1 when the radial distance from the crack tip is 0.5 times of the thickness of the panel at the midline. Hence to capture this state they used a fine mesh which models a cylindrical region closer to the crack front and also they estimated SIF through the thickness considering plane strain condition. Hence the same meshing procedure is adopted in this study and plane strain conditions are used for estimating K field near the crack tip.

9. P.73, mi3ddle para, 4 lines from bottom, 'estimation of peel and shear strain distribution in thin adhesive layer is obtained using magnified optics coupled with 2D DIC setup'. You know the definition of shearing strain. Can you explain how this is measured experimentally?

In this work, peel and shear strain distribution in thin adhesive layer is obtained using magnified optics coupled with 2D DIC setup. 2D DIC is used to measure the in plane displacements u and v. From these displacements it estimates the strains through numerical differentiation scheme. From the displacements u and v the algorithm estimates shear strain by numerical differentiation techniques.

10. P. 119, middle para, 'Further optimal patch length is 1.95 W, patch width is 0.95 W, where W is the width of the panel'. This is O.K. in a laboratory test. How to fix the value of W in the real aircraft structure?.

The width of panel may be fixed based on the crack length. Here, one cannot find exact width of panel from the crack length, to select the width of panel one has to do

the simultaneous study by varying different *a*/*w* ratio i.e, from small scale to large scale. The above said work can be a separate topic by its own and could be explored as a future work.

11. P. 120, last but one para, ' From this study, based on the fatigue life it can be concluded that double sided patch repair performs better and it is recommended for repair applications'. But this is not practical proposition, as only one side of aircraft surface is accessible for repair

Yes, author agrees with reviewer's suggestion. Based on the availability and accessibility of repair location, single sided repair is often used such as aircraft wings as compared to double sided repair. From the load bearing capability and fatigue life estimation double sided repair is recommended. In this work the experimental and numerical analysis of single sided repaired panel is also carried out for clear understanding of its behaviour.

12. P.121, Therefore, appropriate NDT method such as Infrared thermography can be explored to ensure proper adhesive bonding of the patch over the panel. Using NDT methods, one checks only the quality of bonding and the bond strength cannot be improved. If the bonding is not good the work needs to be redone or rejected.

If the bonding is not good the work needs to be redone by removing the patch using acetone or other cleaning agents. To increase the bond strength and lifetime of the repair it's urged to travel for structural health monitoring techniques.

13. 20 node vs 8 node solid elements: Ch. 2, page 32, 3rd line from bottom, it is seen that 20- noded solid elements have been used, whereas, in Ch. 5, page 101, 4th line from bottom, it is seen that you have used 8- nodded solid elements. You have not given reason for this change in the modeling.

We have conducted mesh refinement studies with twenty noded solid element and eight noded solid element for predicting the fatigue crack growth behavior of inclined center cracked panel. Figure E.2 shows the variation of mode-I SIF with relevancy the various kinds of crack blocks. The variation of SIF through the thickness obtained with eight noded solid elements is similar to that of twenty noded solid element model. In order to reduce the computational time, crack block with 8 noded solid element is considered as part of fatigue crack growth analysis.
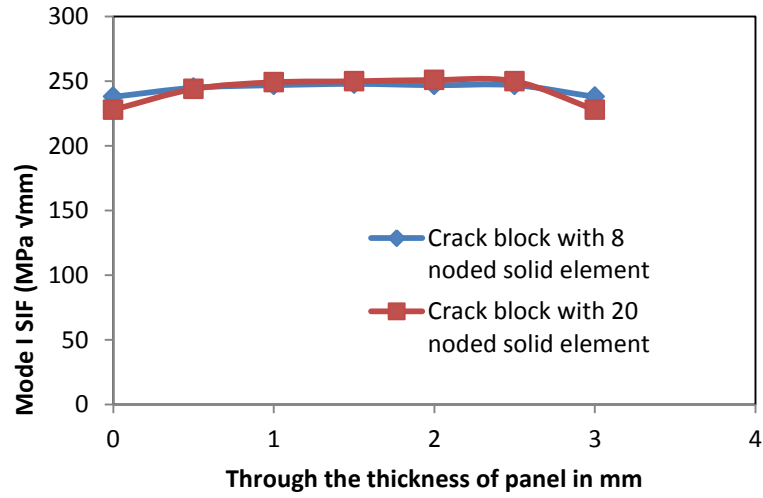
Figure E.2: Variation of mode I SIF with respect to the different kinds of crack blocks

14. Unbalanced laminate: Ch.2, page 42, 5th line from top, 'In case of single sided repair to alleviate SIF especially K_I at unpatched surface, a study is carried out by either increasing patch thickness or usage of unbalanced laminated' You need to explain how unbalanced lamination helps to reduce the SIF at the unpatched surface. Rose's analytical expression for estimating SIF in the repaired panel with single sided patch is :

$$K_R = Y \frac{\sigma_0}{\sqrt{k}} \qquad (E.1)$$

where Y is a geometric factor, which accounts for repairs to center or edge cracks; Y=1 for a repair to a centre crack; σ_0 is the nominal stress that would exist in an un-cracked plate after the application of a patch:

$$\sigma_0 = \frac{\Delta\sigma}{1+S}$$

where $S=E_r t_r / E_p t_p$, k represents a spring constant given by:

$$k = \frac{\beta S}{(1+S)(1-\vartheta_p)}$$

where β is a shear stress transfer length in a representative bonded joint

$$\beta = \sqrt{\left[\frac{G_a}{t_a}\left(\frac{1}{E_p t_p} + \frac{1}{E_r t_r}\right)\right]}$$

In the case of single sided repairs, stress intensity factor is expressed in terms of a bending correction factor:

$$K_R^* = (1+BC)K_R \qquad (E.2)$$

139

where K^{*}_{R} is the stress intensity factor for a one sided repair, the correction term BC is given by:

$$BC = ay_{max} \left(1 - \frac{K_R}{K_U}\right) \frac{t_p(t_p+t_r)}{I}$$

where t_p thickness of the patch, t_r is the thickness of panel, I is the moment of inertia of the repaired panel, K_u is the equivalent SIF of the unrepaired panel.

where y_{max} represents the distance of extreme fiber ply from the neutral axis of the cracked panel

$y_{max} = t_p + Z$

Z is a function of out of plane displacement in the single sided repaired panel. Jones [31] ascertained that usage of unbalanced laminate reduces the out of plane displacement within the single sided repaired panel. The above expressions are valid for single sided repair of straight center cracked panel.

Unbalanced laminate is a fiber composite patch which when under tension exhibits the bending and shear coupling. This counters the bending stresses that present at the unpatched surface of the single sided repaired panel.

15. Page 119, 2nd para, you have concluded that 'extended octagonal patch shape performs better in reducing SIF at the crack tip'. You are trying to justify this based on numerical results. An extended octagonal shape is obtained by simply cutting and removing the four corners of a rectangular piece. That is, by reducing the bonding area, it becomes efficient!

No, it is not acceptable that reducing the bonding area gives more efficiency. Here, we have shown that increasing patch area increases the efficiency interms of SIF reduction. Furthermore the sharp corners are avoided in the extended octagonal patch making it more resistant against debonding as compared to the rectangular patch. Figure E.3 shows the variation of peel stress on the panel along the patch overlap edge for the patch area of 804 mm² and keeping patch length as constant for both the cases. It is observed that peel stresses are high with rectangular patch as compared to extended octagonal patch. Further it is observed that the maximum reduction in peel stress at the sharp corner is of 70% by usage of extended octagonal patch.
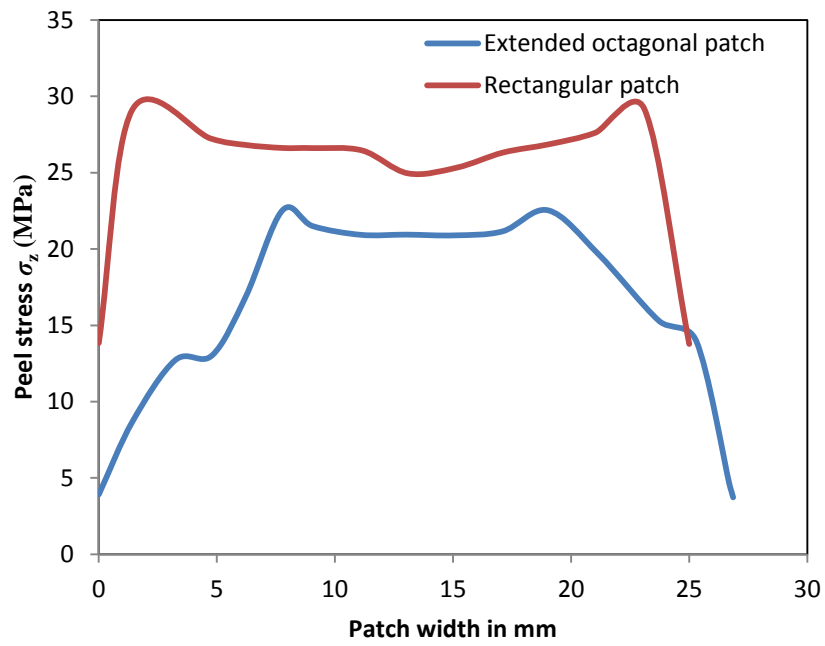
Figure E.3: Comparison of peel stress variation in double sided repair with octagonal and rectangular patch shapes

Appendix F

Reviewer 2: Comments

1. Any repair technology, in general, will not regain full strength. When compared to the static strength of unrepaired plate containing inclined crack, is there any other repair technologies to regain the full strength? A paragraph to show the magnitude of strength regained by repair technology in this study as well as other methods in literature would be useful.

   Yes, author agrees with the reviewer comment. In general, any repair technology will not regain full strength of the panel without any damage. There are other repair technologies such as welding, bolted repair in addition to adhesively bonded repair. As compared to the other repair technologies adhesively bonded repair which is carried out in this study regains the static strength by 12% more than welding and 33% more than bolted repair technology [3]. In particular, there is no literature exists on repair technologies applied over the inclined center cracked panel except adhesively bonded repair [17, 67-70].

2. Similarly, comparative statements between this and any other studies the efficiency of patch repair on fatigue life will be good.

   Baker et.al [3] have carried out experimental fatigue investigation on cracked panel with bolted repairs and boron/epoxy composite doubler under fatigue loading (see Fig. 1.2). They revealed that the fatigue life improvement in adhesively bonded repair is double that of the bolted repair one.

3. The inclined crack appears to always rotate and grow in mode I and fail. Hence, studies on other components, mode II and mode III may not be important in any inclined crack – what is your view?

   Yes, author agrees with the reviewer's suggestion. At the initial crack length there is presence of all modes. As the load increases, the inclined crack appears to always rotate and grow in mode I and fail. Hence, studies on other components, mode II and mode III may not be important and may be neglected.

4. Some typo mistakes: P 34 -Fig. 2.6 (a) caption –Radial, Page 103, Table 5.2 units of fracture toughness is wrong.

Author thanks the reviewer's suggestion. We have corrected the typo mistakes in the caption of Fig. 2.6 (a) and we have included the units of fracture toughness in Table 5.2.

5. What is Mindlin plate layer?- not clear

Sun et.al. [72] performed finite element based study on composite patch repair involving Mindlin plate elements. In their study, Mindlin plate element is used to model both the host plate and patch i.e., aluminium plate and patch are modeled using 2D plane element having four-nodes. The capability of the Mindlin plate finite element in modeling bending effects is apparent. Moreover, the presence of transverse shear deformation in Mindlin plate theory provides a bilinear displacement approximation through the thickness of the aluminium plate. This version of plate theory is used to model plates that are subjected to substantial loading parallel to the plane of the plate (usually due to loads applied at its boundaries). The theory assumes that displacements are small enough to use linearized measures of strain, but includes nonlinear terms associated with the in-plane loading in the equilibrium equations.

6. Although both sided repair is better than single sided as concluded in this study the accessibility for repair in service is a major concern to carry out repair on both sides. Hence, studied in future may be concentrated more towards single sided patch repair technologies.

Yes, author agrees with reviewer's suggestion. In practice, based on the availability and accessibility of repair location, field person can decide the use of single sided or double sided repair. Hence, there is scope exists to carryout research on single sided repair technologies.

Appendix G

Reviewer 3: Comments

1. Page 15, Equation 1.4: "σ_{maxc}" should be replaced with "σ_{max}"

   Author thanks the reviewer for the suggestion. In Equation 1.4: "σ_{maxc}" is replaced with "σ_{max}"

2. Page 23, line 13: The sentence does not read well - "There is lots of research study exists on..".

   Author thanks the reviewer for the suggestion. As per the reviewers suggestion "There is lots of research study exists on.." is replaced with "Many research studies exist on..".

3. Page 23, line 14: "There is very few literatures exist on strain..." may be replaced with "Very few literature exists on strain...".

   Author thanks reviewer for the suggestion. As per the reviewer's suggestion, "There is very few literatures exist on strain..." is replaced with "Very few literature exists on strain..." in the revised manuscript.

4. Page 25, lines 15-16: "there exist out of plane bending leading to more SIF" may be replaced with "there exists an out of plane bending leading to higher SIF.."

   Author thanks reviewer for the suggestion. Appropriately we have got modified "there exist out of plane bending leading to more SIF" with "there exists an out of plane bending leading to higher SIF." in the revised thesis.

5. Page 25, line 4 from bottom: "At last" may be replaced with "Finally"

   Author thanks reviewer for the suggestion. As per the reviewer's suggestion, in Page 25, line 4 from bottom: "At last" is replaced with "Finally".

6. Page 27, line 8: "The estimation of stress..." may be replaced with "The nature of stress..".

   Author thanks reviewer for the suggestion. We have replaced "The estimation of stress..." with "The nature of stress..". in the revised thesis.

7. Page 29, line 3 from the bottom: the layer thickness of the laminate is taken as 0.375 m. But in Figure 2.2 it is shown as 3.175 mm.

   The cracked panel is made of Al 2014 T6 which is of 3.175 mm thickness. The patch is of composite laminate in which each layer thickness is taken as 0.375 mm. For clarity, the above statement is added in the corresponding paragraph in the revised thesis.

8. Page 32, line 15 from bottom: the word "Although" should be removed.

   Author thanks the reviewer for the suggestion. As per the reviewer's suggestion, in page 32, line 15 from bottom: the word "Although" is removed.

9. Page 32, line 14 from bottom:...several researchers [77]. Additional references may be cited.

   Author thanks the reviewer for the suggestion. We have added additional references in the revised thesis.

10. Page 32, line 7 from bottom: 0.8766 t. What is "t" here?

    Author thanks the reviewer for the suggestion. In page 32, line7, "t "represents the thickness of the panel and the same is mentioned in the revised thesis.

11. Page 33, line 8 from bottom "steadied" should be replaced with "steady"

    Author thanks the reviewer for the suggestion. As per the reviewer's suggestion, in page 32, line 15 from bottom: "steadied" is replaced with "steady" in the revised manuscript.

12. Page 34: Fig. 2.6(a): label on the X-axis-"raial" should be replaced with "radial".

    Author thanks the reviewer for the suggestion. In Fig. 2.6(a) label on the X-axis is changed as "radial".

13. Page 35, line 6: "one elements" to be replaced with "one element".

    Author thanks the reviewer for the suggestion. As per the reviewer's suggestion "one elements" is replaced with "one element" in the revised thesis.

14. Page 53, line 16: "configurations is.." to be replaced with "configurations are..".

Author thanks the reviewer for the suggestion. As per the reviewer's suggestion "Configurations is.." is replaced with "configurations are.." in the revised thesis.

15. Page 36, line 7: replace "...reduction of K_I and K_{II} about 78 %.." with "... reduction in K_I and K_{II} of about 78%...".

Author thank reviewer for the suggestion. We have replaced "...reduction of K_I and K_{II} about 78 %.." with "... reduction in K_I and K_{II} of about 78%..." in the revised thesis.

16. Page 47, lines 2-3: The areas 490, 616,706 and 804 does not seem to match with the side length of square with 22, 24, 26 and 28 units, respectively.

Author thank reviewer for the suggestion. As per the reviewer's suggestion the sentence is changed as "..square patch is also modeled same as rectangular patch with side length varying as 22, 24, 26, 28 (all are in mm) having areas 484, 576, 676 and 784 (in mm^2) respectively.

17. Page 72, line 6: "...a need exists to.." may be replace with "...a need arises.."

Author thank reviewer for the suggestion. "A need exists to." is replaced with "...a need arises." in the revised thesis.

18. Page 79, line 8 from bottom: It is mentioned that the strain is obtained from MTS. How does MTS measure the strain? Is it through the platen movement (stroke)?

MTS measure the strain through the extensometer upto the 0.25% of strain and the remaining part is measured using platen movement. The same sentence is appropriately included in the revised thesis.

19. Page 80: Caption of Figure 4.7 (a) and (b) should be interchanged.

Author thank reviewer for the suggestion. Caption of Fig.4.7 (a) and (b) are interchanged in the revised thesis.

20. Page 102, line 11 from bottom: A figure showing the traction – separation relationship may be included.

Suggestion is well taken. As per the reviewer's suggestion we have included the figure 5.4(b) showing the traction –separation relationship in the revised thesis. The figure is described in the below paragraph.

In the bilinear material modeling with increasing interfacial separation the traction across the interface reaches maximum and then decreases gradually and finally vanishes resulting in complete decohesion and failure of the elements at the cohesive zone surface. The normal contact stress (tension) and contact gap behavior is plotted in figure 5.4(b). It shows linear elastic loading (OA) followed by linear softening (AC). The maximum normal contact stress is achieved at point A. Debonding begins at point A and is completed at point C when the normal contact stress reaches zero value. The area under the curve OAC is the energy released due to debonding and is called the critical fracture energy. A cohesive element fails when the separation or fracture toughness of interface attains a material specific critical value.

21. Page 104, line 7: $E'=E/(1-\upsilon^2)$ for plane strain. "Plane strain " is missing.

Suggestion is well taken. We have included the word plane strain in the revised manuscript.

22. Page 114, caption of Table 5.3 should include the units of the numbers presented in the table-(cycles)

Author thanks the reviewer's suggestion. We have included the units of the numbers in the caption of Table 5.3.

References

[1]   http://manokel.com/eng/

[2]   http://www.nytimes.com/2011/04/04/business/04plane.html?_r=0

[3]   A. Baker, L. R. F. Rose and R. Jones. Advances in the Bonded Composite Repair of Metallic Aircraft Structure. 2nd edition. Elsevier Science and Technology, 2002.

[4]   N. Duong and C. H. Wang. Composite Repair - Theory and Design. 1st edition. Elsevier Science and Technology, 2007.

[5]   Alen Baker, Richard Chester and James Mazza. Bonded Repair Technology for aging aircraft. Seminar on Liff Management Techniques for Ageing Air Vehicles, Manchester, United Kingdom, October 2001.

[6]   http://www.google.co.in/imgres/beoing-787-dreamliner-_re

[7]   Quan Wang and Nan Wu. A review on structural enhancement and repair using piezoelectric materials and shape memory alloys. J. Smart Mater. Struct. 21, (2012) 1–14.

[8]   Q. Wang, S. T. Quek and K. M. Liew. On the repair of a cracked beam with a piezoelectric patch. J. Smart Mater. Struct. 11, (2002) 404–410.

[9]   T. L. Anderson. Fracture Mechanics Fundamentals and Applications. 3rd edition, CRC Press, 2004.

[10]   F. Erdogan. Fracture mechanics. International Journal of Solids and Structures 37 (2000) 171–183.

[11]   Y. Murakami, Stress Intensity Factors Handbook, Pergamon, Oxford, 1987.

[12]   B. Cotterell. The past, present, and future of fracture mechanics. , Engineering Fracture Mechanics 69 (2002) 533–553.

[13]   Ronald Krueger. Virtual crack closure technique: History, approach. J. Appl. Mech. Rev 47, (2004) 109–143.

[14]   Hossein Hosseini-Toudeshky, Bijan Mohammadi and Hamid Reza Daghyani. Mixed-mode fracture analysis of aluminum repaired panels using composite patches. Composite Science and Technology 66, (2006) 188–198.

[15]   H. Minnebo, J. Majerus and L. Noels. Displacement extrapolation method: An alternative to J-integral for stress intensity factors computation using X-FEM. IV European Conference on Computational Mechanics (ECCM 2010), Palais des Congres, Paris, France, (May 2010).

[16]   Robert M. Jones. Mechanics of composite materials. 2nd edition. Taylors and Francis, 1999.

[17]   Mohammad Kashfuddoja and M. Ramji. Whole-Field strain analysis and damage assessment of adhesively bonded patch repair of CFRP laminates using 3D-DIC and FEA. Composites Part B Engineering 43, (2013) 46–61.

[18]   Wegman F Raymond. Surface Preparation Techniques for Adhesive Bonding. New Jersey, USA: Noyes Publications, 1989.

[19]   R. L Hastie, R. Fredell and J. W. Dally. A photo elastic study of crack repair. Exp. Mech. 38, (1998) 29–36.

[20]   F. Findik, N. Mrad and A. Johnston. Strain monitoring in composite patched structures. Composite Structures 49, (2000) 331–338.

[21]   Michael A. Sutton, Jean-José Orteu and Hubert W. Schreier, Image Correlation for Shape, Motion and Deformation Measurements: Basic Concepts, Theory and Applications, Springer- Verlag, Berlin, 2009.

[22]   M. A. Sutton, J. H. Yan, V. Tiwari, H. W. Schreier and J. J. Orteu. The effect of out-of-plane motion on 2D and 3D digital image correlation measurements. Optics and Lasers in Engineering 46, (2008) 746–747.

[23]   Bing Pan, Kemao Qian, Huimin Xie and Anand Asundi, Two-dimensional digital image correlation for in-plane displacement and strain measurement: a review, Meas. Sci. Technol. 20, (2009) 2001–2018.

[24]   Shi X. Pang, H. L. J. Zhang, X.R. Liu and M. Ying, Components and Packaging Technologies, IEEE Transactions 27(4), (2004) 649–667.

[25]   C.B. Wang, J. Deng, G. A. Ateshian and C. T. Hung. An automated method for direct measurement of two-dimensional strain distributions within articular

cartilage under unconfined compression, J. of Biomedical Engineering, 124, (2002) 447–467.

[26]   G.F. Xiang, Q.C. Zhang, H.W. Liu, X.P. Wu, and X.Y. Ju. Time resolved deformation measurements of the protevin –le chatelier bands: Scripta Materialia 46, (2007) 721–724.

[27]   B. Pan, A. Asundi, H. Xie and J. Gao, Digital image correlation using iterative least squares and point wise least squares for displacement field and strain field measurements, Optics and Lasers in Engineering 47,(2009) 864–874.

[28]   L. Toubal, M. Karama, and B. Lorrain. Stress concentration in a circular hole in composite plate. Composite Structures 68, (2005) 31–36.

[29]   Jaap Schijve. Fatigue of structures and materials. Kluwar academic publications, 2001.

[30]   Standard Test Method for Measurement of Fatigue Crack Growth Rates. ASTM E647 International. West Conshohocken, Pennsylvania 19428–2949, United States 2001.

[31]   R. Jones. Neutral axis offset effects due to crack patching. Composite Structures 1, (1983) 163–174.

[32]   C. H. Wang, L. R. F. Rose and R. Callinan. Analysis of out-of-plane bending in one-sided bonded repair. J. Solids and Structures. 34, (1998) 1643–1674.

[33]   S. Nabousli and S. Mall. Nonlinear analysis of bonded composite patch repair of cracked alluminium panels. Composite Structures. 41, (1998) 303–313.

[34]   Turaga V. R. S. Umamaheswar and Ripudaman Singh, Modelling of a patch repair to a thin cracked sheet. Engineering Fracture Mechanics 62, (1999) 267–289.

[35]   Chukwujekwu Okafor, Navdeep Singh, U. E. Enemouh and S. V. Rao. Design, analysis and performance of adhesively bonded composite patch repair of cracked aluminium aircraft panels. Composite Structures 71, (2004) 248–270.

[36]   C. H. Duong. A Unified approach to geometrically nonlinear analysis of tapered bonded joints and doublers. International J. Solids and Structures 43, (2004) 3498–3426.

[37] G. J. Tsamasphyros, G. N. Kanderakis, D. Karalekas, D. Rapti, E. E. Gdoutos, D. Zacharopoulos and Z. P. Mariliriga. Study of composite patch repair by analytical and numerical methods. Fatigue Fracture Engineering Mater. Struct. 24, (2001) 631–636.

[38] V. Sabelkin, S. Mall, M. A. Hansen, R. M. Vandawaker and M. Derriso. Investigation into cracked aluminum plate repaired with bonded composite patch. Composite Structures 79, (2007) 44–66.

[39] B. Bachir Bouiadjra, M. Belhouari and B. Serier. Computation of the stress intensity factors for repaired cracks with bonded composite patch in mode I and mixed mode. Composite Structures 46, (2002) 401–406.

[40] A. Mahadesh Kumar and S. A. Hakeem. Optimum design of symmetric composite patch repair to center cracked metallic sheet. Composite Structures 49, (2000) 284–292.

[41] A. Albedah, B. Bachir Bouiadjra, R. Mhamdia, F. Benyahia and M. Es-Saheb. Comparision between double and single sided bonded composite repair with circular shape. Materials and Design 32, (2010) 996–1000.

[42] Mhamdia Rachid B Serier, B. Bachir Bouiadjra, and M. Belhouari. Numerical analysis of the patch shape effects on the performances of bonded composite repair in aircraft structures. Composites Part B Engineering 71, (2011) 1–7.

[43] B. Bachir Bouiadjra, M. Fari Bouanani, A. Albedah, F. Benyahia and M. Es-Saheb. Comparison between rectangular and trapezoidal bonded composite repairs in aircraft structures: A numerical analysis. Materials and Design 32, (2011) 3161–3166.

[44] D. Ouinas, B. Bachir Bouiadjra, B. Achour and N. Benderdouche. Modelling of a cracked aluminium plate repaired with composite octagonal patch in mode I and mixed mode. Materials and Design 30, (2009) 490–494.

[45] D. Ouinas, A. Hebbar, B. Bachir Bouiadjra, M. Belhouari and B. Serier. Numerical analysis of the stress intensity factors for repaired cracks from a notch with bonded composite semicircular patch. Composites: Part B Engineering 40, (2009) 804–810.

[46]   D. Ouinas, M. Sahnoune, N. Benderdouche and B. Bachir Bouiadjra. Stress intensity factor analysis for notched cracked structure repaired by composite patching. Materials and Design 30, (2009) 2302–2308.

[47]   J. D. Mathias, X. Balandraud and M. Grediac. Applying a genetic algorithm to the optimization of composite patches. Composite Structures 84, (2006) 823–834.

[48]   Roberto Brighenti, Andrea Carpinteri and Sabrina Vantadori. A genetic algorithm applied to optimisation of patch repairs for cracked plates. Comput. Methods Appl. Mech. Engg.196, (2006) 466–474.

[49]   D. Ouinas, B. B. Bouiadjra, B. Achour, and N. Benderdouche. Modelling of a cracked aluminium plate repaired with composite octagonal patch in mode I and mixed mode. Materials and Design 30, (2009) 490–494.

[50]   C. Chue and T. J. Liu. The effects of laminated composite patch with different stacking sequences on bonded repair. Composites Engineering 4, (1994) 223–230.

[51]   Ait Yala and A. Megueni. Optimization of composite patches repairs with the design of experiments method. Materials and Design 30, (2009) 200–204.

[52]   T. E. Tay,   F. S. Chau and C. J. Er. Bonded boron-epoxy composite repair and reinforcement of cracked aluminium structures. Composite Structures 34, (1996) 339–347.

[53]   J. J. Schubbe and S. Mall. Investigation of a cracked thick aluminum panel repaired with a bonded composite patch. Engineering Fracture Mechanics 63, (1999) 304–323.

[54]   J. J. Denney and S. Mall. Characterization of disbond effects on fatigue crack growth behavior in aluminum plate with bonded composite patch. Engineering Fracture Mechanics 47, (1997) 407–424.

[55]   Dae- Cheol Seo and Jung-Ju Lee. Fatigue crack growth behavior of cracked aluminium plate repaired with composite patch. Composite Structures 37, (2002) 323–330.

[56]   V. Sabelkin, S. Mall, and J. B. Avram. Fatigue crack growth analysis of stiffened cracked panel repaired with bonded composite patch. Engineering Fracture Mechanics 73, (2006) 1443–1467.

[57]   Woo-Yong Lee and Jung-Ju Lee. Fatigue Behavior of Composite Patch Repaired Aluminum Plate. J. of Composite Materials 39, (2004) 1449–1463.

[58]   Gwo-Chung Tsai and Shyan Bob Shen. Fatigue analysis of cracked thick aluminum plate bonded with composite patches. Composite Structures 64, (2004) 79–90.

[59]   H. Hosseini-Toudeshky, A. Sadegi and H. R. Daghyani. Experimental fatigue crack growth and crack-front shape analysis of asymmetric repaired aluminium panels with glass/epoxy composite patches. Composite structures 71, (2004) 401–406.

[60]   H. Hosseini-Toudeshky and B. Mohammadi. A simple method to calculate the crack growth life of adhesively repaired aluminum panels. Composite Structures, 79, (2007) 234–241.

[61]   M. R. Ayatollahi and R. Hashemi. Mixed mode fracture in an inclined center crack repaired by composite patching. Composite Structures 81, (2007) 264–273.

[62]   M. R. Ayotollahi and R. Hashemi. Computation of stress intensity factors (K_I, K_II) and T-stress for cracks reinforced by composite patching. Composite Structures 78, (2007) 602–609.

[63]   H. K. Chung and W. H. Yang. Mixed-Mode fatigue crack growth in aluminium plates with composite patches. Int. J. Fatigue 24, (2003) 324–333.

[64]   H. Hosseini-Toudeshky and B. Mohammadi. Mixed-mode numerical and experimental fatigue crack growth analyses of thick aluminium panels repaired with composite patches. Composite Structures 91, (2009) 1–8.

[65]   H. Hosseini-Toudeshky, Effects of composite patches on fatigue crack propagation of single-side repaired aluminum panels. Composite Structures 76, (2006) 243–241.

[66]   H. Hosseini-Toudeshky, B. Mohammadi and S. Bakhshandeh. Mixed-mode fatigue crack growth of thin aluminium panels with single-side repair using

experimental and numerical methods. Fatigue Frac Engg Mat Struct 30, (2007) 629–639.

[67]   H. Hosseini-Toudeshky, M. Saber and B. Mohammadi. Mixed-mode 3-D crack propagation of repaired thin aluminum panels using single-side composite patches. Int J Fract 143, (2008) 104–116.

[68]   H. Hosseini-Toudeshky, Ali Jasemzadeh and B. Mohammadi. Investigation of effective parameters on composite patch debonding under static and cyclic loading using cohesive elements. Finite Elements in Analysis and Design74, (2013) 67–74.

[69]   A.J. Comer, K. B Katnam, W. F. Stanley and T. M. Young. Characterizing the behavior of composite single lap bonded joints using digital image correlation. Composite Structures 95, (2013) 500–517.

[70]   M. P. Moutrille, K. Derrien, D. Baptiste, X. Balandraud and M. Grediac. Through-thickness strain field measurement in a composite/aluminium adhesive joint, Composites: Part A 40, (2009) 984–996.

[71]   Steve Vanlanduit, Joris vanherzeele, Roberto lango and Patrick guillaume. A digital image correlation method for fatigue test experiments. Optics and Lasers in Engineering 47, (2009) 371–378.

[72]   C. T. Sun, J. Klug and C. Arendt. Analysis of cracked aluminum plates repaired with bonded composite patches. J. AIAA 34, (1996) 369–374.

[73]   S. Naboulsi and S. Mall. Modelling of a cracked metallic structure with bonded composite patch using the three layer technique, Composite Structures 34, (1996) 294–308.

[74]   J. R. Rice. A path independent integral and the approximation analysis of strain concentration by notches and cracks. J. Applied Mechanics 34, (1968) 379 – 386.

[75]   C. F Shih, B. Moran and T. Nakamura. Energy release rate along a three dimensional crack front in a thermally stressed body. International Journal of Fracture 30, (1986) 79 – 102.

[76]   Ansys version 12.1. User's Documentation. Pennsylvania, U.S: 2009.

[77]   R. Sethuraman, S. K. Maiti. Finite element analysis of doubly bonded crack-stiffened panels under mode I or mode II loading. Engineering Fracture Mechanics 34, (1989) 464–474.

[78]   T. Nakamura and D. M. Parks. Three dimensional stress field near the crack front of a thin elastic plate. J. Applied Mechanics 44, (1988) 804–813.

[79]   J. Barbero Ever. Finite Element Analysis of Composite Materials. Boca Raton, US: CRC Press Taylor and Francis group, 2008, p.90

[80]   L. F. M. D. Silva, J. E. Ramos, M. V. Figueiredo and T. R. Strohaecker. Influence of the adhesive, the adherend and the overlap on the single lap shear strength. Journal of Adhesion and Interface 7(4), (2006) 1–9.

[81]   L. F. M. Da. Silva, R. A. M. Da Silva, J. A. G Chousal and A. M. Pinto. Alternative methods to measure the adhesive shear displacement in the thick Adherend Shear Test. Journal of Adhesion science and Technology 22, (2008) 14–19.

[82]   MATLAB R2010a, Math Works Inc., Natick, USA; 2000

[83]   A. J. Moore and J. R. Tyrer. Phase-stepped ESPI and Moiré Interferometry for Measuring Stress-intensity Factor and *J*-Integral. Experimental Mechanics 34(4), (1994) 306–314.

[84]   C. Taudou and K. Ravi-Chandar. Experimental determination of the dynamic stress-intensity factor using caustics and photoelasticity. Experimental Mechanics 32(3), (1992) 203–210J3

[85]   B. Pan, H. Xie, Z. Wang, K. Qian and Z. Wang. Study on subset size selection in digital image correlation for speckle patterns. Optics Express 16, (2008) 7037–7048.

[86]   Vic Snap/ Vic -3D software, Correlated solutions, Inc; (http:// www.correlatedsolutions.com/)

[87]   K. Naresh Reddy and M. Ramji, Material characterization of al-2014 t6 alloy using 3D-digital image correlation technique, in: Proceedings of International conference on metallurgical and materials processes, products and applications, OPJIT International Journal of Innovation and Research, Raigarh, India, 2014.

[88] K. B Katnam, J. X Dhote and T. M. Young. Experimental analysis of the bond line stress concentrations to characterize the influence of adhesive ductility on the composite single lap joint strength. The Journal of Adhesion 89, (2013) 486–406.

[89] D. Ouinas, B. B. Bouiadjra, S. Himouri and N. Benderdouche. Progressive edge cracked aluminium plate repaired with adhesively bonded composite patch under full width disbond. Journal of composites Part B Engineering 43, (2012) 804–811.

[90] P. Papanikos, K. I. Tserpes and S. P. Pantelakis. Initiation and progression of composite patch debonding in adhesively repaired cracked metallic sheets, Journal of Composite Structures 81, (2007) 303–311.

[91] P. Papanikos, K. I. Tserpes, Labeas G and S. P. Pantelakis. Progressive damage modeling of composite repairs, J. Theoretical and Applied Fracture mechanics, 43, (2004) 189–198.

[92] A. R. Maligno, C. Soutis and V. V. Silberschmidt. An advanced numerical tool to study fatigue crack propagation in aluminium plates repaired with a composite patch. Engineering Fracture Mechanics 99, (2013) 62–78.

[93] S. Vanlanduita, P. Verboven and P. Guillaumea, On-line detection of fatigue cracks using an automatic mode tracking technique, Journal of Sound and Vibration 266 (2003) 805–814.

[94] S. Vanlanduita, P. Guillaumea, Geert Van Der Lindenb, On-line monitoring of fatigue cracks using ultrasonic surface waves, NDT&E International 36 (2003) 601–607.

[95] R. A. Marsh Smith, R. O. Ritchie. Fatigue crack measurement techniques and applications, EMAS publications, West Mldlanda, UK, 1991.

[96] I. Cerny, The use of DCPD method for measurement of growth of cracks in large components at normal and elevated temperatures, Engineering Fracture Mechanics 71 (2004) 837-848.

[97] Zencrack 7.6 User's Manual, London, U.K., 2009.

[98] Chang-Su Ban, Young-Hwan Lee, Jin-Ho Choiand Jin-Hwe Kweon. Strength prediction of adhesive joints using the modified damage zone theory. Composite Structures 86, (2008) 96–100.

[99]   Konstantinos N. Anyfantis. Finite element predictions of composite-to-metal bonded joints with ductile adhesive materials. Composite Structures 94, (2012) 2632–2639.

[100]   Prashant Kumar, Elements of Fracture Mechanics, Tata McGraw Hill Publishing Co. Ltd, New Delhi, 2009.

[101]   Standard Test Method for Tensile Properties of Polymer Matrix Composite Materials. D3039/D3039M-08. 2008.

[102]   Standard test method for compressive properties of unidirectional or cross-ply fiber-resin composites. ASTM D3410-87, 1987.

[103]   Standard Test Method for In-Plane Shear Response of Polymer Matrix Composite Materials by Tensile Test of a ±45˚ Laminate. D3518/D3518M-94, 2007.

[104]   R. M. Christensen. The numbers of elastic properties and failure parameters for fiber composites. J Engg. Mater Technology (1998) 120–110.

[105]   T. K Hellen, On the method of virtual crack extensions. International Journal for Numerical Methods in Engineering, 9, (1974) 187–207.

[106]   Ye Zhang, Anastasios P. Vassilopoulos and Thomas Keller. Mode I and II fracture behavior of adhesively-bonded pultruded composite joints. Engineering Fracture Mechanics 77, (2010) 128–143.

[107]   M. F. S. F., DeMoura, R. D. S. G. Campilho and J. P. M. Gonsalves, Pure mode II fracture characterization of composite bonded joints, International Journal of Solids and Structures 46 (2009) 1589-1595.

List of publications based on the thesis work

International Journal Publications

[1] M. Ramji and R. Srilakshmi. Design of composite patch reinforcement applied to mixed mode cracked panel using Finite element analysis. J Reinforced Plastics and Composites 39, (2012) 484-494.

[2] M. Ramji and R. Srilakshmi and M. Bhanu Prakash. Towards optimization of patch shape on the performance of bonded composite repair using FEM. Composites Part B: Engineering 44, (2013) 710-720.

[3] R. Srilakshmi and M. Ramji. Experimental investigation of adhesively bonded patch repair of an inclined center cracked panel using DIC. J Reinforced Plastics and Composites 33, (2014) 1130-1147.

[4] R. Srilakshmi, M. Ramji and C. Viswanath. Fatigue crack growth study of CFRP patch repaired Al 2014-T6 panel having an inclined center crack using FEA and DIC. Engineering Fracture mechanics, doi:10.1016/j.engfracmech.2014.12.012

International Conference Publications

[1] M. Ramji and R. Srilakshmi. Finite Element Modeling of Composite Patch repair. Proceedings of 4th International Conference on Theoretical, Applied Computational and Experimental Mechanics, Dec 27-29, 2010; IIT Kharagpur, India: 286-288.

[2] R. Srilakshmi and M. Ramji. Composite Repair for mixed mode cracks using unbalanced laminates. Proceedings of International Conference on Computational methods in manufacturing, Dec 14-16, 2011; IIT Guwahati, India: 216-224.

[3] R Srilakshmi and M. Ramji. Fatigue crack growth estimation of three dimensional cracked panel repaired with single and double sided patch. Proceedings of 4th

International Conference on Structural Stability and Dynamics, Jan 4-6, 2012; MNIT Jaipur, India: 478-484.

[4] R. Srilakshmi and M. Ramji. Progressive Damage analysis of adhesively bonded repairs using FEA Proceedings of 4th International Congress on Computational mechanics and Simulation, Dec 9-12, 2012; IIT Hyderabad.

[5] R. Srilakshmi and M. Ramji. Fatigue life estimation of cracked and repaired panel using FEA. Proceedings of International Conference on Computer aided Engineering, Dec 19-21, 2013; IIT Madras, India: 342-348.